

Duquesne University

Duquesne Scholarship Collection

Electronic Theses and Dissertations

Summer 8-5-2023

SYSTEMATIC PRODUCT AND PROCESS DESIGN OF VERSATILE PERFLUOROCARBON NANOEMULSIONS FOR ELIMINATION OF HYPOXIA AND REACTIVE OXYGEN SPECIES

Eric Lambert

Follow this and additional works at: <https://dsc.duq.edu/etd>

 Part of the [Pharmaceutics and Drug Design Commons](#)

Recommended Citation

Lambert, E. (2023). SYSTEMATIC PRODUCT AND PROCESS DESIGN OF VERSATILE PERFLUOROCARBON NANOEMULSIONS FOR ELIMINATION OF HYPOXIA AND REACTIVE OXYGEN SPECIES (Doctoral dissertation, Duquesne University). Retrieved from <https://dsc.duq.edu/etd/2260>

This One-year Embargo is brought to you for free and open access by Duquesne Scholarship Collection. It has been accepted for inclusion in Electronic Theses and Dissertations by an authorized administrator of Duquesne Scholarship Collection. For more information, please contact beharyr@duq.edu.

SYSTEMATIC PRODUCT AND PROCESS DESIGN OF VERSATILE
PERFLUOROCARBON NANOEMULSIONS FOR ELIMINATION OF HYPOXIA
AND REACTIVE OXYGEN SPECIES

A Dissertation

Submitted to the Graduate School of Pharmaceutical Sciences

Duquesne University

In partial fulfillment of the requirements for
the degree of Doctor of Philosophy

By

Eric Lambert

August 2023

Copyright by

Eric Lambert

2023

SYSTEMATIC PRODUCT AND PROCESS DESIGN OF VERSATILE
PERFLUOROCARBON NANOEMULSIONS FOR ELIMINATION OF HYPOXIA
AND REACTIVE OXYGEN SPECIES

By

Eric Lambert

Approved May 31, 2023

Jelena M. Janjic, PhD
Associate Professor of Pharmaceutics
Graduate School of Pharmaceutical
Sciences, Duquesne University
(Committee Chair)

James K. Drennen III, PhD
Dean, School of Pharmacy and Graduate
School of Pharmaceutical Sciences,
Duquesne University
(Committee Member, Dean)

Peter L. D. Wildfong, PhD
Associate Professor of Pharmaceutics
Graduate School of Pharmaceutical
Sciences, Duquesne University
(Committee Member)

Kevin J. Tidgewell, PhD
Associate Professor of Medicinal
Chemistry
Graduate School of Pharmaceutical
Sciences, Duquesne University
(Committee Member)

Vijay S. Gorantla, MD, PhD
Professor, Wake Forest Institute for
Regenerative Medicine
(Committee Member)

ABSTRACT

SYSTEMATIC PRODUCT AND PROCESS DESIGN OF VERSATILE PERFLUOROCARBON NANOEMULSIONS FOR ELIMINATION OF HYPOXIA AND REACTIVE OXYGEN SPECIES

By

Eric Lambert

August 2023

Dissertation supervised by Jelena M. Janjic, PhD.

According to a 2022 report, organs destined for transplantation are discarded 15% of the time for various reasons (Israni *et al.* 2022). This highlights a critical need in transplant practices. Transplant donor tissues are in need of essential nutrients, including molecular oxygen, to maintain integrity during preservation. A current trend in preservation is to perfuse the *ex vivo* tissue graft with nutrient-rich aqueous perfusate on a closed circuit. This practice, known as machine perfusion (MP) is limited by the absence of an oxygen-carrying component in the perfusate. Additionally, injuries to the recipient are sustained on reperfusion of the transplanted graft. Reactive oxygen species (ROS) are produced during ischemia-reperfusion (IR) events such as transplantation and contribute to secondary oxidative damage. Perfluorocarbon (PFC) materials, which are characteristically good oxygen carriers, can be utilized to fulfill the

role of oxygen carrier. PFCs are hydrophobic and must therefore be formulated as a liquid dispersion (*e.g.*, PFC-in-water nanoemulsion (NE)) in order to be considered as a biomedical-grade product. Stability difficulties is one reason why PFC-NEs have not acquired commercial success. We believe that utilization of systematic Quality by Design (QbD) principles may hold the key to overcoming poor stability and generating a stable, proficient oxygen carrier. The central hypothesis of this work is that QbD-centered development can yield colloiddally stable antioxidant- and molecular-oxygen-co-loaded PFC-NEs for action against oxidative stress and hypoxia in *ex vivo* machine perfusion preservation. We test this hypothesis by adapting QbD concepts to the development of PFC-NEs. We used quality risk management and multivariate statistical modeling to deepen the understanding of the process and composition of PFC-NEs. We proposed an optimal formulation and demonstrated its process robustness. Finally, we illustrate its impact in scavenging radical species and delivering oxygen intracellularly in macrophages.

DEDICATION

I dedicate this dissertation to my grandparents Joanne and Silas.

ACKNOWLEDGEMENT

This dissertation would not have been possible without the support and encouragement of many people, and I am grateful for all who played a role.

I am eternally grateful to my supervisor and committee chair, Dr. Jelena M. Janjic who generously gave me this opportunity and who gave me an environment to find my talents. I am equally grateful for my committee members for offering guidance and critical thinking directed towards this project.

I want to thank all those who assisted experimental design and data collection for this project, including my lab members and dedicated members of collaborating groups.

A tip of my cap to others from the greater scientific community for their contributions, in particular, those from the galactosemia research community, who inspired me to make this commitment.

Loyal, good-hearted friends from Duquesne, in particular Mike Wasko and Michele Herneisey for offering premium editing services at a moment's notice, and for making this place memorable.

Burley. Yes, there actually IS an adorable big-eyed cat hiding under that enormous fluffy black ball of fur. I adopted him on Friday the 13th, and while some say that the overwhelming bad luck accrued from this superstitious combination caused a worldwide pandemic, the fact is the WHO officially declared COVID-19 a pandemic just 2 days prior.

Mom, Dad, and Mike for their unconditional love and support.

TABLE OF CONTENTS

ABSTRACT	iv
DEDICATION	vi
ACKNOWLEDGEMENT	vii
LIST OF TABLES	xiii
LIST OF FIGURES	xvi
LIST OF ABBREVIATIONS.....	xxv
Chapter 1. Introduction	1
1.1. Statement of the problem.....	1
1.2. Hypothesis and specific aims.....	5
1.2.1. Specific aim 1	5
1.2.2. Specific aim 2	5
1.2.3. Specific aim 3	6
1.3. Dissertation content outline	7
1.4. Literature review	8
1.4.1. Acknowledgements.....	8
1.4.2. Unique Properties of Perfluorocarbons Applicable for Regenerative Medicine	9
1.4.3. Perfluorocarbon Nanoemulsions as Versatile Nanomedicines	10
1.4.4. Ischemia and Reperfusion Injury – Key Challenges in Regenerative Medicine	12
1.4.5. Preservation Solution and Perfusate Composition and Present Status	15
1.4.6. Hemoglobin Based Oxygen Carriers (HBOCs) – Progress and Pitfalls	17
1.4.7. Perfluorocarbon Oxygen Carriers – Premise and Potential	18
1.4.8. PFC Nanoemulsions as Oxygen Therapeutics in the Clinic	21
1.4.9. PFC Nanoemulsions for Oxygen Delivery - Current Challenges for Pharmaceutical Development	26
1.4.10. Future Perspectives	37
Chapter 2. Multiple Linear Regression Applied to Predicting Droplet Size of Complex Perfluorocarbon Nanoemulsions for Biomedical Applications	38
2.1. Acknowledgements.....	38

2.2. Abstract	38
2.3. Introduction.....	39
2.4. Materials and Methods.....	42
2.4.1. Materials	42
2.4.2. Solubility of PFPE-tyramide.....	43
2.4.3. Experimental Design.....	43
2.4.4. Preparation of Nanoemulsions	43
2.4.5. Nanoemulsion Characterization	44
2.4.6. Centrifugation Stability Test.....	44
2.4.7. Serum Incubation Stability Test.....	44
2.4.8. Percent Size Change and PDI Change Calculations	45
2.4.9. Regression Model	45
2.4.10. Data Analysis	46
2.5. Results and Discussion	46
2.5.1. Formulation Development	46
2.5.2. Experimental Design.....	47
2.5.3. Formulation Characterization	49
2.5.4. Stress Stability.	51
2.5.5. Linear Regression Model.....	53
2.6. Conclusions.....	58
Chapter 3. Quality by Design Approach Identifies Critical Parameters Driving Oxygen Delivery Performance in Vitro for Perfluorocarbon Based Artificial Oxygen Carriers.....	61
3.1. Acknowledgements.....	61
3.2. Abstract	61
3.3. Introduction.....	62
3.4. Materials and Methods.....	65
3.4.1. Materials	66
3.4.2. Failure Mode, Effects, and Criticality Analysis.....	66
3.4.3. Design of Experiments.....	67
3.4.4. Production of Triphasic Nanoemulsions.....	68
3.4.5. Colloidal Characterization and Quality Control	68
3.4.6. Oxygen Release Kinetics	69

3.4.7. ¹⁹ F Nuclear Magnetic Resonance Characterization.....	70
3.5. Results and Discussion	71
3.5.1. Definition of Product Quality Attributes and Target Specifications ..	71
3.5.2. Production, Characterization, and Quality Control of PFC-NEs	73
3.5.3. Evaluation of Biphasic PFC-NEs as Design Controls to Triphasic Systems	77
3.5.4. Risk Management and Design of Experiments.....	79
3.5.5. Evaluation of Triphasic PFC Nanoemulsions.....	84
3.5.6. Regression Model Construction and Evaluation.....	89
3.5.7. Scale-up of PFOB Nanoemulsions	92
3.6. Conclusions.....	93
Chapter 4. Multivariate Process Analysis of Perfluorocarbon Nanoemulsion- Based Artificial Oxygen Carriers.....	95
4.1. Materials and Methods.....	100
4.1.1. Materials	100
4.1.2. Indocyanine green stearylamine (ICG-SA) stock preparation	100
4.1.3. Nanoemulsion preparation	101
4.1.4. Dynamic light scattering	101
4.1.5. Colloidal attributes and quality control evaluation	102
4.1.6. Near infrared fluorescent attributes evaluation.....	102
4.1.7. In vitro oxygen release evaluation	103
4.1.8. ¹⁹ F quantitative nuclear magnetic resonance (qNMR) spectroscopy	104
4.1.9. Principal components analysis (PCA)	104
4.1.10. Hierarchical clustering	105
4.2. Results and discussion	105
4.2.1. Composition modification and optimization.....	105
4.2.2. In vitro oxygen release characterization and model reexamination..	111
4.2.3. Comparison of production scale and high shear processing equipment	114
4.2.4. Failed batch rescue.....	121
4.2.5. Principal components analysis	122
4.3. Conclusions.....	128
4.4. Acknowledgements.....	129

Chapter 5. Multifunctional Perfluorocarbon Nanoemulsions Eliminate Hypoxia and Reactive Oxygen Species in Murine Macrophages <i>in vitro</i>	130
5.1. Materials and Methods.....	132
5.1.1. Materials	132
5.1.2. Nanoemulsion preparation	132
5.1.3. Dynamic light scattering	133
5.1.4. Colloidal attributes and quality control evaluation.....	133
5.1.5. ¹⁹ F quantitative nuclear magnetic resonance (qNMR) spectroscopy	133
5.1.6. Resveratrol (RSV) drug quantification	134
5.1.7. In vitro resveratrol drug release	134
5.1.8. Resveratrol chemical stability evaluation	135
5.1.9. In vitro oxygenation stability	135
5.1.10. Cellular viability	135
5.1.11. Image-iT Hypoxia Green flow cytometry.....	136
5.1.12. Nitrite/nitrate colorimetric assay.....	136
5.2. Results and discussion	137
5.2.1. Preparation and characterization of resveratrol-loaded PFC-NE.....	137
5.2.2. BCS Class II model small molecule antioxidant loading and stability	140
5.2.3. G2-NE stability in machine perfusion circuit	145
5.2.4. Pharmacological effects of oxygen and RSV in murine macrophages	147
5.3. Conclusions.....	150
5.4. Acknowledgements.....	151
Chapter 6. Optical Microscopy as a Complementary Tool to Capture Oversized Population in Droplet Size Distribution of Nanoemulsions	152
6.1. Materials and Methods: Materials	154
6.1.1. Nanoemulsion preparation	154
6.1.2. Filtration, centrifugation, and serum incubation colloidal stability tests	155
6.1.3. Thermal cycling quality control test	155
6.1.4. Dynamic light scattering	155
6.1.5. Optical microscopy image acquisition.....	155

6.1.6. Image processing and analysis	156
6.1.7. Automation of image processing and analysis.....	156
6.2. Results.....	157
6.2.1. DLS characterization of nanoemulsions	157
6.2.2. Optical microscopy characterization.....	160
6.2.3. Image analysis automation.....	166
6.2.4. PFAT5 calculation	171
6.3. Discussion and conclusions	172
Chapter 7. Summary	174
References.....	181
Appendix A. Chapter 2 Supplemental Data.....	209
Appendix B. Chapter 3 Supplemental Data	220
Appendix C. Chapter 4 Supplemental Data	236
Appendix D. Chapter 5 Supplemental Data.....	243
Appendix E. Chapter 6 Supplemental Data	245

LIST OF TABLES

Table 1.1. Composition of selected commonly reported clinical preservation solutions. UW, University of Wisconsin; IGL, Institute Georges Lopez, E, extracellular; I, intracellular.	15
Table 1.2. Select Commercial Examples of PFC Nanoemulsions for Oxygen Delivery and Tissue Preservation.	24
Table 1.3. Composition Diversity in PFC Formulations for Oxygen Delivery Applications.	30
Table 2.1. Composition and z-average droplet size of nanoemulsions. Reported as mean \pm standard deviation of 3 measurements. Note: Component levels are proportional to the excipient concentration, % v/v. In all NEs, oil(s) plus solubilizer was present at 8% v/v and tyramide was at 0.0013% w/v (if present). Non-ionic surfactant was present at 2.3% w/v.	48
Table 2.2. Regression coefficients and model assessment for crossed quadratic model. .	54
Table 2.3. Regression coefficients and model assessment for reduced least squares model.	56
Table 2.4. Droplet size, polydispersity index, and zeta potential for NE 15 and its four replicates. Reported as mean \pm standard deviation of three measurements.	58
Table 3.1. Critical quality attributes (CQAs) for the reported perfluorocarbon nanoemulsions, specifications, and justifications. PDI, polydispersity index; d, diameter; mV, millivolt; nm, nanometer.	73
Table 3.2. List of formulations and the design matrix in 2-level, 6-factor d-optimal screening design of experiments. The micelle solution was comprised of 2% w/v Pluronic P-105 and 3% w/v Pluronic P-123. X1, Internal phase fraction by vol [-1=0.08, +1=0.1428]; X2, hydrocarbon-to-perfluorocarbon (HC:PFC) ratio by volume [-1=0.857, +1=1.857]; X3, Number of passes [-1=4, +1=6]; X4, Proportion transcutol in internal phase (IP) by vol [-1=0.05, +1=0.3]; X5, PFC type [a=perfluoro-15-crown-5-ether (PCE), b=perfluorooctyl bromide (PFOB)]; X6, Continuous media type [a=deionized water, b=normal saline]. BN, biphasic nanoemulsion; TN, triphasic nanoemulsion; MCT, medium chain triglyceride. Note: definitions and discussion of coded factors follows in the end of section Risk Management and Design of Experiments.	75
Table 3.3. Evaluation of critical quality attributes (CQAs). Cells shaded gray meet the CQA specification. NE, nanoemulsion; BN, biphasic nanoemulsion; TN, triphasic nanoemulsion; PDI, polydispersity index; C_{max} , maximum dissolved O ₂ concentration.	76

Table 3.4. Reduced regression model terms and goodness-of-fit for C_{\max} and thermal stability Δ size. HC, hydrocarbon; PFC, perfluorocarbon; IP, internal phase; R^2 , Coefficient of Determination; RMSE, root mean square error.....	90
Table 4.1. Compositions, processing, and attributes of all G2-NE batches considered in this study. PFOB, perfluorooctyl bromide; PBS, phosphate-buffered saline; RSV, resveratrol; NA, not applicable; ICG, indocyanine green; NM, not measured...	108
Table 4.2. Reproducibility statistics of G2-NEs across batch size and processor. z-averages are the mean of 3 measurements.....	120
Table 5.1. Subset of second-generation PFC-NEs used in <i>in vitro</i> evaluation. The naming convention from the previous chapter (Chapter 4) is preserved. PFOB, perfluorooctyl bromide; PBS, phosphate-buffered saline; RSV, resveratrol; PDI, polydispersity index.....	139
Table 5.2. G2-NE stability to syringe filtration and centrifugation. Data are reported as mean and standard deviation of z-average (nm) ($n = 3$ measurements per group).	139
Table 5.3. G2-NE stability to 72-hr incubation in fetal bovine serum (FBS) at 37 °C. Data are reported as mean and standard deviation of z-average (nm) ($n = 3$ measurements per group).....	140
Table 5.4. RSV-NE encapsulation and oxidation stability.	142
Table 6.1. DLS droplet size summary of the cycling and the control age-matched samples. Droplet size descriptors are the average of three measurements reported in nm, and PDI is the average of three measurements.....	159
Table 6.2. Descriptive statistics of nanoemulsion droplets imaged with the optical microscope.	163
Table 6.3. Automatic thresholding algorithms.	167
Table 7.1. Quality Target Product Profile (QTPP) for perfluorocarbon nanoemulsion artificial oxygen carriers.	177
Table A.1. PFPE-tyramide solubility results by visual analysis. Scale bar reads 100 μm . Transcutol was selected as the carrier for PFPE-tyramide on the basis of appearance of each sample to the naked eye and appearance under 40x magnification.	210
Table A.2. Regression coefficients for PFPE-tyramide in simple linear regression.	212
Table A.3. Regression coefficients for special cubic model.....	213

Table B.1. Multiple linear regression (MLR) was used to fit models to two attributes (responses): oxygen release C_{max} and thermal stability % size change. These two responses make up the backbone of a successful artificial oxygen carrier. Goodness of fit statistics for reduced models is demonstrated by R^2 , root mean square error (RMSE), and leave-one-out cross validation (LOOCV) RMSE. ...	224
Table B.2. Analysis of variance (ANOVA) for reduced MLR models. ANOVA compares the variance explained by the model and the variance unaccounted for (error) and based off this calculates the F ratio. From the F ratio at the specified degrees of freedom (DF), a p-value (Prob > F) is calculated for each model. Significance was taken at $p < 0.05$	225
Table C.1. General compositions of generation 1 and 2 nanoemulsions. G2-NE1 (bottom row) was used to validate the C_{max} model developed in Chapter 3. PFC, perfluorocarbon; PCE, perfluoro-15-crown-5-ether; PFOB, perfluorooctyl bromide; IP, internal phase; HC, hydrocarbon; CP, continuous phase; MLR, multiple linear regression.....	237
Table C.2. Eigenvalues and variance explained from the first 10 principal components from PCA on all data.	241

LIST OF FIGURES

Figure 1.1. General flow chart of a machine perfusion circuit. 2

Figure 1.2. Oxygen release profile in PFCs as compared to cell-free hemoglobin. Heme molecules in cell-free Hb coordinate O₂ at a specific partial oxygen pressure (pO₂) range, resulting in the sigmoidal relationship between pO₂ and O₂ content. The uptake and release of O₂ from PFCs is driven by Henry’s Law, in which the amount of O₂ incorporated into PFCs in nanodroplet is linearly related to pO₂. Figure reproduced with permission from Farris *et al.* (2)..... 20

Figure 1.3. Comparison of biphasic nanoemulsion cross-section (left) and triphasic nanoemulsion cross-section (right). 28

Figure 1.4. Actual by observed response plots from PLS regression models. Multivariate modeling generated predictive paradigms in which design parameters including composition and processing conditions were used to estimate nanoemulsion critical quality attributes including droplet size, long-term stability, and drug loading efficiency. Data reproduced with permission from Herneisey *et al.* (1).. 36

Figure 2.1. Structures of perfluorocarbon oils used in this study and of perfluoropolyether-tyramide. Perfluoro-15-crown-5-ether (PCE) is prone to Ostwald ripening and perfluoropolyether oxide (PFPE) is resistant to Ostwald ripening. 47

Figure 2.2. Heat map and ternary diagrams representative of the design matrix used for data collection in the MLR model. 49

Figure 2.3. Long term stability of selected nanoemulsions. Panels A, B, and C show z-average over time. Panel D shows polydispersity index followed over time. Panel E shows zeta potential followed over time. All samples were stored at 4 °C without humidity control. Reported as mean of 3 measurements ± standard deviation. Panel F shows effect of PFPE-tyramide on zeta potential, where Tyramide is PFPE-tyramide, ‘-’ is absence (n=16), and ‘+’ is presence (n=8). ** indicates $p < 0.01$ 51

Figure 2.4. Percent size change and PDI change after 24-hr incubation in culture media at the specified concentration (% v/v) of FBS. *, **, and *** represent p -value < 0.05, 0.01, and 0.001 compared to PFC-NE response (two-sided t-test), respectively. n=6 for PFC and HC nanoemulsions and n=12 for triphasic nanoemulsions. Error bars are one SEM..... 52

Figure 2.5. Plots of observed size by predicted size, where the solid line is the line $y = x$, (A) and residual by predicted size, where the solid blue line is the $y = 0$ reference line (B). 56

Figure 2.6. Root mean square error associated with all possible models. 57

Figure 2.7. Size distributions by intensity (A) and by volume (B) for nanoemulsions composed of PCE (top) and PFPE (bottom).....	57
Figure 2.8. Ternary diagrams with overlaid size contours.....	58
Figure 3.1. Summary of PFC nanoemulsions (PFC-NEs) for oxygen delivery. (A) Scatterplot of nanoemulsion z-average size and polydispersity index (PDI) of biphasic and triphasic nanoemulsions (BNs and TNs, respectively). (B) Illustration of the configurations of triphasic and biphasic nanoemulsions (TN and BN, respectively). (C) Step-by-step <i>in vitro</i> oxygen loading and release experiments. (D) Schematic showing simplified sequence of interfaces that oxygen equilibrates across in the <i>in vitro</i> oxygen release setup. (E) Representative oxygen release data. (F, G) Dissolved O ₂ maximum concentration (C_{max}) relationship to both theoretical PFC concentration, in percent volume, and PFC concentration quantified by ¹⁹ F NMR spectroscopy, in percent weight PFC per weight of NMR sample.....	79
Figure 3.2. Balancing of opposing key attributes of PFC-NE O ₂ carriers. Highly concentrated PFC-NEs are sought for their high capacity for oxygen loading. However, biphasic PFC-NEs can be poorly stable. A key objective is to find a balance between these opposing quality attributes. Conceptual scatterplots were formed by normalizing CQAs C_{max} and Thermal stability $\Delta size$ into a number ranging from 0 to 1 by dividing each by the maximum respective CQA measurement.	82
Figure 3.3. Description and summary of failure mode, effects, and criticality analysis (FMECA) results. (A) Definition of Risk Priority Number (RPN) scoring system. (B) Summary of averaged RPN across failure mode categories composition, oxygenation, processing, or operator error.	83
Figure 3.4. Dissolved oxygen vs. time profiles in <i>in vitro</i> oxygen release experiments for select samples. (A) Release profiles compiled for formulations ranging from 0 to 14.3 vol% PFC. (B) Comparison of BNs composed of different PFC types, both at the highest level of PFC. (C, D) Comparison of 2 TNs composed of different PFC types at identical PFC levels. (E, F) comparison of BNs and TNs of the same PFC type. (G) Comparison of TN-PFOB of different internal phase volume fractions. (H, I) Comparison of TN-PFOB to biphasic hydrocarbon nanoemulsion and DI water control. Where standard error bars are shown, each point is mean of three measurements \pm SD. Asterisks label time points or intervals where the two overlaid dissolved oxygen values are significantly different from one another. *, **, *** indicate $p < 0.05$, $p < 0.01$, and $p < 0.001$, respectively.	87

Figure 3.5. Characterization of triphasic PFC nanoemulsions. (A) For TNs, oxygen release is virtually identical among PFC types comparison in (see Figure 3.4). Thermal stability Δ size for 2 representative samples shows a colloidal stability discrepancy exists between PFC types. (B) Least squares fit demonstrating the relationship of C_{\max} and Thermal stability Δ size. (C, D) Size distribution overlays reflect colloidal stability of TNs after 30 min of oxygen bubbling. (E, F) Shelf-stability reflected by z-average of samples stored at 4 °C. (G, H) ^{19}F NMR spectra of representative examples, TN3 and TN8. (I) PFC loading calculated from ^{19}F qNMR spectroscopy..... 88

Figure 3.6. Multiple linear regression output to predict size change after thermal storage and C_{\max} in oxygen release. (A) Contour plot representing the formulation space in X1 and X2 identified by regression models for both responses. Shaded regions are out-of-specification regions for C_{\max} (blue) and Thermal stability Δ size (red). (B-C) Regression term estimates for C_{\max} (blue) and Thermal stability Δ size (red). (D-E) Observed by predicted graphs visualize the goodness of fit for both models, where C_{\max} is blue squares and Thermal stability Δ size is red squares. 91

Figure 3.7. Characterization and scale-up of PFC nanoemulsions. (A) Dependence of 100 mL NE size on processing amount ($n=1$ measurement/ data point). (B) Size distribution overlays of biphasic PFOB, BN1, at 25- and 100-mL scale. (C) Size distribution overlays of triphasic PFOB, TN2, at 25- and 100-mL scale. 93

Figure 4.1. Manufacturing sequence of large-scale perfluorocarbon nanoemulsions. ... 107

Figure 4.2. Validation, reexamination, and refinement of the multivariate model for *in vitro* oxygen release C_{\max} constructed in the earlier screening design. (A) Previous multivariate model fit with G1-NE data. (B) Projection of G2-NE data into the model ($C_{\max} = 3.6$ mg/L). (C) Representation of raw data normalized by f_{PFC} . The arrow on the inset rescaled data indicates the direction in which f_{PFC} increases. (D) Refitting C_{\max} model as a univariate model. (E) Projection of G2-NE data into the refined univariate model. (F) Linearized form of the C_{\max} univariate model. 114

Figure 4.3. Batch size comparisons made on G2-NEs. (A) Size distribution representations of batch size increase from 25 to 100 mL ($1\times$ to $4\times$) on the M-110S processor. (B) Batch size increase from $1\times$ on M-110S to $5\times$ on the LM20. (C) Size distributions of representative $1\times$, $5\times$, and $24\times$ scale batches. (D) Z-average by pass number across batch sizes. (E) Representative ^{19}F NMR spectra of samples across batch sizes. (F) Representative PFOB incorporation calculations across batch sizes. 116

- Figure 4.4. Comparisons of different high shear Microfluidizer processors at 24× scale. (A) Representative size distributions of G2-NEs across processors. LM20 samples are enclosed by solid rectangle, and M-110P samples are enclosed by a dashed rectangle. (B) Aggregate means and standard deviations of z-average grouped by processor. (C) Z-average at each discrete pass of representative samples across processors. LM20 samples are enclosed by a solid rectangle, and M-110P samples by a dashed rectangle. (D) Aggregate means and standard deviations of z-average at each pass grouped by processor. (E) Fluorescent properties of representative samples across processors. (F) Representative ¹⁹F NMR spectra of samples across processors. (G) Representative PFOB incorporation calculations across processors..... 118
- Figure 4.5. Attributes of NE17 and NE18. (A) z-average during processing compared to NE16 for reference. (B) PDI during processing compared to NE16 for reference. (C) Size distributions of freshly processed NEs compared to NE16 for reference. (D) Fluorescent comparison of NE18. (E) PFOB incorporation comparison of NE18. 122
- Figure 4.6. Principal components analysis (PCA) of the aggregated G2-NE size distribution dataset. (A) Score 1 and 2 coordinate plot with Cluster 1 and 2 ellipses and labels. (B) Color scale representing z-average applied to the Score 1 and 2 plot. (C) Color scale representing number of passes applied to the Score 1 and 2 plot. (D) Averaged size distributions of Cluster 1 and 2 data. 124
- Figure 4.7. PCA performed independently on partitioned clusters. (A) Color scale representing z-average applied to Scores 1 and 2 plot of Cluster 1 data. (B) Color scale representing number of passes applied to Scores 1 and 2 plot of Cluster 1 data. (C) Color scale representing z-average applied to Scores 1 and 2 plot of Cluster 2 data. (D) Color scale representing number of passes applied to Scores 1 and 2 plot of Cluster 1 data. (E) Color scale representing z-average after the first processing pass applied to Scores 1 and 2 plot of aggregated data. (F) Frequency histogram of NE z-average after the first pass grouped by cluster. 126
- Figure 4.8. Average size distributions during processing of G2-NEs partitioned by cluster. A dashed line at size = 200 nm is drawn for reference. 128
- Figure 5.1. Colloidal characteristics of the G2-NE formulations considered in this chapter. (A) Day 0 size distributions. (B) Temporal stability during routine 4 °C storage. 138
- Figure 5.2. Resveratrol stability and *in vitro* release kinetics. (A) Temperature-dependent resveratrol degradation in aqueous drug release buffer solution. (B) Stability difference between RSV-SOL and RSV-NE. (C) Reaction rate constant dependence on temperature. (D) *In vitro* release kinetics..... 145

Figure 5.3. Stability of NE07 on the oxygen perfusion circuit. (A) Size distribution after 45 min of perfusion circuit compared to bulk before circulation. (B) Time series of z-average up to 45 min of circulation. (C, D) DMEM incubation stability of non-circulated and circulated sample, respectively. (E) Centrifugation stability of circulated and non-circulated sample..... 146

Figure 5.4. Effect of oxygen-loaded G2-NE in murine macrophages. (A) Flow cytometry histograms representing the response of Hypoxia Green reagent (HGR) to pO₂. The inset shows the quantified mean fluorescent signal of the associated histogram. (B) Response of hypoxic macrophages labeled with HGR to oxygen-loaded G2-NE14. 148

Figure 5.5. Effect of RSV-loaded G2-NE on nitric oxide production in murine macrophages. (A) Independently generated nitrite standard curves. Curves are labeled by the preparation date. (B) Nitric oxide production in response to RSV NE (NE15), blank carrier control (NE16), and RSV solution. Unactivated macrophages were marked by a black dash on the y-axis (between 0 and 0.02). *, **, ***, **** represent $p < 0.05$, $p < 0.01$, $p < 0.001$, and $p < 0.0001$, respectively. 150

Figure 6.1. Colloidal stability of the perfluorocarbon-in-hydrocarbon-in-water nanoemulsion in response to various stressors. z-average and size distribution comparisons in syringe filtration(A-B), centrifugation (C-D), and serum incubation. 7-wk stability of z-average (G) and size distribution (H). 158

Figure 6.2. DLS summary of thermal cycling accelerated stability test performed on a perfluorocarbon nanoemulsion. (A) Comparison of size distributions of the cycling and the control age-matched sample. D10 and D90 are indicated by dotted vertical lines for control (red) and cycling (black) samples. (B) Z-average of the fresh, cycling and control samples. (C) PDI of the fresh, cycling and control samples..... 159

Figure 6.3. Core elements in the image acquisition and analysis sequence of perfluorocarbon nanoemulsions. Screenshots from ImageJ software..... 161

Figure 6.4. Example photograph of perfluorocarbon nanoemulsions and resulting binary processed image of outlined droplets. The scale bar is 200 μm 162

Figure 6.5. Scatterplot of *Feret* and $22A\pi$ where *Feret* and *A* are expressed in μm and μm^2 , respectively. Solid line is the line $y = x$ and dashed line is the linear regression line fit to the data. 163

Figure 6.6. Image analysis applied to reference particles taken in scanning electron microscopy. Original image from “Theoretical calculation of uncertainty region based on the general size distribution in the preparation of standard reference particles for particle size measurement.” by Yoshida, H in *Advanced Powder Technology*, 23(2), 185-190. Copyright 2011 by The Society of Powder Technology Japan. Reused and adapted with permission..... 164

Figure 6.7. Lognormal density and cumulative distributions fit to particle area for comparison of perfluorocarbon nanoemulsion conditions.....	165
Figure 6.8. Frequency histograms of particle area for comparison of perfluorocarbon nanoemulsion conditions.	166
Figure 6.9. Comparisons between automatic thresholding algorithms and the manual threshold selection for sample photomicrograph of a perfluorocarbon nanoemulsion after thermal cycling. The solid line is the line $y = x$	170
Figure A.1. Nanoemulsions were stored at 4 °C and monitored for change in size over time to demonstrate shelf-life. Lines are put in place only to aid the reader.....	214
Figure A.2. Nanoemulsions were stored at 4 °C and monitored for change in PDI over time to demonstrate shelf-life. Lines are put in place only to aid the reader.....	215
Figure A.3. Nanoemulsions were stored at 4 °C and monitored for change in zeta potential over time to demonstrate shelf-life. Lines are put in place only to aid the reader.....	216
Figure A.4. Size distribution overlays for selected nanoemulsions. Solid lines represent measurements made within the first wk of production. Dashed lines represent measurements made at a later follow up time (23 wk post-production).....	217
Figure A.5. Zeta potential distribution overlays for selected nanoemulsions. Solid lines represent measurements made within the first wk of production. Dashed lines represent measurements made at a later follow up time (23 wk post-production).	217
Figure A.6. Size distribution overlays for selected nanoemulsions. Solid lines represent measurements made within the first wk of production. Dashed lines represent measurements made at a later follow up time (37, 53, and 53 wk post-production for NEs 3, 17, and 18, respectively).....	218
Figure A.7. Zeta potential distribution overlays for selected nanoemulsions. Solid lines represent measurements made within the first wk of production. Dashed lines represent measurements made at a later follow up time (37, 53, and 53 wk post-production for NEs 3, 17, and 18, respectively).	218
Figure A.8. Centrifugation conditions elicited very small responses for all two-phase nanoemulsions and consequently the test was abandoned for remainder of emulsions.	219

Figure B.1. Z-average diameter evaluation of biphasic and triphasic nanoemulsions (BN and TN, respectively). (A) Stability to filtration through 0.22 μm syringe filter was good in all samples. (B) Stability in centrifugation conditions (218 \times g for 5 min) was good in all samples. (C) Storage in 50 $^{\circ}\text{C}$ for 2 wk resulted in destabilization of biphasic emulsions. (D) 30-day storage at 4 $^{\circ}\text{C}$ shows a 30-day z-average measurement compared to a 1-day-old measurement for comparison. 4 $^{\circ}\text{C}$ storage resulted in destabilization of PFOB biphasic formulation only (BN1). All measurements are mean \pm standard deviation from 3 measurements. ns, *, **, *** indicate not significant, $p>0.05$, $p<0.05$, $p<0.01$, and $p<0.001$, respectively. 220

Figure B.2. Size distribution (PDI) and zeta potential evaluation of biphasic and triphasic nanoemulsions (BN and TN, respectively). (A, B) Nanoemulsion PDI was followed for 30 d to evaluate stability in refrigerated storage conditions (4 $^{\circ}\text{C}$). (C) Nanoemulsion zeta potential was followed for 30 d to evaluate stability in refrigerated storage conditions (4 $^{\circ}\text{C}$). No evidence of destabilization occurs from observing PDI and zeta potential. (D) Stability to filtration through 0.22 μm syringe filter was good in all samples. (E) Stability in centrifugation conditions (218 \times g for 5 min) was good in all samples. (F) Storage in 50 $^{\circ}\text{C}$ for 2 wk resulted in destabilization of biphasic PFOB emulsion. (G) 30-day storage at 4 $^{\circ}\text{C}$ shows a 30-day z-average measurement compared to a 1-day-old measurement for comparison. 30-day storage at 4 $^{\circ}\text{C}$ was acceptable in all emulsions. All measurements are mean \pm standard deviation from 3 measurements. ns, *, **, *** indicate not significant, $p>0.05$, $p<0.05$, $p<0.01$, and $p<0.001$, respectively. %vol concentration numbers indicate the concentration of perfluorocarbon..... 221

Figure B.3. Size distribution overlays of representative perfluorocarbon nanoemulsions (PFC-NEs). Each panel overlays one representative NE at 3 different ages, up to 31 d after production, as indicated in the figure legends. Selected PFC-NEs are biphasic perfluorooctyl bromide (PFOB) and perfluoro-15-crown-5-ether (PCE) NEs, and triphasic NEs comprised of highest and lowest PFC concentration. PFOB NEs appear in A, B, and C, while PCE NEs appear in D, E, and F. These comparisons show that the size distribution of BN1 shifts to higher sizes rapidly, while BN2 and TNs approximately maintain constant distribution. BN, biphasic nanoemulsion; TN, triphasic nanoemulsion. 222

Figure B.4. Graphs of z-average size in response to serum stability test. Samples were incubated for 72 hr in biological media at 37 $^{\circ}\text{C}$ and size was recorded before and after. All measurements are mean \pm standard deviation from 3 measurements. TN, triphasic nanoemulsion; BN, biphasic nanoemulsion; DI, deionized; DMEM, Dulbecco's Modified Eagle's Medium; FBS, fetal bovine serum. 223

Figure B.5. Graphs of polydispersity index (PDI) in response to serum stability test. Samples were incubated for 72 hr in biological media at 37 $^{\circ}\text{C}$ and PDI was recorded before and after. All measurements are mean \pm standard deviation from 3 measurements. DI, deionized; DMEM, Dulbecco's Modified Eagle's Medium; FBS, fetal bovine serum. 223

Figure B.6. ^{19}F NMR spectra of TN1. Reference compound trifluoroacetic acid displays chemical shift at -76 ppm.....	226
Figure B.7. ^{19}F NMR spectra of TN2. Reference compound trifluoroacetic acid displays chemical shift at -76 ppm.....	227
Figure B.8. ^{19}F NMR spectra of TN3. Reference compound trifluoroacetic acid displays chemical shift at -76 ppm.....	228
Figure B.9. ^{19}F NMR spectra of TN4. Reference compound trifluoroacetic acid displays chemical shift at -76 ppm.....	229
Figure B.10. ^{19}F NMR spectra of TN5. Reference compound trifluoroacetic acid displays chemical shift at -76 ppm.....	230
Figure B.11. ^{19}F NMR spectra of TN6. Reference compound trifluoroacetic acid displays chemical shift at -76 ppm.....	231
Figure B.12. ^{19}F NMR spectra of TN7. Reference compound trifluoroacetic acid displays chemical shift at -76 ppm.....	232
Figure B.13. ^{19}F NMR spectra of TN8. Reference compound trifluoroacetic acid displays chemical shift at -76 ppm.....	233
Figure B.14. ^{19}F NMR spectra of BN1. Reference compound trifluoroacetic acid displays chemical shift at -76 ppm.....	234
Figure B.15. Cause and effect diagrams for oxygen loading & release and size change after thermal stability. All branches of the diagram represent sources of variability of the quality attribute in question.	235
Figure C.1. Nanoemulsion sizes of four different perfluorocarbon (30 wt%) & hydrocarbon (6 wt%) pairs. Selection of the optimal pair was made based off the minimization of z-average.	236
Figure C.2. <i>In vitro</i> oxygen release profile of a representative G2-NE, NE01.....	238
Figure C.3. Size distribution comparisons at each batch size demonstrate the process reproducibility within batch size and processor.....	239
Figure C.4. Long term colloidal stability of G2-NEs. Left panel shows the z-average for selected batches. The inset shows the same data rescaled to show only the first 60 d in greater detail. Right panel shows 280-day ^{19}F qNMR follow ups for two representative G2-NEs.	240

Figure C.5. Stress stability of G2-NE16 as a representative sample. From left to right: serum incubation stability, centrifuged stability, and filtration stability. From top to bottom: z-average size and PDI. DMEM, Dulbecco’s Modified Eagles Medium; FBS, fetal bovine serum.	240
Figure C.6. Examination of factor variance in PCA scores space from Cluster 1 defined in the text.....	241
Figure C.7. Examination of factor variance in PCA scores space from Cluster 2 defined in the text.....	242
Figure D.1. Resveratrol <i>in vitro</i> drug release data without accounting for drug degradation.....	243
Figure D.2. Cell viability of macrophage hypoxia conditions measured by Cell Titer Glo. pO ₂ in the hypoxic environment was 1%. pO ₂ in the normoxic environment ranged from 18-20%. Treatment concentration was constant at 40 µL/mL. O ₂ indicates the treatment was equilibrated with O ₂ for 10 min prior to treating the cells. NT, no treatment; PBS, phosphate buffered saline.	243
Figure D.3. Cell viability of representative G2-NEs measured by Cell Titer Glo. (A) Resveratrol-free formulations, and (B) resveratrol-loaded formulations.	244
Figure D.4. Cell viability of lipopolysaccharide (LPS) conditions used in the nitrite/nitrate assay measured by Cell Titer Glo.	244
Figure E.1. Automatic thresholding algorithm montage resulting from imageJ’s ‘try all’ menu option. Algorithms in alphabetical order of panel labels (a-q): Default, Huang, Huang2, Intermodes, Isodata, Li, MaxEntropy, Mean, MinError(I), Minimum, Moments, Otsu, Percentile, RenyiEntropy, Shanbhag, Triangle, Yen.	245

LIST OF ABBREVIATIONS

^{19}F MRI	fluorine-19 magnetic resonance imaging
2,3-DPG	2,3-diphosphoglycerate
AOC	artificial oxygen carrier
ATP	adenosine triphosphate
BCS	Biopharmaceutical Classification System
BN	biphasic nanoemulsion
C_{max}	maximum dissolved O_2 concentration
CO_2	carbon dioxide
CP	continuous phase
CPP	critical process parameter
CQA	critical quality attribute
DI	deionized
DLS	dynamic light scattering
DMEM	Dulbecco's Modified Eagle's Medium
DO	dissolved oxygen
DoE	design of experiments
FBS	fetal bovine serum
FDA	Food and Drug Administration
FLC	fluorophilic-lipophilic conjugate
FMECA	failure modes, effects, and criticality analysis
f_{PFC}	PFC fraction
GRAS	generally recognized as safe
HBOC	hemoglobin oxygen carrier
HC	hydrocarbon
HGR	Hypoxia Green reagent
HLB	hydrophilic-lipophilic balance
HPLC	high-performance liquid chromatography
ICG	indocyanine green
ICH	International Council on Harmonization
IP	internal phase
IR	ischemia-reperfusion
LOOCV	leave-one-out cross validation
LPS	lipopolysaccharide
MCT	medium chain triglycerides
MLR	multiple linear regression
MP	machine perfusion
MW	molecular weight
NE	nanoemulsion
NIR	near infrared

NMR	nuclear magnetic resonance
NO	nitric oxide
O ₂	molecular oxygen
OFAT	one-factor-at-a-time
PBS	phosphate buffered saline
PCA	principal components analysis
PCE	perfluoro-15-crown-5-ether
PDI	polydispersity index
PFC	perfluorocarbon
PFC-NE	perfluorocarbon nanoemulsion
PFD	perfluorodecalin
PFOB	perfluorooctyl bromide
PFPE	perfluoropolyether
PLS	partial least squares
pO ₂	partial oxygen pressure
PRESS	prediction error sum of squares
QbD	Quality by Design
QRM	quality risk management
QTPP	quality target product profile
RMSE	root mean square error
ROS	reactive oxygen species
RPM	revolutions per minute
RPN	risk priority number
RSV	resveratrol
SA	stearylamine
SCS	static cold storage
SFH	stroma-free hemoglobin
SOL	solution
TFA	trifluoroacetic acid
TLR	toll-like receptor
TN	triphasic nanoemulsion
USP	United States Pharmacopeia
VCA	vascularized composite allotransplantation
WB	whole blood

Chapter 1. Introduction

1.1. Statement of the problem

Modern medicine has saved countless lives and facilitated improvements in quality of life made possible by transplantation. Global Observatory on Donation and Transplantation reports that nearly 130,000 solid organs were transplanted worldwide in 2020 (2022 data produced by the WHO-ONT collaboration) (3). This number does not account for tissues classified within vascularized composite allotransplantation (VCA), which consist of a collection of different tissues (connective tissue, muscle, bone, and nerves). Despite the ubiquity and health impact of transplantation, standard practices have areas in need of improvement. Two areas in need of improvement in transplantation are 1) the preservation of tissue after procurement from the donor and 2) ischemia-reperfusion events at the time of transplant. The Scientific Registry of Transplant Recipients (SRTR) reported that, in 2020, discards (organs that were procured but not transplanted) occurred 15 times in every 100 procured organs (4). Additionally, in the 2022 SRTR report, prolonged ischemic time is cited as a reason for discarding (4). Addressing the problems in these areas may contribute to reducing discarded organs and expanding the donor pool. During preservation, the tissue requires access to adequate nutrition and regulation of metabolism and osmotic pressure. In standard clinical practice, tissues are preserved in aqueous preservation solutions in static cold storage (SCS). As the name suggests, SCS involves submerging the tissue in a solution containing provisions for nutrition and osmotic pressure balance and is maintained close to 0 °C to suppress metabolic rate (5, 6). The simplicity of SCS has led to its widespread use. However, tissues in SCS are prone to cold ischemic damage (7). More sophisticated

preservation methods can be employed to allow interventions in preservation to improve the quality of transplanted tissue grafts (8). *Ex vivo* machine perfusion (MP), where the preservation solution, or perfusate, is circulated through the vasculature of the tissue, has the potential to improve graft preservation. MP is attractive because it could prolong the maximum acceptable duration of ischemic preservation and expand the criteria for accepted tissue grafts which consequently increases the donor pool. During MP, the perfusate passes through a hollow fiber membrane oxygenator and a temperature regulator before perfusing the tissue. The MP general flow diagram is illustrated in Figure 1.1. However, the full potential of the oxygenation equipment is not realized because of the poor solubility of oxygen in aqueous solutions. Importantly, this results in a significant limitation in oxygen transport to ischemic tissue despite the technological advancements in preservation practices.

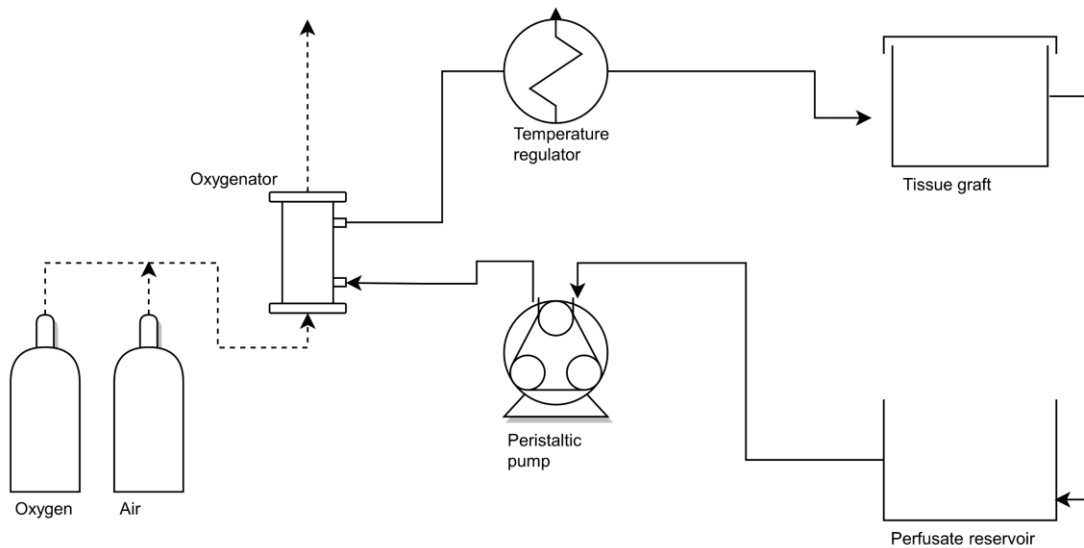


Figure 1.1. General flow chart of a machine perfusion circuit.

The cellular response elicited by ischemia can result in rejection (9). During oxygen deprivation, the endothelial barrier is compromised in response to adenyate

cyclase activity reduction (10, 11). In addition, toll like receptor (TLR)-dependent stabilization of nuclear factor κ B (NF- κ B) results in upregulation and activation of transcription of genes that are involved in inflammatory signaling pathways (10, 12, 13). This directly results in an innate and adaptive immune response that activates and recruits macrophages to the graft. In their activated state, macrophages begin to upregulate the production of reactive oxygen species. This response resembles how the immune system protects against a pathogen invasion.

At the time of transplantation, ischemia-reperfusion (IR) events continue. Neutrophils and macrophages can more easily infiltrate the transplanted graft through the compromised endothelium. A large amount of ROS is generated from the immune response. ROS are known to directly cause oxidative stress, by altering DNA, proteins, and lipid membranes. ROS can also indirectly contribute to tissue damage by participating in the creation of neutrophil extracellular traps (NET) (14, 15). In a liver IR study, the authors observed protection of hepatocytes and reduction in inflammation in response to inhibition of NETs. (16) To address the need for oxygen supply and defense against ROS in transplantation, we have proposed the use of a perfluorocarbon nanoemulsion (PFC-NE) artificial oxygen carrier (AOC) loaded with the antioxidant resveratrol. PFC oils are hydrophobic liquid materials characterized by low cohesive energy densities, which imparts an unusually high capacity for dissolution of respiratory gases. To make suitable for administration to oxygen-deprived tissues, PFCs are typically prepared as PFC-in-water (PFC/W) NEs. NEs lack thermodynamic stability, and consequently, proper action must be taken to design NEs with slow destabilization kinetics. The conventional formulation development approach is facing difficulty in

producing stable PFC-NEs. Laboratory scale development of PFC-NE AOCs is reported, but conventional methods are limited to the ‘one factor at a time’ (OFAT) philosophy. The OFAT approach is defined by the testing of a single factor at a time. In the development of a complex pharmaceutical drug product, resources can be minimized, and a more precise understanding of the drug product can be acquired by utilizing alternative systematic multifactor experimental designs. Very few reports exist in which sophisticated systematic development and production studies are extended to PFC-NE AOCs. Consequently, there has been a need for systematic product and process development efforts to advance the field. To exemplify this need, only one PFC-NE AOC, Fluosol, has received FDA approval (for use in coronary angioplasty) in six decades of research of PFCs as oxygen carriers. Fluosol’s withdrawal shortly after was, in part, a consequence of its poor shelf-life (17). The Quality by Design (QbD) philosophy offers a systematic methodology to understand the sources of variability of a process and accordingly control the product quality. Here, we have proposed to adapt the QbD methodology to development of PFC-NE AOCs in order to have a deep understanding of the oxygen delivery capabilities and emulsion stability. Transplantation is one of the several potential applications of PFC AOCs. PFC-NEs have been utilized in ophthalmology, decompression sickness, liquid ventilation, cancer therapy, balloon angioplasty, and a variety of other ischemic events (17). In summary, there is a critical need for improved systematic methodologies to advance the field of PFC AOC formulation development.

1.2. Hypothesis and specific aims

The working hypothesis of this dissertation project is the following:

Quality by Design-centered development can yield colloiddally stable antioxidant- and molecular-oxygen-co-loaded NEs for action against oxidative stress and hypoxia in ex vivo machine perfusion preservation.

This hypothesis was tested using three specific aims, each composed of various sub-aims.

1.2.1. *Specific aim 1*

Identify critical formulation and processing factors and relationships that govern oxygen delivery and kinetic stability of PFC-NEs.

1.2.1.1. *Specific aim 1: sub-aim 1*

Leverage Quality by Design principles to understand the impact of internal phase composition and process of PFC-NEs on quality attributes.

1.2.1.2. *Specific aim 1: sub-aim 2*

Form in depth comparisons between *in vitro* oxygen transport and kinetic stability of PFC-NEs.

1.2.1.3. *Specific aim 1: sub-aim 3*

Propose an optimal formulation and process, and demonstrate oxygen transport and kinetic stability in a macrophage model for hypoxia.

1.2.2. *Specific aim 2*

in vitro resveratrol (RSV) loading, stability, and release characterization of PFC-NEs.

1.2.2.1. *Specific aim 2: sub-aim 1*

Prepare the optimal PFC-NE loaded with RSV (RSV-PFC-NE).

1.2.2.2. *Specific aim 2: sub-aim 2*

Characterize the *in vitro* release rate of RSV-PFC-NE.

1.2.2.3. *Specific aim 2: sub-aim 3*

Form comparisons of the chemical stability of RSV-PFC-NE and RSV free solution.

1.2.2.4. *Specific aim 2: sub-aim 4*

Demonstrate RSV pharmacological action in a macrophage model.

1.2.3. *Specific aim 3*

Evaluation of PFC-NE process scalability.

1.2.3.1. *Specific aim 3: sub-aim 1*

Prepare the optimal PFC-NE at 5x scale and 24x scale labeled with fluorescent dye.

1.2.3.2. *Specific aim 3: sub-aim 2*

Form comparisons of colloidal characteristics, fluorescent dye stability, and oxygen release between production scale and between high shear processors.

1.2.3.3. *Specific aim 3: sub-aim 3*

Assess the process sensitivity to process modifications.

1.3. Dissertation content outline

In the chapters that follow, we describe the methods and results in testing our hypothesis. First, the core elements of PFC artificial oxygen carriers are discussed. This includes the material properties of PFC materials that make them candidate materials for oxygen carriers. Their past success and clinical trial status as imaging tracers is discussed. We evaluate the development of commercial PFC oxygen carriers in the form of NEs and highlight the potential of systematic Quality by Design in providing tools for overcoming challenges in PFC-NE colloidal stability.

Next, we establish the general methodology for construction of multivariate process models for colloidal attributes of complex NEs. Specifically, we develop multiple linear regression (MLR) models to describe how the droplet diameter of compositionally diverse NEs is impacted by the oil type(s) and amount present in the formulation. In the following chapter, we describe the formalization of the QbD approach to PFC-NE artificial oxygen carrier development. In this study, we used a custom *in vitro* oxygen release method to get a preliminary understanding of the PFC-NE oxygen delivery profiles. We also studied the colloidal stability of these formulations. After application of the MLR modeling strategy, we form a formulation design space to manage the oxygen release and colloidal stability of our PFC-NEs.

Then we describe final modifications of the PFC-NE formulation which allow for higher oxygen loading. In this study we examined our manufacturing process. We made comparisons of PFC-NE reproducibility across three different Microfluidizer processors and across a 24× batch size increase. We employed principal components analysis to

investigate how the implementation of different sources of process variability affected the droplet size distribution of the PFC-NEs.

Next, we studied the *in vitro* pharmacological properties of the optimized PFC-NEs. We used murine macrophages, which are key players in the pathophysiology of ischemia-reperfusion injury. We evaluated how oxygen-loaded PFC-NEs could supply oxygen to macrophages cultivated in hypoxic conditions. We also evaluated how RSV-loaded PFC-NEs could decrease nitric oxide, a reactive radical species, generated by lipopolysaccharide (LPS)-activated macrophages.

In the final chapter, we describe a novel quality control method for detecting oversized droplet size distribution of NEs that is intended to be complementary to the standard analytical method, dynamic light scattering.

1.4. Literature review

1.4.1. Acknowledgements

The text below is adapted from a published manuscript authored by Eric Lambert, Vijay S. Gorantla, and Jelena M. Janjic. The full citation is: Nanomedicine (Lond). (2019) Pharmaceutical design and development of PFC nanocolloids for oxygen delivery in regenerative medicine. 14(20), 2697-2712. Reused with permission of Future Medicine Ltd. DOI: 10.2217/nmm-2019-0260. Jelena M. Janjic and Eric Lambert contributed to Sections 1.4.1, 1.4.3, 1.4.7, 1.4.8, and 1.4.9; Vijay S. Gorantla contributed to 1.4.4 and 1.4.6.

1.4.2. *Unique Properties of Perfluorocarbons Applicable for Regenerative Medicine*

PFCs have been investigated in biomedical research since the 1960s and their unique properties have been well characterized. Their vastly broad medical uses, from triggered drug delivery, to oxygen delivery and molecular imaging, have been extensively reviewed in the literature (18-25). By definition, PFCs represent a class of organic materials characterized by linear, branched, or cyclic carbon-carbon skeletons where hydrogens are replaced by fluorine. Some PFC materials incorporate oxygen and other heteroatoms. The exchange of hydrogens for fluorines is accountable for a dramatic cascade of changes in physicochemical properties when contrasted to hydrocarbons (HCs) (2). PFCs are equipped with the strongest known covalent bond, carbon-fluorine. Fluorine is electronegative which causes intramolecular forces in PFC liquids to be low, which promotes high vapor pressures and low surface tensions (26). Further, large atomic radius of fluorine results in an electron-dense protective sheath surrounding perfluorinated entities, effectively adding a barrier to any modes of metabolism (27). PFCs themselves act as contrast media as background-free tracers for ^{19}F magnetic resonance imaging (^{19}F MRI). ^{19}F MRI can be used to detect quantitatively and in real time the pharmacokinetic parameters of PFC (28, 29). Owing to their weak intermolecular interactions, PFCs are susceptible to phase transformation in response to certain types of external energy (*e.g.*, high intensity focused ultrasound) which cause liquid droplets to vaporize, forming microbubbles (diameter $\sim 1\text{-}10\ \mu\text{m}$) which act as excellent contrast agents in diagnostic ultrasound (30, 31). These unique physicochemical properties deem PFCs very attractive materials for regenerative medicine applications from therapeutic cell tracking to ultrasound triggered and targeted drug delivery and

finally, what we will focus on in this article, organ preservation. PFCs offer exceptional oxygen carrying capacity while being remarkably chemically and metabolically inert (32-36). The focus of this review is on advancing PFCs with special emphasis on pharmaceutical design and development strategies for tissue and organ preservation. Further, we also discuss imaging and drug delivery as an added functionality that can complement their use regenerative medicine.

1.4.3. *Perfluorocarbon Nanoemulsions as Versatile Nanomedicines*

PFCs are immiscible with water and lipids and for this reason cannot be administered as raw materials. PFCs formulated as nanometer-sized colloids, such as kinetically stable NEs (droplet diameters $< \sim 500$ nm), are a type of product that is useful for injection and has been utilized extensively. PFCs can be designed and formulated into stable nanocolloids (NEs) with unique capability of not only oxygen carriage but also intracellular or extracellular delivery of added drug or imaging agent payloads (37, 38). NEs can function as carriers of drugs and diagnostic moieties. Drugs exhibiting poor water solubility, high affinity for serum protein binding, or extensive hepatic metabolism can be protected and performance-enhanced (*e.g.*, increased bioavailability, half-life) through nanoemulsification. Clearance rates following intravenous administration of NEs are influenced by droplet size. NEs with large enough droplet size are recognized by the reticuloendothelial system and are cleared from circulation quickly (39). Targeting can be accomplished either actively, by tagging the NE surface with homing ligands (40), or passively, as it occurs in the enhanced permeability and retention effect observed with nanoparticle treatment in cancer (41). Consequently, drug dose and dosing frequency can be reduced. Additionally, tagging a NE with imaging reagent (*e.g.*, near-infrared (NIR))

dyes, fluorescence biosensors, metal chelators) affords the ability to monitor the biodistribution of the system and to monitor pathogenesis of disease (38, 42-44).

^{19}F MRI emerged as a unique non-invasive quantitative molecular imaging technique where ^{19}F nuclei provide highly selective and specific signal for the biodistribution of immune cells labeled with PFC-NEs (45, 46). The key advantage of this method is that ^{19}F images are extremely selective for labeled cells because of the negligible fluorine background signal from the subject's tissues. In addition to visualization of the cell location *in vivo*, cell numbers can be quantified directly from the spin-density-weighted ^{19}F MR images. The utility of PFC-NEs for ^{19}F MRI is highly dependent on PFC chemical structure, which determines NE droplet formulation, biological half-life, and retention in tissues (47). Optimal PFC-NEs for ^{19}F MRI applications must satisfy the following criteria: (I) stability under biological conditions and long shelf life (at least 6 months), (II) a simple spectrum, ideally showing a single, narrow resonance to maximize sensitivity and prevent chemical shift imaging artifacts, and (III) NE droplet with a high PFC volume fraction to maximize ^{19}F nuclei concentration for maximal ^{19}F MR signal/cell. The concept of '*in vivo* cytometry' has been developed by labeling cells with PFC *in vivo* or *ex vivo* for cell detection using ^{19}F MRI (46, 48-50). This approach was extensively utilized for imaging monocyte derived cells as the means of quantitatively and qualitatively assessing inflammation in a variety of preclinical models (51-54) and as a measure of response to treatment (55, 56). Non-invasive imaging of inflammation with PFCs can provide invaluable insights into organ rejection therapeutic outcomes by providing unbiased long-term monitoring. Furthermore, PFCs are particularly useful for regenerative medicine applications as non-

invasive stable cell tracking agents for sensitive cell populations such as progenitor and stem cells (24, 57, 58).

Clinical trials have been conducted successfully for ^{19}F MRI (59). When PFCs were administered to patients they can be unambiguously imaged with ^{19}F MRI because low levels of naturally-occurring fluorine result in extremely high contrast-to-noise ratio and specificity (19, 59). Because of the chemical inertness of PFCs, time-course studies can be conducted using ^{19}F MRI. Extensive efforts are underway to overcome known problems in ^{19}F MRI such long imaging times and low sensitivity which include re-designing PFC-NEs and imaging sequences (19, 42). In addition to tracking introduced PFCs, molecular oxygen concentrations can be monitored with ^{19}F MR spectroscopy (60). The technology to synthesize PFCs in bulk exists and is well understood. The same can be said about manufacturing NEs in bulk (61). Additionally, many of the materials available to construct a NE product are generally recognized as safe (GRAS) and approved by the FDA. The success in clinical use of PFCs as imaging agents supports the notion of their safety for use elsewhere. This is important for obtaining regulatory approval of the NE platforms in organ preservation applications. Therefore, in the further discussion we will focus on designing clinically translatable PFCs as a solution to one of the major problems in regenerative medicine – organ and tissue preservation.

1.4.4. *Ischemia and Reperfusion Injury – Key Challenges in Regenerative Medicine*

Tissue ischemia can occur secondary to hemorrhage/shock with global hypoperfusion, isolated compression-crush syndrome of an extremity or during *ex vivo* preservation of organs prior to transplantation. Oxygen and glucose are key metabolic precursors in adenosine triphosphate (ATP) synthesis. A reduction in ATP results in cell

death due to breakdown of intracellular respiration and energy dynamics associated with derangement of membrane transport mechanisms. In the case of neurotized tissues, warm ischemia secondary to devascularization results in irreversible deterioration of muscular tissue after 4 hr and neural tissue beyond 8 hr (62, 63). Reperfusion of ischemic tissue causes an extension of damage inflicted by hypoxia known as ischemia-reperfusion injury (IRI). Disruption of the endothelial barrier is the hallmark of IRI. The effects of IRI on the microcirculation include constriction of arteriolar beds and endothelial leakage and tissue edema coupled with leucocyte adhesion and transmigration across a deranged endothelial barrier. Most of the tissue damage and inflammation during IRI is mediated by macrophages and is driven by proinflammatory cytokines, reactive oxygen metabolites, and nitric oxide (NO) derived from macrophages (64, 65). IRI thus has a profound proinflammatory impact on devascularized tissues that dramatically increases risks of poor rescue or resuscitation outcomes leading to extremity amputation after attempted salvage surgery.

The logistic simplicity SCS preservation (at 4°C) for prolongation of cold ischemia time (CIT) is appealing for tissue preservation or salvage. However, SCS leads to anaerobic metabolism with loss of cell membrane integrity, reduced interstitial osmotic pressure (causing tissue edema and acidosis), and mitochondrial disruption with cell death. Unlike solid organs that rely primarily on vascular perfusion for function, extremity or neurotized tissue function depends on neuroregeneration and muscle reinnervation. Importantly, SCS also causes perivascular, intramuscular and intramyelinic edema, and axonal vacuolization. In fact, non-immunologic factors that impact outcomes of tissue resuscitation, the implications of SCS, and subsequent IRI on the short and long

term functionality (motor and sensory reinnervation and outcomes) of secondarily reconstructed neurotized tissues (such as limbs) are least studied (66). Unlike in SCS, normothermic temperatures are neuroprotective but most normothermic preservation solutions lack effective oxygen-carriers or rely on the use of blood as the preferential perfusate (67, 68). Nanoformulated PFCs, as we discuss below, are an attractive alternative to acellular Hbs given their exceptional oxygen carrying capacity while being remarkably chemically and metabolically inert (32-36).

Table 1.1. Composition of selected commonly reported clinical preservation solutions. UW, University of Wisconsin; IGL, Institute Georges Lopez, E, extracellular; I, intracellular.

Solution	Osmotic agent(s)	Buffer(s)	Energy substrate(s)	Type
EuroCollins	Glucose	Phosphate Bicarbonate	None reported	I
UW	Lactobionate Hydroxyethyl starch Raffinose	Phosphate	Adenosine	I
Histidine-tryptophan-ketoglutarate	Mannitol	Histidine	α -ketoglutarate Tryptophan	E
Celsior	Manitol Lactobionate	Histidine	Glutamate	E
Kyoto University ET-K	Gluconate Hydroxyethyl starch Trehalose	Phosphate	None reported	E
Kyoto University IT-K	Gluconate Hydroxyethyl starch	Phosphate	None reported	I
IGL-1	Lactobionate PEG-35 Raffinose	Sulfate Phosphate	Adenosine	E

1.4.5. Preservation Solution and Perfusate Composition and Present Status

As mentioned previously, the preservation solutions and perfusates that are employed in clinical practice are not effective oxygen carriers. They consist of aqueous solutions with electrolytes, osmotic agents, buffers, and energy substrates. In general, they are classified as intracellular (I) or extracellular (E) solutions. This designation is based off of the K^+ and Na^+ concentration. Solutions which are designed to resemble intracellular environment have low Na^+ and high K^+ concentrations, while the reverse is

characteristic of E solutions. Table 1.1 summarizes some of the commonly used preservation solutions (69-74).

It is common for certain components of the preservation solution to serve more than one purpose. For example, polysaccharides can be effective osmotic agents and act as a source of energy. Sometimes, more sophisticated components are present, such as antioxidants, endothelial vasculature protection agents, signaling pathway blockers, and hormones (72). In the solutions summarized in Table 1.1, UW solution is supplemented with allopurinol and glutathione as antioxidants. Kyoto IT-K contains nitroglycerine and dibutyryl cyclic adenosine monophosphate as vasculature protectors and N-acetylcysteine as antioxidant (75).

When molecular oxygen supplementation is performed during organ preservation, unmodified aqueous perfusates or red blood cell preparations are conventionally chosen (76-78). However, both of these options have significant risks and limitations. Aqueous solutions are poor oxygen carriers. Studies that use oxygenated unmodified perfusate in machine preservation come to opposing conclusions. A study that used UW solution in oxygenated hypothermic machine preservation of kidneys reported no differences of this group compared to the standard SCS group where no oxygenation supplementation was used (79). Alternatively, different researchers using oxygenated hypothermic machine perfusion of human liver grafts reported better outcomes in the oxygenated group in comparison to the SCS control group (80). Further, the logistics and risks of red blood cells makes its use a significant complication (81). Therefore, the efforts to develop an artificial oxygen carrier for machine perfusion are justified. There exist reports of preclinical and clinical use of alternative oxygen carriers. Hemoglobin oxygen carriers

were utilized in normothermic machine perfusion of kidneys and livers (77, 81, 82) and were evaluated to be comparable to packed red blood cells. The following sections discuss more about the two main candidates for artificial oxygen carriers.

1.4.6. *Hemoglobin Based Oxygen Carriers (HBOCs) – Progress and Pitfalls*

Treatment options of ischemic tissues generally comprise delivery platforms capable of mimicking hemoglobin or exhibit alternative oxygen-carrying modes that can perform systemic oxygen replenishment and CO₂ removal. Viable treatment strategies include hemoglobin-based and PFC-based oxygen carriers. Acellular hemoglobin (Hb) oxygen carriers (HBOCs) have potential advantages over human blood, including availability, compatibility, and superior stability compared to packed red blood cells. Early results of HBOCs in clinical trials across US and Europe have been disappointing with reports of serious adverse effects (AEs) leading to premature termination of some studies. This has stalled or hampered FDA approval of these agents as satisfactory blood substitutes. Most AEs of HBOCs may be attributed to highly concentrated, free low molecular weight Hb species interacting with the endothelial cells in several organs and systems at isosmotic conditions. Some of the AEs with HBOCs include but are not limited to capillary vasoconstriction (with systemic and pulmonary hypertension and reduced oxygenation of capillary beds) due to endothelial nitric oxide (NO) scavenging, nephrotoxicity, decreased macrophage function, antigenicity, oxidation on storage leading into high levels of the inactive form of hemoglobin, methemoglobin (metHb), activation of complement, kinin and coagulation, iron deposition, gastrointestinal distress, and neurotoxicity (83). Acellular oxy-Hb scavenges endothelial NO when extravasating through the endothelium. This process can negatively impact the

bioavailability of endothelium-derived NO. However, NO is an endogenous vasodilator that can also bind to the same heme (Fe^{2+}) sites as oxygen that is being delivered, leading to oxidation of ferrous heme to the ferric state, further increasing metHb and worsening vasoconstriction and ischemia (32, 84). NO control is therefore required to come from the appropriately designed perfusion solution. PFC-NEs could be an attractive option to solve this problem, considering their ability to carry both oxygen and small molecules, such as NO scavengers (37).

Stroma-free hemoglobin (SFH) has been linked to the prolongation of both the extrinsic (aPTT) and intrinsic (PT) pathways, as well as a decrease in fibrinogen concentration. Studies have shown a similar deleterious impact in platelet function and aggregation. Large molecular size, NO scavenging during cell-free preservation (for ischemia mitigation), formation of methemoglobin by oxidation and interference with platelet function have been some of the mechanisms proposed as etiologic agents for downstream coagulopathies associated with the use of HBOCs (85). Both platelet aggregation and activation have also resulted from the oxidation of the HBOC SFH into metHb (86, 87). The reality is that the true potential of HBOCs is poorly understood; since most research done by industry is proprietary, and there is only minimal access to transparent data.

1.4.7. *Perfluorocarbon Oxygen Carriers – Premise and Potential*

PFC materials have shown potential to overcome oxygenation hurdles in tissue preservation. PFCs are equipped with the strongest known covalent bond, carbon-fluorine. Fluorine is electronegative and the C-F bond non-polarizable. This causes intramolecular forces in PFC liquids to be low, which promotes high vapor pressures and

low surface tensions (26). Further, large atomic radius of fluorine results in an electron-dense protective sheath surrounding perfluorinated entities, effectively adding a barrier to any modes of metabolism (27). Vapor pressure influences the clearance rate of a PFC *in vivo*. Because PFCs are not metabolized, they are routed out of the body primarily via the lungs and exchanged into the air. Generally, molecular weight negatively correlates with clearance time (26). The presence of heteroatoms often results in deviations from this relationship. A single bromine substitution on perfluorooctane results in significantly more lipophilicity and shorter tissue residence time. PFCs have demonstrated very high affinity for dissolving various gas species including oxygen, carbon dioxide, and nitric oxide (26, 88, 89). The presence of low intermolecular forces explains the high capacity of PFCs for gaseous species. Creating a vacancy for a gas between liquid molecules is easier in such conditions. PFC materials dissolve gaseous species in a predictable and regular manner. The gas dissolution is governed by Henry's law, where the solubility is linearly proportional to the partial pressure of the gas. This behavior is important and presents advantages over whole blood oxygenation behavior. With a perfluorinated product, the fraction of inspired oxygen can be adjusted to an optimal range; in contrast, hemoglobin's sigmoidal-shaped dissociation profile with oxygen makes manipulation of the oxygen loading difficult (90).

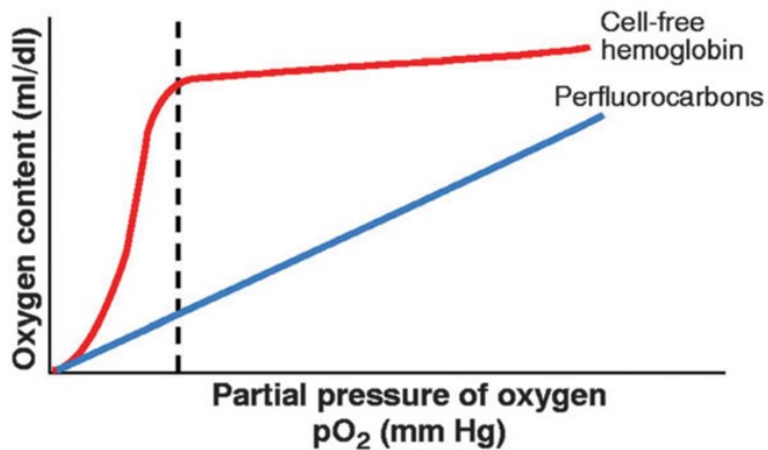


Figure 1.2. Oxygen release profile in PFCs as compared to cell-free hemoglobin. Heme molecules in cell-free Hb coordinate O_2 at a specific partial oxygen pressure (pO_2) range, resulting in the sigmoidal relationship between pO_2 and O_2 content. The uptake and release of O_2 from PFCs is driven by Henry's Law, in which the amount of O_2 incorporated into PFCs in nanodroplet is linearly related to pO_2 . Figure reproduced with permission from Farris *et al.* (2).

Oxygen dissociation curves for PFC and hemoglobin are demonstrated in Figure 1.2. PFCs do not rely on allosteric effectors for oxygen unloading as does hemoglobin. The only driving force for oxygen unloading from PFCs is a partial pressure differential between the oxygen (O_2) carrier and the tissue (2). Environmental factors such as temperature, length of storage time, and pH have negligible effect on oxygen loading and unloading in PFCs. Gas transfer behavior of PFCs remains consistent in conditions such as hypothermia. Also, PFCs can be produced in bulk quantity and stored long-term before use. The effectiveness of Hb, on the other hand, is affected by storage length. Chemically inert PFCs are not susceptible to oxidation, where hemoglobin can be oxidized to an ineffective form, methemoglobin. These properties give PFCs a fundamental advantage as oxygen carriers: high affinity for oxygen (as well as other gases) and complete chemical inertness. PFCs first rose to popularity as 'blood substitutes' in the 1960s

shortly after Clark *et al* (91) demonstrated that mice could survive submerged in liquid PFC. The high oxygen affinity, complete biological inertness and safety profile of PFC have been confirmed by extensive research into PFC-based oxygen therapeutics in medicine (90, 92). PFC products have been adopted in fields such as biochemistry, where they increase the permeability of oxygen and carbon dioxide in bioreactors. Despite the volume of data that has resulted, there exists no clinically available PFC product for respiratory gas transport. Such a product is desired in a variety of disease states, including IRI that wreaks havoc in tissue preservation and many other conditions where tissues undergo ischemia for prolonged periods of time.

1.4.8. *PFC Nanoemulsions as Oxygen Therapeutics in the Clinic*

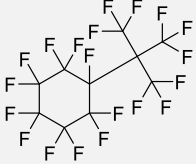
On the order of one-tenth the scale of erythrocytes, NEs can distribute into microcirculation and offer an abundant surface area for gas exchange. Their preclinical safety has also been demonstrated. Accordingly, a handful of PFC-based oxygen therapeutics in the form of PFC-in-water (PFC/W) NEs have been commercialized and entered clinical trials (93-96). One way or another, the trials were terminated prematurely, or the product was not sustainable and was withdrawn from the market after the trial. Reasons for failure include off-target effects and insufficient colloidal stability (92). Development of PFC-NEs as oxygen therapeutics took off in the 1970s and remains today in a state of development. The developmental stages have been roughly broken down into ‘first-generation’ and ‘second-generation’ products. A trademark of the ‘first-generation’ PFC-NEs was the surfactant component. These were comprised of a PFC phase stabilized with synthetic non-ionic surfactant, Pluronic F68. One of the most prevalent first-generation products, Fluosol (Green Cross Corp., Osaka, Japan) was an


FDA-approved treatment option in percutaneous transluminal coronary artery balloon angioplasty (17). Not long after approval, the FDA retracted Fluosol due to insufficient long-term stability and handling difficulty (84). Development of Perftoran (first-generation, Ftorosan, OJCS SPF Perftoran Russian, Moscow, Russia) was likewise discontinued due to limited stability and long organ half-life (92). Oxypherol (Green Cross Corp.), initially named Fluosol-43, was discontinued due to excessive organ retention and long clearance times (90).

The challenges that first-generation products met were insurmountable at the time, but some experimental findings were of value. In 1982, a report presented data that suggested F68 is responsible for activation of complement (93). Consequently, 'second-generation' products utilized egg-based phospholipids in place of F68 as the surfactant and increased PFC concentrations (92, 97). Oxyfluor (HemaGen/PFC) and Oxygent (Alliance Pharmaceutical Corp) were two of the more prevalent second-generation products. As with the first-generation products, second-generations were hindered by clinical side effects. Oxygent and Oxyfluor both caused flu-like symptoms, which were attributed to macrophage uptake of the injected emulsion and subsequent downstream effects related to arachidonic acid conversion to prostaglandins (98). A combination of Alliance Pharmaceutical's financial situation and a rise in the stroke prevalence in the Oxygent group during Phase II trials led the trial to a halt (99). Double-Crane Pharmaceutical Co. Ltd. resumed clinical trials of Oxygent, but this trial was again discontinued after Phase II (92). Oxyfluor's innovation was adding a small amount of safflower oil to enhance the colloidal stability. However, experimental data were not strong enough to indicate a clear advantage. Oxycyte, another second-generation product,

gathered attention and entered phase II clinical trials for severe non-penetrating traumatic brain injury. However, the trial was terminated by 2014 (96).

Table 1.2. Select Commercial Examples of PFC Nanoemulsions for Oxygen Delivery and Tissue Preservation.

Product name	<i>In Vivo</i> Study	Application	Commercialized by:	Reference
Oxycyte	Hamster chamber window model	Ischemia/reperfusion injury	Synthetic Blood International, Inc	(100)
PFC: perfluoro(t-butylcyclohexane) 	Isovolemic hemodilution in male Sprague-Dawley rats	Brain tissue oxygenation		(101)
	Lateral fluid percussion Injury in male Sprague-Dawley rat	Brain tissue oxygenation		(102)
	Oleic acid lung injury in swine	Tissue preservation	Oxygen Biotherapeutics, Inc., Morrisville, NC	(103)
Emulsifiers: Purified egg phospholipids, NF or egg lecithin.	NA	Oxygen supply in 3D hepatic tissue culture		(104)
PFC content: 60% w/v	Middle cerebral artery Occlusion in rats	Tissue oxygenation in ischemic stroke		(105)
	Sprague-Dawley rats	Biocompatibility of PFC emulsions in CNS		(106)
Nanoemulsion size: 200-400 nm		O ₂ and CO transport in sickle cell disease		(107)
	Sprague-Dawley rat arterial gas embolism	Air bubble reabsorption in air embolism		(36)
Manufacturing method: NA	Transgenic sickle cell mice infected with <i>S. pneumoniae</i>	Intravenous tissue oxygenation		(108)
	TBI in rats	Brain oxygenation		Tenax Therapeutics
Oxygent	Swine acute cardio-pulmonary decompression sickness	Respiratory gas transport to and from tissue		Alliance Pharmaceutical Corp, San Diego, CA

Product name	<i>In Vivo</i> Study	Application	Commercialized by:	Reference
PFC: Perfluorooctyl bromide (PFOB) 	Rat isolated heart ischemia/reperfusion	Attenuate neutrophil activation, preservation of myocardial function		(111)
Emulsifiers: egg yolk phospholipids (2%-3.6 w/v) Perfluorodecyl bromide (additive, optional)	dorsal skin fold chamber hamster model	Compatibility of colloid plasma expanders in acute normovolemic hemodilution		(112)
PFC content: 60% w/v	NA (<i>ex vivo</i> study)	Model development of oxygen transport in bioengineered tissue		(113)
Nanoemulsion size: 160-180 nm	NA (<i>ex vivo</i> study)	Perfusion of tissue engineered tracheal construct		(114)
Manufacturing method: NA	Human studies	Clinical immune safety of Oxygent to reduce allogeneic blood transfusion		(115)
	Human studies	Reduce allogeneic erythrocyte transfusions in surgery		(116)

In 2018, clinical trials for Oxycyte, which is currently under the code name ABL-101 (Aurum Biosciences Ltd), were relaunched in the United Kingdom for acute ischemic stroke after showing promise in preclinical setting (95, 105, 117). This clinical trial is novel because it is using the PFC-NE as a theranostic platform; that is, it relays metabolic status of tissues under oxidative stress to identify salvageable tissue regions (diagnostic) and at the same time reduces ischemic lesion growth compared to saline (therapeutic). Problems observed with PFC-NEs extend beyond the scope of clinical product performance. For instance, a recent review identified fatal problems centered on issues with manufacturing standards. Perftech (KEM Laboratories), a product previously available in Mexico, was suspended due to noncompliance with Good Manufacturing Practice standards (118). The two most extensively studied, commercially available PFC-NE products, Oxygent and Oxycyte, are described in more detail in Table 1.2 with included summary of tested applications as oxygen therapeutics in diverse preclinical and clinical studies.

1.4.9. PFC Nanoemulsions for Oxygen Delivery - Current Challenges for Pharmaceutical Development

In the context of oxygen therapeutics, optimal PFC emulsion formulation has proven to be challenging in nature. NEs composed of PFC oils are required to achieve a balance between temporal colloidal stability and *in vivo* excretion rate. Colloidal stability is mainly governed by a mechanism of NE destabilization known as Ostwald ripening which is driven by the internal oil phase composition (119). The rate of NE droplet radius r growth follows the relation $\frac{dr^3}{dt} = \frac{8C_\infty\gamma V_m D}{9\rho RT}$, where C_∞ is the bulk phase solubility of the internal phase in the continuous phase, γ is the interfacial tension, V_m is the molar volume

of the internal phase, D is the diffusion coefficient of the internal phase in the continuous phase, ρ is the density of the internal phase, R is the gas constant, and T is the absolute temperature (119).

PFC properties such as molecular weight (MW) and water solubility directly influence the rate at which an emulsion undergoes Ostwald ripening (26, 120). Low MW and high solubility hasten the rate of Ostwald ripening, driving an emulsion towards rapid destabilization and high probability of product failure (*e.g.*, via phase separation). On the other hand, regulatory bodies (*e.g.*, Food and Drug Administration) may not be partial to long tissue residence times resulting from high MW and low solubility. This makes clinical regulatory approval much more difficult. A plethora of additional properties are related to these, including vapor pressure, *etc.* Thus, it is critical in product formulation to settle on acceptable criteria for colloidal stability and *in vivo* elimination characteristics of an oxygen therapeutic to facilitate selection of the most appropriate PFC. Furthermore, conventional PFC-NE designs are typically limited in their functionalities. As mentioned previously, a single NE can serve several functionalities simultaneously. Oxygen delivery, drug delivery, and multimodal imaging capabilities could be used all together to obtain a more effective formulation. Our group has historically used multifunctional platforms to simultaneously utilize both therapeutic and diagnostic elements of NE design. The triphasic system, introduced by our group in prior work (44), is highlighted in Figure 1.3. In contrast, the convention has been to use the configuration on the left for drug loading, which limits the space available for drug loading to the surfactant layer. This structure is ideal for maintaining high loading of lipophilic drugs in the hydrocarbon oil compartment while simultaneously providing ^{19}F MRS capability with the PFC core.

Notably, adding a component of lower vapor pressure than the continuous phase is reported to increase colloidal stability (121).

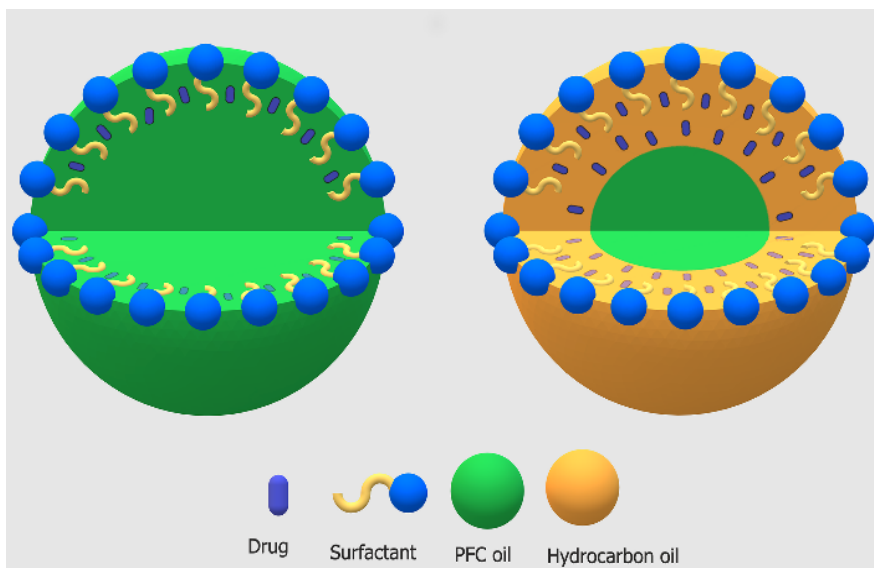


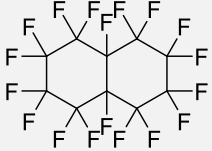
Figure 1.3. Comparison of biphasic nanoemulsion cross-section (left) and triphasic nanoemulsion cross-section (right).

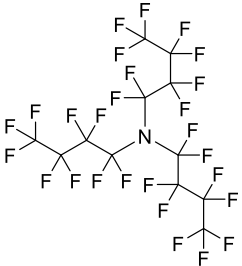
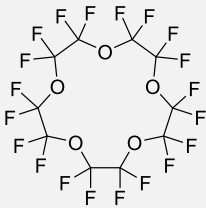

After surveying the relevant oxygen therapeutics literature, characterization of PFC-NE systems is lacking completeness. Table 1.2 shows two most extensively studied commercially available formulations, Oxygent and Oxycyte, including the names of their manufacturers. Extensive evaluation of patent and peer reviewed literature gave us rather limited insight into these compositions. Both formulations are rather similar in size (200-400 nm), have high content of PFC (60% w/v) and are stabilized by egg-based phospholipids. Information on manufacturing methods is limited and data showing their long term colloidal and chemical stability is rare.

Although the PFC materials used for emulsions have been widely explored, its other components (surfactants and additives) have not been as thoroughly investigated. Table 1.3 briefly summarizes a few select examples illustrating the current diversity of PFC-NEs composition in oxygen delivery applications in respect of the choice of PFC

and surfactants. First-generation PFC-NEs used synthetic emulsifiers, such as Pluronic F68, and second-generation products experienced an abrupt swap to naturally-derived phospholipid materials. More recently, proteins and red blood cell membranes were explored for stabilization of PFCs and increasing their biocompatibility (117, 122). There remains a vast domain of uncharted materials which can be investigated as appropriate surfactants. The most common manufacturing method remains to be sonication and sparse use of microfluidization, Table 1.3.

Table 1.3. Composition Diversity in PFC Formulations for Oxygen Delivery Applications.

Product name	Emulsifiers and additives:	PFC content:	Particle size	Manufacturing method	Reference
Ftoemulsion III, Perftoran Plus (Perfluorodecalin)	Proxanol 268, Perfluoromethylcyclohexylpiperidine	20% w/v	NA	high pressure homogenization	(123)
Perfluorodecalin 	Proprietary surfactants (undisclosed)	88% w/v	NA	NA	(36)
	Pluronic F68 (0.125-2% w/v) + Pluronic F127 (0.125-2% w/v) blend	5-40% v/v	206.6-259.8 nm	Microfluidization	(124)
	Pluronic F-68 (5% w/v)	50% w/v	NA	NA	(125)
	Span 20 (5% w/v)				
	L- α -Phosphatidylcholine (5% w/v)				
	Pluronic F68 (2.7% w/v) Yolk phospholipids (0.4% w/v)	20% w/v	NA	NA	(126)
	egg yolk lecithin (4% w/v)	40% w/v	200 nm	NA	(105)
Globin (0.33% w/v) and red blood cells membranes	13.3% v/v	220 nm	ultrasonication	(127)	
perfluorotributylamine	NA		150 nm	sonication	(128)
	Human serum albumin, Red blood cell membranes; indocyanine green; DiD	10.7% v/v	180 nm	sonication	(122)
	lecithin E80 (9% w/v)	33.3% v/v		ultrasonication	(129)
	egg yolk lecithin (9% w/v)	40% v/v	1-2 μ m	ultrasonication	(130)

Product name	Emulsifiers and additives:	PFC content:	Particle size	Manufacturing method	Reference
	egg yolk lecithin (9.5% w/v)	40% v/v		ultrasonication	(131)
Perfluoro-15-crown-5-ether 	Human serum	7 % v/v	160 nm	Sonication	(132)
	Lutrol F68		164.2 nm	Sonication	(133)
Perfluorooctyl bromide 	F8TAC11 Tris(hydroxymethyl)aminomethane head, hydrophobic perfluorinated tail	10% v/v	177 nm 259 nm	sonication homogenization	(134)
	Span 80, PLGA-PEG polymer		302 nm	Sonication	(135)
	Red blood cell membranes		170 nm	Sonication	(117)

The conditions of manufacturing are not typically described in enough depth to warrant easy scale up and further development. Apparent lack of systematic studies on the impact of composition and manufacturing methods on the overall performance as oxygen carriers likely contributes to persistent challenges in advancing these materials to their clinical potential. We propose that this can be remedied by fully exploring the design space of PFC-NEs by systematic investigations of both composition and processing parameters.

Our group has historically used a variety of surfactants and surfactant blends to formulate extremely stable NEs (48, 136, 137). Reporting of fundamental properties such as zeta potential, polydispersity index (PDI), and shelf-stability of NEs is not always present. These are essential elements of formulation characterization and design and are important to monitor and understand because they represent additional indicators of stability and performance independent of average droplet size (138). Particularly for a product in the clinic intended to be used intravenously in large doses, product quality attributes should be thoroughly understood, and the methods used to procure these quality attributes should be standardized. Furthermore, NE manufacturing conditions are at times not described in enough detail to be easily reproduced. A manufacturing technique that yields products with consistent and uniform properties is crucial. Our group has historically used microfluidization to produce NEs with consistent and uniform properties (1, 138). The systematic lack of accessible information precludes identification of which attributes have contributed to PFC-NEs success. Taken altogether, oxygen delivery using PFC-NEs exhibits valuable potential, but is at a product development impasse and needs

more advanced systematic formulation strategies. Therefore, we propose a new approach that builds upon these experiences and would overcome current development setbacks.

Overall, PFC-NE formulations designed for oxygen therapeutics have shown strong preclinical results. Positive outcomes have repeatedly been observed in hypoxic and ischemic conditions in a collection of diverse animal models, and the benefits have been reported to traverse the blood brain barrier. However, conditions such as tissue preservation have needs beyond respiratory gas transport, where reactive oxygen species regularly accumulate. A technology capable of co-delivering oxygen and additional therapeutic entity (*e.g.*, NO scavenger, antioxidant) during preservation and after replantation would be of considerable value. Commonly reported PFC/water NE structures are not ideal for carrying drugs because of the lipophobic and hydrophobic nature of PFCs. To solve this problem, our group has focused on triphasic systems for drug delivery with internal phase composed of two oils, PFC and hydrocarbon, Figure 1.3. We have demonstrated that triphasic NEs can be produced on large scale and with high control of quality attributes (37, 38, 61, 136). We also demonstrate that quality by design (QbD) approaches can significantly improve triphasic systems development and allow for in depth understanding of the impact of the composition of the NE on manufacturing and final product quality (1). Based on these findings we propose that the future of oxygen delivery lies in the more complex PFC nanosystems such as triphasic NEs which offer high stability, pharmaceutical development friendly processes for scale up and overall high level of quality control.

We strongly believe that adoption of methods such as QbD will serve to bring PFCs for organ preservation successfully into clinical application. According to the

International Council on Harmonization (ICH) Q8 (R2) guideline, QbD is defined as a “systematic approach to development that begins with predefined objectives and emphasizes product and process understanding, as well as process control, based on sound science and quality risk management” (139). In general, QbD is implemented to achieve sufficient product and process knowledge to design a product which “consistently delivers the intended performance of the product.” Critical quality attributes (CQAs) are measurable product attributes and are selected to closely reflect product performance. One key feature encouraged by the FDA and an essential in QbD is quality risk management (QRM). This process seeks to identify and rank in order of importance high-risk formulation and processing variables. This in turn can provide rationale for identifying potential critical process parameters (CPPs), *i.e.*, parameters which can have a significant influence on product CQAs. The relationships between potential CPPs and CQAs can be more deeply studied by using design of experiments (DoE).

Another element which is stressed in QbD methodology and finds widespread use elsewhere is process modeling (140). Building models supports process/product understanding and can be used in predictive capacity to monitor and control processes. Mathematical models can exist in various forms, including first-principles models and statistical models. Notable instances in which first-principles modeling is conducted in oxygen therapeutics includes finite element modeling of *in vitro* oxygen diffusivity in 10% v/v perfluorodecalin (PFD) or perfluorotributylamine NE systems (124); oxygen transport using Oxygent in cardiac tissue construct (113); and oxygen consumption and diffusion in assemblies of islet of Langerhans tissue supported by a PFD (70% w/v) NE suspended in alginate gel matrix (141). The first study revealed a strong dependence of

oxygen diffusivity on droplet size and indicated that small droplet diameter is essential for enhanced oxygen transport. The second study concluded that oxygen spatial distribution in PFC-free and PFC-supplemented culture media were similar, but this was attributed to heightened oxygen consumption and cell density with PFC emulsion conditions. The third study highlighted the role of PFC in maintaining oxygen partial pressure homogeneity in transplanted tissue. The presence of the PFC-NE consistently increased the pO_2 in islet cell arrangements of several different geometries and boosted the insulin-releasing capabilities. Notable statistical modeling in oxygen therapeutics include formulation design of lipid-based oxygen microbubbles (142). The authors utilized DoE and constructed regression models which relate the composition to bubble diameter and stability. Carrying out both process modeling and QRM requires intimate knowledge of the overall process.

QbD has been adopted by the pharmaceutical industry and has potential in pre-commercial product development to speed up the discovery of a more promising candidate for clinical translation if applied in formulation of PFC-based oxygen therapeutics and would make it more likely to identify what the cause of failures is and may inform researchers on how to correct them. QbD principles have been broadly applied in NE formulation (143-146). Recently, QbD methodologies have been applied in development of PFC-NEs (1, 138). In these studies, the authors followed QbD guidelines which led to quantitative relationships in the form of multivariate models between the process/product and the product's critical quality attributes. Herneisey *et al* (1) reported a PFC-NE formulation optimization that examined NE composition and manufacturing

parameters and their effects on droplet diameter, long-term stability, and drug loading as CQAs.

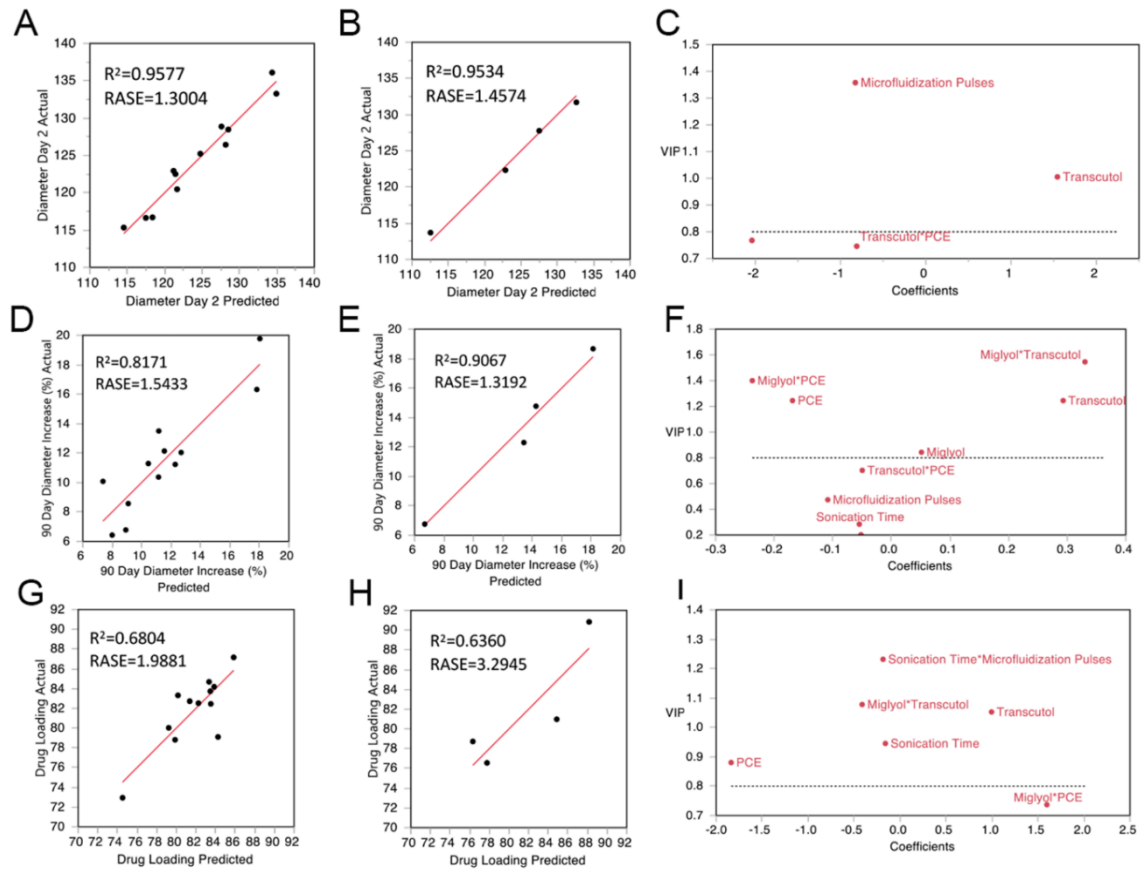


Figure 1.4. Actual by observed response plots from PLS regression models. Multivariate modeling generated predictive paradigms in which design parameters including composition and processing conditions were used to estimate nanoemulsion critical quality attributes including droplet size, long-term stability, and drug loading efficiency. Data reproduced with permission from Herneisey *et al.* (1).

The authors initiated the study with a formal risk management strategy which served to inform which process conditions would most severely affect NE quality attributes. This was followed by design of experiments where those process parameters were scrutinized in detail and concluded by constructing a collection of multivariate regression models to establish relationships that describe how formulation composition and processing parameters affect NE quality attributes. Partial least squares (PLS)

regression models are represented by the predicted by observed response plots in Figure 1.4. The QbD strategy yielded important process information such as length of sonication time during manufacturing inversely correlated with drug loading efficiency. The authors collected extensive data on product quality attributes (*e.g.*, size, zeta potential, PDI, shelf-stability, sterility, pH, stress-stability under destabilizing conditions). Mathematical modeling can be used to establish PFC-NE composition parameters to achieve long term stability and desired colloidal properties (1, 138). More recently, we have shown that these methods can be used to fully develop scale up processes for nanosystems (147).

1.4.10. *Future Perspectives*

The ideal oxygen carrier must be completely safe and perform at par or better than whole blood, without attendant limitations. However, generation of such a “blood substitute” may be an ambitious goal for the next decade of research and development. New advances and innovations in the field of PFC colloid-based oxygen therapeutics such encapsulation of PFCs in red blood cell membranes are promising but require significant validation in translational models prior to clinical use. Quality control metrics should be central to characterizing colloidal stability of PFC and establishing standards in formulation of PFC-NEs is an attainable near-term goal. PFC-NEs are not merely oxygen carriers but are multifunctional agents that are imaging capable across multimodality platforms. These features can help inform *in vitro* formulation, *in vivo* validation, therapeutic monitoring and decision-making, and improving safety, efficacy and feasibility of use across a wide range of applications necessitating mitigation of the deleterious effects of ischemia and reperfusion injury.

Chapter 2. Multiple Linear Regression Applied to Predicting Droplet Size of Complex Perfluorocarbon Nanoemulsions for Biomedical Applications

2.1. Acknowledgements

The text (lines 1341-1713) is a reprinted published manuscript: Lambert, E., & Janjic, J. M. (2019). Multiple linear regression applied to predicting droplet size of complex perfluorocarbon nanoemulsions for biomedical applications. *Pharmaceutical Development and Technology*, 24(6), 1-11. doi:10.1080/10837450.2019.1578372. Copyright 2019. Reprinted by permission of Informa UK Limited, trading as Taylor & Taylor & Francis Group, <http://www.tandfonline.com>.

The authors acknowledge Shikhar Mohan and Yuxiang Zhao for technical insight in statistical analysis. This work was in part supported by National Institute of Biomedical Engineering and Imaging award R21EB023104-02 and AFMSA Department of Defense Award FA8650-17-2-6836.

2.2. Abstract

Multiple linear regression modeling as a novel methodological advancement for design, development and optimization of PFC-NEs is presented. The goal of the presented work is to develop MLR methods applicable to design, development and optimization of PFC-NEs in a broad range of biomedical uses. Depending on the intended use of PFC-NEs as either therapeutics or diagnostics, NE composition differs in respect to specific applications (*e.g.*, magnetic resonance imaging, drug delivery, *etc.*). PFC-NE composition can significantly impact on PFC-NE droplet size which impacts the NE performance and quality. We demonstrated earlier that microfluidization combined with

sonication produces stable emulsions with high level of reproducibility. The goal of the presented work was to establish correlation between droplet size and composition in complex PFC-in-oil-in-water NEs while manufacturing process parameters are kept constant. Under these conditions we demonstrate that MLR model can predict droplet size based on formulation variables such as amount and type of PFC oil and hydrocarbon oil. To the best of our knowledge this is the first report where PFC-NE composition was directly related to its colloidal properties and multiple linear regression used to predict colloidal properties from composition variables.

2.3. Introduction

The FDA recognized the frequency at which nanomedicine clinical translation and commercialization fall short of the mark as early as 2004, when it included nanotechnology in medicine as a priority in its Critical Path Opportunities List (148). The accompanying report highlighted the importance of model-based product development to understand safety and efficacy of medicine (149). Nanomedicine development poses unique challenges for the industry and regulators (150). Challenges that nanomedicine development faces, such as scalability, quality control, and reproducibility, can hinder clinical translation and commercialization. Clinical translation relies on the physical stability of the formulation, as it impacts product performance through its life time (151). Monitoring particle size and size distribution changes over time is fundamental for understanding stability during storage (shelf-life) and use. Predictive model-based paradigms offer solutions to clinical nanomedicine translation by directly addressing these challenges. Recently it was shown that multivariate regression as well as complex nonlinear methods (*e.g.* artificial neural networks) could be applied to model composition

and process parameters in order to optimize NE, as a representative class of nanomedicine formulation, colloidal properties (152-154). More recently, application of “nano-quantitative structure-activity relationships” (QSAR) was evaluated effects of nanoparticle surface chemistry on bioactivity (155). This strategy requires complete characterization of the nanoparticles, in which particle size, shape, and core material are typical descriptors. Others have also utilized nano-QSAR, exploring both linear and nonlinear statistical methods, to describe biological phenomena including cell apoptosis and cell uptake during nanoparticle treatment (156, 157). They found that nanoparticle core material was the most important factor in determining apoptosis. Taken together, these studies suggest mathematical modeling holds potential to streamline nanomedicine optimization for biomedical uses and should be applied across nanomedicine development.

The focus of this study is on NEs, as a representative, broadly used class of colloidal nanomedicine formulations. NEs are typically oil-in-water emulsions with small droplet size (<500 nm). NEs are well suited for nanomedicine development due to their surface-area-to-volume ratio that allows for effective drug loading, sustained release, and the ability to functionalize the surface with targeting ligands and imaging moieties (targeting agents, metal chelates, dyes, *etc.*) (158). NEs are used widely to increase bioavailability of poorly soluble drugs (159-163), can be further incorporated into other dosage forms, and can be produced at industrial scale (163-165). Unique subclass of NEs are PFC-NEs, which have been extensively studied as blood substitutes (34, 166-168) and fluorine-19 magnetic resonance agents. Monocyte/macrophage targeted PFC-NEs have been well established for the purpose of *in situ* ¹⁹F MRI detection of inflammation in

varied inflammatory states (abscess, transplantation, cancer, etc.) (51, 53, 54, 169). PFCs are highly biologically inert, background-free MRI reagents that can be quantitatively detected *in vivo* by ^{19}F MRI (45, 46). ^{19}F MRI emerged as a unique non-invasive quantitative molecular imaging technique where ^{19}F nuclei provide highly selective and specific signal for the biodistribution of immune cells labeled with PFC molecules and nanoimaging agents (PFC-NEs) (45, 46). Additionally, drug-loaded PFC-NEs utilize surfactant layer as the drug carrying component in the PFC-NEs (170, 171) and have been used as theranostics (an simultaneous ‘therapeutic’ and ‘diagnostic’ use in a single nanoformulation) (52, 172-175). PFC-NEs as theranostics were reported to successfully deliver fumagillin to tumors and while used for monitoring delivery effectiveness (176). Others also reported delivery of doxorubicin (177), paclitaxel (177), and rapamycin (178) with PFC-NEs as theranostic nanoformulations. Our group has previously reported macrophage-targeted theranostic PFC-NEs formulated from biocompatible, FDA-approved excipients (38, 52, 179). These NEs are deemed triphasic as they are formulated with three immiscible liquid phases and represent PFC-in-hydrocarbon-in-water (PFC/HC/W) complex NEs (38, 44, 173, 180). In these systems, we demonstrated that the drug loading and release are not influenced by the presence of PFC oil phase (37). These complex PFC-NEs can incorporate fluorescent dye-PFC conjugates for the purpose of bimodal imaging (48) and can incorporate fluorophilic-lipophilic conjugates (FLC) (181, 182).

Mechanistic modeling applied to development of oxygen-loaded PFC-NEs suggests that thorough characterization of formulation components is crucial for producing consistently effective formulations (124). Specifically, they found that type of

oil impacts the shelf-life and droplet size impacts oxygen delivery rate. Others have demonstrated that variations in droplet size can affect drug release behavior, cell uptake, bioactivity, and half-life (183-187).

The aim of this work is development of interpretable and broadly applicable mathematical modeling strategies for predicting critical properties (*e.g.*, size, size distribution) of NEs with aim to accelerate their development as future nanomedicines. Because NE size is one of the most indicative factors regarding their colloidal stability (188-190), we used an augmented D-optimal mixture design to select NE formulation variables and studied their effects on droplet size. To demonstrate utility of MLR on PFC-NE formulation design, we studied effects of known PFC oils, HC oils, a commonly used solubilizer and an example FLC on the droplet size in biphasic and triphasic NEs.

2.4. Materials and Methods

2.4.1. Materials

Perfluoro-15-crown-5-ether (PCE) and perfluoropolyether (PFPE) dimethyl ester were purchased from Exflur Research Corporation (Round Rock, TX). PFPE oxide was a gift from Celsense Inc. (Pittsburgh, PA). Kolliphor® EL (CrEL) was purchased from Sigma Aldrich. Pluronic® P105 was purchased from BASF Corp. Super Refined® Olive Oil NF-LQ (MH) was a gift from CRODA, Inc. (NJ, USA). Miglyol 812N was purchased from Sasol. Transcutol (2-(2-Ethoxyethoxy)ethanol) was purchased from Spectrum Chemicals (NJ, USA). Tyramine was purchased from Aldrich. Dulbecco's modified Eagle medium (DMEM) (Mediatech Inc., Manassas, VA) was used to simulate biological conditions. All reagents were used as received without further purification. Deionized (DI) water was used.

2.4.2. Solubility of PFPE-tyramide

PFPE-tyramide was weighed in a glass vial. Each excipient was added to equal a concentration of PFPE-tyramide of 50 mg/mL. The samples were shaken for 16 hr and let to rest for another 24 hr. Then the samples were imaged and prepared for microscopy on EVOS (ThermoFisher Scientific).

2.4.3. Experimental Design

The data under consideration were collected from an augmented D-optimal mixture design with constraints. The mixture variables included the two hydrocarbon oils, Miglyol 812 (A) and olive oil (B); two PFC oils, perfluoro-15-crown-5-ether (C) and perfluoropolyether (D); and a solubilizer (S), transcitol. The four oils were constrained such that no more than one PFC oil and one HC oil co-existed in a given experimental run at a 1:1 v/v ratio. The solubilizer was constrained such that $S \leq 0.3$. The levels for mixture variables in each experimental run summed to 1. The D-optimal mixture design was augmented to accommodate a process variable, PFPE-tyramide (T), which was not measured by volume and was treated as a binary variable (0-absent, 1-present). A representative formulation was replicated four times.

2.4.4. Preparation of Nanoemulsions

Preparation of 3% w/w Kolliphor EL/ 2% w/w Pluronic P105 surfactant solution is reported previously (44). Emulsification protocol developed previously (48, 182) was partially modified. First, surfactant solution was added to the oil(s). If present, solubilizer or PFPE-tyramide dissolved in transcitol (at 50 mg/mL) was added to the mixture. Then, coarse emulsions were produced with an analog vortex mixer (VWR, Radnor, PA) on

high for 30 s. Triphasic emulsions were sonicated for 30 s at 29% amplitude with Model 500 Ultrasonic Dismembrator (FisherScientific, Pittsburgh, PA). Microfluidization was performed on all coarse emulsions by Microfluidizer M110S (Microfluidics Corp., Westwood, MA) at 15,000 psi liquid pressure for 20 pulses over ice cold interaction chamber. Emulsions were stored at 4 °C in glass vials. This method was used to produce all presented formulations. Microfluidization processing parameters were kept constant throughout the study.

2.4.5. *Nanoemulsion Characterization*

Droplet diameter (reported as z-average), polydispersity index (PDI), and zeta potential were measured using dynamic light scattering (DLS) at a 1:40 v/v dilution on a Zetasizer Nano (Malvern Instruments, Worcestershire, UK), as reported earlier (38). NEs size and PDI were followed for at least 148 d to evaluate their shelf-life.

2.4.6. *Centrifugation Stability Test*

Previously reported protocol was used with minor modifications (38). Briefly, the centrifugation tests were conducted on 2 mL samples of two-phase NEs ($n=12$) at a dilution of 1:40 v/v. Samples were centrifuged for 5 min at 1100 revolutions per minute (RPM) ($218 \times g$) on Centrifuge 5804R (VWR, Eppendorf AG, 22331 Hamburg). NE size and PDI were measured before and after centrifugation and were compared.

2.4.7. *Serum Incubation Stability Test*

For the serum incubation test, NEs were diluted in DMEM, 10 vol% fetal bovine serum (FBS) in DMEM, or 20 vol% FBS in DMEM. NE diluted in water was used as a control. Samples were incubated for 24 hr at 37 °C. Size and PDI were measured before

and after serum incubation and were compared. Two-sided, unpaired t-tests compared: 1) the PFC emulsions ($n=6$) and HC emulsions ($n=6$), and 2) the PFC emulsions and the triphasic emulsions ($n=12$).

2.4.8. Percent Size Change and PDI Change Calculations

To determine how large a response was elicited by centrifugation and serum stressors, we calculated a percent size change and raw PDI change as $(d_{bl} - d)/d_{bl} * 100\%$ and $PDI_{bl} - PDI$, respectively, where d_{bl} is baseline z-average droplet diameter, d is z-average droplet diameter post-incubation or post-centrifugation, PDI_{bl} is baseline polydispersity index, and PDI is polydispersity index post-incubation or post-centrifugation.

2.4.9. Regression Model

Main effect and second order regression coefficients β_i and β_{ij} were obtained, resulting in a quadratic Cox equation (191) of the form $y = \beta_0 + \sum_i \beta_i X_i + \sum_{i,j} \beta_{ij} X_i X_j$ where X_i is the volume fraction of component i in the dispersed phase, $j > i$, y is the response, and β_0 is the intercept. Variable selection in regression modeling used a p -value threshold where regression coefficients having $p > 0.05$ were eliminated from the full model to produce a reduced model containing terms with $p \leq 0.05$. Root mean square error (RMSE) was used as a metric to confirm the quality of the regression model. The prediction error sum of squares (PRESS) RMSE was examined with leave-one-out cross-validation and served to validate the model.

2.4.10. *Data Analysis*

JMP Pro 13.2.1 was used for statistical analysis, including evaluation of experimental design, hypothesis testing via performing two-sided, unpaired Student's t test, ANOVA, and least squares regression modeling. p -value ≤ 0.05 was taken to indicate significance.

2.5. Results and Discussion

2.5.1. *Formulation Development*

The construction of a NE library began with formulation design. As oil structure and properties are known to impact NE properties and function, a careful examination of potential excipient characteristics was conducted. High molecular weight PFC oils were chosen to compensate for high PFC volatility (192). This precautionary measure reduces likelihood of evaporative loss encountered during high shear processing and prolongs colloidal stability over that of short-chain PFCs (193-195). Of the two PFC oils, one is prone to Ostwald ripening (perfluoro-15-crown-5-ether, PCE) and one is resistant to Ostwald ripening (perfluoropolyether, PFPE) (192). PCE and PFPE structures are shown in Figure 2.1. Likewise, one short-chain HC oil prone to Ostwald ripening (Miglyol 812) and one long-chain HC oil resistant to Ostwald ripening were chosen (olive oil). By selecting oils of dissimilar behaviors as internal phase in NEs, we aimed to cover a broad range of the formulation design space.

PFPE-tyramide (T) is a was chosen as an exemplar FLC (181, 182) and because it can serve as a future scaffold for chemical conjugation, which, with modifications, could be used to link dyes and other imaging agents, emulsifiers, targeting ligands, and drugs (196). The solubilizer (S), transcitol, was used to facilitate easier incorporation of PFPE

tyramide, which showed incredibly low solubility in many other excipients (Table A.1). PFPE-tyramide was synthesized using a previously published method with minor adjustments (182).

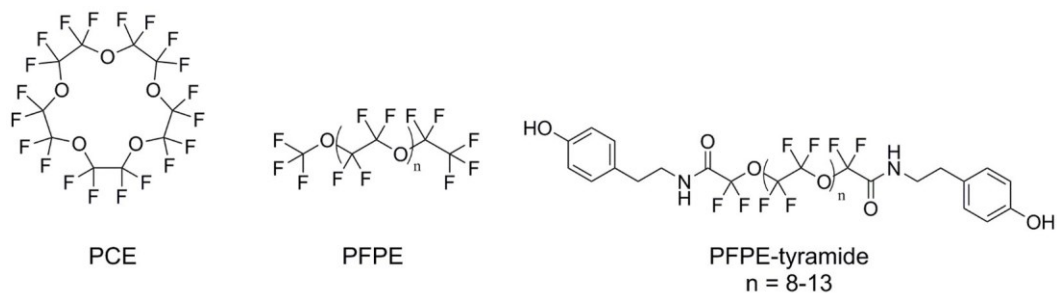


Figure 2.1. Structures of perfluorocarbon oils used in this study and of perfluoropolyether-tyramide. Perfluoro-15-crown-5-ether (PCE) is prone to Ostwald ripening and perfluoropolyether oxide (PFPE) is resistant to Ostwald ripening.

2.5.2. Experimental Design

We utilized an augmented D-optimal mixture design to study the effect of NE composition on droplet size. This design is illustrated in the heat map and ternary diagrams in Figure 2.2. Table 2.1 summarizes all formulations in full, where amounts of each mixture component represent the volume fraction of each component in the dispersed phase. Oil component constraints, disclosed in full in the Materials and Methods section, were put in place due to the impracticality of blending more than one of either PFC or HC oil as well as the increasingly complicated physical interpretation of combining more than two oils in a single trial.

Table 2.1. Composition and z-average droplet size of nanoemulsions. Reported as mean \pm standard deviation of 3 measurements. Note: Component levels are proportional to the excipient concentration, % v/v. In all NEs, oil(s) plus solubilizer was present at 8% v/v and tyramide was at 0.0013% w/v (if present). Non-ionic surfactant was present at 2.3% w/v.

ID	Type	Miglyol (A)	Olive Oil (B)	PCE (C)	PFPE (D)	S	T	Size (nm) \pm S.D.
1	2 phase	1						133 \pm 1.1
2		0.7				0.3		130 \pm 2.5
3			1					158 \pm 3.7
4			0.7			0.3		144 \pm 0.7
5				1				148 \pm 4.3
6				0.7		0.3		141 \pm 3.5
7					1			178 \pm 2.2
8					0.7	0.3		156 \pm 0.8
9			0.7			0.3	1	134 \pm 3.3
10				0.7		0.3	1	146 \pm 4.9
11					0.7	0.3	1	150 \pm 2.7
12						0.7	0.3	1
13	3 phase	0.5		0.5				129 \pm 2.6
14		0.5			0.5			134 \pm 0.9
15			0.5	0.5				147 \pm 3.7
16			0.5		0.5			147 \pm 2.7
17		0.35		0.35		0.3	1	140 \pm 2.6
18			0.35		0.35	0.3	1	151 \pm 0.7
19		0.35			0.35	0.3	1	133 \pm 1.2
20			0.35	0.35		0.3	1	149 \pm 1.9
21		0.35		0.35		0.3		133 \pm 0.9
22		0.35			0.35	0.3		140 \pm 1.9
23			0.35	0.35		0.3		143 \pm 3.4
24			0.35		0.35	0.3		148 \pm 3.5

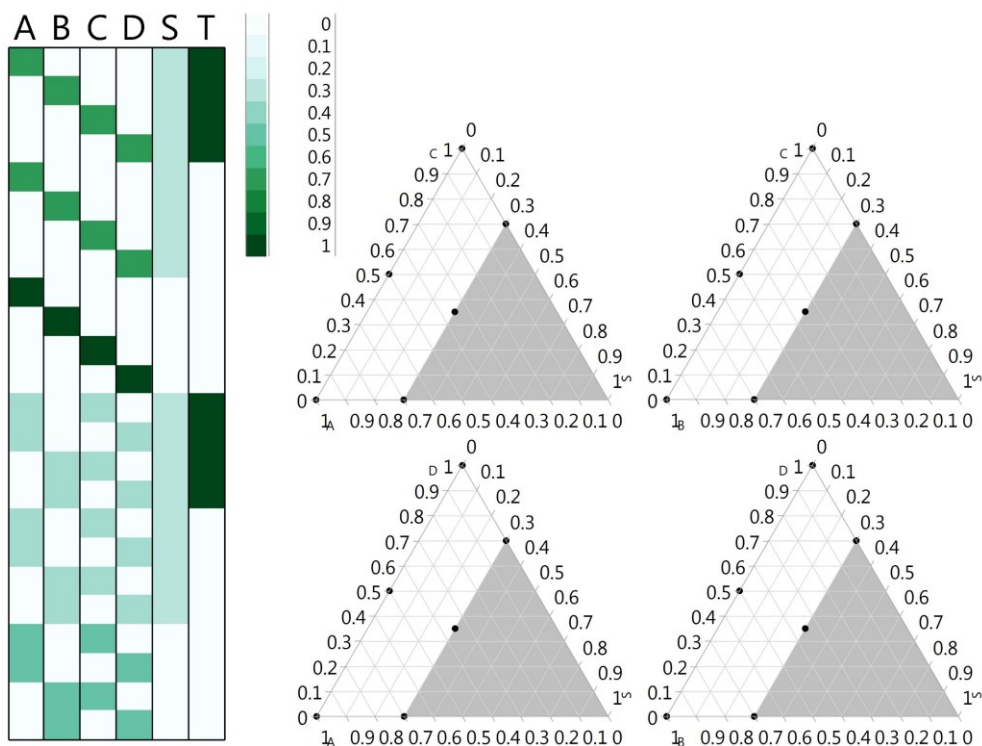


Figure 2.2. Heat map and ternary diagrams representative of the design matrix used for data collection in the MLR model.

2.5.3. Formulation Characterization

Long-term stability (size, PDI, zeta potential) was monitored periodically over time and is shown in Figure 2.3A-E for select emulsions, while Figure A.1, Figure A.2, and Figure A.3 in Appendix A show the full dataset. Temporal stability, measured by droplet size constancy, was exceptional in all emulsions and was not affected by complex nature of the formulation (*i.e.*, blended oils; presence of S and T). The average size and PDI profiles over time for NEs 5, 6, and 11, composed of PCE oil (Figure 2.3A and D), illustrate that in a given two-phase formulation, the presence of S and T is inconsequential over the time frame followed. Further, the addition of a second oil to the PCE formulation resulted in a comparable level of storage stability. This is demonstrated in Figure 2.3A and D, where a moderate deviation in size (\sim less than 15%) is observed

with the addition of the hydrocarbon, either olive oil or Miglyol to the PCE NE, while temporal constancy is maintained. The DLS measurements therefore indicate that all formulations considered were stable and robust to compositional modifications. It was observed that zeta potential measurements were significantly impacted by incorporation of PFPE-tyramide (unpaired, two-sided t-test, $p < 0.01$), which is evident from Figure 2.3E and F. Non-zero zeta potential is expected to enhance colloidal stability through electrostatic repulsion (197). To demonstrate the reproducibility of the emulsification protocol used, NE 15 was selected to be replicated four additional times. This emulsion endured serum incubation with minimal size and PDI changes and thus would be a desirable formulation to continue developing (drug loading, *etc.*). Table 2.4 shows the size, PDI, and zeta potential of the replicates with good agreement of measured properties among the replicates.

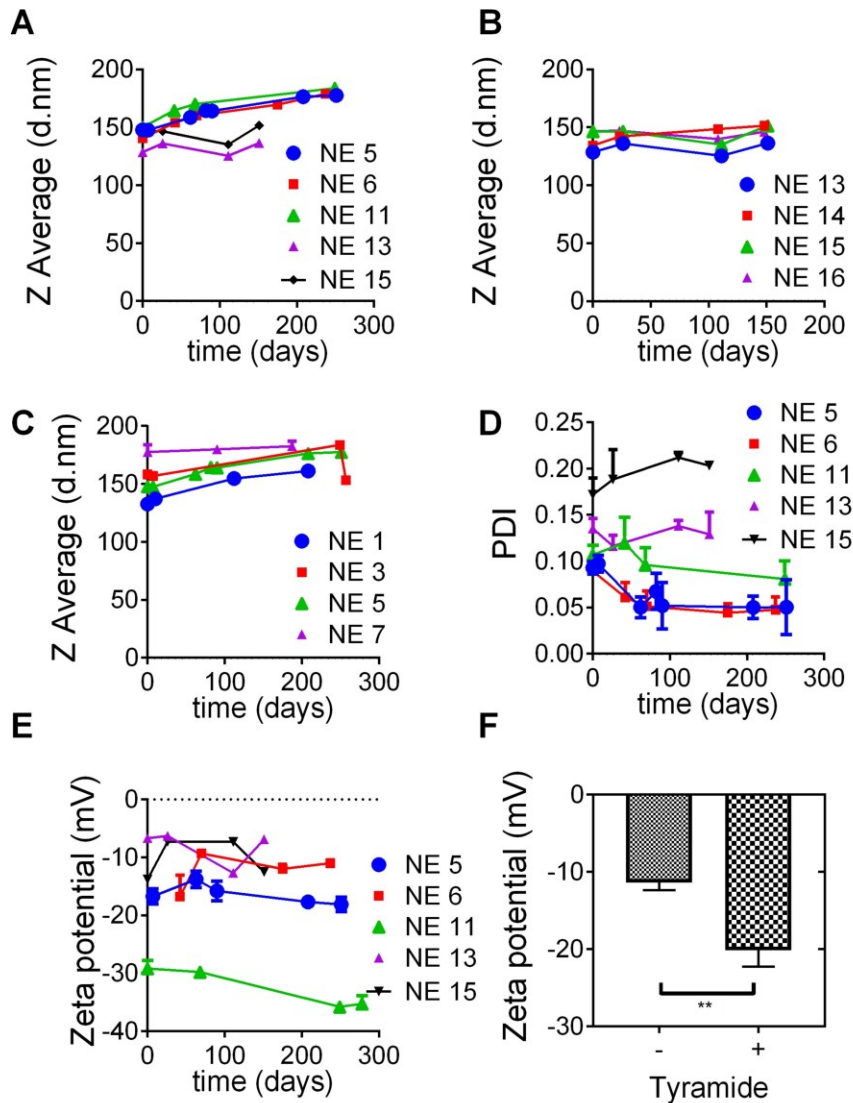


Figure 2.3. Long term stability of selected nanoemulsions. Panels A, B, and C show z-average over time. Panel D shows polydispersity index followed over time. Panel E shows zeta potential followed over time. All samples were stored at 4 °C without humidity control. Reported as mean of 3 measurements \pm standard deviation. Panel F shows effect of PFPE-tyramide on zeta potential, where Tyramide is PFPE-tyramide, ‘-’ is absence ($n=16$), and ‘+’ is presence ($n=8$). ** indicates $p < 0.01$.

2.5.4. Stress Stability.

Our group routinely uses various *in vitro* stress tests for quality control.

Centrifugation stability test is in place to screen emulsions for stability in cell culture

conditions because centrifuging cells is a routine task when treating cells. Centrifugation was conducted on all twelve two-phase formulations without eliciting response, shown in Figure A.8. Serum incubation test, which accelerates mechanisms of instability and can result in rapid droplet size increase, was used as reported previously (181) for formulation robustness characterization. In this study, PFC-NEs consistently exhibit poorer stability than HC NEs in serum tests. Figure 2.4 illustrates colloidal behavior in which average droplet size before and after serum incubation tests was compared. With the addition of a HC phase, the size change and PDI change, which inversely correlate to stability in the context of this assay, were stifled relative to biphasic PFC-NEs ($n=12$ and $n=6$, respectively). This result supports prior literature which suggests that (1) the addition of a third component of lower vapor pressure to a two-phase emulsion stabilizes against Ostwald ripening by reducing surface tension (121) and (2) a HC component added to PFC emulsion adheres to the droplet surface and stabilizes the emulsion and provides better interaction with the surfactant (198). Considering high lipophobicity and hydrophobicity of PFCs, it is expected that surfactants primarily interact with O/W interface, which is also supported by existing literature (199, 200).

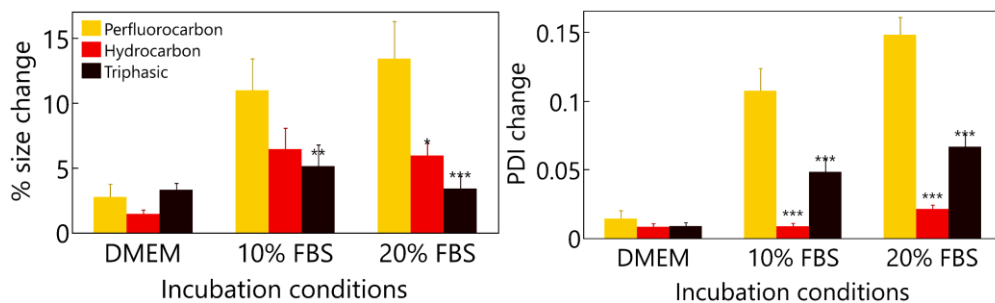


Figure 2.4. Percent size change and PDI change after 24-hr incubation in culture media at the specified concentration (% v/v) of FBS. *, **, and *** represent p -value < 0.05, 0.01, and 0.001 compared to PFC-NE response (two-sided t-test), respectively. $n=6$ for PFC and HC nanoemulsions and $n=12$ for triphasic nanoemulsions. Error bars are one SEM.

2.5.5. *Linear Regression Model*

The augmented D-optimal mixture design (191) was comprised of five mixture variables representing the components of the dispersed phase of the NE and a process variable. This mixture-process variable experimental design was convoluted by the need to multiply the fitted mixture model with the process model in the event of nonlinear effects and the inability to properly evaluate the process variable linear effect among the mixture variables (201). Consequently, a preliminary MLR analysis was conducted on all possible main effects and two-way and three-way T interactions, followed by a simple linear regression of droplet size on T. These analyses, shown in Table A.2 and Table A.3, indicated that T and its interactions were not found significant in influencing droplet size and thus T was excluded from the formal regression analysis. This result suggests that implementing additional formulation modifications such as extending targeting ligands from the scaffolding provided by PFPE-tyramide's structural features is a feasible strategy. Implementing such a targeting strategy to add function to the emulsion without affecting the colloidal size of the formulation would be of substantial value.

Table 2.2. Regression coefficients and model assessment for crossed quadratic model.

Term	Estimate	Std Error	t Ratio	p-value
Intercept	132.95	4.89	27.2	<0.0001
A	-0.89	6.75	-0.13	0.8974
B	21.63	6.75	3.2	0.0059
C	16.66	6.75	2.47	0.0261
D	41.55	6.75	6.15	<0.0001
AC	-38.06	16.48	-2.31	0.0355
AD	-79.47	16.48	-4.82	0.0002
BC	-16.17	16.48	-0.98	0.3421
BD	-62.21	16.48	-3.78	0.0018
R^2	0.9169			
RMSE (nm)	4.1071			
Mean (nm)	144.6971			
Press RMSE (nm)	5.4709			

With the removal of T from the regression analysis, only mixture variables, which are inherently collinear, remained. To minimize the degree of collinearity among the predictor variables, component S was treated as a ‘filler’ since its only function was as a carrier of T. Exclusion of S from the analysis left four continuous independent variables and their interactions. Table 2.2 shows the regression coefficients and relevant statistics for the initial full quadratic model, which includes insignificant terms ($p>0.05$). After removal of insignificant terms, the RMSE was reduced and coefficient of determination, R^2 , remained high as shown in Table 2.3. Size was estimated with a reduced model consisting of three main effects and three interaction terms:

$$\widehat{Size} = 132.46 + 21.08B + 16.11C + 42.16D - 36.23AC - 80.29AD - 59.76BD \quad (2.1)$$

The presence of second-order terms in Equation (2.1) could indicate non-linear mixing effects are prevalent between HC and PFC oils. This supports existing literature detailing the ‘gas-like’ compressible behavior of liquid PFCs (27). From Equation (2.1), negative directionality observed in the crossed regression coefficients for oil interactions governs that blending of oils in these NEs reduces particle size. Observations of size distribution overlay curves, demonstrated in Figure 2.7, are consistent with this interpretation. In NEs with mixed oil composition, the size distribution curves tend to shift towards the left compared to NEs composed of a single oil. Others report similar findings when blending lipids and PFCs in NEs (38). Model fit and residuals are shown in Figure 2.5. Residuals appear to be normally distributed as visualized in the q-q plot (Figure 2.5C). Ternary diagrams with overlaid contours convey how the droplet size is related to the composition (Figure 2.8A-D). These illustrations of the regression equation would serve to guide product formulators when interested in developing new NEs.

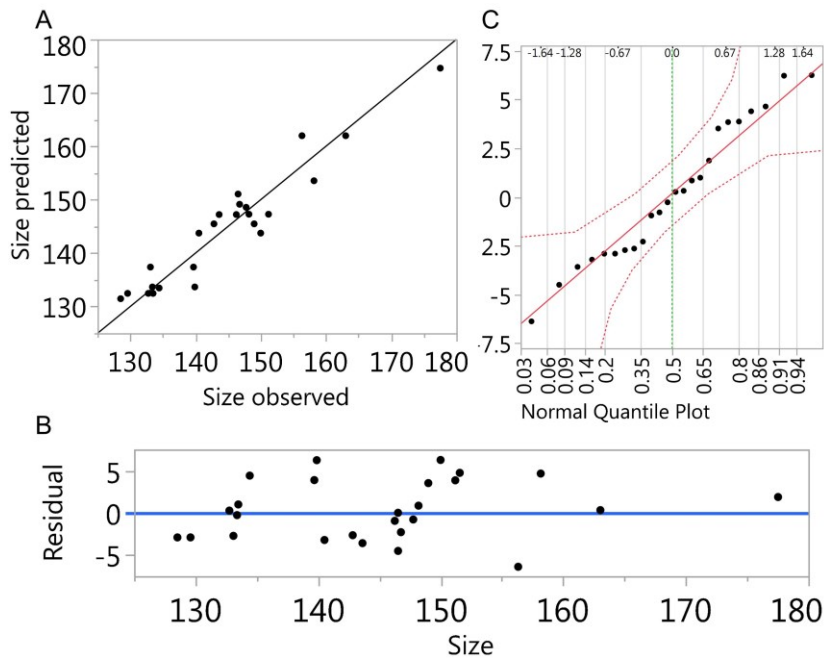


Figure 2.5. Plots of observed size by predicted size, where the solid line is the line $y = x$, (A) and residual by predicted size, where the solid blue line is the $y = 0$ reference line (B).

Table 2.3. Regression coefficients and model assessment for reduced least squares model.

Term	Estimate	Std Error	t Ratio	p-value
Intercept	132.46	2.03	65.14	<0.0001
B	21.08	3.58	5.89	<0.0001
C	16.11	3.59	4.48	0.0003
D	42.16	3.80	11.1	<0.0001
AC	-36.23	15.26	-2.37	0.0297
AD	-80.29	15.44	-5.2	<0.0001
BD	-59.76	15.72	-3.8	0.0014
R^2	0.9113			
RMSE (nm)	3.9858			
Mean (nm)	144.6971			
Press RMSE (nm)	5.0463			

To further justify this model selection, RMSE from fitting all possible model permutations using backwards stepwise regression was inspected. In Figure 2.6, labels highlight the model with like number of terms associated with the lowest error. Error was minimized when main effects B , C , and D and second order terms AC , AD , and BD appeared in the models which had more than 3 terms. As these terms were also the found in the reduced model above, we were assured of the best model selection. To assess the model's predictive capability with limited data, we utilized a well-known leave-one-out cross-validation method, where PRESS RMSE was collected and indicated the prediction capability. PRESS RMSE was improved upon removal of insignificant regression terms and was similar to the reduced model RMSE, which in turn was comparable to the intra-measurement standard deviations.

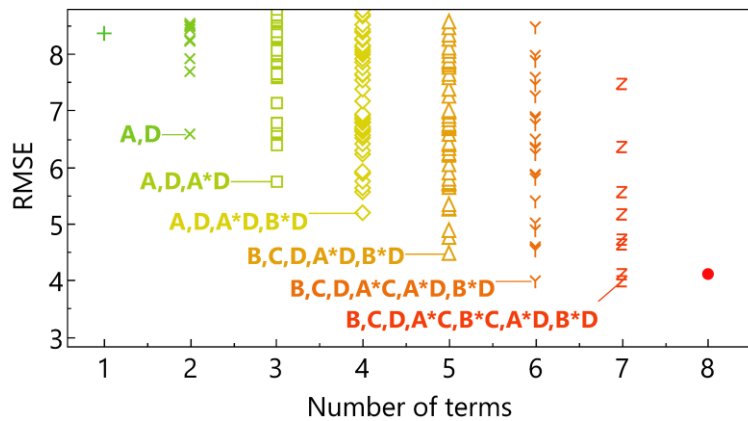


Figure 2.6. Root mean square error associated with all possible models.

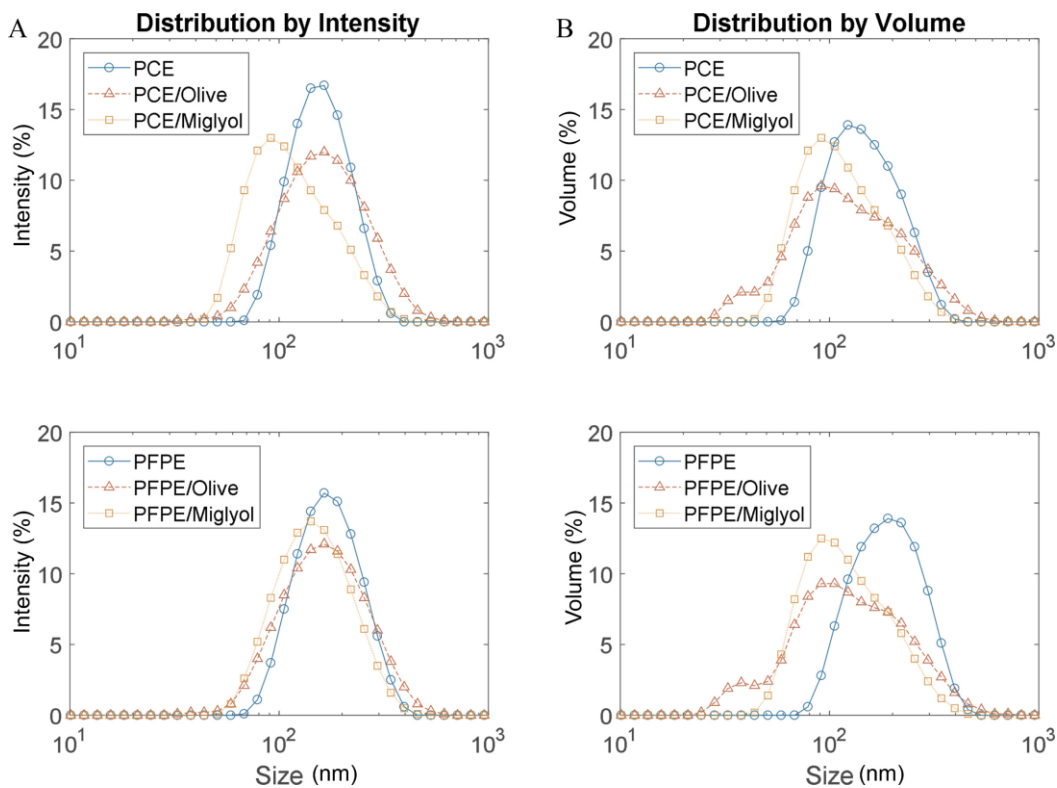


Figure 2.7. Size distributions by intensity (A) and by volume (B) for nanoemulsions composed of PCE (top) and PFPE (bottom).

Table 2.4. Droplet size, polydispersity index, and zeta potential for NE 15 and its four replicates. Reported as mean \pm standard deviation of three measurements.

	Size \pm SD	PDI \pm SD	Zeta \pm SD
NE15	146.53 \pm 3.72	0.172 \pm 0.018	-13.8 \pm 0.67
NE15R1	145.50 \pm 0.82	0.187 \pm 0.007	-14.6 \pm 0.50
NE15R2	143.67 \pm 1.66	0.189 \pm 0.012	-17.4 \pm 0.26
NE15R3	143.60 \pm 0.36	0.175 \pm 0.016	-15.2 \pm 0.15
NE15R4	146.67 \pm 0.78	0.198 \pm 0.007	-14.0 \pm 0.50
Mean	145.19 \pm 1.30	0.184 \pm 0.011	-15.0 \pm 1.50

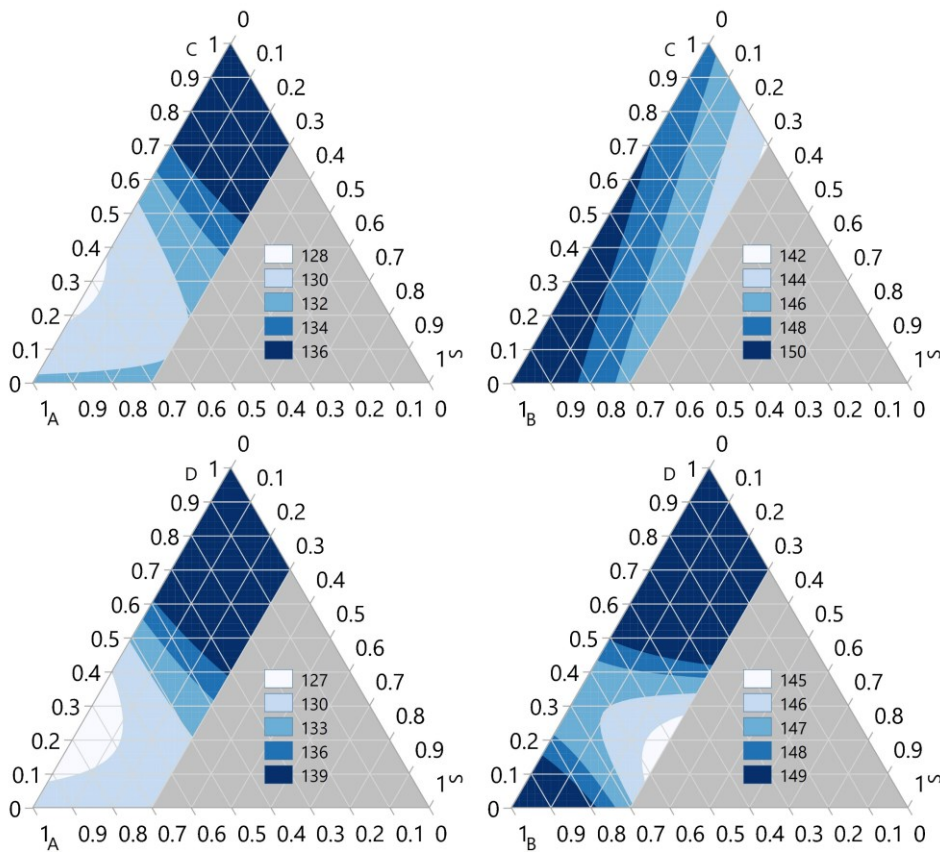


Figure 2.8. Ternary diagrams with overlaid size contours.

2.6. Conclusions

We demonstrate, to the best of our knowledge, the first use of MLR modeling applied to predicting droplet size of complex PFC-NEs. This multivariate methodology

will be employed in the systematic analysis of PFC-NEs as oxygen carriers described in Chapter 3.

These multifunctional triphasic formulations have previously demonstrated imaging and treatment functionalities in inflammatory models. Characterization and long-term follow up of the presented NEs indicate that these formulations are robust to compositional modifications and are resistant to Ostwald ripening. Further, serum incubation stability data illustrate the value of supplementing PFC-NEs with a HC oil phase. Not only does it allow for drug loading functionality, but it also contributes to a higher degree of colloidal stabilization. Through replication of one formulation, we show the degree of reproducibility inherent to the microfluidization protocol used. After performing adequate characterization, we employed an augmented D-optimal mixture design of experiments to establish a multivariate regression model to identify the impact of NE composition on the z-average droplet size. The predictive model development in this work serves as an example of how to efficiently explore the formulation design space with regulatory barriers in mind. Our results suggest that the NE droplet size can be tuned by modifying both oil type and amount. Moreover, an example fluorophilic-lipophilic conjugate had minimal bearing on droplet size. We expect that the *in silico* regression modeling methodology presented here will have further implications in building desired imaging, treatment, and bioactivity properties into innovative nanoformulations in a bottom-up fashion and modulating existing formulations.

We have demonstrated here a general methodology to construct meaningful multivariate models that can describe the NE droplet size. The model represents a strategy to modulate the droplet size, which is a critical attribute of NEs, by adjusting the

composition. This a valuable tool which we can utilize in the remainder of Specific aim 1 to learn more about oxygen delivery and kinetic stability of similar perfluorinated systems.

Chapter 3. Quality by Design Approach Identifies Critical Parameters Driving Oxygen Delivery Performance *in Vitro* for Perfluorocarbon Based Artificial Oxygen Carriers

3.1. Acknowledgements

The following text is adapted from the published manuscript: Lambert, E., & Janjic, J. M. (2021). Quality by design approach identifies critical parameters driving oxygen delivery performance *in vitro* for perfluorocarbon based artificial oxygen carriers. *Scientific Reports*, 11(1), 5569. doi:10.1038/s41598-021-84076-1. Copyright 2021 Nature Portfolio.

The authors would like to acknowledge Valerie Flores for assisting with data collection of colloidal attributes.

3.2. Abstract

PFCs exhibiting high solubility for oxygen are attractive materials as AOC, an alternative to whole blood or HBOCs. PFC-based AOCs, however, met clinical translation roadblocks due to product quality control challenges. To overcome these issues, we present an adaptation of QbD practices to the optimization of PFC-NEs as AOCs. QbD elements including quality risk management, DoE, and multivariate data analysis facilitated the identification of composition and process parameters that strongly impacted PFC colloidal stability and oxygen transport function. The resulting quantitative relationships indicated a composition-driven tradeoff between stability and oxygen transport. It was found that PFC content was most predictive of *in vitro* oxygen release, but the PFC type (perfluoro-15-crown-5-ether, PCE or perfluorooctyl bromide, PFOB) had no effect on oxygen release. Furthermore, we found, under constant processing

conditions, all PFC-NEs, comprised of varied PFC and hydrocarbon content, exhibited a narrow droplet size range (100-150 nm) and narrow size distribution. Representative PFOB-NE maintained colloidal attributes upon manufacturing on larger scale (100 mL). QbD approach offers unique insights into PFC AOC performance, which will overcome current product development challenges and accelerate clinical translation.

3.3. Introduction

Regenerative medicine and organ transplantation rely on successful organ preservation. Whole blood (WB) is a standard choice to restore oxygen in clinical settings, but it is far from a perfect product. For the patient, there are infectious risks, immune modulations, acute transfusion reactions, transfusion-related lung injury, volume overload, and hemolytic reactions (202). Further, there are chemical and pharmacological drawbacks. First, there exist pH and temperature dependencies of oxygen dissociation from hemoglobin. This is problematic in conditions such as hypothermia, which is typically used in organ preservation. Second, hemoglobin relies on an allosteric effector, 2,3-diphosphoglycerate (2,3-DPG), to function properly. 2,3-DPG levels decrease with storage time which reduces performance (90). Artificial oxygen carriers (AOC) have been developed with the goal of reducing need for WB (202).

In the search for a versatile AOC, PFCs emerged as attractive materials because of their physicochemical properties that allow them to dissolve high amounts of gaseous species, including respiratory gasses (203). In contrast to WB or blood products, PFC oxygen carrier function is minimally impacted by the environmental, chemical, and pharmacologic factors. Due to the nature of the association-dissociation mechanism of oxygen with PFCs that follows Henry's Law linear dependence, PFCs as oxygen carriers

are functionally resistant to pH and temperature influence. Due to the strength of the carbon-fluorine covalent bond, PFCs are chemically resistant to heat and do not undergo metabolic transformation *in vivo*. Therefore, PFCs are safer alternatives to HBOCs, which can cause hypertension, immune reactions, and have short half-life (202, 204). Overview of AOC clinical translation challenges is discussed elsewhere (202, 205).

Injectable PFC-NEs have adopted a range of uses such as blood transfusion substitutes (116), support of cell growth in bioreactors (206-209), wound healing (210, 211), and in ischemia-reperfusion injury and tissue preservation (111, 212-214). However, clinical translation and approval of PFC-NEs are often met with challenges such as poorly-controlled colloidal stability. (215) Here we focus on the roadblocks of PFC-based AOC development, which we hypothesize can be overcome by utilizing a systematic product development strategy, Quality by Design (216). Recently, we proposed QbD as a comprehensive approach to understanding colloidal attributes of PFC-NEs and their impact on performance across multiple biomedical applications, from imaging to oxygen delivery (216). QbD has been applied to a variety of pharmaceutical systems ranging from powder blends to NEs (217, 218). Here, QbD is applied to PFC-NE colloidal stability and oxygen transport characterization, resulting in designation of formulation and processing design space for a model PFC AOC in which both attributes can be controlled.

QbD is a collection of practices that systematically facilitates pharmaceutical product development aimed at assuring product quality (218). In QbD, critical quality attributes are defined as measurable product qualities that are crucial to the quality throughout the product lifetime. Quality risk management tabulates and ranks all ways in

which CQAs can fail to meet CQA specifications (known as failure modes) leading to rational DoE. DoE facilitates efficient use of resources and eliminates the conventional resource-consuming one-factor-at-a-time approach to product optimization (219).

In earlier notable PFC-AOC studies, authors derived mathematical equations to describe relationships between oxygen tension and distribution in blood vessels and tissue oxygenation under the influence of PFC emulsions (220, 221). More recently, empirical data was used to confirm finite element modeling findings showing that PFC-NE shelf-stability is impacted by PFC type and that oxygen diffusivity from PFC-NEs is impacted by interfacial area (124). One study used response surface methodology to describe how droplet size and PFC loading efficiency were affected by processing parameters such as emulsification temperature, mixing time, and speed (222). Others utilized an orthogonal design to evaluate the impact of composition on the particle size, PDI, and zeta potential of perfluorooctyl bromide (PFOB) NEs (223). However, none of these studies employed QbD. Here, we demonstrate the utility of QbD as opposed to one-factor-at-a-time approach.

Despite advances in preclinical models and computational studies, PFC-NEs have remained difficult to translate due to inadequate colloidal instability (224). Enriching the dispersed PFC phase with a small amount of poorly water soluble hydrocarbon revealed a quick way to enhance stability (225). However, the oils that opposed instability tended to have unacceptable organ residence times (224). Alternatively, perfluorinated surfactants have been investigated to desired stability (203). While they may be effective (226), these structurally-novel materials have unknown toxicity and are thought to be environmental pollutants (227). Therefore, creative and inventive solutions to development of PFC

AOCs which provide rigorous understanding of colloidal attributes are in demand (216). As an alternative to the above strategies, our group reported PFC-NEs with high colloidal stability by introducing hydrocarbon oil to the internal phase to form triphasic NEs, as opposed to biphasic, PFC in water systems (37, 38, 52, 61, 181, 228). These PFC-NEs achieved shelf-life beyond 360 d and were stable when mixed with biological media (no change after 14 d exposure).

Utilization of QbD elements has facilitated construction of predictive models for colloidal attributes (138) and guided decisions in formulation and processing of triphasic NE (1). In this study, PFC-NEs were supplemented with medium chain triglycerides, a generally regarded as safe ingredient, to impart stability and a co-solubilizer to offer drug loading functionality in future efforts. Because the hydrocarbon shell component could restrict the oxygen release, both colloidal stability and *in vitro* oxygen transport ability were the primary focal attributes. A systematic product development approach was utilized: a detailed risk assessment (failure modes, effects, and criticality analysis, FMECA) identified key risks in formulation and processing. The risk assessment guided the construction of a DoE which sought to simultaneously evaluate colloidal stability and oxygen transport relationships, yielding meaningful product knowledge that screened for factors that impacted product attributes and identified a design space offering a visualization of the tradeoff existing between the two critical attributes. A representative NE was manufactured at 4× scale to demonstrate scalability.

3.4. Materials and Methods

3.4.1. *Materials*

Pluronic P-105 was purchased from BASF (Florham Park, New Jersey, USA). Pluronic P-123 was purchased from Millipore Sigma (St. Louis, Missouri). Perfluorooctyl bromide and perfluoro-15-crown-5-ether were purchased from Exflour Research Corp (Round Rock, Texas, USA). Miglyol 812 (capric acid/caprylic acid triglycerides, known as medium chain triglycerides, MCT) was obtained from CREMER Oleo (Hamburg, Germany). Transcutol was purchased from Spectrum Chemical Mfg Corp (New Brunswick, New Jersey, USA). Trifluoroacetic acid and deuterium oxide, 99.8% were obtained from Acros Organics (Thermo Fisher Scientific, Waltham, Massachusetts, U.S.). Dulbecco's Modified Eagle's Medium was supplied by Corning (Corning, New York, U.S.), and fetal bovine serum was supplied by ATCC (Manassas, Virginia). All chemicals and reagents were used without modification.

3.4.2. *Failure Mode, Effects, and Criticality Analysis*

Formulation and manufacturing of NEs was examined one unit operation at a time. In each unit operation, all sources of variability of critical quality attributes were identified and treated as a failure mode. All failure modes in all critical quality attributes were evaluated by assigning a Risk Priority Number (RPN), which was calculated as (147, 229):

$$RPN = Severity \times Frequency\ of\ Occurrence \times Detectability \quad (3.1)$$

Severity, frequency of occurrence, and detectability associated with a failure mode were scored on a scale of 1-5, low to high risk. Specifically, 'no appreciable consequence to batch quality', 'has not happened', and 'readily detected' corresponded to a score of 1 for

severity, frequency of occurrence, and detectability, respectively. ‘Total batch loss’, ‘happens regularly’, and ‘not detectable within current unit operation’ corresponded to a score of 5 for severity, frequency of occurrence, and detectability, respectively. Scores of 2 and 4 would indicate the failure mode is between 1 and 3, and between 3 and 5, respectively. Accordingly, the higher the RPN, the more risk associated with the corresponding failure mode.

3.4.3. *Design of Experiments*

Five composition factors and one processing factor were each varied at two levels in a D-optimal screening design (230) of experiments (DoE) consisting of 8 experimental runs created using JMP Pro 14.3.0 (SAS, Cary, NC, USA). In this design, the impact of all 6 main effects on emulsion attributes was statistically evaluated. Composition factors included PFC type, continuous media type, internal phase (IP) volume fraction, hydrocarbon-to-perfluorocarbon ratio by volume (HC:PFC ratio), and proportion transcutol in IP by volume. The lone processing factor was the number of recirculations (passes) through microfluidization interaction chamber. Table 3.2 compiles all experimental runs in the DoE. Emulsion attributes included droplet diameter, polydispersity, zeta potential, resistance to size change (i) under storage at 4 °C, (ii) under exposure to centrifugation, (iii) under filtration, (iv) and under storage at elevated temperature, and oxygen release profile (see Colloidal Characterization in Methods section).

Data Processing and Regression Model Construction. Regression models were constructed using multiple linear regression. Using backwards stepwise variable selection and selecting p value <0.05 as the significance threshold, model terms with $p > 0.05$ were

removed one at a time to form reduced regression models. Coefficient of determination (R^2), RMSE, and leave-one-out cross validation (LOOCV) were used to assess model goodness-of-fit. ANOVA and model fit statistics are given in full detail in Table B.1 and Table B.2.

3.4.4. *Production of Triphasic Nanoemulsions*

All NEs were produced following earlier published protocols (1, 38, 52, 216). Briefly, a micelle solution of blended non-ionic surfactants (2% Pluronic P-105, 3% Pluronic P-123 w/v) was made by following previously reported protocol with minor modifications (173). To prepare NEs, micelle solution was added to the mixture of PFC and HC oils, or single (PFC or HC) oil. Then, coarse pre-emulsions were produced with an analog vortex mixer (VWR, Radnor, PA, USA) on high for 30 s. Coarse emulsions were sonicated on ice for 30 s at 29% amplitude (equivalent of 3480 W s) with Model 450 Digital Sonifier (BRANSON Ultrasonics Corporation, Danbury, CT, USA). Microfluidization was performed on all coarse emulsions by Microfluidizer M110S (Microfluidics Corp., Westwood, MA, USA) at 15,000 psi liquid pressure for the specified number of pulses (5 pulses to 1 pass) over an ice-cold interaction chamber. Emulsions were packaged in glass vials and stored at 4 °C.

3.4.5. *Colloidal Characterization and Quality Control*

Fresh NE samples were diluted 1:40 v/v in DI water and size distribution (described by a z-average droplet diameter and PDI) and zeta potential were measured by DLS on Zetasizer Nano (Malvern Instruments, Worcestershire, UK). DLS operating parameters were as follows: refractive indices of material, 1.59, and dispersant 1.33; viscosity of the dispersant, 0.8872 cP; temperature, 25 °C; duration of measurements,

automatically determined by the number of runs, with each run 10 s; and 173 degrees backscatter angle. Size distribution and zeta potential of refrigerated samples were monitored periodically over time as a measure of shelf stability. Alternative measures of colloidal stability included centrifugation, filtration, serum incubation stability, and thermal stability, in which size was measured before and after each stability test. Percent size change relative to the size before stress was recorded. For the centrifugation test, sample was diluted 1:40 v/v in DI water and centrifuged (Centrifuge 5804 R, VWR, Eppendorf AG, Hamburg, Germany). at 1100 RPM ($218 \times g$) for 5 min at room temperature. For the filtration test, the sample was filtered through 0.22 μm -pore mixed cellulose ester syringe filter. For the serum test, the sample was diluted 1:40 v/v in DI water, DMEM, or 20% fetal bovine serum in DMEM. The sample was stored for 72 hr at 37 °C. For the thermal stability test, sample was aliquoted and stored at 50 °C for two weeks. All colloidal stability tests were begun on samples 1 wk or less after preparation. Figure B.1 – Figure B.5 show graphically the results of all tests. Individual unpaired, two-tail t-tests were done on the quality control tests and are annotated on the bar graphs where applicable. DLS data were summarized by mean \pm standard deviation of 3 measurements unless otherwise specified.

3.4.6. *Oxygen Release Kinetics*

2.5 mL of sample (AOC or control) was dispensed into a 100-mL 3-necked round bottom flask under magnetic stirring. Oxygen gas was bubbled into the sample through glass Pasteur pipette for 30 min. Oxygen gas was then passed over the sample to fill the headspace volume with pure oxygen and the flask was sealed from the surrounding environment with rubber stoppers. Meanwhile, deionized water (25 mL) in a 100-mL 3-

necked round bottom flask under magnetic stirring as the release medium was degassed with nitrogen gas until the submerged dissolved oxygen (DO) probe (HI5421 Dissolved Oxygen Benchtop meter Hanna Instruments, Woonsocket, Rhode Island, USA) gave a stable reading of zero oxygen in the aqueous release medium. Nitrogen gas was passed over the water to remove any residual oxygen in the headspace, and the flask was sealed from the surroundings with rubber stoppers. Oxygenated sample (1 mL) was removed with syringe and needle and injected into flask containing degassed release medium and dissolved oxygen probe. Dissolved oxygen levels were monitored and recorded over time using the HI5421 probe. From the resulting dissolved oxygen – time profiles, a maximum concentration (C_{\max}) was extracted for each sample and used as a measure of oxygen loading and release. Statistical comparisons were conducted by performing unpaired two-tailed t-tests of dissolved oxygen measurements at each time. All experiments were done in triplicate on samples less than 1 wk after preparation.

3.4.7. ^{19}F Nuclear Magnetic Resonance Characterization

Nuclear magnetic resonance (NMR) spectroscopy was used qualitatively in all PFC-NEs and to measure the concentration of ^{19}F nuclei in representative NEs. ^{19}F NMR chemical shifts were reported as ppm using a 0.4% (v/v) trifluoroacetic acid (TFA) solution as internal reference with chemical shift set at -76.0 ppm. PCE NEs showed a singlet peak at -92.4 ppm and PFOB NEs showed a triplet peak at -83.7 ppm chosen for quantitation. The resulting spectral peaks were integrated, and the resulting areas were used to calculate the mean ^{19}F concentration ($n=1$ per NE). Spectra were obtained on a Bruker Avance III at 500 MHz. Samples were prepared by adding 200 μL emulsion, 200 μL 0.4 % w/v TFA as an internal standard, and 50 μL deuterium oxide in a NMR sample

tube (7" length, 4.1 mm inner diameter) (Wilmad-LabGlass, Vineland, NJ, USA). PFC loading was calculated as purity of analyte (P_{ana}):

$$P_{ana} = \frac{I_{ana}}{I_{Std}} \times \frac{N_{Std}}{N_{ana}} \times \frac{M_{ana}}{M_{Std}} \times \frac{m_{Std}}{m_{Sample}} \times P_{Std} \quad (3.2)$$

where I_{ana} , N_{ana} , M_{ana} , are the NMR peak integral, number of nuclei, and molecular weight for the analyte (PFC), and I_{Std} , N_{Std} , M_{Std} , and P_{Std} are the NMR peak integral, number of nuclei, molecular weight, and purity of the internal standard (231). NMR spectra are shown in Figure B.6 - Figure B.14.

3.5. Results and Discussion

Here, we present QbD-based development adapted to PFC-NE-based AOCs with two PFC molecules commonly reported from clinical studies: perfluoro-15-crown-5-ether, (PCE) (90, 203) and perfluorooctyl bromide (PFOB) (111, 232). These two molecules have been extensively used in regenerative medicine preclinical studies and have the most well established biodistribution kinetics *in vivo* (216). The present PFC-NEs are formulated with MCT, Miglyol 812, to impart colloidal stability and a solubilizer, transcitol, to impart drug loading capacity for later use.

3.5.1. Definition of Product Quality Attributes and Target Specifications

As an essential preliminary-stage action and part of the QbD guidelines, product quality was defined by identifying CQAs and assigning acceptable specifications for each attribute. This step implemented measurable metrics to assess the degree of success of the oxygen carriers. CQAs were selected to reflect NE colloidal stability and oxygen delivery performance (Table 3.1). The specifications or limits were chosen from a combination of prior knowledge and relevant literature reports (1, 138, 202, 216, 220, 221). For example, it is widely accepted that the larger the size of a nanoparticle, the more readily it is taken

up by monocytes and macrophages. This results in rapid clearance from the body, which is undesirable in oxygen carriers. In summary, development of an oxygen carrier with both stability and oxygen loading has been an ongoing challenge; thus, defining product quality in this stage facilitated the development of a stable product proficient in oxygen transport. Definition of CQAs and target specifications makes up only part of the much broader quality target product profile within the QbD methodology, which is not within the scope of this report.

Table 3.1. Critical quality attributes (CQAs) for the reported perfluorocarbon nanoemulsions, specifications, and justifications. PDI, polydispersity index; d, diameter; mV, millivolt; nm, nanometer.

CQA	Specification	Justification
Size (droplet diameter, nm)	$100 < d < 200$	Standard quality attribute in the field; necessary to understand the surface area available for release
PDI	< 0.2	Standard quality attribute in the field – indicative of stability
Zeta potential (mV)	-25 ± 20	Standard quality attribute in the field – indicative of electrostatic repulsion
Δ Size after filtration	$< 10\%$ change from size measured before test	Sterilization required for parenterals
PDI after filtration	< 0.2	Sterilization required for parenterals
Δ Size after centrifugation	$< 10\%$ change from size measured before test	Cell culture demands centrifuging step
PDI after centrifugation	< 0.2	Cell culture demands centrifuging step
Δ Size after thermal storage at 50°C	$\leq 20\%$ diameter change from day of production	Measure of accelerated stability
PDI after thermal storage at 50°C	< 0.2	Measure of accelerated stability
Δ Size after 30 d storage at 4°C	$\leq 20\%$ diameter change from day of production	Indication of shelf-stability
PDI after 30 d storage at 4°C	< 0.2	Indication of shelf-stability
O_2 loading & release	Dissolved oxygen maximum concentration in <i>in vitro</i> release, $C_{\text{max}} \geq 1.5 \text{ mg/L}$	Therapeutic evaluation

3.5.2. Production, Characterization, and Quality Control of PFC-NEs

Freshly prepared PFC-NEs were uniform, opaque liquids which ranged from 95-145 nm in diameter with polydispersity index < 0.2 and negative zeta potential. All formulations were periodically monitored for changes in size and size distribution for 30

d to measure colloidal stability during refrigeration. Additionally, samples were exposed to 50 °C for 2 wk to simulate accelerated stability conditions, and size was recorded after exposure. The size change was converted to percent of initial size for analysis. This so-called thermal storage stability was of interest to verify stability was maintained during prolonged temperature rise. Ostwald ripening destabilization is governed by solubility, molar volume, and diffusion coefficient of the dispersed phase material (233, 234). All of these factors exhibit a temperature dependency that could accelerate mass transfer and droplet size growth. Following a detailed study reported in the literature of the colloidal behavior during autoclaving of triglyceride NEs stabilized by Poloxamers along with other reports of the prevalence of Ostwald ripening in PFC-NEs (235), it was expected that Ostwald ripening is the predominant mode of destabilization (236). In the present study, three NEs exhibited size change beyond the specification for thermal storage. Samples were also sterile filtered through 0.22- μm -pore syringe filter and separate samples were centrifuged; in both cases samples retained droplet size and polydispersity. These two steps simulated sterilization and cell culture treatments, respectively. Table 3.2 provides all composition variables and processing conditions, and Table 3.3 tabulates CQA evaluations for all NEs. Figure B.1, Figure B.2, Figure B.3, Figure B.4, and Figure B.5 from Appendix B give a graphical summary of the NE characterization.

Table 3.2. List of formulations and the design matrix in 2-level, 6-factor d-optimal screening design of experiments. The micelle solution was comprised of 2% w/v Pluronic P-105 and 3% w/v Pluronic P-123. X1, Internal phase fraction by vol [-1=0.08, +1=0.1428]; X2, hydrocarbon-to-perfluorocarbon (HC:PFC) ratio by volume [-1=0.857, +1=1.857]; X3, Number of passes [-1=4, +1=6]; X4, Proportion transcutol in internal phase (IP) by vol [-1=0.05, +1=0.3]; X5, PFC type [a=perfluoro-15-crown-5-ether (PCE), b=perfluorooctyl bromide (PFOB)]; X6, Continuous media type [a=deionized water, b=normal saline]. BN, biphasic nanoemulsion; TN, triphasic nanoemulsion; MCT, medium chain triglyceride. Note: definitions and discussion of coded factors follows in the end of section Risk Management and Design of Experiments.

Description (PFC concentration, %vol)	PFOB Volume (mL)	PCE	Miglyol (MCT oil)	Transcutol	Micelle	Water	X1	X2	X3	X4	X5	X6
							Coded factor					
TN1 (2.8)	0.7	0	0.7	0.6	11.5	11.5	-1	+1	-1	+1	b	a
TN2 (5.0)	1.2495	0	1.2495	1.071	20.5275	0.9025	+1	+1	-1	+1	b	a
TN3 (7.7)	0	1.9225	0.5765	1.071	20.5275	0.9025	+1	-1	-1	+1	a	b
TN4 (5.0)	0	1.2495	2.142	0.1785	20.5275	0.9025	+1	+1	-1	-1	a	b
TN5 (4.3)	0	1.0770	0.8230	0.1	11.5	11.5	-1	-1	-1	-1	a	a
TN6 (4.3)	1.0770	0	0.8230	0.1	11.5	11.5	-1	-1	-1	-1	b	b
TN7 (2.8)	0	0.7	0.7	0.6	11.5	11.5	-1	+1	+1	+1	a	b
TN8 (7.7)	1.9225	0	1.4690	0.1785	20.5275	0.9025	+1	-1	+1	-1	b	a
BN1 (14.3)	3.57	0	0	0	20.5275	0.9025						
BN2 (14.3)	0	3.57	0	0	20.5275	0.9025						

Table 3.3. Evaluation of critical quality attributes (CQAs). Cells shaded gray meet the CQA specification. NE, nanoemulsion; BN, biphasic nanoemulsion; TN, triphasic nanoemulsion; PDI, polydispersity index; C_{max} , maximum dissolved O_2 concentration.

NE code	CQA									
	Size (nm)	PDI	Zeta (mV)	Dissolved O_2 C_{max} (mg/L)	Thermal stability Δ Size (%)	Thermal stability PDI	Filtration Δ Size (%)	Centrifugation Δ Size (%)	Day 30 Δ Size at 4 °C (%)	Day 30 PDI at 4 °C
BN1	142.5	0.078	-11.0	2.46	151.7	0.163	-2.1	-0.2	125.8	0.062
BN2	135.3	0.072	-13.1	2.18	26.3	0.042	-1.5	-1.5	7.7	0.045
TN1	118.7	0.167	-5.2	1.16	-0.6	0.169	-3.6	-1.2	6.8	0.141
TN2	105.8	0.169	-9.0	1.55	9.4	0.156	-4.0	-1.8	18.7	0.143
TN3	120.9	0.120	-3.1	1.86	24.0	0.154	-5.4	-1.5	10.2	0.128
TN4	121.9	0.105	-1.9	1.46	-3.2	0.106	-2.4	-0.2	5.9	0.088
TN5	127.2	0.135	-20.0	1.32	-2.3	0.168	-2.3	-0.1	5.8	0.128
TN6	109.2	0.193	-3.8	1.31	1.8	0.186	-5.6	-0.3	9.8	0.132
TN7	115.1	0.122	-2.9	1.27	-4.6	0.140	-5.3	-0.4	6.8	0.108
TN8	98.1	0.153	-7.6	1.77	9.5	0.171	2.8	5.1	19.9	0.100

3.5.3. Evaluation of Biphasic PFC-NEs as Design Controls to Triphasic Systems

We evaluated the oxygenation performance of biphasic NEs (BNs), (Figure 3.1B, right configuration). We formulated biphasic PFC-NEs as comparison systems to triphasic NEs (TNs), (Figure 3.1B, left configuration). Oxygen release measurements were conducted using an experimental setup illustrated in Figure 3.1C. As oxygen partitioned from the NE droplets, it passed through the release medium, where dissolved oxygen levels were measured, and finally equilibrated into the headspace of the flask. Figure 3.1D details the compartments and boundaries across which oxygen equilibrated. After loading the PFC-NE with O₂, the majority of the dissolved oxygen resides in the PFC phase. There is no O₂ in the release medium or the headspace of the round bottom flask. A concentration gradient drives the oxygen from the PFC core first into the hydrocarbon shell in the case of TN, then into the release medium, and finally into the headspace of the vessel. The resulting oxygen release data, Figure 3.1E, reflected the initial accumulation and subsequent dissipation of oxygen in the release medium. Full details appear in Materials and Methods. While this experimental setup demonstrated oxygen transport in a closed system well enough to allow us to differentiate between samples having different oxygen affinities, it is important to acknowledge that oxygen would be consumed by a living system and shear forces in the vasculature space would likely affect the convective diffusion.

Oxygen release was quantified and compared by extracting a maximum concentration from each dissolved oxygen release profile (C_{\max}), illustrated in Figure 3.1E for biphasic NEs. This overlay compares a biphasic NE comprised of 14.3 %vol PCE (BN-PCE) to a PFC-free NE (internal phase comprised of MCT at the same volume

fraction) and to deionized water (containing no internal phase). Water as a control was important as it simulated the effect of using UW solution, the current gold standard in organ preservation (237). The BN-PCE exhibited an increased oxygen transport activity compared to PFC-free NE and deionized water controls. The BN-PCE had a C_{\max} of $\sim 4\times$ and $\sim 5\times$ those of PFC-free and water control. The 14.3 %vol biphasic PFOB NE (BN-PFOB) also demonstrated higher oxygen transport activity compared to the controls. These data support the potential of PFC-NEs in oxygen delivery.

Further evaluation of the oxygen transport activity revealed the linear nature of the oxygen affinity for PFC materials. Figure 3.1F shows this relationship among all 8 TNs with respect to theoretical volume fraction of PFC. Expanding the search radius to include both BNs and TNs (TN3-TN8 and BN1, Figure 3.1G) and employing quantified PFC concentration demonstrated the linear relationship was preserved. This suggested that the hydrocarbon shell had little effect on the oxygen release. Taking the oxygen release findings at face value suggested the biphasic PFC-NE was the optimal formulation. However, evaluation of the colloidal stability highlighted the risk associated with the biphasic formulation. Table 3.3 and Figure B.1 present key stability issues observed with biphasic formulations compared to triphasic NEs. Taking stability to be indicated by droplet size change and polydispersity changes over time and in response to accelerated conditions, it was readily noticed that BN-PFOB destabilized rapidly during shelf-storage conditions at 4 °C. BN-PCE maintained size through one month of storage but did not endure the thermal storage test. Because both BNs failed to meet all colloidal stability CQA specifications, an alternative formulation was needed.

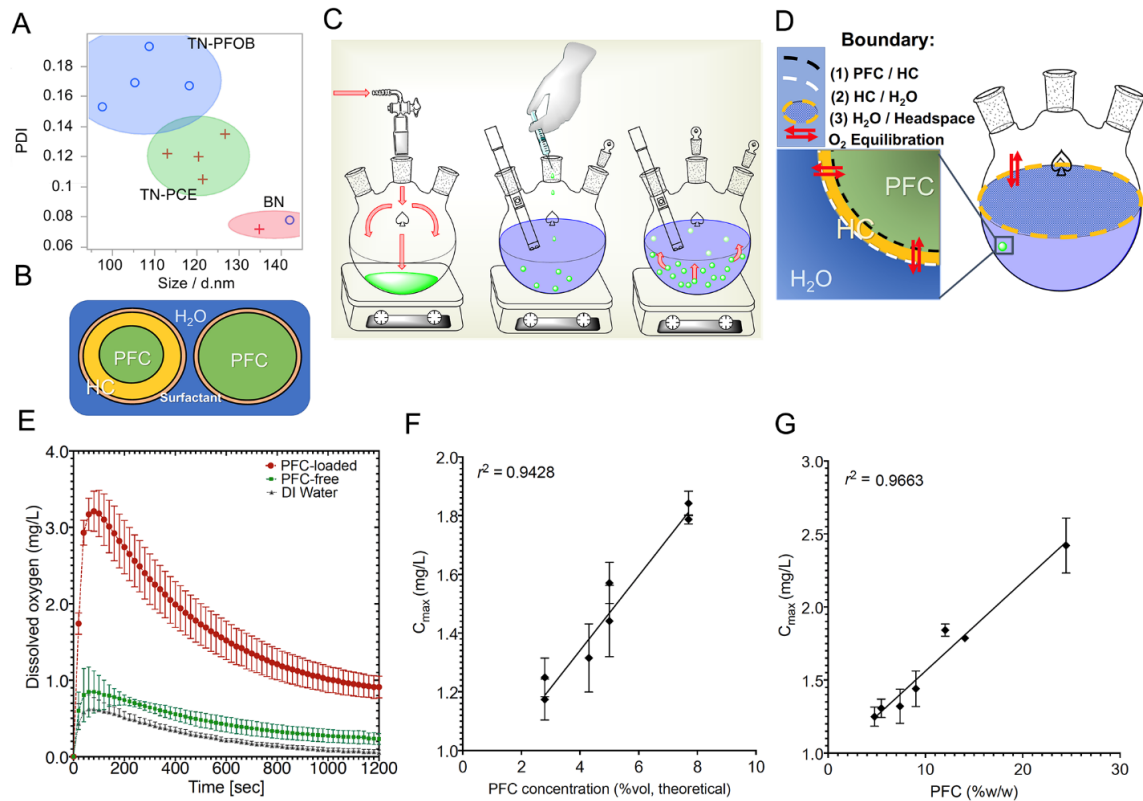


Figure 3.1. Summary of PFC nanoemulsions (PFC-NEs) for oxygen delivery. (A) Scatterplot of nanoemulsion z-average size and polydispersity index (PDI) of biphasic and triphasic nanoemulsions (BNs and TNs, respectively). (B) Illustration of the configurations of triphasic and biphasic nanoemulsions (TN and BN, respectively). (C) Step-by-step *in vitro* oxygen loading and release experiments. (D) Schematic showing simplified sequence of interfaces that oxygen equilibrates across in the *in vitro* oxygen release setup. (E) Representative oxygen release data. (F, G) Dissolved O₂ maximum concentration (C_{max}) relationship to both theoretical PFC concentration, in percent volume, and PFC concentration quantified by ¹⁹F NMR spectroscopy, in percent weight PFC per weight of NMR sample.

3.5.4. Risk Management and Design of Experiments

Previously collected data (138) indicated that formulation modifications increased stability of PFC-NEs. Lambert and Janjic (138) demonstrated that inclusion of MCT shielded PFC-NEs from destabilization in serum- and salt-rich media. Other reports demonstrated similar claims, including supplementing with an insoluble oil decreases the Ostwald ripening rate (119, 238). This information provided guidance in our formulation

development of stable PFC oxygen carriers, and we subsequently modified the composition to include an additional hydrocarbon component. These triphasic PFC-NEs have been considered for a variety of applications (*e.g.*, small molecule anti-inflammatory and imaging reagent carriers). Here triphasic NEs, comprised of a hydrocarbon phase (MCT and transcutool) and either PFOB or PCE, were investigated for their oxygen release performance *in vitro*.

It was anticipated that adding a hydrocarbon oil could compromise the activity of the oxygen-rich PFC phase, so subsequent product development applied concepts of QbD to investigate the i) colloidal stability and ii) oxygen transport activity of this triphasic configuration (PFC-in-HC-in-water). The schematic in Figure 3.2 illustrates the conceptual balance of these two opposing attributes. Data throughout the text reinforce that understanding and controlling this balance is crucial to the development of an AOC. To provide direction and structure within this formulation space in this stage of product development, risk management followed by statistical design of experiments played a central role in evaluating triphasic NEs.

A risk management strategy called failure mode, effects, and criticality analysis (FMECA) examined and ranked potential sources and mechanisms of CQA specification failure. Full details on FMECA risk calculations appear in Materials and Methods. This methodology identified that composition-related factors were the most critical failure modes. Figure 3.3 summarizes the initial risk assessment. Here, the average risk priority number (RPN) for all failure modes is collected for each CQA, highlighting the risk associated with the collective average of entries for each of four broad failure modes categories (composition, oxygenation, processing, or operator error). This highlighted

which of the 4 broad failure modes categories were most likely to present challenges in PFC-NE development. In the unabridged FMECA, each entry is broken down further by the specific failure mode causes. For example, inappropriate HC:PFC ratio (belonging to the broad failure mode inappropriate composition) causes oxygen release to fall out of specification because the hydrocarbon shell limits the oxygen transfer rate at high ratios. To appreciate a more comprehensive look at the failure modes, cause and effect diagrams are shown Figure B.15 for Thermal stability Δ size and C_{\max} in which sources of variability for both responses appear in expanded detail. FMECA results directly informed which factors appeared in the experimental design. Because FMECA assigned the highest risk to composition-related factors, a d-optimal design of experiments selected five composition factors and one processing factor to study. Design factors and levels are provided in Table 3.2.

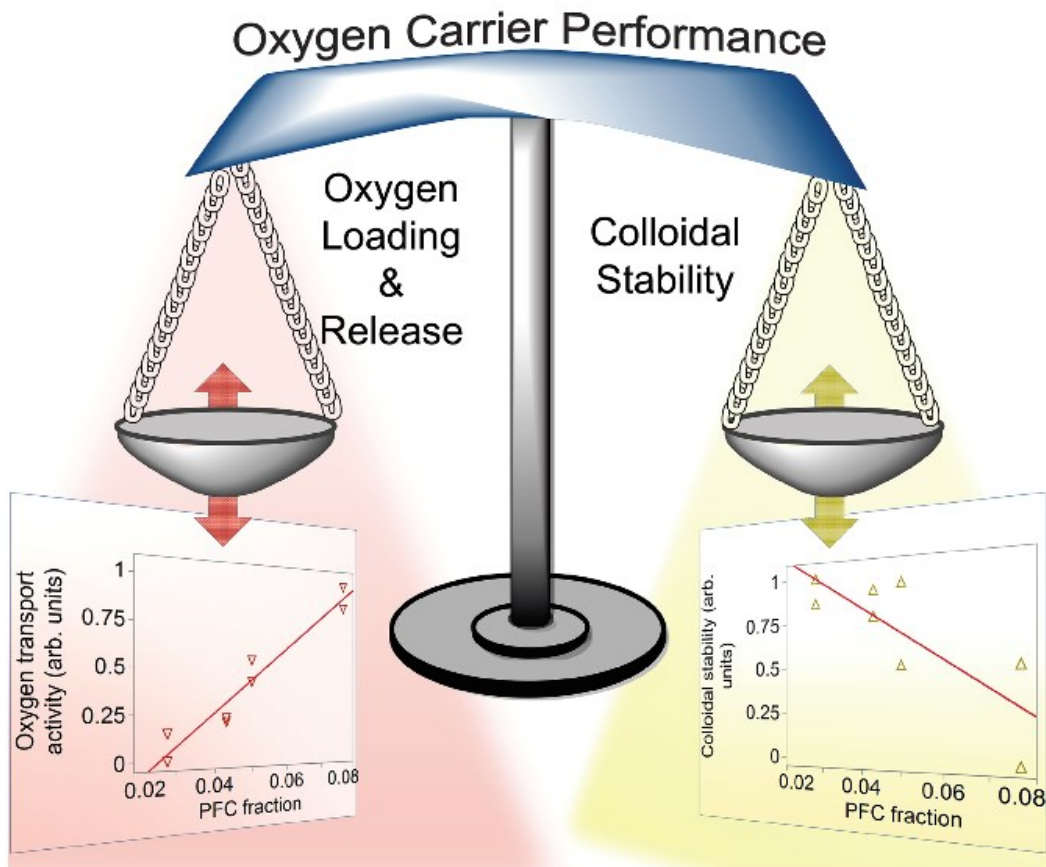


Figure 3.2. Balancing of opposing key attributes of PFC-NE O₂ carriers. Highly concentrated PFC-NEs are sought for their high capacity for oxygen loading. However, biphasic PFC-NEs can be poorly stable. A key objective is to find a balance between these opposing quality attributes. Conceptual scatterplots were formed by normalizing CQAs C_{\max} and Thermal stability Δ size into a number ranging from 0 to 1 by dividing each by the maximum respective CQA measurement.

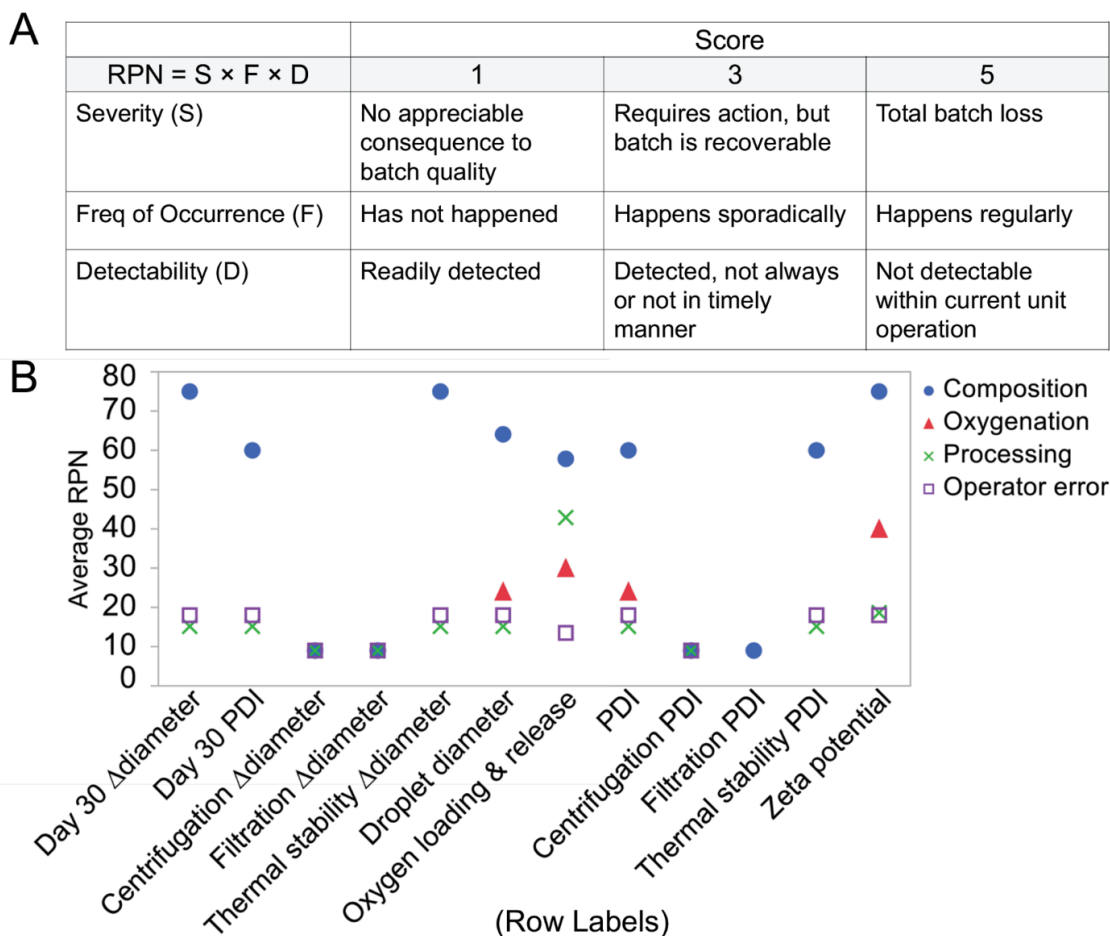


Figure 3.3. Description and summary of failure mode, effects, and criticality analysis (FMECA) results. (A) Definition of Risk Priority Number (RPN) scoring system. (B) Summary of averaged RPN across failure mode categories composition, oxygenation, processing, or operator error.

In this screening experimental design, PFC-NE composition was represented by five factors: PFC type, continuous media type, internal phase (IP) volume fraction, HC:PFC ratio, and proportion transcutol in IP by volume. Three of these: IP volume fraction (X1), HC:PFC ratio (X2), and proportion transcutol (X4) reflected the absolute and relative concentrations of IP components. X1 was the volume of internal phase components divided by the total NE volume. This was a measure of emulsion droplet concentration. In all cases, the surfactant amount was adjusted such that all emulsion formulations had identical surfactant to oil ratios.

X2 was a unitless quantity indicative of relative volumes of PFC (core compartment) and HC (shell compartment) components in the internal phase. The higher the ratio, the lower the PFC amount in the formulation. This also meant the hydrocarbon shell surrounding the PFC phase was thicker, which possibly imparted resistance to oxygen release. X4 was the volume fraction of the internal phase that was comprised of transcutool, a versatile co-solubilizer. Our group previously used transcutool to increase loading of celecoxib by 10 times the dose of a NE delivery platform which had effect treating rat chronic pain model (1, 136). When adjusting X4, it was added at the expense of the MCT oil. These three were chosen as they collectively reflect the concentration of internal phase components and could be varied in DoE to reduce multicollinearity in statistical regression analysis. PFC type (X5) and continuous medium (X6) were categorical formulation factors. PFOB and PCE are nonvolatile PFC oils (boiling points are 142 and 145 °C, respectively). PFOB has been documented extensively for oxygen carrying purposes (239). PCE, on the other hand, has not received attention as oxygen carrier, but rather as ¹⁹F NMR tracer for cell tracking (240). Number of passes (X3) was the single processing parameter chosen to study based on our prior work (1, 138, 216). It was anticipated that NE droplet size would impact the oxygen release profile by affecting the surface area available for oxygen exchange. Adjusting the number of re-circulations on the microfluidizer was a direct way to manipulate droplet size while keeping composition and concentration constant. This 6-factor, 2-level DoE was suited to screen and identify factors active in impacting attributes.

3.5.5. *Evaluation of Triphasic PFC Nanoemulsions*

Table 3.3 shows that triphasic NEs exhibited a small but consistent size reduction

and increase in size distribution compared to biphasic NEs. Further, a discrepancy in size and PDI was seen between PFC types. This is highlighted in a scatterplot of size vs. PDI and cluster analysis which defined three distinct clusters (Figure 3.1A). Zeta potential remained negative, but four TNs exhibited zeta magnitude lower than the CQA specification. Even so, it was evident that TNs exhibited improved colloidal stability compared to the BNs. All triphasic NEs maintained size in both centrifuge and filtration test. Only one TN failed to meet thermal stability Δ size specification and none failed to meet the day 30 Δ size specifications. TN3, the triphasic formulation that failed to meet thermal stability spec, consisted of the lowest amount of MCT. These observations suggested that electrostatic repulsion was not the principal mode of stabilization and that MCT acted as a stability enhancer.

After observing the corresponding shift in colloidal stability with the introduction of MCT oil, oxygen transport activity of TNs was assessed. Presented in Figure 3.4A-I are notable dissolved oxygen concentration-time comparisons. Maximum concentration (C_{\max}) was attained on the order of one min into the release for all samples. The C_{\max} numbers observed in this experiment matched those reported by others (117, 241) in similar experimental setups. Panel A compares TNs consisting of three different levels of PFC concentration for each PFC type along with the BNs. The C_{\max} increased with increasing PFC amount, and all PFC-NEs had higher C_{\max} than water. Figure 3.4B-D each compare PFC type. Figure 3.4B contrasts PFC type for BNs. There was a difference in C_{\max} for PFC type for BNs. Figure 3.4C displays TN samples with different PFC types for 7.7 %vol and Figure 3.4D displays TN samples with different PFC types for 5 %vol. PFC type had no detectable effect on the oxygen release of TNs. This apparent

contradiction may be explained by considering the poor colloidal stability of BNs. Droplet size of BN-PFOB rapidly grew in storage, whereas BN-PCE maintained size for 1 month (see Figure 3.5E-F as well as Figure B.1.). This size increase would decrease the surface area available for release and could account for the apparent difference in C_{\max} between PFC type in the BN comparison. Figure 3.4E-F compare BN and TN samples of like PFC. Figure 3.4G compares TNs comprised of different volume fractions. The oxygen release was significantly greater for the sample with higher volume fraction for nearly six min of the release and remained, on average, higher for the duration of the release. This effect was attributed to the higher amount of material in the NE. This trend is supported by Figure 3.1F-G. Although the TN exhibiting the higher C_{\max} contained 1.8× higher PFC concentration (5.0 vs. 2.8 %vol), the C_{\max} was less than 1.4× higher (1.546 vs. 1.162 mg/L) than the TN consisting of less PFC. This was because the aqueous continuous phase and hydrocarbon compartment of the internal phase were saturated with oxygen and contributed to the release. Figure 3.4H shows the TN-PFOB (5% vol) compared to HC biphasic NE (PFC-free). These two NEs had the same volume fraction, and thus made a clear comparison between PFC and HC material. Figure 3.4I compares TN-PFOB (5% vol) to water. These comparisons showed a higher C_{\max} for the TN-PFOB and confirmed that PFC material was essential for oxygen transport. Overall, the oxygen release was highly affected by PFC content. This was observed in NEs containing higher overall volume fraction (Figure 3.4G), and in NEs comprised of equal volume fractions but differing in concentration of PFC (Figure 3.4H). It is worth noting that exchanging PFC type had negligible effect, suggested by Figure 3.4C-D and the linear nature of the

C_{\max} —PFC loading relationship (Figure 3.1F-G). Further, the presence of salt in the continuous media did not impact the oxygen release profile.

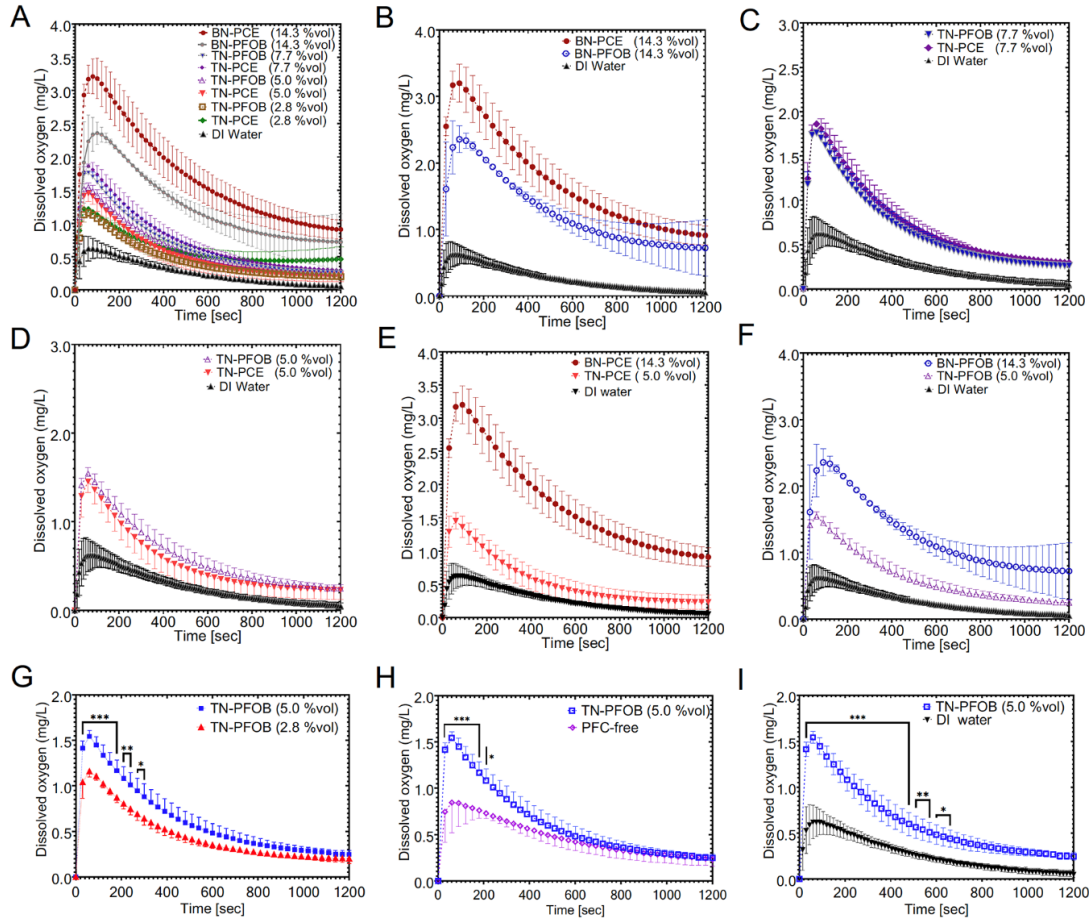


Figure 3.4. Dissolved oxygen vs. time profiles in *in vitro* oxygen release experiments for select samples. (A) Release profiles compiled for formulations ranging from 0 to 14.3 vol% PFC. (B) Comparison of BNs composed of different PFC types, both at the highest level of PFC. (C, D) Comparison of 2 TNs composed of different PFC types at identical PFC levels. (E, F) comparison of BNs and TNs of the same PFC type. (G) Comparison of TN-PFOB of different internal phase volume fractions. (H, I) Comparison of TN-PFOB to biphasic hydrocarbon nanoemulsion and DI water control. Where standard error bars are shown, each point is mean of three measurements \pm SD. Asterisks label time points or intervals where the two overlaid dissolved oxygen values are significantly different from one another. *, **, *** indicate $p < 0.05$, $p < 0.01$, and $p < 0.001$, respectively.

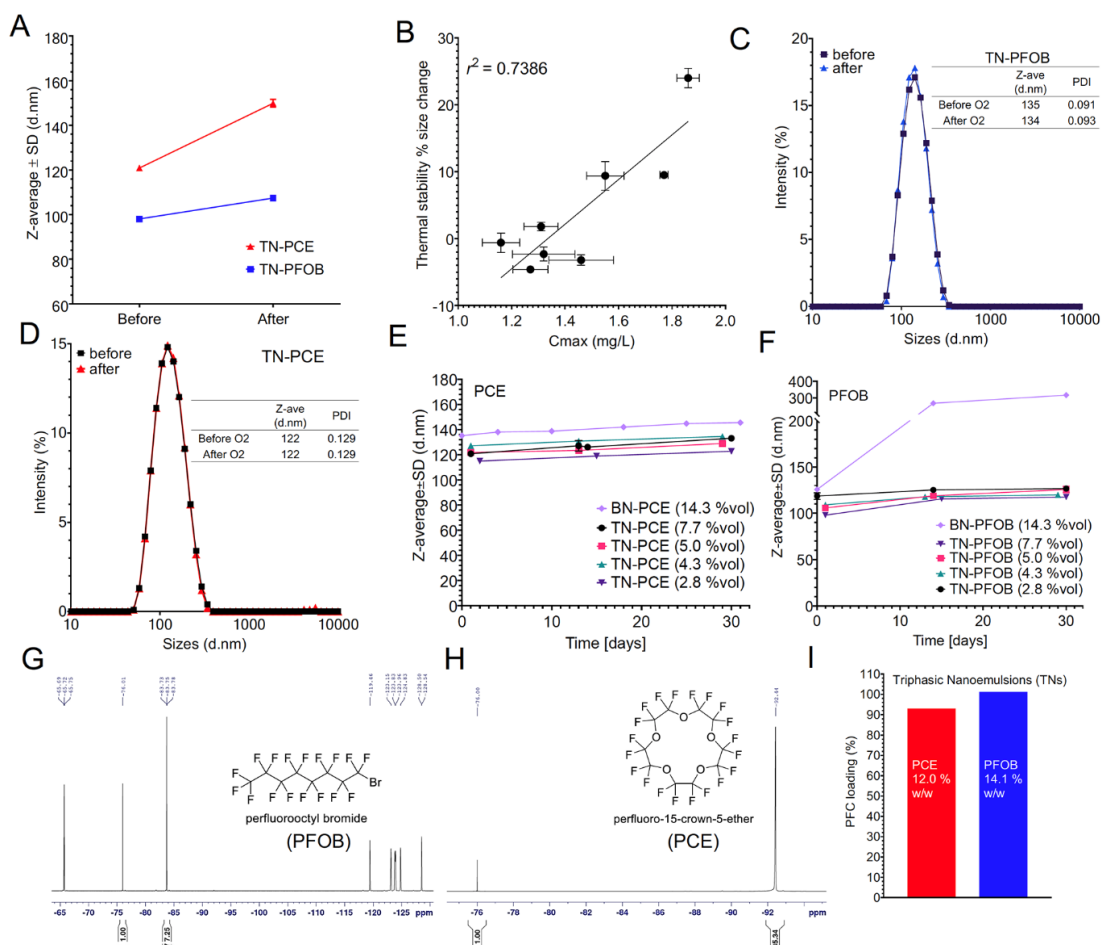


Figure 3.5. Characterization of triphasic PFC nanoemulsions. (A) For TNs, oxygen release is virtually identical among PFC types comparison in (see Figure 3.4). Thermal stability Δ size for 2 representative samples shows a colloidal stability discrepancy exists between PFC types. (B) Least squares fit demonstrating the relationship of C_{max} and Thermal stability Δ size. (C, D) Size distribution overlays reflect colloidal stability of TNs after 30 min of oxygen bubbling. (E, F) Shelf-stability reflected by z-average of samples stored at 4 °C. (G, H) ^{19}F NMR spectra of representative examples, TN3 and TN8. (I) PFC loading calculated from ^{19}F qNMR spectroscopy.

Evaluation of triphasic NEs revealed virtually identical oxygen release profile between PFC type (Figure 3.4C-D) and slight discrepancies in thermal stability Δ size between PFC type (Figure 3.5A) that appeared to be a result of low MCT amount. Additionally, it was observed that C_{max} and thermal stability Δ size were positively correlated (Figure 3.5B). This finding represented the key challenge and was central in supporting other reports of PFC oxygen carriers. Recognizing the stability differences

between PFC types, we further evaluated colloidal stability of triphasic PFC-NEs. While bubbling gas through a NE was a simple way to perform oxygen loading, we wanted to ensure this step would not mechanically disturb the emulsion and lead to destabilization. Figure 3.5C-D are representative size distribution measurements taken before and after the oxygen bubbling step. It was observed that both TNs maintained size distribution. While no significant difference between PFC types in C_{\max} was observed, we wanted to verify the PFC loading was not different. Figure 3.5I shows representative ^{19}F NMR quantification, suggesting PFC loading in triphasics was similar for two PFC types. NMR spectra corresponding to Figure 3.5I are shown in Figure 3.5G-H.

3.5.6. Regression Model Construction and Evaluation

Multiple linear regression (MLR) was utilized to fit models that described C_{\max} and Thermal stability Δsize in terms of the DoE factors. Reduced MLR models for both C_{\max} and Thermal stability Δsize appear in Table 3.4.

The terms X1, X2, X3, and X4 were present in the reduced C_{\max} model. While the oxygen solubility governed how much oxygen can be loaded and released, PFOB and PCE had similar enough oxygen affinities to not see a significant difference between their oxygen transport activities. This was first suggested by data in Figure 3.4C and corroborated by elimination of X5 from the model. Similarly, X6 was removed during regression analysis. While salinity affects gas solubility in water, the main carrier of oxygen in the NE was the PFC phase. Therefore, the reduction in oxygen loading in the aqueous phase when adjusting for tonicity resulted in negligible oxygen-carrying loss. Estimates for X1 and X2, terms which represented the amount of PFC, had positive and negative signs, respectively. Consistent with data shared in previous sections, higher C_{\max}

resulted from pairing higher internal phase fraction (positive X1) with lower HC:PFC ratio (negative X2), ultimately yielding more PFC content. Further, C_{\max} was dependent on X3. More passes resulted in more surface area available for oxygen transfer.

Table 3.4. Reduced regression model terms and goodness-of-fit for C_{\max} and thermal stability Δ size. HC, hydrocarbon; PFC, perfluorocarbon; IP, internal phase; R^2 , Coefficient of Determination; RMSE, root mean square error.

Response	Model Term	Model Term Estimate	Model Term Standard Error	t Ratio	p-value	Model R^2	Model RMSE
C_{\max}	Intercept	1.480	0.0110	134.32	<.0001	0.995	0.027 (mg/L)
	X1 (Internal phase fraction)	0.198	0.0095	20.78	0.0002		
	X2 (HC:PFC ratio)	-0.136	0.0110	-12.30	0.0012		
	X3 (Number of passes)	0.038	0.0110	3.41	0.0422		
	X4 (Proportion transcutole in IP)	0.065	0.0110	5.89	0.0098		
Thermal stability Δ Size	Intercept	4.250	0.7705	5.52	0.0053	0.971	2.179 (%)
	X1 (Internal phase fraction)	5.675	0.7705	7.37	0.0018		
	X2 (HC:PFC ratio)	-7.200	0.8896	-8.09	0.0013		
	X4 (Proportion transcutole in IP)	6.400	0.8896	7.19	0.0020		

For the reduced thermal stability Δ size model, X1, X2, and X4 appeared as model terms. X2 and X4 collectively determined the amount of MCT. As anticipated, high X2, where MCT oil is high, suppressed size growth and high X4, where MCT oil is reduced, promoted size growth. Both models had these three terms in common, but they had opposing effects in each response's model, supporting data in Figure 3.5B.

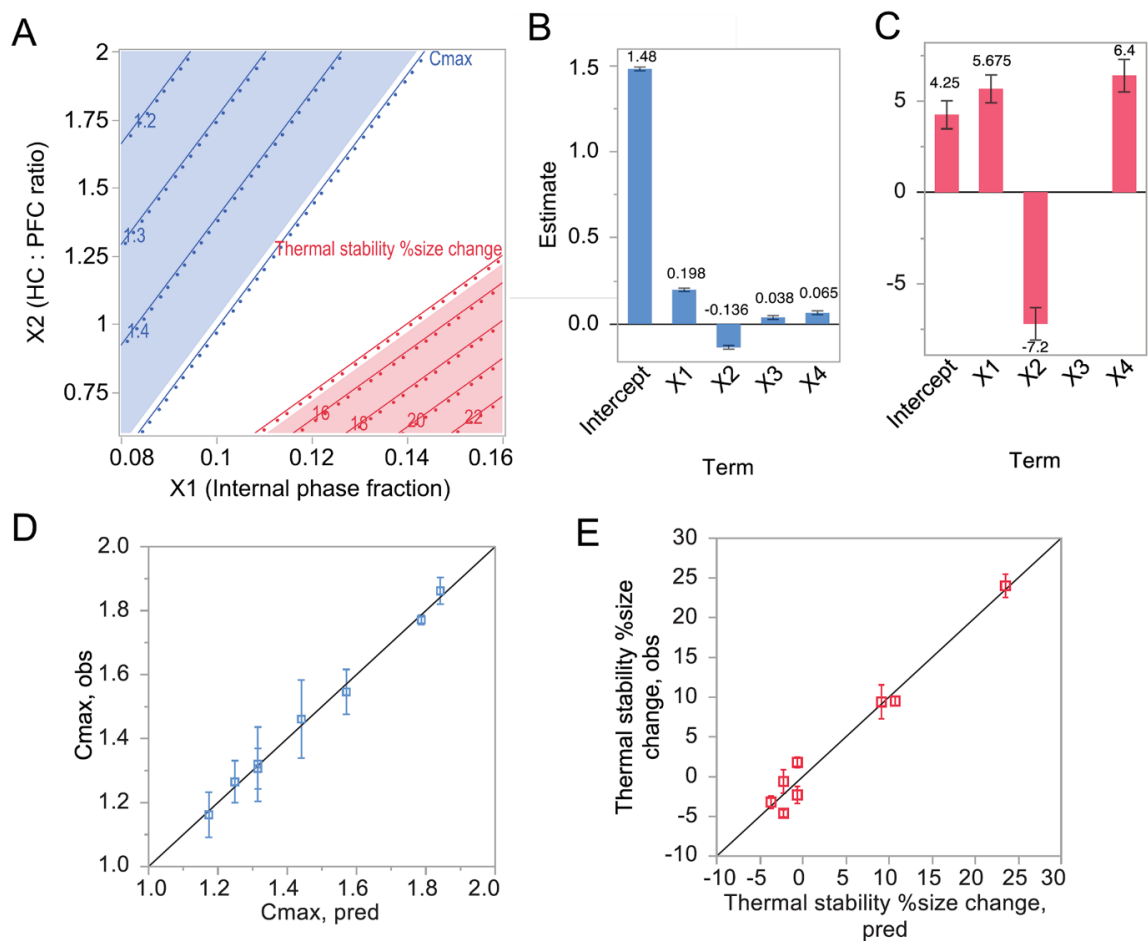


Figure 3.6. Multiple linear regression output to predict size change after thermal storage and C_{max} in oxygen release. (A) Contour plot representing the formulation space in X1 and X2 identified by regression models for both responses. Shaded regions are out-of-specification regions for C_{max} (blue) and Thermal stability Δ size (red). (B-C) Regression term estimates for C_{max} (blue) and Thermal stability Δ size (red). (D-E) Observed by predicted graphs visualize the goodness of fit for both models, where C_{max} is blue squares and Thermal stability Δ size is red squares.

The formulation space described by regression models for C_{max} and Thermal stability Δ size is summarized in Figure 3.6A along with regression term estimates (B-C) and actual by predicted plots (D-E). Panel A shows a plot overlaying contours of both responses in formulation space X1 and X2. The shaded blue and red regions represent where C_{max} and Thermal stability Δ size, respectively, were outside of specifications, highlighting this opposing nature of the two responses.

Model goodness-of-fit was reflected by the appearance of the data observed by predicted plots falling along the diagonal 1:1 line in Panels D and E. In the triphasic formulations, the makeup of the dispersed phase (*i.e.*, volume fraction, proportion transcutool, HC:PFC ratio) was the most critical feature for both responses. C_{\max} and thermal stability were both described by these factors, but with opposing outcomes. This tradeoff highlights the difficulty in formulating a high-quality PFC-NE AOC. It is vital for any commercialized drug product to have high kinetic stability. Therefore, it may be a higher priority to first satisfy the Thermal stability Δ size attribute in the final optimized AOC product. Importantly, the DoE regression analysis provided quantitative relationships describing both responses. This allowed simultaneous monitoring of both CQAs during product development to achieve a PFC-NE formulation that satisfied both CQA specifications while minimizing material and time resources. In addition, analysis highlighted X3 impacted C_{\max} but not Thermal stability Δ size. This key finding indicated processing could be tuned to enhance oxygen transport without affecting colloidal stability.

3.5.7. Scale-up of PFOB Nanoemulsions

To demonstrate scalability, one of the more PFC-rich TNs (TN2) and a BN of like PFC type (BN1) were chosen to be produced at 4 \times scale (100 mL). Figure 3.7B-C shows that the scaled-up emulsions maintained monomodal size distribution. Because producing NEs in larger batches is essential for moving into pre-clinical and clinical phases of development, this finding was encouraging. Figure 3.7A shows the dependence of size on number of passes for 100-mL NEs. The biphasic formulation had a steeper dependence on processing time compared to the triphasic. This indicates the triphasic NE was

produced at a specified size with less processing than the biphasic NE, which was important to acknowledge alongside the finding that more recirculations improves C_{\max} without affecting Thermal stability Δ size.

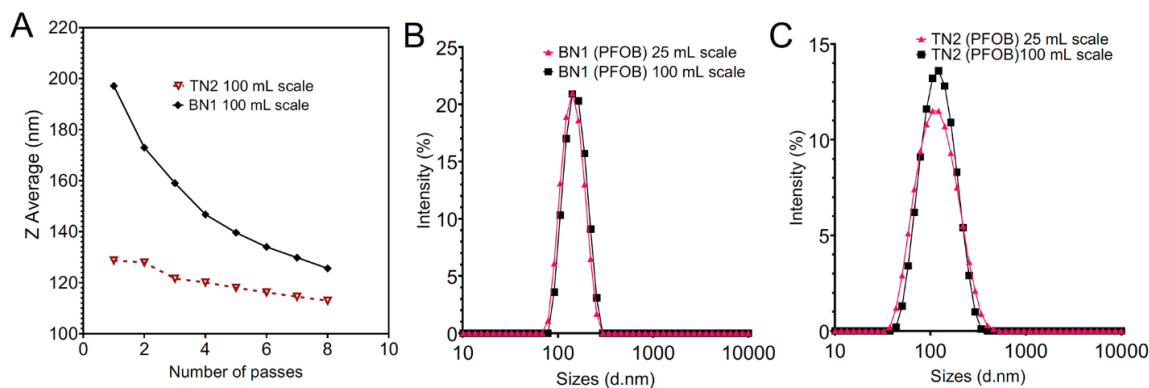


Figure 3.7. Characterization and scale-up of PFC nanoemulsions. (A) Dependence of 100 mL NE size on processing amount ($n=1$ measurement/ data point). (B) Size distribution overlays of biphasic PFOB, BN1, at 25- and 100-mL scale. (C) Size distribution overlays of triphasic PFOB, TN2, at 25- and 100-mL scale.

3.6. Conclusions

We have presented an implementation of systematic pharmaceutical product development methodology, QbD, to formulation of PFC-NEs as AOCs. Through this process, we identified critical quality attributes that reflected colloidal stability and oxygen delivery performance. Furthermore, quality risk management was implemented to enable rational formulation development where both composition and processing parameters were evaluated. The risk assessment guided creation of DoE used to construct regression models which described two competing quality attributes, oxygen release and colloidal stability. We found that the triphasic NE colloidal stability exceeded colloidal stability of biphasic NE, while the biphasic NEs demonstrated highest oxygen loading. Further, increase in PFC loading led to increase in oxygen loading. We posit that, while both oxygen release and thermal stability are critical quality attributes, shelf stability is a

higher priority in the formation of a high-quality, commercially-available AOC. In the next chapter, we describe the optimization of the PFC-NE AOC described here and reexamine the oxygen release model. We showed that presented NEs remained stable under oxygen exposure *in vitro* (Figure 3.5C-D). We also established scalable processing parameters which was deemed successful by producing 100 mL-scale NEs.

This study in its current form presents certain limitations. First, only two commonly used PFCs were used. Second, all oxygen release studies were performed *in vitro* under very controlled conditions. Future studies will expand to assessing presented PFC-NEs in organ preservation testing. Due to small sample size, we were not able to fully quantify the impact of hydrocarbon layer on the oxygen loading. Our data suggested that regardless of hydrocarbon presence, the loading capacity of presented NEs was directly linearly correlated to PFC content levels.

In the next chapter, the importance of the PFC content and the impact of the hydrocarbon phase on oxygen release are examined more closely.

Chapter 4. Multivariate Process Analysis of Perfluorocarbon Nanoemulsion-Based Artificial Oxygen Carriers

NEs are kinetically stable liquid dispersions characterized by droplet diameters $< \sim 500$ nm (242) (120). Typically, surface-active agents are added to the nanodroplets to oppose destabilization. Pharmaceutical hydrocarbon oil-in-water NEs are commonly used to deliver cargo such as small molecule active ingredients or imaging entities such as near infrared fluorescent (NIRF) dyes or magnetic resonance imaging (MRI) tracers to biological systems. This is an advantage when the cargo is lipophilic. Consequently, the encapsulated cargo can have better pharmacokinetics, controlled release, and higher chemical stability which can lead to reduction of dose and dose frequency.

Biomedical-grade perfluorocarbon (PFC) NEs are innovative systems. The PFC oil is a versatile component. In one capacity, it can be considered a diagnostic imaging tracer. Fluorine-19 (^{19}F) MRI has served as a quantitative, minimally invasive technique for *in vivo* bioimaging and has seen extensive clinical use. Organic fluorine levels in living systems are negligible, so ^{19}F MR spectroscopy yields imaging with extraordinarily high signal-to-noise ratio (59). PFC-NEs have been used by researchers aiming to understand biodistribution of certain cells and therapies (49, 243). PFCs can also be utilized in ultrasound contrast imaging (244). PFCs exhibiting low boiling points can be converted to bubbles under ultrasound stimulus. The bubbles offer excellent ultrasound imaging contrast (245). In another capacity, liquid PFC oils are good solvents for dissolution of O_2 . Delivery of O_2 via PFC-NEs in place of whole blood can be vital to tissue salvage in surgical blood loss, battlefield medicine, transplantation, or other acute ischemic conditions. The oxygen-carrying characteristic is a consequence of the low

polarizability of the carbon-fluorine bond, which imparts low cohesive energy densities. For this reason, PFC-NEs have been studied for use as artificial oxygen carriers (AOCs) for several decades (26).

NE preparation can be classified into one of two methods. Use of high-energy methods such as microfluidization involves the addition of mechanical energy to reduce droplet size. Low-energy methods such as phase inversion composition rely on the chemical energy of the dispersed phases to spontaneously form (246). The low-energy methods exhibit key limitations. For example, low surfactant concentrations are typically not feasible with low-energy methods, but can be tolerated with high-energy methods. Careful selection of surfactant system is required, whereas high-energy methods can be utilized on a wider variety of surfactant systems (247). The externally-supplied mechanical energy contributes to two primary mechanisms, occurring simultaneously during high-energy emulsification: (i) droplet break-up and (ii) coalescence (247). Droplet break-up must dominate in order to form a uniform nanoemulsion.

We have previously developed triphasic (PFC/HC/W) PFC-NEs stabilized by a blend of biocompatible nonionic surfactants. These have had functions ranging from multimodal imaging tracers (48) to small molecule cargo delivery vehicles to theranostic entities (37, 52, 179, 182). We use a microfluidization method, owing to the superior size reduction efficiency and scaleup capabilities compared to other high energy methods (61, 248-250). In fact, we have shown that this process is amenable to scale-up operations (61). Microfluidization is a type of high shear processing that forces a coarse dispersion through an interaction chamber consisting of a fixed geometrical array of microchannels under high pressure. The microchannels divide the inlet stream into two paths which are

then forced to collide with one another at a 180-degree angle. The high shear resulting from the turbulent flow and liquid impingement in the interaction chamber acts to break the droplets (251, 252). It is established that factors such as composition, temperature, pressure, and number of passes influence the size of the nanoemulsion. One challenge associated with microfluidization is its susceptibility to a phenomenon called overprocessing (253, 254). During overprocessing, the balance of droplet break-up and coalescence shifts so that coalescence dominates and the droplets grow in size (255). Consequently, it is important to take steps to ensure the reproducibility and robustness of the emulsification method.

Commercial drug products must endure processing modifications during their transfer from lab to industrial scale equipment. During these transfer steps, product quality must be preserved. A concept known as pharmaceutical process validation aims to demonstrate the ability of a process to consistently and reliably deliver high quality products (256). The importance of completing process validation is emphasized by recognizing that it is an expectation by the regulatory authorities (*e.g.*, FDA) that a pharmaceutical process scientifically demonstrate consistent high quality products before commercially distributing the product (257).

Further, commercial drug products must exhibit long-term stability to be accessible. In the reported literature and in our experience, concentrated PFC-NEs have been exceptionally challenging to stabilize. Fluosol, the only formerly FDA-approved PFC-NE AOC, required frozen storage and was only stable for 8 hr after thawing (258). Weers, Liu (259) proved that if a second, heavier PFC oil was added to the primary PFC oil of a NE, droplet growth rate could be suppressed. However, the risk in selecting heavy

PFCs is the associated organ retention half-life cost that must be considered (26).(258). (37, 52, 179, 182) risk-based process development provide a structure to systematically build quality into a product to improve the odds of creating a product of high quality.

We have recently adapted QbD methodology in attempt to consider our triphasic formulations for oxygen delivery for the first time in *ex vivo* machine perfusion as would be used in tissue preservation applications (260). This study, summarized in Chapter 3, involved the development of a customized *in vitro* oxygen release method, which was crucial in offering a way to compare the relative oxygen delivery proficiencies of our PFC-NEs. Using the QbD methodology, we constructed multivariate regression models from a screening design of experiments to describe the tradeoff between colloidal stability and oxygen release performance in PFC-NEs and the relationship between composition and these critical quality attributes.

In the triphasic formulations, both the advantages of the organic (hydrocarbon) and fluororous (perfluorocarbon) type NEs are conserved. The hydrocarbon oil phase allows for loading of lipophilic cargo while the PFC oil phase allows for the diagnostic and oxygen loading functions. Additionally, our data suggested the hydrocarbon oil also leads to substantially more resistance to destabilization (138), resulting in a PFC-NE with high kinetic stability and without the extensive organ retention half-life.

The oxygen transport mechanism characteristic of PFCs is a weaker association compared to the O₂ binding mechanism of hemoglobin. As a result, PFC oil must be present in high concentrations. Our prior formulations did not achieve PFC oil concentrations reported in other commercially developed PFC AOCs. We have now identified a number of improvements of the PFC-NE composition in favor of kinetic

stability and oxygen delivery. The first section of this work describes the composition modifications. We then validated our earlier oxygen loading & release regression model with the adjusted formulation. The validation results prompted us to reexamine and propose simplifications to the model. The simplifications resulted in better prediction statistics.

In consideration of the significance of process validation, here we demonstrated the scalable nature, reproducibility, and robustness of the nanoemulsion formation process. We looked at size distributions of 27 batches of our improved PFC-NE and investigated how changes made to the batch size, payload, dispersant, Microfluidizer processor, and processing pressure affected the size distributions of the PFC-NEs. As a part of this investigation, we came across trends that were difficult to interpret, so we employed principal components analysis (PCA) to look for patterns in the data during and after manufacturing. PCA is a sophisticated exploratory multivariate data analysis technique that can reduce the dimensions of large datasets. PCA has been widely used in the development and process monitoring of solid oral dosage forms (261), but has been used very sparingly on nanoemulsion process and product analysis. Despite this, PCA has the potential to facilitate product analysis and process control of NEs. To appreciate this, we can consider how PCA has been leveraged in the low-energy formation of emulsions. Boonkhao, Li (262) reported the use of PCA to monitor electrical resistance tomography data collected during the formation of a sunflower oil-in-water emulsion using membrane emulsification. PCA-driven process control allowed the researchers to identify poor mixing conditions in real time and initiate fault diagnosis. de Oliveira Honse, Kashefi (263) employed PCA to analyze near-infrared spectroscopy data during emulsion

inversion. They were able to detect the emulsion inversion point from PCA using four different inversion methods. In our present work, PCA helped examine the size distribution data and identify similar groups of samples quickly. Our analysis suggested that the improved formulation we selected was robust to the composition and processing modifications.

4.1. Materials and Methods

4.1.1. Materials

Miglyol 812 was purchased from CREMER Oleo Division (Hamburg, Germany). Perfluorooctyl bromide and perfluoro-15-crown-5-ether were purchased from Exflour Research Corporation (TX, USA). Olive oil was purchased from Spectrum Chemical Mfg. Corp. (NJ, USA). Pluronic P105 was acquired from BASF (NJ, USA). Kolliphor EL was acquired from Sigma Aldrich. Indocyanine green (ICG) was acquired from Sigma Aldrich. Transcutol was acquired from Spectrum Chemical. Resveratrol (RSV) was purchased from TCI America (OR, USA). Methanol was purchased from Fisher Scientific. Stearylamine (SA) (octadecylamine) was purchased from Sigma Aldrich. DiR (1,1'-dioctadecyl-3,3,3',3'-tetramethylindotricarbocyanine iodide) and DiI ((*Z*)-2-[(*E*)-3-(3,3-dimethyl-1-octadecylindol-1-ium-2-yl)prop-2-enylidene]-3,3-dimethyl-1-octadecylindole) were acquired from Molecular Probes (Thermo Fisher Scientific, MA, USA). Dulbecco's Modified Eagle's Medium was acquired from Corning (AZ, USA). Fetal bovine serum was purchased from ATCC (VA, USA).

4.1.2. Indocyanine green stearylamine (ICG-SA) stock preparation

A 20 mM stock of ICG-SA was prepared by adding ICG and SA at a 1:1.8 molar

ratio to a glass vial and vortexing on high to achieve a blend of dry ingredients.

Transcutol: dimethyl sulfoxide (1:1 v/v) was added 1 mL at a time to the vial. Solution was stirred overnight and stored in the screwtop vial at room temperature.

4.1.3. *Nanoemulsion preparation*

Surfactant solution was prepared by mixing surfactants in aqueous dispersant (DI water or PBS) to form a 2% Pluronic P105 3% Kolliphor EL solution. Hydrocarbon and PFC phases were mixed in a beaker with surfactant solution using magnetic stirring at 400 rpm for 30 min. For RSV or NIR dye loading, RSV was dissolved in transcutol 24 hr in advance, and ICG was bound to stearylamine in advance, and added to the beaker of excipients during magnetic stirring. Coarse emulsion pre-processing was done on batches < 100 mL using a Model 450 Digital Sonifier (BRANSON Ultrasonics Corporation, Danbury, CT, USA) at 29% amplitude for 30 s on ice. Pre-processing was done on batches > 100 mL by pulsing with a Cuisinart 300-Watt Hand Blender HB-900PC fitted with a stainless-steel blending blade 5 times for 0.6 L batches or 3 times for 0.125 L batches for 1 s/pulse. The coarse emulsion was then charged into the Microfluidizer (Microfluidics Corp., Westwood, MA, USA) and processed at the specified set pressure on an iced interaction chamber for a specified number of passes. Sampling was done between discrete passes for preliminary characterization. The product was collected and stored at 4 °C.

4.1.4. *Dynamic light scattering*

NEs were diluted in deionized water 1:80 v:v and well mixed in disposable cuvettes. The sample was allowed to equilibrate for one min before measurement on a Malvern Zetasizer ZS fitted with a laser of wavelength 632.8 nm, angle of detection

173° at 25 °C. Three measurements were taken per sample. An intensity-weighted size distribution and an intensity-weighted mean hydrodynamic diameter of the particles, or z-average, were collected from the cumulants analysis of each sample. Size distribution was represented by polydispersity index (PDI, also called dispersity).

4.1.5. *Colloidal attributes and quality control evaluation*

4.1.5.1. *Serum incubation stability test*

This was completed as earlier reported. Briefly, NE sample was diluted 1:80 v:v in water, DMEM, or 20% FBS in DMEM and stored at 37 °C. After 72 hr storage, samples were allowed time to equilibrate to room temperature and measured for size on DLS. The z-average after was compared to control samples.

4.1.5.2. *Centrifugation stability test*

NE sample was diluted 1:80 v:v in water and centrifuged at 1100 or 3000 RPM for 5 min (Eppendorf 5804R, Framingham, MA, USA). Samples were then measured for size on DLS. The z-average after was compared to control samples.

4.1.5.3. *Filtration stability test*

NE sample was filtered through a Millex-GS syringe filter with pore size of 0.45 µm. Samples were then measured for size on DLS. The z-average after was compared to control samples.

4.1.6. *Near infrared fluorescent attributes evaluation*

NE samples were diluted in DI water 1:5 v:v. From this stock, serial dilutions were made up to 1:160 v:v and arranged in triplicate in a clear 96-well plate. Fluorescent

scans were completed on the Li-cor Odyssey at the 800 nm channel at intensity and focus set to 0.5 and 0.0, respectively. Data were analyzed in Image Studio.

4.1.7. *In vitro* oxygen release evaluation

Method was completed as reported earlier (260). Pure oxygen was bubbled into the sample in a 100-mL round bottom flask under magnetic stirring through a glass Pasteur pipette for 30 min. Oxygen gas was then passed over the sample to fill the headspace volume with oxygen and the flask was sealed from the surrounding environment with rubber stoppers. Meanwhile, 25 mL of deionized water in a 100-mL 2-necked round bottom flask under magnetic stirring was degassed with nitrogen until the submerged dissolved oxygen probe (HI5421 Dissolved Oxygen Benchtop meter Hanna Instruments, Woonsocket, Rhode Island, USA) gave a stable reading of zero oxygen in the aqueous release medium. Nitrogen gas was passed over the water to remove any residual oxygen in the headspace, and the flask was sealed from the surroundings with rubber stoppers. A volume of 1 mL of oxygenated sample was removed with syringe and needle and injected into flask containing the dissolved oxygen probe submerged in the degassed release medium. Dissolved oxygen levels were monitored and recorded over time. From the resulting dissolved oxygen – time profiles, a maximum concentration (C_{\max}) was extracted for each sample and used as a measure of oxygen loading and release. Statistical comparisons were conducted by performing unpaired two-tailed t-tests of dissolved oxygen measurements at each time. All experiments were done in triplicate on samples less than 1 wk after preparation.

4.1.8. ^{19}F quantitative nuclear magnetic resonance (qNMR) spectroscopy

4.1.8.1. ^{19}F NMR acquisition

200 μL of NE sample was added to a borosilicate NMR sample tube and mixed with 200 μL of 0.4 vol% TFA in water as an internal reference and 50 μL deuterium oxide. Samples were scanned 16 times on a 400 MHz NMR spectrometer (Bruker, MA, USA) with acquisition time of 1 s and recycle delay time of 5 s. Bruker TopSpin software was used to acquire spectra.

4.1.8.2. NMR spectrum processing and analysis

Spectra were processed in MestReNova v.6.0.2-5475 (Mestrelab Research, CA, USA). Automatic phase correction and baseline correction were applied to the frequency domain spectra. If required, manual adjustments were made to the phase and/or baseline. The TFA resonance peak was manually set to -76 ppm. Integration limits were set by taking the peak width at half maximum multiplied by 75 on both sides of the peak center. The fluorine nuclei were calculated using the relation $\frac{I_{PFC}}{N_{PFC}} = \frac{I_{ref}}{N_{ref}}$, where I indicates the area under the curve of the integrated resonance peak and N indicates the number of ^{19}F nuclei contributing to the integrated peak. The subscripts PFC and ref indicate the PFC-NE sample and the reference (TFA), respectively.

4.1.9. Principal components analysis (PCA)

The data were organized into a matrix \mathbf{X} consisting of p columns and n rows (*i.e.*, an $n \times p$ matrix) where each column was the intensity of a predetermined size bin of the size distribution and each row was a unique sample replicate of DLS measurement sample. The data were mean-centered before processing. PCA decomposes \mathbf{X} into a new

set of matrices such that $\mathbf{X} = \mathbf{TP}^T + \mathbf{E}$ where \mathbf{T} is the $(n \times a)$ matrix of principal component scores, \mathbf{P} is the $(p \times a)$ matrix of principal component loadings, superscript T indicates transpose operation, and \mathbf{E} is the $(n \times p)$ matrix of residuals (264). a is the number of principal components, which is the smallest dimension of \mathbf{X} . JMP Pro 15.2.0 was used to manage the data files and run the PCA analysis.

4.1.10. Hierarchical clustering

Hierarchical clustering analysis of the first 2 principal component scores was completed using the Hierarchical Cluster platform in JMP 15.2.0. Ward's method (265) was used to form the data into clusters.

4.2. Results and discussion

4.2.1. Composition modification and optimization

This section explains the strategy and rationale for adjusting the previous formulation. PFC materials are attractive because of their high affinity for carrying molecular oxygen. Our earlier formulation (260) was a triphasic PFC/HC/W NE with a volume fraction (*i.e.*, IP fraction) as high as 14.28%, stabilized by a binary mixture of nonionic surfactants (2% Pluronic P105 and 3% Pluronic P123, w/v) and produced using high shear microfluidization. The IP makeup was a hydrocarbon oil and a PFC oil, and their volume ratio was described by the term *HC:PFC ratio*. The hydrocarbon oil phase was composed of a medium-chain triglyceride mixture (Miglyol 812), which contributed to the NE kinetic stability and minimized droplet size, and a small amount of a versatile solubilizer, transcitol. The remainder of the internal phase consisted of a PFC oil, the component capable of carrying oxygen. The general manufacturing sequence, which was

not adjusted, is illustrated in Figure 4.1. This formulation was studied in a screening design of experiments where regression models described how the formulation and processing factors impacted the NE attributes (260) (described in Chapter 3). These attributes included droplet size change in accelerated stability conditions and maximum dissolved oxygen concentration observed *in vitro* oxygen release testing (C_{\max}). Table C.1 in Appendix C describes the factors considered in the screening design of experiments (260) and the modified formulation (bottom row, described in this chapter). Factors which were found significant in our reduced regression models for oxygen release are marked. This table also contains the column header ' $C_{\max} / \log f_{\text{PFC}}$ ' where f_{PFC} is the fraction of the NE that is comprised of PFC oil. The significance of this quantity, which was not considered in the prior study, will be discussed here in a later section. The NEs of the prior generation (Chapter 3) (260) will broadly be referred to as generation 1 NEs (G1-NEs). In a similar fashion, NEs which incorporated the modifications detailed in this section will be referred to as generation 2 NEs (G2-NEs). The overall PFC concentration was only as high as 14.9 wt% in G1-NEs, so the present objective was to increase the PFC to beyond 15%, which is in the range of reported PFC concentration of commercially developed PFC oxygen carriers (92). The other attempts in the biomedical industry and academic research to commercialize PFC oxygen carriers incorporated PFC oil ranging from 15 to 90 wt%. Previously, the impact of the volume fraction and the HC:PFC ratio of G1-NEs on *in vitro* oxygen release were determined to be substantial (260). With G2-NE formulations, we adjusted the overall volume fraction and kept the hydrocarbon oil phase volume approximately the same as in G1, which, with the increase in PFC oil phase volume, reduced the HC:PFC ratio by as much as 4.6-fold over that of

the G1-NEs. This adjustment yielded a 30 wt% PFC-NE comparable to others' commercially developed PFC oxygen carriers (92).

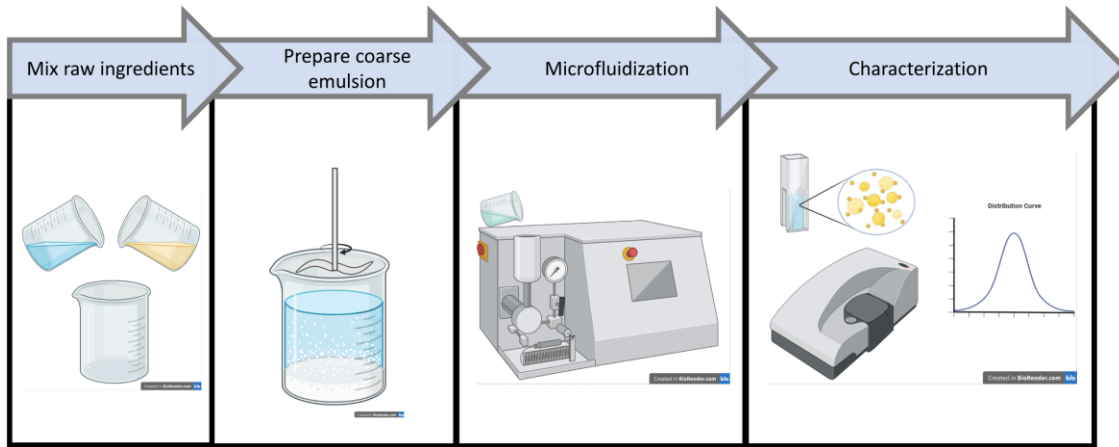


Figure 4.1. Manufacturing sequence of large-scale perfluorocarbon nanoemulsions.

Table 4.1. Compositions, processing, and attributes of all G2-NE batches considered in this study. PFOB, perfluorooctyl bromide; PBS, phosphate-buffered saline; RSV, resveratrol; NA, not applicable; ICG, indocyanine green; NM, not measured

NE	PFOB (mL)	Miglyol (mL)	Transcutol (mL)	Surfactant (mL)	Dispersant	[RSV] (mg/mL)	Dye	Batch size (mL)	Processor	<i>N</i> passes	Set pressure (PSI)	Size (d.nm)	PDI
1	93.26	37.92	0.00	469	1.68× PBS	0.00	NA	600	LM20	8	17800	205	0.208
2	93.26	37.92	0.00	469	1.68× PBS	0.00	ICG	600	LM20	5	18500	79	0.182
3	93.26	37.92	0.00	469	1.68× PBS	0.00	ICG	600	LM20	5	18500	97	0.222
4	77.72	31.60	0.00	391	1× PBS	0.00	NA	500	LM20	8	18400	228	0.188
5	77.72	31.60	0.00	391	1× PBS	0.00	NA	500	LM20	6	17800	208	0.180
6	93.26	37.92	0.00	469	1.68× PBS	0.00	NA	600	LM20	6	17800	195	0.186
7	93.26	37.92	0.00	469	1.68× PBS	0.00	NA	600	LM20	6	17800	190	0.129
8	93.26	37.92	0.00	469	1.68× PBS	0.00	ICG	600	LM20	6	18267 ^a	123	0.247
9	93.26	37.92	0.00	469	1.68× PBS	0.00	ICG	600	LM20	4	19000 ^b	76	0.177
10	93.26	37.92	0.00	469	1.68× PBS	0.00	ICG	600	LM20	8	18089 ^c	83	0.179
11	19.43	7.23	0.67	98	1× PBS	1.23	NA	125	LM20	6	17800	210	0.197
12	19.43	7.23	0.67	98	1× PBS	0.00	NA	125	LM20	6	17800	205	0.197
13	19.43	7.23	0.67	98	1× PBS	0.69	NA	125	LM20	5	16500	93	0.225
14	19.43	7.23	0.67	98	1× PBS	0.00	NA	125	LM20	5	16500	96	0.228
15	19.43	7.23	0.67	98	1× PBS	0.69	NA	125	LM20	5	16500	98	0.223
16	93.26	37.92	0.00	469	1.68× PBS	0.00	ICG	600	LM20	5	18500	81	0.216
17	93.26	37.92	0.00	469	1.68× PBS	0.00	ICG	600	LM20	6	NM ^d	352	0.242
18	93.26	37.92	0.00	469	1.68× PBS	0.00	ICG	600	LM20	10	19333 ^e	134.5	0.23

^a Average set pressure across multiple processing passes is used.

^b Average set pressure across multiple processing passes is used.

^c Average set pressure across multiple processing passes is used.

^d Pressure gauge was malfunctioning.

^e Average set pressure across multiple passes, excluding the processing passes for NE17.

NE	PFOB (mL)	Miglyol (mL)	Transcutol (mL)	Surfactant (mL)	Dispersant	[RSV] (mg/mL)	Dye	Batch size (mL)	Processor	<i>N</i> passes	Set pressure (PSI)	Size (d.nm)	PDI
19	93.26	37.92	0.00	469	1.68× PBS	0.00	ICG	600	M-110P	6	18500	94	0.131
20	93.26	37.92	0.00	469	1.68× PBS	0.00	ICG	600	M-110P	6	18500	80	0.208
21	93.26	37.92	0.00	469	1.68× PBS	0.00	ICG	600	M-110P	5	18500	98	0.123
22	3.89	1.58	0.00	20	DI water	0.00	DiI	25	M-110S	6	18640	99	0.200
23	3.89	1.45	0.13	20	DI water	1.23	DiI and DiR	25	M-110S	6	18640	97	0.239
24	3.89	1.45	0.13	20	DI water	0.00	DiI and DiR	25	M-110S	6	18640	105	0.237
25	3.89	1.45	0.13	20	DI water	0.685	DiI and DiR	25	M-110S	6	18640	105	0.193
26	3.89	1.45	0.13	20	DI water	0.00	NA	25	M-110S	6	18640	104	0.231
27	15.54	6.30	0.00	78.	1.68× PBS	0.00	ICG	100	M-110S	6	18640	127	0.179

All G1 batches exhibited visible phase separation after 2-3 months. It was prudent to address this observation. The hydrophilic-lipophilic balance (HLB) is a classification convention to describe the lipophilic and hydrophilic character of one or more surfactants in solution. The HLB is a scale ranging from 0-20, where 10 indicates equal balance of lipophilic and hydrophilic character, 0 indicates lipophilic character only, and 20 indicates lipophobic character only. In general, $HLB > 7$ is favorable for oil-in-water emulsions while $HLB < 7$ is favorable for water-in-oil emulsions. An analogous quantity is the required HLB of an oil. In HLB theory, a more stable emulsion results from matching the emulsifier HLB to the required HLB of the oil (266). The HLB of our previous surfactant mixture was approximately 10.8. Rao, Aghav (267) experimentally determined the required HLB of propylene glycol monocaprylate (tricaprylin forms one major component of Miglyol 812), reporting it to be 15. Assuming the required HLB of these two structurally similar oils is comparable, we modified the surfactant blend to increase the HLB. Pluronic P123 ($HLB = 8$) was removed and replaced by Kolliphor EL ($HLB = 13$), which raised the overall HLB by 3 units. After monitoring the HLB-adjusted formulation for >11 months, there have been no signs of phase separation. This is confirmed by visual inspection, droplet size measurements, and ^{19}F NMR characterizations (Figure C.4).

The earlier study considered the impact of type of PFC on the oxygen release profile of G1-NEs. Finding no significant impact, we can now consider the ideal combination of hydrocarbon oil and PFC oil type by comparing colloidal attributes and stability. Miglyol 812, a blend of saturated MCTs, or olive oil, composed of a mixture of saturated and unsaturated long-chain triglycerides, at 6 wt% was paired with PCE, a cyclic molecule, or PFOB, a linear molecule, at 30 wt%. Both of the PFC oils are thoroughly documented materials used primarily in ^{19}F magnetic resonance imaging and oxygen delivery. Figure C.1 illustrates the four PFC/HC

oil comparisons that were made in a 2-month colloidal stability follow-up. Selecting perfluorooctyl bromide paired with Miglyol 812 resulted in NEs exhibiting a z-average of approximately 100 nm, which was sustained over the 2-month follow-up. This combination minimized the droplet size and was chosen as the G2-NE internal phase.

The defining adjustments made to G2-NEs, outlined above, included surfactant HLB, PFC amount, and PFC-HC oil types. Within the G2-NE formulation domain, additional variations were considered: a near infrared fluorescent (NIRF) dye or a lipophilic small molecule model drug were utilized as cargo, and continuous phase adjustment to 1.68 \times -concentrated buffered saline. After attempting dyes such as DiI and DiR, ICG was chosen as the preferred NIRF dye. ICG was added to the hydrocarbon phase as an ion pair with stearylamine, imparting it a higher degree of lipophilicity. ICG has been clinically used as a diagnostic imaging contrast agent (268, 269) and can fulfill the same role here. It can also be used as a marker of batch reproducibility. A model Biopharmaceutical Classification System (BCS) Class II drug, RSV, was encapsulated to demonstrate a traditional drug delivery function. RSV has been documented as having antioxidant properties. As oxidative stress is a secondary threat to tissue viability in ischemic events, RSV makes a natural choice in this attempt. Phosphate buffered saline (PBS) as the continuous phase (CP) was a natural choice after noting that our earlier analysis found no impact imparted by the choice of CP (260). Table 4.1 summarizes all G2-NE batches considered in this work. The colloidal properties for representative G2-NEs are provided in full in the supplemental section.

4.2.2. *In vitro oxygen release characterization and model reexamination*

Our next objective was to use the G2-NE to validate the oxygen release model developed earlier on G1-NE in Chapter 3. The model is a least-squares multiple linear regression fit of the

factors indicated in Table C.1 on the maximum oxygen concentration (C_{\max}) data collected during *in vitro* oxygen release testing (260). This model was used in parallel with an equivalent model that described the formulation's kinetic stability to identify a viable design space for the G1-NEs. G2-NE release profile follows the same pattern, where a maximum dissolved oxygen concentration occurs in the release medium rapidly followed by a more gradual decline. The C_{\max} is nearly 4 mg/L, and the time at which C_{\max} occurs, t_{\max} , is 30 s, roughly half of that for the G1-NEs. Figure 4.2A-B presents the actual-by-predicted values for the previous C_{\max} model fit to G1-NE data and the projection of G2-NE data into the model, respectively. The multivariate model strongly underpredicted the oxygen-carrying capacity of the G2-NE. This initial attempt to validate the model highlighted its limitations and prompted a reexamination. The initial multivariate model was fit using a total of four predictors, of which, two exhibited collinearity: *IP fraction* and *HC:PFC ratio*. By algebraic manipulation, it can be demonstrated that the *IP fraction* is related to *HC:PFC ratio* by the factor *PFC fraction* (f_{PFC}):

$$f_{\text{PFC}} = \frac{\text{IP fraction}}{1 + \text{HC:PFC}} \quad (4-1)$$

where f_{PFC} is the volume fraction of PFC in the NE. Further, the idea that G2-NE formulation adjustments could not all be captured by the multivariate model was posited. For example, the model was not trained to handle the adjustment to surfactant HLB. In addition, the model parameters extrapolated beyond the upper and lower limits of *IP fraction* and *HC:PFC* when predicting the response for G2-NE data. It was proposed that the high deviation in prediction of G2-NE data was possibly the result of overfitting, which would explain the poor prediction. We directed our attention to removing the collinearity and simplifying the model. Figure 4.2C presents the oxygen release profiles in an alternative fashion. The dissolved oxygen concentrations were normalized by f_{PFC} for the given NE and the release profiles were color-

coded according to the f_{PFC} , providing an insightful perspective. When the axes were rescaled to magnify only the release profiles of G1-NEs, it was readily observed that the normalized oxygen release profiles clustered together based on the f_{PFC} while showing little additional variation, despite the formulations having several sources of variability. A univariate model was then refit to G1-NE C_{max} data using f_{PFC} , summarized in Figure 4.2D. Log-transforming the X and/or Y data showed no obvious best fit. Consequently, the G2-NE data were used to select and validate the refined models (Figure 4.2E). Figure 4.2F illustrates the improved model prediction using only f_{PFC} to predict the log10-transformed C_{max} . The simplification of the multivariate to a univariate model is important because it suggests that the hydrocarbon oil phase, which does not carry molecular oxygen, does not interfere with the oxygen release kinetics or extent. Therefore, PFC amount is the only influential factor of oxygen release in the PFC-NEs reported here. It also presents the idea that the relationship between PFC amount and C_{max} follows an exponential growth model.

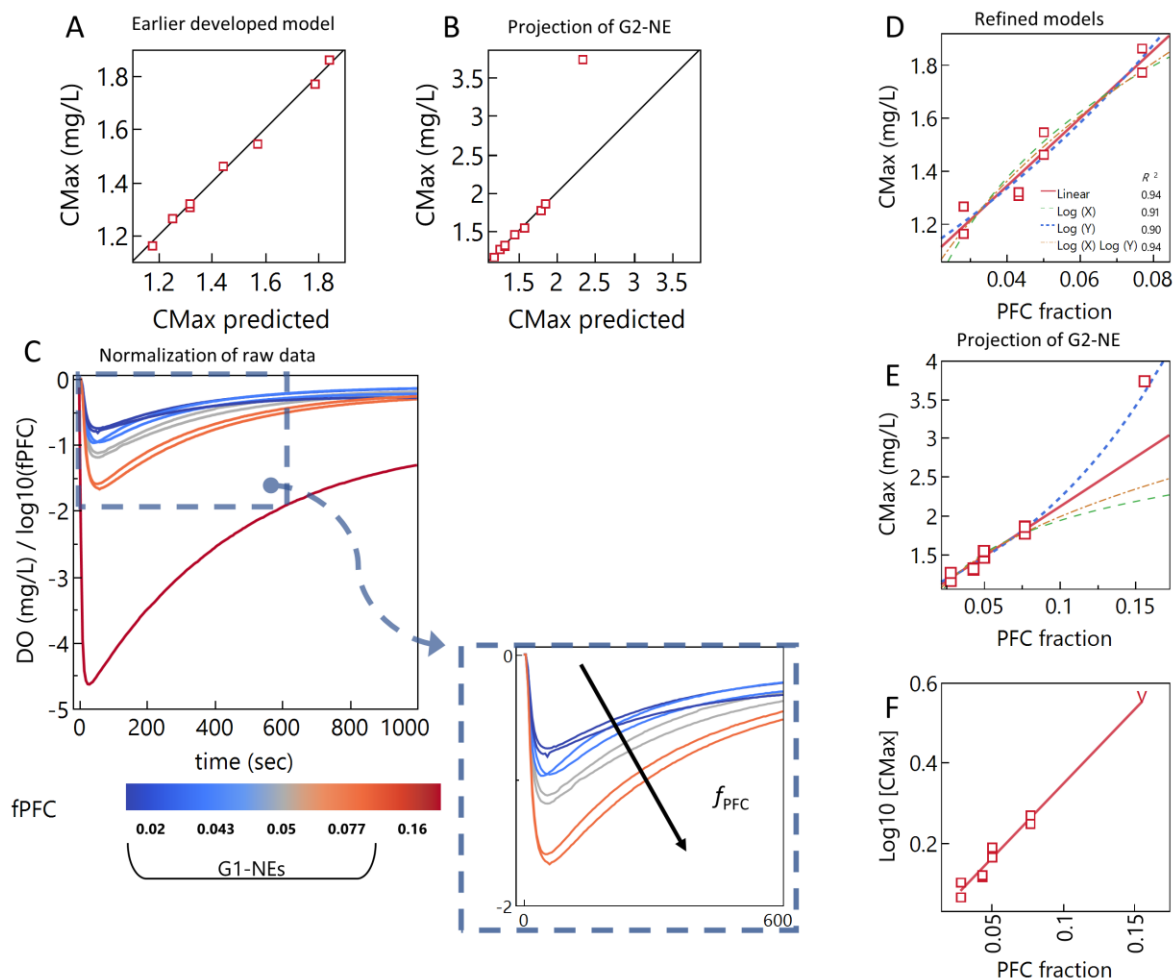


Figure 4.2. Validation, reexamination, and refinement of the multivariate model for *in vitro* oxygen release C_{\max} constructed in the earlier screening design. (A) Previous multivariate model fit with G1-NE data. (B) Projection of G2-NE data into the model ($C_{\max} = 3.6$ mg/L). (C) Representation of raw data normalized by f_{PFC} . The arrow on the inset rescaled data indicates the direction in which f_{PFC} increases. (D) Refitting C_{\max} model as a univariate model. (E) Projection of G2-NE data into the refined univariate model. (F) Linearized form of the C_{\max} univariate model.

4.2.3. Comparison of production scale and high shear processing equipment

The emulsion processing method for G1-NEs was developed on a small bench Microfluidizer processor, M-110S, which was convenient for production of 25 mL batches. This material volume is ideal for preformulation and composition optimization, but cannot sustain testing in animals, translation, and commercialization. Accordingly, we attempted to increase the

batch size of the G2-NEs. Presented in Figure 4.3 are comparisons made with representative samples. 4 \times -scale G2-NE (100 mL) processed on the M-110S exhibited z-average of 127 nm after six passes through the processor. This significantly differed from the droplet size (100 nm) of 1 \times -scale 25-mL batches under identical processing conditions. This comparison is illustrated in Figure 4.3A by observing the 4 \times size distribution shift to larger sizes. Following this attempt, the emulsion process was transferred from the M-110S to a larger benchtop Microfluidizer (LM20). This is designed to comfortably produce batches >0.3 L. When the LM20 was used to process a 5 \times -scale G2-NE, the resulting size after five passes was in good agreement with the 1 \times batch at six passes (Figure 4.3B). The observation that the 4 \times batch on the M-110S was not consistent with the small batch (1 \times) could be related to the associated drop in heat exchanging efficiency when increasing the batch size. The associated temperature increase would change the material properties and processing conditions. The LM20 showed higher droplet size reduction efficiency and was again utilized to process a 24 \times -scale G2-NE. The resulting droplet size was \sim 92 nm after five passes. The size distributions of the 1 \times , 5 \times , and 24 \times G2-NE are shown in Figure 4.3C. The size of discrete pass samples was measured during processing, shown in Figure 4.3D for 4 \times and 24 \times batches. As an additional measure of quality comparison, ^{19}F NMR spectra were collected on these batches of G2-NEs. The spectra are presented in Figure 4.3E, while the quantification of PFOB incorporation from the integrated spectra is presented in Figure 4.3F. The % incorporation between batches ranged from 80 to 95%, reinforcing the suitability of the LM20 for handling larger batch sizes.

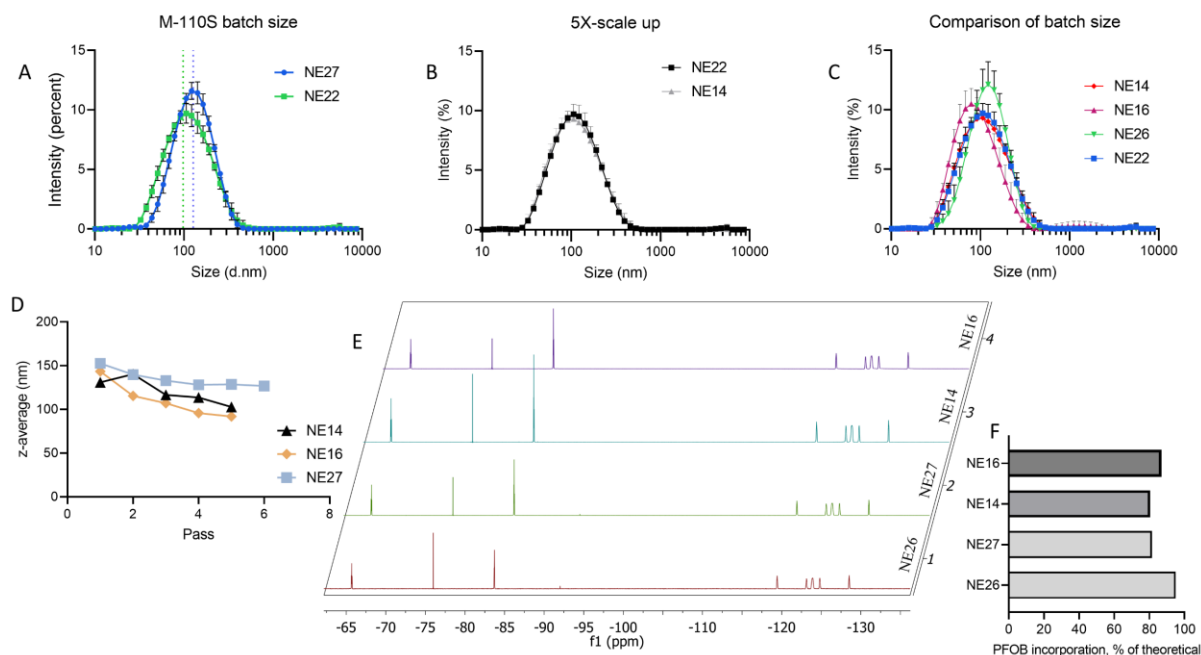


Figure 4.3. Batch size comparisons made on G2-NEs. (A) Size distribution representations of batch size increase from 25 to 100 mL (1× to 4×) on the M-110S processor. (B) Batch size increase from 1× on M-110S to 5× on the LM20. (C) Size distributions of representative 1×, 5×, and 24× scale batches. (D) Z-average by pass number across batch sizes. (E) Representative ¹⁹F NMR spectra of samples across batch sizes. (F) Representative PFOB incorporation calculations across batch sizes.

Manufacturing technology transfer is inevitable during the life cycle of any product at the commercial scale. This process would involve the transfer of the manufacturing process to a new manufacturing unit and reproducing the process. Quality control measures are taken to verify that process transfer. After establishing the LM20's ability to scale the G2-NE, we introduced a second large benchtop Microfluidizer (M-110P) to transfer the 24×-scale G2-NEs process. Size distributions, fluorescence profiles, and ¹⁹F NMR spectra of selected representative samples as well as aggregated data, presented in Figure 4.4, serve to assess this processing equipment exchange. Samples made on the LM20 had a wider spread of z-average measured on day 0 than samples made on the M-110P (Figure 4.4A-B). Some LM20 batches closely matched the initial 1× (NE22), 5× (NE14), and 24× (NE16) G2-NEs, which were described in Figure 4.3. From the

selected representative batches in Figure 4.4, NE02 resembled NE16, but NE01 was considerably different in size. Figure C.3 provides an alternative representation of size distributions where this comparison can be illustrated. In this layout, the batches have been grouped according to batch size and equipment. Note that the LM20 24 \times -scale batches are split between 2 panels. Each panel is comprised of batches that have a high degree of inter-batch reproducibility.

The mean z-average of M-110P batches was 96 nm, roughly 50 nm smaller than LM20 batches. The z-averages of each discrete pass followed the same pattern, shown in Figure 4.4D. We again noticed that the in-process z-averages of NE01 were consistently higher than those of NE16 (Figure 4.4C). We initially attributed this to the slightly higher operating pressure used during processing NE02 and NE16 compared to NE01. However, other LM20 batches (notably, NEs 11, 12, 13, and 14) were found to follow a reversal of the trend in which lowering operating pressure resulted in smaller droplet size.

Figure 4.4E presents the close agreement of the fluorescent properties between the LM20 and M-110P batches. Finally, the ^{19}F NMR quantification of PFOB incorporation showed no differences between the two high shear processors (Figure 4.4F-G). The agreement between fluorescence and NMR suggests that the two processors produce uniform, homogeneous NEs, while the droplet size variability indicates that the M-110P can more consistently produce reproducible size distributions. We suspect the auxiliary processing module (APM), which is fitted to the M-110P only, could be responsible for this observation. This APM is marketed by the vendor (MicrofluidicsTM) as a strategy to stabilize the fluid flow and increase the effectiveness of the interaction chamber.

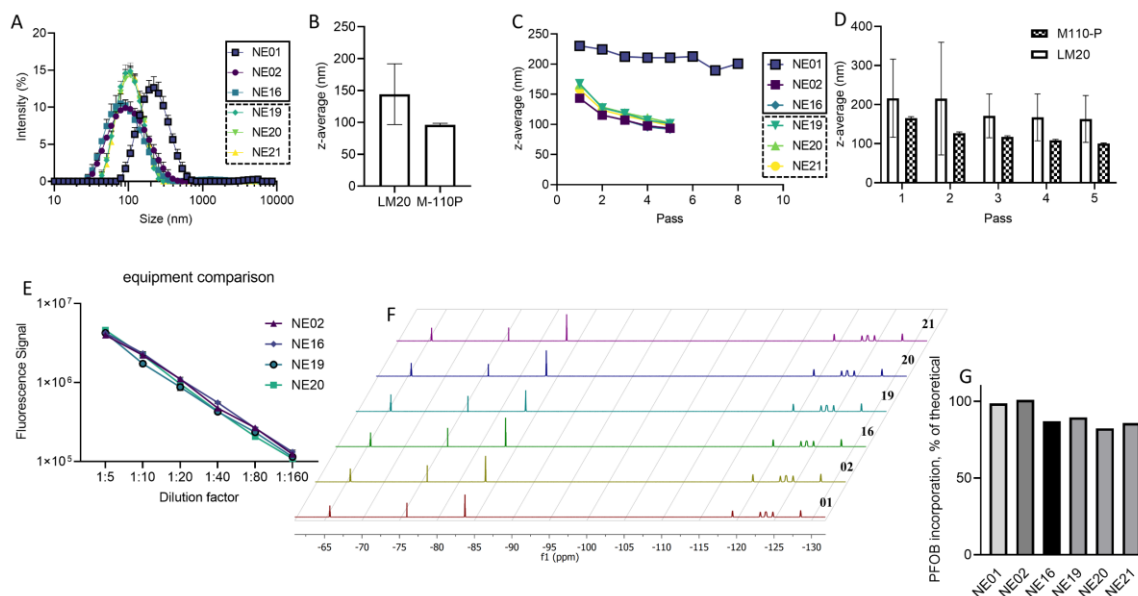


Figure 4.4. Comparisons of different high shear Microfluidizer processors at 24 \times scale. (A) Representative size distributions of G2-NEs across processors. LM20 samples are enclosed by solid rectangle, and M-110P samples are enclosed by a dashed rectangle. (B) Aggregate means and standard deviations of z-average grouped by processor. (C) Z-average at each discrete pass of representative samples across processors. LM20 samples are enclosed by a solid rectangle, and M-110P samples by a dashed rectangle. (D) Aggregate means and standard deviations of z-average at each pass grouped by processor. (E) Fluorescent properties of representative samples across processors. (F) Representative ¹⁹F NMR spectra of samples across processors. (G) Representative PFOB incorporation calculations across processors.

Reproducibility is a key concern in pharmaceutical manufacturing processes. The International Council for Harmonisation (ICH) Q10 Pharmaceutical Quality System guidance document states the pharmaceutical quality system should assure that the desired product quality is routinely met. Droplet size and size distribution, which are defining characteristics and one of the critical quality attributes of NEs, of repeated batches made by different operators on different days were compared to understand the process reproducibility. Table 4.2 compares size of repeated batches produced at 4 different scales and across three different Microfluidizer processors. 1 \times -scale 25-mL batches produced on the M-110S exhibited a coefficient of variation of 3.8%. Batches made with the LM20 had a coefficient of variation of higher than 40%

regardless of the batch size, while batches made on the M-110P had a coefficient of variation of 10.2%.

Table 4.2. Reproducibility statistics of G2-NEs across batch size and processor. z-averages are the mean of 3 measurements.

Batch size	Processor	NE	Z-average (d.nm)	Mean z-average	Reproducibility Standard deviation of z-average	Coefficient of variation (%) of z-average	
25 mL	M-110S	22	99	102	3.9	3.8	
		23	97				
		24	105				
		25	105				
		26	104				
125 mL	LM20	11	210	140	61.2	43.7	
		12	205				
		13	93				
		14	96				
		15	98				
600 mL	LM20	16	81	125	55.4	44.2	
		1	205				
		2	79				
		3	97				
		6	195				
		7	190				
		8	123				
		9	76				
		10	83				
		M-110P					19
	20			80			
21	98						

4.2.4. *Failed batch rescue*

During processing, NE17 failed to reach the droplet size or distribution specifications outlined in the Chapter 3 CQA specifications. Despite passing through the LM20 processor 6 times, the size remained >300 nm and PDI remained >0.24 (Figure 4.5A-C). NE16, which was a successfully processed batch, was used here as a visual reference. This prompted the operators to inspect the LM20 where it was observed that the operating pressure valve was not reading the set pressure. The batch was recovered and reprocessed the next day as NE18 on the LM20 after troubleshooting the problem. NE18 was passed 4 additional times through the LM20. Evaluation of NE18 found the z-average nearly return to within the allowable specifications while PDI returned to the expected level. The fluorescent properties and the PFOB incorporation were similar to NE16 (Figure 4.5D-E). These comparisons indicate that if this product is mistakenly under-processed, action can be taken to salvage the batch.

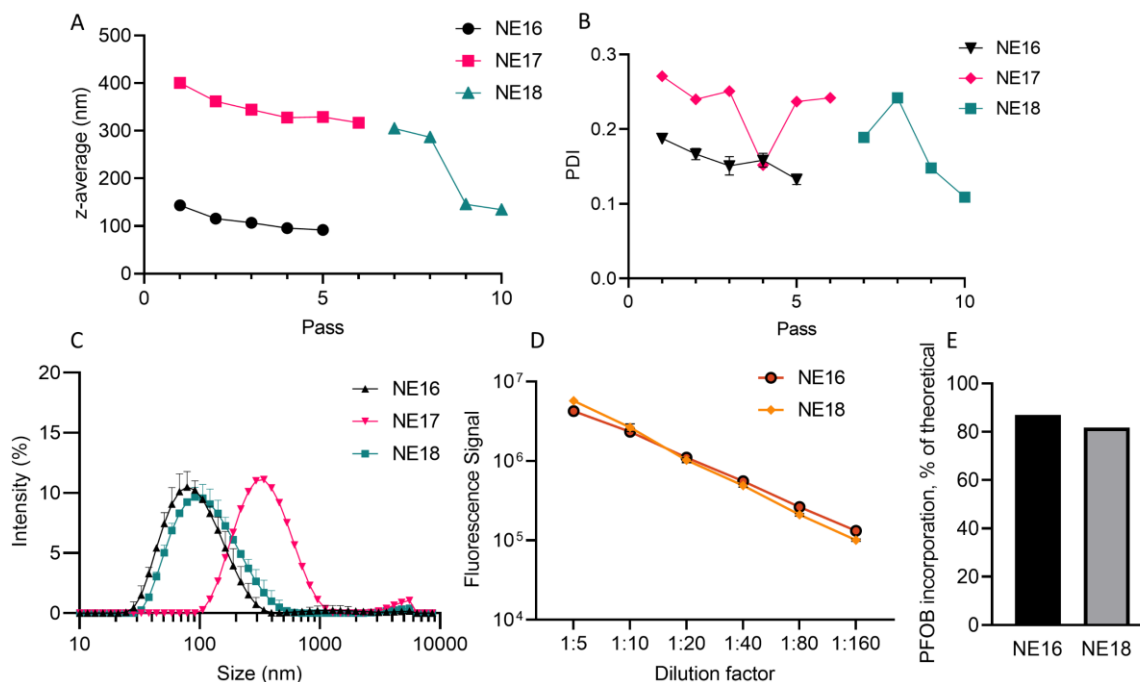


Figure 4.5. Attributes of NE17 and NE18. (A) z-average during processing compared to NE16 for reference. (B) PDI during processing compared to NE16 for reference. (C) Size distributions of freshly processed NEs compared to NE16 for reference. (D) Fluorescent comparison of NE18. (E) PFOB incorporation comparison of NE18.

4.2.5. Principal components analysis

By inspecting the size distributions of repeated G2-NE batches, differences between high shear processors emerged. Interestingly, there appeared to be two centers of the LM20 size distributions rather than a continuous spread of the data. This observation was the motivation to employ more sophisticated methods to examine variability in the data. Intensity-weighted size distributions of G2-NEs during and immediately after processing were analyzed using principal components analysis after mean-centering. PCA has previously been used to study size distributions in fields of study such as environmental science to describe atmospheric aerosol spatial and temporal trends (270) and drug product formulation to classify and describe size fractions of the excipient

lactose in a dry powder inhaler product (271). In the present work, PCA was implemented to understand to what extent the known variability within G2-NEs (*e.g.*, batch size) accounted for the droplet size distribution variance. For this analysis, the size distribution bins ($n=69$ variables per sample) were the analyzed factors. The component scores, which are representations of the size distribution of each sample in the PCA coordinate space, were used to discover patterns and form comparisons. The initial analysis with all data resulted in the formation of two distinct populations in the first and second scores scatterplot. The distinct populations were designated Cluster 1 and Cluster 2, illustrated in Figure 4.6A. Next, color scales representing various factors were applied to the scores plots. The z-average droplet size described the scores 1 and 2 of these subgroups. This can be observed in Figure 4.6B where the size increases left to right in a ‘v’-shaped fashion. Next, a color scale representing the number of passes through the high shear processor (*n pass*) was applied. Both clusters were observed to have different relationships to *n pass*. *n pass* increased along the same direction as z-average decreased for Cluster 1, while no discernable trend existed for Cluster 2 (Figure 4.6C). Figure 4.6D shows the averaged size distribution for the Cluster 1 and 2 data. The mean size distribution of Cluster 1 is close to 100 nm, while that of Cluster 2 is close to 200 nm.

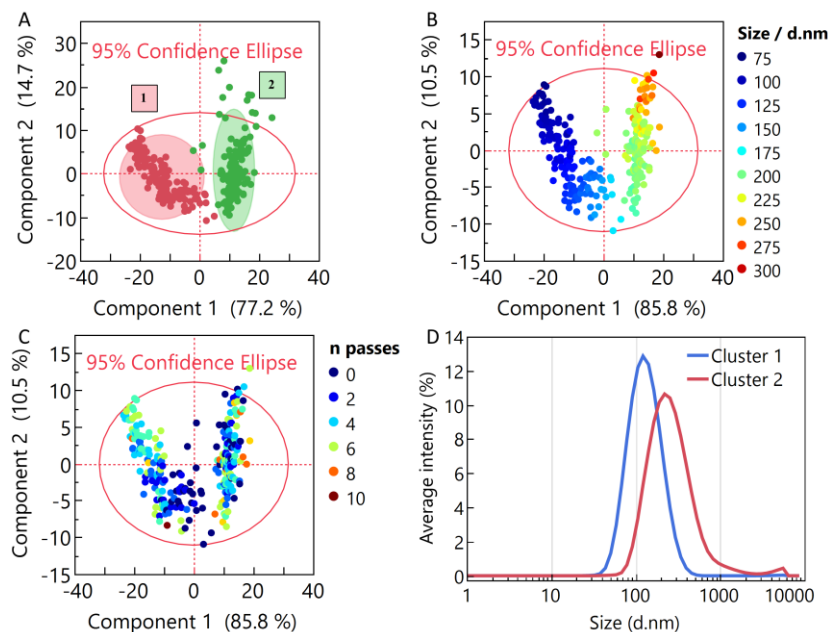


Figure 4.6. Principal components analysis (PCA) of the aggregated G2-NE size distribution dataset. (A) Score 1 and 2 coordinate plot with Cluster 1 and 2 ellipses and labels. (B) Color scale representing z-average applied to the Score 1 and 2 plot. (C) Color scale representing number of passes applied to the Score 1 and 2 plot. (D) Averaged size distributions of Cluster 1 and 2 data.

The data were then partitioned and Cluster 1 and 2 were analyzed as two independent groups. When examined individually, Cluster 1 scores preserved the diameter and *n pass* trends as seen from the scores 1 and 2 color scales in Figure 4.7A-B. Likewise, analysis of Cluster 2 did not change the initial observations of the diameter relationship to scores 1 and 2 (Figure 4.7C). *n pass* does not elicit any trends in the scores plot, as the full *n pass* range is equally distributed across the score space (Figure 4.7D). Importantly, examination of high shear processor, batch scale, processing set pressure, dye labeling, drug encapsulation, or date of manufacture did not reveal any discernible trends for Cluster 1. Similarly, examination of Cluster 2 found no direct influence from any of the same investigated factors. This indicates that the G2-NE process is robust to these sources of variability.

We then examined the size after the first pass, which could hold information about the quality of the coarse emulsion before processing. This color scale was applied to the aggregated scores data (Figure 4.7E). There was a divide between the two clusters. Compared to Cluster 1, Cluster 2 had a larger droplet size at pass 1. We hypothesize that the premixing steps, which are not closely characterized, are primarily responsible for the observed distinct clusters in PCA score space. If this hypothesis is accurate, it would be reasonable to expect to have difficulty determining trends in this sub-population during processing. Coarse emulsion quality has been cited by others to be an important factor in droplet size reduction in high-energy nanoemulsification (272, 273).

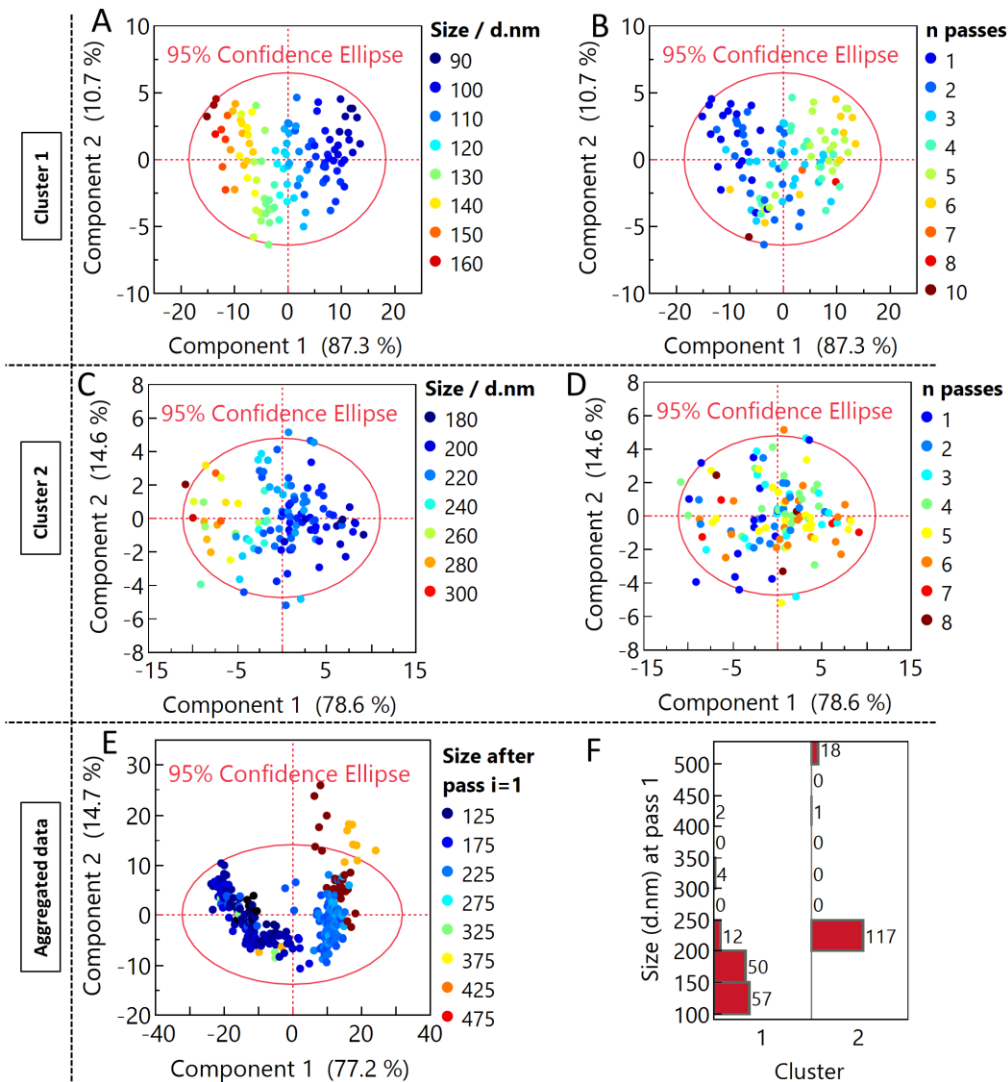


Figure 4.7. PCA performed independently on partitioned clusters. (A) Color scale representing z-average applied to Scores 1 and 2 plot of Cluster 1 data. (B) Color scale representing number of passes applied to Scores 1 and 2 plot of Cluster 1 data. (C) Color scale representing z-average applied to Scores 1 and 2 plot of Cluster 2 data. (D) Color scale representing number of passes applied to Scores 1 and 2 plot of Cluster 1 data. (E) Color scale representing z-average after the first processing pass applied to Scores 1 and 2 plot of aggregated data. (F) Frequency histogram of NE z-average after the first pass grouped by cluster.

Figure 4.8 provides a pass-by-pass perspective of the averaged size distributions within each cluster which can be utilized to draw comparisons with the PCA. It was immediately evident that the Cluster 2 distributions at pass 1 were more positively skewed than Cluster 1 distributions. This could indicate the quality of coarse emulsion

prior to processing was poorer with Cluster 2 batches. A similar observation was made in the data with PCA. With each additional pass, the tail of the Cluster 2 distribution diminished, while the location of the peak maximum did not appear to change. Note that even though the peak maximum location remains constant, the mean of the distribution changes as the tail disappears. The tail of the Cluster 1 distribution diminished through the first 4 passes and the location of the peak maximum shifted from a larger to a smaller size. The peak maximum of Cluster 1 approached 100 nm during processing, while that of Cluster 2 remained static at 200 nm throughout processing. The depiction in Figure 4.8 is consistent with the PCA findings. PCA suggested that *n pass* accounted for the droplet size reduction in Cluster 1 but not Cluster 2.

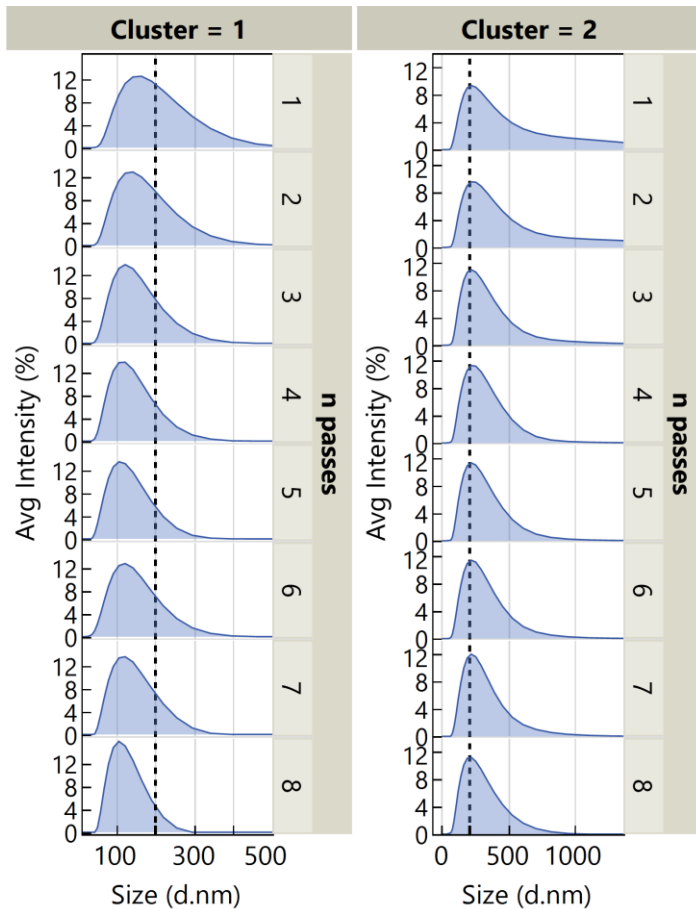


Figure 4.8. Average size distributions during processing of G2-NEs partitioned by cluster. A dashed line at size = 200 nm is drawn for reference.

4.3. Conclusions

In this chapter, we optimized the formulation of a PFC-based artificial oxygen carrier. We compared the oxygen release kinetics of the optimized G2-NE to our previous generation of PFC-NEs. The G2-NEs were formulated with more PFC content, and the oxygen release attributes were consequently improved. This comparison prompted us to reexamine the earlier constructed models that described the oxygen release. Notably, we proposed simplifications to our model which produced a similar fit with superior ability to predict oxygen delivery of new samples. We then attempted to increase the PFC-NE production throughput by increasing batch size. We investigated different Microfluidizer

processors in addition to several formulation modifications to understand if there were similar degrees of reproducibility and robustness. To evaluate this, we looked at droplet size, fluorescent properties, and ^{19}F NMR spectra across different batches. To confirm our observations here and to identify other data trends, we implemented principal components analysis. Among the known sources of processing and composition variability, we noted that the number of passes was highly influential in explaining the variance in a subset of the size distribution data, but none of the factors produced discernible trends in the remainder of the data. Overall, the formulation modifications described here result in a versatile artificial oxygen carrier. We next look to understand the pharmacological characteristics of the G2-NEs in *in vitro* experiments.

4.4. Acknowledgements

Anneliese Troidle, Caitlin Crelli, and Jelena M. Janjic, PhD contributed to Figure 4.4 as co-manufacturers of batches of material Anneliese and Caitlin also assisted in running fluorescence quality control measurements. Anneliese, Rebecca McCallin, and Dr. Janjic contributed to Figure 4.5 as co-manufacturers. Anneliese also assisted in running fluorescence quality control measurements. Dr. Janjic prepared the ICG-SA dye. Jacob Guess assisted in the implementation of principal components analysis (Figure 4.6 and Figure 4.7).

Chapter 5. Multifunctional Perfluorocarbon Nanoemulsions Eliminate Hypoxia and Reactive Oxygen Species in Murine Macrophages *in vitro*

Molecular oxygen (O₂) is an essential component for cellular respiration. When the blood supply is interrupted, dire consequences follow. Supply and delivery of oxygen in ischemic conditions is an ongoing pursuit in biomedical research. AOCs are useful when whole blood is not available or is not an option. In transplant medicine, preservation of donor tissue exemplifies a situation in which oxygen delivery interventions are of interest, but currently not the standard procedure. Practitioners in transplantation are looking to advance preservation outcomes by using machine perfusion, where a liquid perfusate continuously flushes the tissue to remove waste byproducts and deliver fresh nutrients, in place of SCS preservation, the current standard (274). AOCs could have a natural implementation in MP.

Transplantation has an inevitable period of ischemia starting when the donor's heart stops. This ischemic time can be minimized, but not eliminated. Therefore, the condition known as IRI cannot be avoided. IRI is characterized by the activation of the innate and adaptive immune response upon restoration of blood flow (reperfusion) and the subsequent influx of leukocytes and macrophages to the graft. This response leads to an increased production of ROS (10). ROS are radical species that are generated primarily by phagocytes (including macrophages) and intended to combat infection (275). In the context of transplantation, ROS are associated with cytotoxicity and can lead to oxidative stress resulting in impaired graft function or rejection (276). ROS have a multitude of pathological pathways. Among them is the generation of peroxynitrite. NO and superoxide radicals are known to react, producing peroxynitrite (277, 278). In turn,

peroxynitrite oxidizes lipid membrane and promotes nitration in proteins (278). Data strongly suggests that inhibition of the formation of peroxynitrite eliminates lipid membrane oxidation (279). In clinical practice, preservation solutions are at times spiked with antioxidants. However, many small-molecule antioxidants are lipophilic, making the aqueous perfusate environment non-ideal.

Recently, we adapted QbD methodologies to the development of PFC-NE AOCs formulation and process (260). After developing a customized *in vitro* oxygen release method, we constructed multivariate regression models to describe the tradeoff between colloidal stability and oxygen release performance. Chapter 3 describes these results. We have since made significant efforts to optimize the PFC-NE AOC composition to further improve the stability and oxygen release attributes (described in Chapter 4). We designated this optimized formulation the second-generation PFC-NE (G2-NE) and continue this naming convention in the results reported here. By leveraging principal components analysis, we demonstrated that our nanoemulsification process is scalable, reproducible, and robust to process and formulation modifications.

We present here the preliminary pharmacological evaluation of the G2-NE AOC in *in vitro* ischemia-reperfusion-related models. Here, we took advantage of the organic phase of the triphasic NE to load a model antioxidant into the PFC-NE AOC. We selected RSV, which has been reported to have action in ischemia-reperfusion injury and in general against oxidative stress in macrophages (280, 281), endothelial cells (282, 283) and *in vivo* (284-286). We describe the chemical stability of the observed encapsulated form and employ a dialysis bag method to characterize the drug release profile. We describe the stability of the PFC-NE in a model machine perfusion circuit. We then

establish the effects of the oxygen- and antioxidant-loaded formulations in the reversal of hypoxia and reduction of reactive oxygen species in murine macrophages.

5.1. Materials and Methods

5.1.1. Materials

Miglyol 812 was purchased from CREMER Oleo Division (Hamburg, Germany). Perfluorooctyl bromide was purchased from Exflur Research Corporation (TX, USA). Pluronic P105 was acquired from BASF (NJ, USA). Kolliphor EL was acquired from Sigma Aldrich. Transcutol was acquired from Spectrum Chemical. Resveratrol was purchased from TCI America (OR, USA). Methanol was purchased from Fisher Scientific. Dulbecco's Modified Eagles Medium was acquired from Corning (AZ, USA). Fetal bovine serum was purchased from ATCC (VA, USA).

5.1.2. Nanoemulsion preparation

HC and PFC phases were mixed in a beaker with aqueous surfactants using magnetic stirring at 400 rpm for 30 min. For RSV loading, RSV was dissolved in transcutol 24 hr in advance and added to the beaker of excipients during magnetic stirring. Pre-processing was done by pulsing with a Cuisinart 300-Watt Hand Blender HB-900PC fitted with a stainless-steel blending blade 5 times for 0.6 L batches or 3 times for 0.125 L batches for 1 s/pulse. The coarse emulsion was then charged into the Microfluidizer LM20 processor (Microfluidics Corp., Westwood, MA, USA) and processed at 18500 psi on an iced interaction chamber for a specified number of passes. Sampling was done on discrete passes for preliminary characterization. The product was collected and stored at 4 °C.

5.1.3. *Dynamic light scattering*

NEs were tested as described in Section 4.1.4.

5.1.4. *Colloidal attributes and quality control evaluation*

5.1.4.1. *Serum incubation stability test*

This was completed as earlier reported. See Section 4.1.5.1.

5.1.4.2. *Centrifugation stability test*

This was adapted from an earlier reported method (1). See Section 4.1.5.2.

5.1.4.3. *Filtration stability test*

This was adapted from an earlier reported method (44). See Section 4.1.5.3.

5.1.4.4. *Machine perfusion circuit stability*

NE was run through the machine perfusion oxygenator equipment at 8.0 mL/min for 45 min. NE was sampled at various time points and size was measured via DLS immediately or was subject to further testing including centrifugation stability test and a modified version of the serum incubation stability test which omitted the FBS incubation group.

5.1.5. *¹⁹F quantitative nuclear magnetic resonance (qNMR) spectroscopy*

5.1.5.1. *¹⁹F NMR acquisition*

See Section 4.1.8.1.

5.1.5.2. *NMR spectrum processing and analysis*

See Section 4.1.8.2.

5.1.6. Resveratrol (RSV) drug quantification

NE samples were diluted in methanol and agitated on a vortex mixer on high to break the emulsion. Samples were then further diluted such that the analyte was in the linear range of detection on UV-vis. High-performance liquid chromatography (HPLC) DIONEX Ultimate 3000, fitted with a C18 Hypersil Gold 150x4.6 mm (Thermo Scientific) chromatography column was used to quantify RSV. An isocratic method at 30 °C was used, where the mobile phase consisted of methanol:water 0.75:0.25 v/v, and the flow rate was 0.5 mL/min. Detection was used with UV-vis at a wavelength of 305 nm. RSV reference standards ranging from 0.1 to 20 µg/mL were prepared, and the area under the curve (AUC) associated with each reference standard was calculated to construct a standard curve.

5.1.7. In vitro resveratrol drug release

An earlier protocol was adapted (287). Slide-A-Lyzer™ Dialysis Cassettes (Thermo Fisher) consisting of a molecular weight cut off of 20K Da and volume of 0.5-3 mL were used as directed. After soaking the cassette in dialysate (1% w/v Tween 80 in phosphate-buffered saline), 3 mL of sample was added to the cassette and air was removed. A buoy was fitted to the cassette and the assembly was placed in a beaker containing 200 mL of dialysate at ambient temperature. The beaker contents were agitated using magnetic stirring at 125 RPM and protected from light. Each time a sample was removed, it was replaced with an equivalent volume of dialysate. Samples were taken in triplicate. Amount of released RSV (Q) was calculated using the relation $Q =$

$$\frac{C_n V_t + \sum_{i=1}^{n-1} C_i V_s + m_d}{C_0 V_b}$$
 where C_n is concentration at n th sampling point; V_i is volume of

recipient compartment; C_i is concentration at $(n-1)^{\text{th}}$ sample point; V_s is sampling volume; C_0 is initial concentration in donor compartment; V_b is volume of sample in the donor compartment; m_d is mass RSV lost to degradation predicted from the chemical stability study.

5.1.8. *Resveratrol chemical stability evaluation*

NE or drug solution samples were aliquoted into a screw-top glass vial and placed in storage at 4, 25, or 37 °C and protected from light. Samples were removed periodically, and RSV concentration was characterized by HPLC.

5.1.9. *In vitro oxygenation stability*

Method was completed as reported earlier (260). Pure oxygen was bubbled into the sample in a 100-mL round bottom flask under magnetic stirring through a glass Pasteur pipette for 30 min. Oxygen gas was then passed over the sample to fill the headspace volume with oxygen and the flask was sealed from the surrounding environment with rubber stoppers. The oxygenated sample was then sampled and tested for RSV content using the HPLC method.

5.1.10. *Cellular viability*

RAW 264.7 murine macrophages were seeded in 96-well plates at 3,000 cells/well. They were cultured in 5% CO₂ at 37 °C for 2 d to allow cells to attach. Treatment or control was diluted in cell culture growth medium at the highest treatment dose. This treatment stock was serially diluted in growth medium to produce cell treatment solutions ranging in concentration from 160 to 0.78 μL/mL. Before the cells reached confluency, the treatments were added to the existing growth medium in the plate

wells and incubated for 20 hr . The wells were washed with growth medium and the CellTiter-Glo® protocol was performed as instructed in the user manual. Cells given only growth medium as treatment were used as the control.

5.1.11. *Image-iT Hypoxia Green flow cytometry*

RAW 264.7 murine macrophages were seeded in 6-well plates at 0.5 million cells/well. They were cultured in 5% CO₂ at 37 °C for 36 hr to allow cells to attach. Treatment solutions were prepared by diluting NE or control in growth medium at 80 µL/mL. Treatment solutions were equilibrated with oxygen by bubbling with USP Medical Grade Oxygen (Airgas, PA, USA) for 10 min and immediately tightening with a screw top to prevent air exchange. The cells were labeled with 0.2 µM Image-iT™ Hypoxia Green reagent (Thermo Scientific) in DMSO followed by incubation for 0.5 hr in the cell culture incubator. The cells were then washed with medium, and the treatments or controls were added to the cells at 40 µL/mL. The pO₂ of the cells was modified using the nBIONIX Hypoxia Culture kits (Bulldog Bio, NH, USA) and then incubated in the cell culture incubator for 4 hr . The cells were washed 3 times with PBS. Cells were collected after detachment with trypsin and resuspended in 2% paraformaldehyde in PBS. Attune™ NxT Flow Cytometer (Thermo Scientific) fitted with a blue laser (wavelength 488 nm) and BL1 emission filter (wavelength 530 nm with 30 nm bandwidth) was used to analyze the resulting cell suspension. Samples of untreated normoxically-cultured cells were used as controls.

5.1.12. *Nitrite/nitrate colorimetric assay*

RAW 264.7 murine macrophages were seeded in 96-well plates at 10k cells/well. They were cultured in 5% CO₂ at 37 °C for 24 hr to allow cells to attach. Treatment

solutions were prepared by serially diluting the most concentrated treatment stocks to produce treatment solutions ranging in concentration from 80 to 5 $\mu\text{L}/\text{mL}$. RSV was dissolved in DMSO, then further diluted in growth medium to form RSV-free solution (RSV SOL) such that its RSV concentration was equal to the NE RSV concentration. Treatments were added to existing medium in the wells and incubated for 24 hr . Cells were washed twice with PBS and growth medium. 100 ng/mL lipopolysaccharide (LPS) was added, and the cells were incubated for 24 hr . Cell supernatant was collected, and the Nitrite/Nitrate Colorimetric assay (Sigma-Aldrich) was performed as described in the kit manual.

5.2. Results and discussion

5.2.1. Preparation and characterization of resveratrol-loaded PFC-NE

We prepared in total two 3 mM RSV-loaded G2-NEs. Two drug-free versions were prepared to serve as controls. Table 5.1 summarizes the composition and processing conditions for these formulations. These data are a subset of the complete G2-NE composition Table 4.1 presented in Chapter 4. Note that the RSV-NEs were identical replicates, while the drug-free NEs were prepared at various batch sizes, transcutol amount, and different phosphate buffer concentration. Our previous work (Chapter 4) suggested that these composition modifications did not impact the attributes of the PFC-NEs. To assess whether the RSV payload had any effect on the colloidal properties of the G2-NEs, we measured the droplet size on fresh NEs immediately after preparation. Then we stored them at 4 °C and periodically measured the size. We also assessed the droplet size change in response to syringe filtration through 0.45- μm pores, 5 min of centrifugation at 1100 RPM and FBS incubation. Figure 5.1 shows the 0-day size

distributions and size evolution over time. These results confirmed that the RSV payload did not affect the initial properties or the routine storage. Table 5.2 shows the filtration and centrifugation stability and Table 5.3 contains the serum incubation stability. In general, there was very little size fluctuation after filtration or centrifugation. There was a consistent increase in size after dilution in FBS. This is expected because the serum proteins are prone to adsorb to the droplet surface. These data confirm the stability of the PFC-NEs described here.

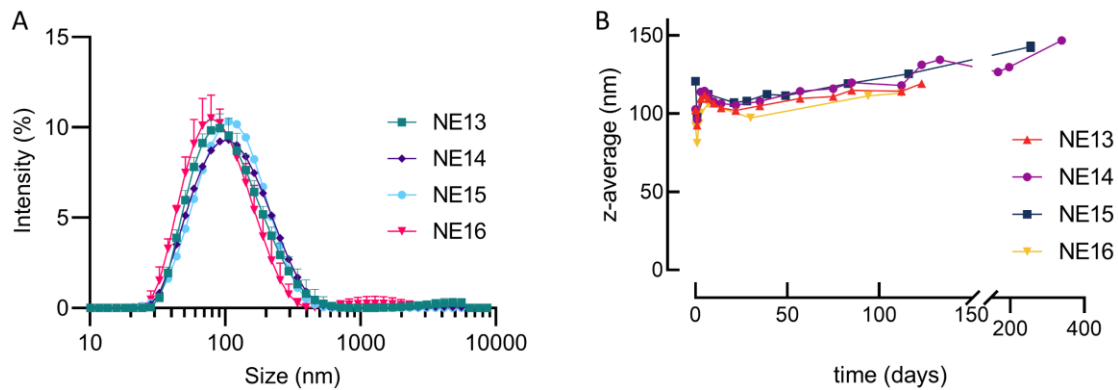


Figure 5.1. Colloidal characteristics of the G2-NE formulations considered in this chapter. (A) Day 0 size distributions. (B) Temporal stability during routine 4 °C storage.

Table 5.1. Subset of second-generation PFC-NEs used in *in vitro* evaluation. The naming convention from the previous chapter (Chapter 4) is preserved. PFOB, perfluorooctyl bromide; PBS, phosphate-buffered saline; RSV, resveratrol; PDI, polydispersity index.

NE	PFOB (mL)	Miglyol (mL)	Transcutol (mL)	Surfactant (mL)	Dispersant	[RSV] (mg/mL)	<i>N</i> passes	Set pressure (PSI)	Size (d.nm)	PDI
7	93.26	37.92	0.00	469	1.68× PBS	0.00	8	17800	190	0.129
13	19.43	7.23	0.67	98	1× PBS	0.69	5	16500	93	0.225
14	19.43	7.23	0.67	98	1× PBS	0.00	5	16500	96	0.228
15	19.43	7.23	0.67	98	1× PBS	0.69	5	16500	98	0.223
16	93.26	37.92	0.00	469	1.68× PBS	0.00	5	18500	81	0.216

Table 5.2. G2-NE stability to syringe filtration and centrifugation. Data are reported as mean and standard deviation of z-average (nm) (*n* = 3 measurements per group).

NE	Before filtration		After filtration		Before centrifugation		After centrifugation	
	mean	SD	mean	SD	mean	SD	mean	SD
13	119.2	0.5	125.6	1.5	109.5	1.2	110.5	1.2
14	131.2	1.5	120.8	0.3	113.8	1.2	113.4	2.0
15	112.3	0.6	111.4	0.7	112.3	0.6	111.2	1.1
16	113.1	1.3	110.9	1.4	113.1	1.3	112.2	0.7

Table 5.3. G2-NE stability to 72-hr incubation in fetal bovine serum (FBS) at 37 °C. Data are reported as mean and standard deviation of z-average (nm) ($n = 3$ measurements per group).

NE	0 hr		72 hr		0 hr		72 hr	
	Water				20% FBS			
	Mean	SD	Mean	SD	Mean	SD	Mean	SD
13	111.8	0.7	107.2	1.4	121.5	2.6	112.5	2.0
14	114.5	1.2	109.5	0.5	120.6	1.2	112.5	2.2
15	112.6	0.7	108.4	0.5	127.6	0.2	118.2	1.0
16	118.9	2.4	119.1	0.4	120.6	2.9	123.9	1.1

5.2.2. BCS Class II model small molecule antioxidant loading and stability

During hypoxia and reperfusion, there is an elevation in ROS production (288, 289). ROS play a crucial role in ischemic and hypoxic events and cause oxidative damage if gone unchecked. Therefore, many conditions which could benefit from oxygen intervention would also likely benefit from ROS-scavenger. Classically, pharmaceutical NEs have been utilized for encapsulation of lipophilic drugs to improve their bioavailability. Further, there are reports of enhanced chemical stability when utilizing NEs. There exist several commercial NE preparations designed to deliver small molecule active ingredients to various targets (290). However, PFCs are poor candidates for carrying active ingredients because of their lipophobicity. In the G2-NE formulation, the hydrocarbon oil can be utilized as a cargo compartment. Here, we selected RSV, a BCS Class II substance, as a model drug to encapsulate in the HC phase of a G2-NE to demonstrate the versatility of this G2-NE. The risk of oxidation of the RSV was anticipated to be high in an O₂-saturated system. Consequently, the chemical stability of the RSV NE (NE15) was determined after performing the O₂-loading step used in the *in vitro* oxygen release testing (refer to Methods for details). Details of the encapsulation and oxidation stability of the NE15 are given in Table 5.4. The payload encapsulation

efficiency was determined by HPLC to be 75%. After oxygen loading, the RSV concentration rose by 11.9%. This unusual result led us to discard the assumption that evaporative losses are insignificant during oxygen bubbling. Consequently, we measured the weight loss of the oxygen loading assembly (flask plus sample) after bubbling to determine the evaporative loss. The percent weight loss was 0.22%, and using this figure to calculate the expected change in RSV concentration assuming no chemical degradation gives an increase by 6%. The recorded weight loss was assumed to be entirely due to evaporation of the aqueous continuous phase, but additional variation is likely from the sample material sticking to the glass Pasteur pipet used in bubbling, which was not accounted for in the calculation. This oxidation stability experiment was repeated using a RSV aqueous buffer solution, where the flask weight loss was measured on the same sample used in oxygen loading, just like before. Similar results were observed with RSV in solution. The RSV concentration rose by 2.7% in the buffer solution, while its anticipated concentration gain based off the weight loss during bubbling was 4.5%. Overall, RSV was stable to oxygen loading in both formulations.

Table 5.4. RSV-NE encapsulation and oxidation stability.

	RSV-NE		RSV-SOL	
	Mean	SEM	Mean	SEM
Resveratrol concentration (mM)	2.26	0.017	2.35	0.002
Resveratrol Encapsulation Efficiency (%)	75.2	0.6	--	--
Measured [RSV] change during oxygen on-loading (%)	+11.9	18.6	+2.7	0.6
Evaporative weight loss during oxygen bubbling (%)	0.22	--	0.15	--
Predicted [RSV] change during oxygen on-loading (%)	+6.0	--	+4.5	--

RSV stability was followed longitudinally under routine storage conditions in both the NE and in the buffer solution at 4, 25, and 37 °C for up to 3 wk. It was observed that RSV solution was stable only at 4 °C (Figure 5.2A), while the form encapsulated in the NE remained stable even at 37 °C. Figure 5.2B demonstrates the stability at 37 °C, in which the RSV-NE lost 11.6% over 21 d compared to 90% loss from RSV-SOL in 18 d. Negligible loss was observed at 4 and 25 °C in the RSV-NE. These results are in agreement with previous accounts of RSV aqueous solution stability (291). To characterize the degradation kinetics and provide information on the reaction activation energy, the order of reaction was determined numerically. The RSV loss data in aqueous solution was log-transformed, resulting in a linear form (Figure 5.2A). From this linearized form, the first order reaction rate, k , can be directly obtained from the slope: $\ln[RSV] = -kt + \ln[RSV_0]$. Here, t is time, $[RSV]$ is the concentration at time t , and

$[RSV_0]$ is the concentration at time $t = 0$. k is dependent on temperature, and the rate constants can provide insight on the activation energy E_A of RSV depletion with the use of the Arrhenius Law: $k = Ae^{-\frac{E_A}{RT}}$, where A is the pre-exponential factor, R is the gas constant, and T is the absolute temperature. The fit to the linearized Arrhenius equation (Figure 5.2C) gave an E_A of approximately 80 kJ/mol, which is in close agreement with other reports on activation energy of RSV degradation in aqueous solution (291). The thermal stability reported by Silva, Teixeira (292) demonstrated that RSV does not undergo thermal decomposition until it melts at 240 °C. As our data are carried out in conditions only as high as 37 °C, it is unlikely that this type of degradation pathway is occurring. Based on other RSV stability reports, we believe that RSV's degradation in aqueous solution is induced by the dissociation of a proton from the 4' hydroxy group which has a pK_a of 8.8 (293). In nonenzymatic oxidation reactions of phenolic compounds, this leads directly to the formation of semiquinone radical (294, 295), which readily reacts with other species. Several reports (291, 296-298) provide details on the pH dependency of RSV and polyphenol solution stability. These observations support our hypothesized degradation pathway.

Nanocarriers are often used to modify the release rate of cargo. Therefore, characterization of release kinetics in nanocarriers is important. RSV *in vitro* release was investigated using a dialysis membrane method at ambient temperature. The initial release data from solution showed three distinct phases in the analyzed acceptor compartment: 1) an interval of cargo accumulation over time, 2) a brief plateau, followed by 3) an interval of decrease over time (Figure D.1). The unusual decrease in released cargo (phase 3) led us to consider the possibility of RSV degradation during the release

testing. Accordingly, the chemical stability in release buffer was used to account for degraded RSV in aqueous solution (Figure 5.2A). This was possible because the composition of the release buffer was identical to the buffer solution used in stability testing. The resulting adjusted release profile gave the first two phases without the unexpected 3rd phase. Figure 5.2D compares the release kinetics from NE15 and from RSV-SOL as a control group. The encapsulation efficiency of the control is provided in Table 5.4. The release profile of NE15 resembled a sustained release behavior. The RSV-SOL released 68% of its cargo in 96 hr where it began to plateau, while NE15 continued to release for more than 192 hr . The kinetics and extent of release here is similar to previously reported RSV-loaded NEs (37).

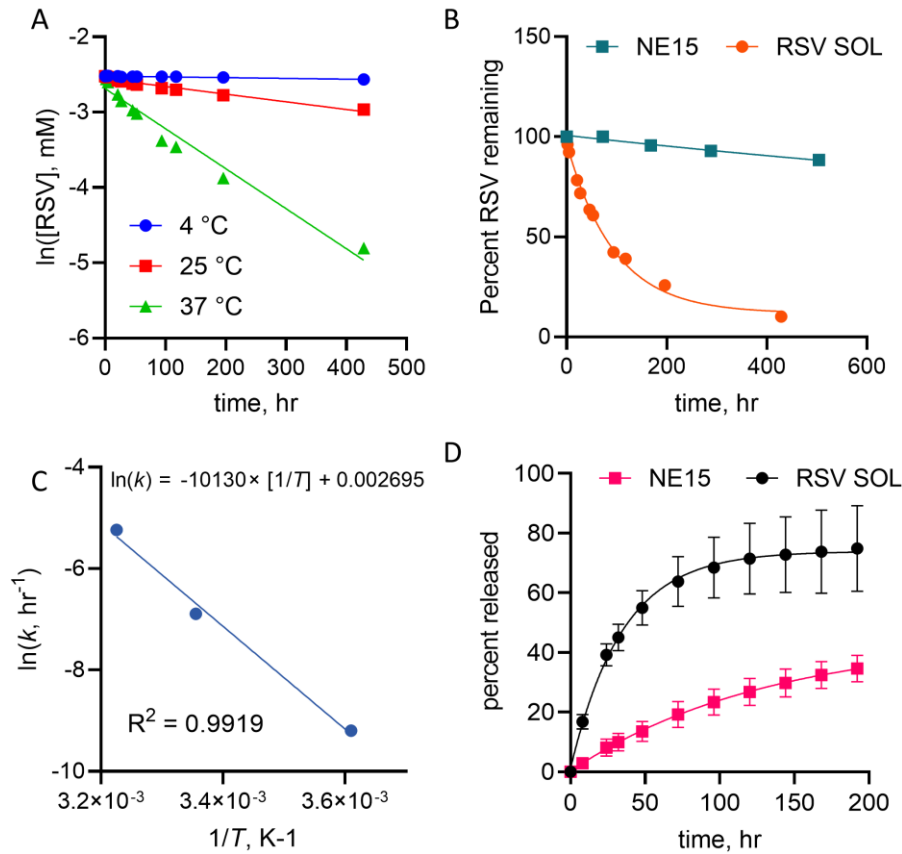


Figure 5.2. Resveratrol stability and *in vitro* release kinetics. (A) Temperature-dependent resveratrol degradation in aqueous drug release buffer solution. (B) Stability difference between RSV-SOL and RSV-NE. (C) Reaction rate constant dependence on temperature. (D) *In vitro* release kinetics.

5.2.3. G2-NE stability in machine perfusion circuit

Machine perfusion consists of circulating a perfusate through a closed circuit to preserve tissue. The main components of the perfusion circuit include a perfusate reservoir, an oxygenator fitted to an air/oxygen mixer, a temperature regulator, and a chamber which contains the preserved tissue graft. MP provides better outcomes in transplantation and has the potential to prolong preservation times and accept more marginal donor tissues. We tested the stability of the G2-NE in a model perfusion circuit fitted with a peristaltic pump, a hollow fiber membrane oxygenator, and a temperature

regulator. After 45 min of circulation, the droplet size distribution was unchanged (Figure 5.3A). Z-averages of NEs sampled at 10 and 30 min likewise were unchanged (Figure 5.3B). After 45 min, samples were taken and set aside for further stability testing. Figure 5.3C shows the z-average of non-circulated NE07 (control) in the modified serum incubation stability (where the FBS incubation group is omitted; details in Materials and Methods), while Figure 5.3D shows the modified serum incubation stability of the circulated sample. The machine perfusion operation did not elicit any destabilization. Figure 5.3E shows the centrifugation stability of both control and circulated samples.

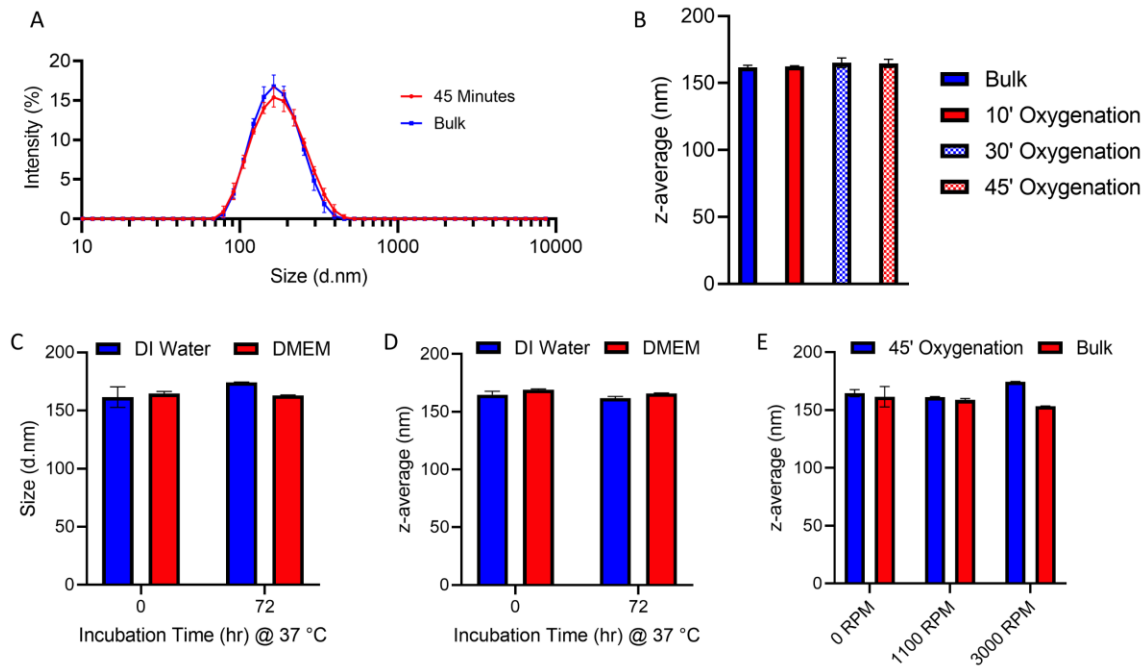


Figure 5.3. Stability of NE07 on the oxygen perfusion circuit. (A) Size distribution after 45 min of perfusion circuit compared to bulk before circulation. (B) Time series of z-average up to 45 min of circulation. (C, D) DMEM incubation stability of non-circulated and circulated sample, respectively. (E) Centrifugation stability of circulated and non-circulated sample.

5.2.4. Pharmacological effects of oxygen and RSV in murine macrophages

In our previous work, we created a custom method to characterize the *in vitro* oxygen release of G1-NEs (described in Chapter 3). Earlier in the current chapter, we reexamined the oxygen release model. We now describe the implications of the oxygen release by demonstration of oxygen replenishment in hypoxic murine macrophages after treatment with oxygen-loaded NE14. We employed a surrogate marker of intracellular oxygen tension (pO_2), Hypoxia Green reagent (HGR). This exhibits a fluorescent response to pO_2 . First, we verified and examined the fluorescent response to pO_2 using flow cytometry by modulating the pO_2 with nBIONIX hypoxia kits. In the range of 20% to 1% O_2 , the fluorescent response was linear during a 4-hr exposure to the pO_2 condition (Figure 5.4A). This length of time has been reported to be in line with the observed pharmacological response to hypoxia (299). Next, macrophages labeled with HGR were dosed with oxygen-loaded NE14 or control and exposed to a 1% pO_2 environment. The HGR fluorescent response is provided in Figure 5.4B. Exposure to hypoxia produced a large mean fluorescent signal, but treatment with NE14 significantly reduced the signal. The fluorescence of the treated group returned to 85% of the control group. This implicates that the oxygen-loaded G2-NEs are delivering the oxygen payload intracellularly to hypoxic macrophages. Cell viability of the conditions in this (Figure D.2 and Figure D.3) confirm that the effects seen here are not due to cell death.

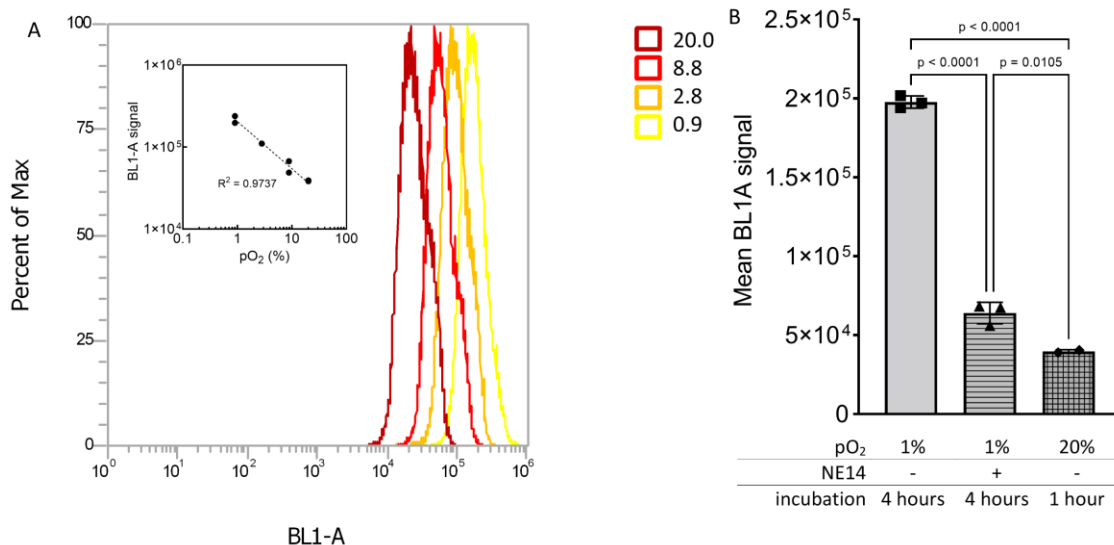


Figure 5.4. Effect of oxygen-loaded G2-NE in murine macrophages. (A) Flow cytometry histograms representing the response of Hypoxia Green reagent (HGR) to pO₂. The inset shows the quantified mean fluorescent signal of the associated histogram. (B) Response of hypoxic macrophages labeled with HGR to oxygen-loaded G2-NE14.

NO is an unstable reactive radical species which becomes upregulated in activated macrophages. It is a reactant in the formation of peroxynitrite, which is known to be a risk for DNA damage and lipid peroxidation among other damaging oxidation reactions (300). Basal NO also has a role in vascular relaxation. Complete eradication of NO can also lead to problems. Nitrate (NO₂⁻) is a byproduct of NO which is conventionally measured to assess the production of NO. Consequently, it was selected as a marker of oxidative stress in activated macrophages. To demonstrate the repeatability of the nitrate assay, the standard curves resulting from standards independently prepared 6 days apart (prepared on February 1 and February 7, 2023) were compared. The resulting curves very closely superimposed (Figure 5.5A). Next, activated macrophages were treated with NE14, NE15, or RSV solution. The RSV SOL was prepared such that the overall treated cells received an equal dose of RSV to that of NE15 at a given treatment concentration. Figure 5.5B illustrates the comparisons made at each treatment concentration. Note the

additional tick on the y-axis which indicates the nitrite concentration of unstimulated cells. It can be observed that RSV SOL and NE15 exhibited a clear dose-dependent response across the full treatment concentration range. This dose dependency is a crucial observation because of the dual nature of NO. The RSV dose can be tuned such that the NO levels fall back to the basal levels. NE15 returned the nitrite levels back to 61% of unstimulated at 2.5 and 93% of unstimulated at 20 $\mu\text{L}/\text{mL}$. RSV SOL had more potent effect compared to NE15 from 5 up to 40 $\mu\text{L}/\text{mL}$, although this difference was only significant at 10 $\mu\text{L}/\text{mL}$. Further, NE15 had more potent action on NO shutdown compared to NE16 up to 20 $\mu\text{L}/\text{mL}$. At 40 $\mu\text{L}/\text{mL}$, there was no longer any difference between NE15 and NE16. It was interesting to observe an effect of the RSV-free NE16. However, we are now aware of other reports of the effect of medium chain fatty acids on oxidative stress response in macrophages (301). Because the internal phase is composed of medium chain triglycerides and macrophages are capable of metabolizing triglycerides to free fatty acids (302), it is likely that the response seen from NE16 is a result of this effect. In addition, this could potentially explain why NO was lower at the 2.5 $\mu\text{L}/\text{mL}$ treatment concentration for NE15 group compared to the RSV SOL group. Cell viability of the NO assay conditions (Figure D.3 and Figure D.4) confirms the effects here are not due to cell death.

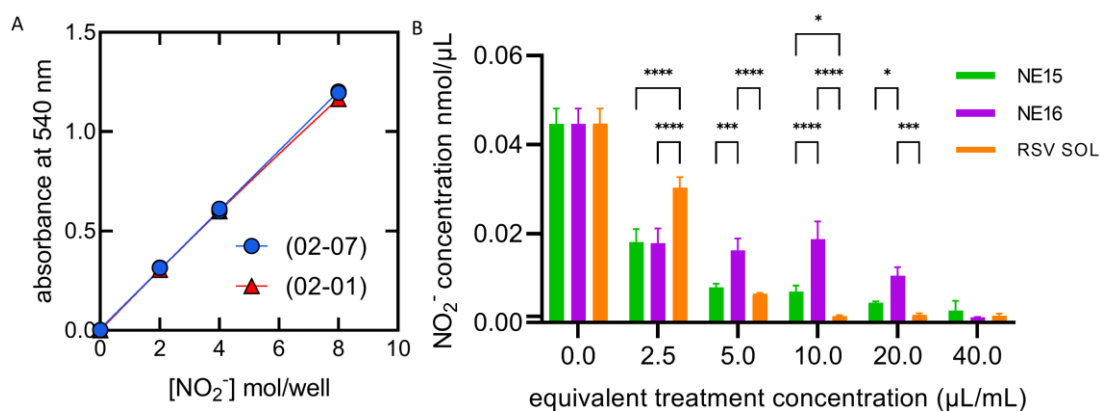


Figure 5.5. Effect of RSV-loaded G2-NE on nitric oxide production in murine macrophages. (A) Independently generated nitrite standard curves. Curves are labeled by the preparation date. (B) Nitric oxide production in response to RSV NE (NE15), blank carrier control (NE16), and RSV solution. Unactivated macrophages were marked by a black dash on the y-axis (between 0 and 0.02). *, **, ***, **** represent $p < 0.05$, $p < 0.01$, $p < 0.001$, and $p < 0.0001$, respectively.

5.3. Conclusions

We demonstrated the versatility of a PFC-NE AOC by characterizing the loading, release, and stability of a model BCS Class II drug, RSV, encapsulated in the HC oil phase. We observed that RSV in the aqueous environment was very unstable, and a significant increase in stability was attributed to encapsulation in the oil phase. We investigated the kinetics of RSV degradation and proposed a mechanism for its aqueous decomposition. We also demonstrated an extended release behavior attributed to the RSV NE. We verified the PFC-NE was stable after running through the machine perfusion oxygenation circuit. Finally, we demonstrated the pharmacological effects of oxygen- and RSV-loaded PFC-NEs in murine macrophage models. These effects are important for several reasons. IRI is marked by the activation and infiltration of immune cells such as macrophages. Activated macrophages are primary contributors to damage and rejection in the transplanted tissue graft (10, 64, 65). Our results showcase that the PFC-NE AOC

can modulate the hypoxic environment and NO generation of macrophages, which should result in more positive outcomes in IRI. Further, a dose dependent NO shutdown was observed in response to RSV. This has significant implications because the basal levels of NO are important for cell signaling (303). Overall, the results observed here produce a versatile artificial oxygen carrier that has promising results in *in vitro* experiments.

5.4. Acknowledgements

Anneliese Troidle and Caitlin Crelli contributed to the installation and operation of the machine perfusion circuit. Rebecca McCallin assisted in seeding cells. Rebecca, Anneliese, and Caitlin assisted in developing the fluorescence spectroscopy method and data collection. Manisha Chandwani, PhD assisted in the development of the flow cytometry method.

Chapter 6. Optical Microscopy as a Complementary Tool to Capture Oversized Population in Droplet Size Distribution of Nanoemulsions

NEs are liquid-liquid dispersions used as drug carriers to enhance solubility and bioavailability of lipophilic small-molecule drugs (304). One key challenge in their formulation is the absence of thermodynamic stability. The free energy of the NE is higher than the phase-separated liquids, and the NE will consequently follow a path toward phase separation over time (158). As the NE follows this path, the droplet size distribution will continue to shift to larger sizes. Even if complete phase separation does not occur, a significant shift in droplet size can be enough to compromise the quality of the NE. The most common modes of destabilization for NEs are Ostwald ripening and coalescence (120, 158). These processes can complete on the timescale of minutes to years depending on the kinetic stability of the NE. To successfully produce and sustain commercial NEs, long-term kinetic stability must be achieved. It is desired to have kinetic stability of two years. Enhancing kinetic stability is done by adding an appropriate surface-active agent, or surfactant, to form a barrier between the dispersed and continuous phases. This slows down the destabilization rate by lowering the interfacial tension and/or providing steric hindrance at the interface (120, 158). However, routinely assessing a product during development for two years is a time-prohibitive task. Accelerated stability tests can play a role in hastening the timescale of NE destabilization and facilitating decision-making in early development stages. Herneisey *et al.* (147) demonstrated that quality control and accelerated stability tests were instrumental in formulation decision-making for a microemulsion system during early product development. The authors utilized fresh microemulsion colloidal attributes (*e.g.*, diameter

and size distribution) coupled with colloidal properties in response to temperature cycling (4 cycles, 48 hr /cycle) to predict colloidal attributes after one month of storage (an indicator of long-term stability). This allowed the formulators to make a decision 8 d after microemulsion production rather than waiting an extended time to reach a decision. Recent studies have rigorously determined the rates of Ostwald ripening and coalescence increase with temperature (305, 306). For these reasons, we utilized a temperature cycling test to obtain accelerated stability information of a model triphasic (PFC/HC/W) NE.

The presence of large oil droplets in a parenteral emulsion can put a patient at risk of embolism. Pulmonary capillary diameter is roughly 4-9 μm , and droplets of this size can accumulate in and occlude the capillary space (307). The allowable limit for droplets $>5 \mu\text{m}$ in a lipid injectable emulsion (PFAT5) set by United States Pharmacopeia (USP) in chapter <729> is 0.05 % based on the volume-weighted size distribution (308, 309). Hence, it is evident that thorough characterization of droplet size distribution is a key requirement of injectable NEs. Dynamic light scattering has been established as the industry standard analytical tool for measuring the size distribution of nanocarriers. However, DLS has limits on the maximum particle size it can tolerate. The information it can provide on large droplet populations of diameter $>1 \mu\text{m}$ is unreliable (309, 310). To address this limitation of DLS, digital optical microscopy coupled with digital image analysis was used to capture information about the oversized droplet population undetectable in DLS. Microscopy is attractive because the sample preparation methods are simple, these methods can be fully or partially automated, and the technique gives information on the absolute particle size. Optical microscopy cannot be used as a

replacement of DLS, but rather as a complementary quality control technique, which together produce an ensemble droplet size analysis. This can be utilized to understand colloidal properties of freshly prepared nanoparticle formulations as well as monitoring various quality control stability measures of formulations. Here, we describe a preliminary method to acquire and analyze images of NEs taken with a digital optical microscope. The NE stability is evaluated in a series of stressing conditions using the conventional dynamic light scattering. Then the microscopy imaging and analysis assessment is described and applied to a NE in a temperature cycling stress test. Automation of the image analysis method is discussed. Finally, a preliminary attempt to estimate the PFAT5 is made.

6.1. Materials and Methods: Materials

6.1.1. Nanoemulsion preparation

NEs were produced following earlier published protocols (1, 38, 52, 216). Briefly, a micelle solution of blended non-ionic surfactants (2% Pluronic P-105, 3% Pluronic P-123 w/v) was made by following previously reported protocol with minor modifications (173). First, aqueous surfactant solution was added to the mixture of PFC and HC oils. Then, coarse emulsions were produced with an analog vortex mixer (VWR, Radnor, PA, USA) on high for 30 s. Coarse emulsions were sonicated on ice for 30 s at 29% amplitude (equivalent of 3480 W s) with Model 450 Digital Sonifier (BRANSON Ultrasonics Corporation, Danbury, CT, USA). Microfluidization was performed on all coarse emulsions by Microfluidizer M-110S (Microfluidics Corp., Westwood, MA, USA) at 18,640 psi liquid pressure for the specified number passes over an ice-cold interaction chamber. Emulsions were packaged in glass vials and stored at 4 °C.

6.1.2. *Filtration, centrifugation, and serum incubation colloidal stability tests*

6.1.2.1. *Serum incubation stability test*

See Section 4.1.5.1.

6.1.2.2. *Centrifugation stability test*

See Section 4.1.5.2.

6.1.2.3. *Filtration stability test*

See Section 4.1.5.3.

6.1.3. *Thermal cycling quality control test*

One-week-old NE samples were aliquoted into 10-mL glass screw top vials wrapped in Parafilm and alternated between storage at 4 and 50 °C for 24 hr at a time, where one cycle was defined as one storage interval at 4 °C immediately followed by one storage interval at 50 °C. After 4 cycles, the samples were allowed to equilibrate to room temperature and characterized by dynamic light scattering and optical microscopy.

6.1.4. *Dynamic light scattering*

NEs were tested as described in Section 4.1.4.

6.1.5. *Optical microscopy image acquisition*

NEs were diluted in deionized water at a dilution factor equal to that used in dynamic light scattering sample preparation. 20 μ L of the diluted sample was transferred to a clean glass-bottomed well of a chamber slide. An EVOS optical microscope collected representative images with a 20 \times objective lens. During the acquisition, 5 areas

of the chamber slide well were photographed: each of the 4 corners and the center of the well. Images were processed and analyzed in ImageJ software.

6.1.6. *Image processing and analysis*

All steps were done in ImageJ after defining the spatial scale of the digital image. If necessary, image brightness and contrast were adjusted. A 3-pixel×3-pixel (3×3) median image filter was applied to reduce image noise. Then, a 3×3 variance filter was applied to accentuate the particle edges. Manually, the operator set pixel threshold upper and lower bounds to isolate the background from the foreground. Fill holes, watershed, erosion, and dilation operations were applied to the binary image to form filled particles, separate neighboring particles, and remove noise. The Analyze Particles platform was utilized to calculate particle dimensions. The extracted particle features included Feret's diameter (*Feret*), Perimeter (*P*), Area (*A*), and Circularity (*Circ*). *Feret* is defined as the longest distance between any two points along the particle boundary and *Circ* is defined as Equation (6-1):

$$Circ = 4\pi \frac{A}{P^2} \quad (6-1)$$

Lognormal *Feret* and area distribution fits and all other statistical analysis were completed using JMP Pro 15.2.0.

6.1.7. *Automation of image processing and analysis*

The image processing and analysis described in the above subsection was recorded in a macro script window and saved. The pixel threshold operation was automated by choosing the threshold algorithm that produced particle size distribution that best matched the size distributions obtained when manually choosing a threshold. To

compare automatic threshold algorithms, log-normal area density functions created using manual and automatic thresholding were plotted in a x-y scatterplot. An exact match would yield a best-fit regression line with slope = 1 and intercept = 0. The automatic algorithm that corresponded to the closest match was selected. The macro was then applied to new images with the Run Macro menu option.

6.2. Results

6.2.1. DLS characterization of nanoemulsions

The NE initially appeared as a uniform, milky-white dispersion. The size distribution was monomodal, with a z-average mean of 126 nm and dispersity index of 0.11. Quality control tests were completed to confirm the colloidal stability of the formulation by monitoring size changes after stress. It was demonstrated that the formulation was resistant to 0.45 μm syringe filtration (Figure 6.1A-B), centrifugation (Figure 6.1C-D), and serum protein-induced destabilization (Figure 6.1E-F). The NE maintained its z-average and particle size distribution in these tests with the exception of the 72 hr 20% FBS incubation. Serum proteins are known to interact with surfaces, including adsorption and formation of an additional layer at the surfaces of particles (311). Therefore, this size change is not a reflection of destabilization. The NE also exhibited at least 7 wk of shelf stability (Figure 6.1G). Over this length of time, the size distribution remained monomodal and underwent minimal growth (z-average = 142; PDI = 0.15). The quality control evaluation confirms the stability of the described formulation.

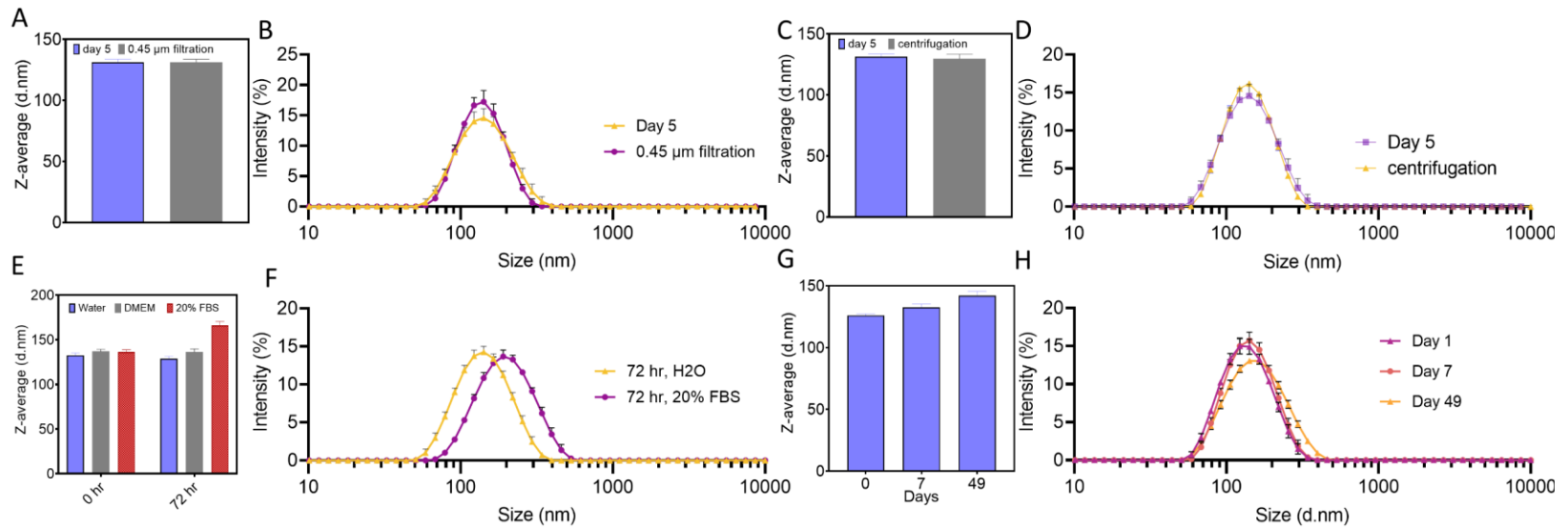


Figure 6.1. Colloidal stability of the perfluorocarbon-in-hydrocarbon-in-water nanoemulsion in response to various stressors. z-average and size distribution comparisons in syringe filtration(A-B), centrifugation (C-D), and serum incubation. 7-wk stability of z-average (G) and size distribution (H).

In response to temperature cycling, it was expected that the NE would destabilize more rapidly in part because of the influence of elevated temperature. Figure 6.2 summarizes the NE droplet size analysis of the cycling sample obtained from DLS. Although the z-average remained unchanged (Figure 6.2B), the intensity-weighted size distribution (Figure 6.2A) after cycling broadened in comparison to the 15-day control sample. This observation is consistent with the larger spread of D10 and D90 and the increase in dispersity after cycling (Table 6.1). The size distribution remained monomodal without any formation of oversized droplet populations.

Table 6.1. DLS droplet size summary of the cycling and the control age-matched samples. Droplet size descriptors are the average of three measurements reported in nm, and PDI is the average of three measurements.

	Day 15	Cycling
d10	88.6	77.6
d50	143	152
d90	233	293
z-ave	135.3	136.1
dispersity	0.119	0.193

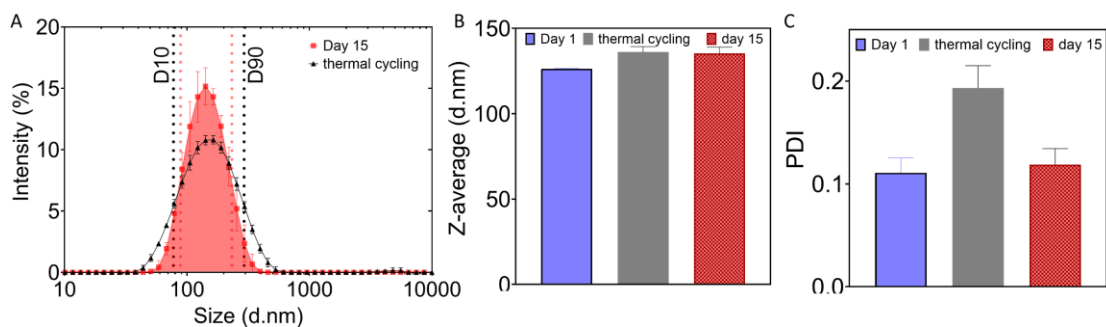


Figure 6.2. DLS summary of thermal cycling accelerated stability test performed on a perfluorocarbon nanoemulsion. (A) Comparison of size distributions of the cycling and the control age-matched sample. D10 and D90 are indicated by dotted vertical lines for control (red) and cycling (black) samples. (B) Z-average of the fresh, cycling and control samples. (C) PDI of the fresh, cycling and control samples.

6.2.2. Optical microscopy characterization

Figure 6.3 represents the flowchart of image acquisition and analysis methods. Figure 6.4 shows a representative unprocessed and the corresponding processed image of the NE captured using the EVOS optical microscope and analyzed by ImageJ software. The droplets appear nearly perfectly circular. Circularity (*circ*) of the particles was examined and confirmed the spherical nature of the droplets, which is to be expected because the sphere minimizes the interfacial area of a globule. *circ* is defined in Equation (6-1). As the circularity of an object approaches 1, the more it resembles a circle. Table 6.2 summarizes the statistics for *circ* of the droplets. For both thermal cycling and the control, the mean *circ* was >0.95. Furthermore, a scatterplot of *Feret* vs. $2\left(\sqrt{\frac{A}{\pi}}\right)$ was constructed and examined. With perfectly circular objects, this yields a line of best fit with a slope equal to 1. The slopes obtained for cycling and control groups were 0.86 and 0.92 (Figure 6.5).

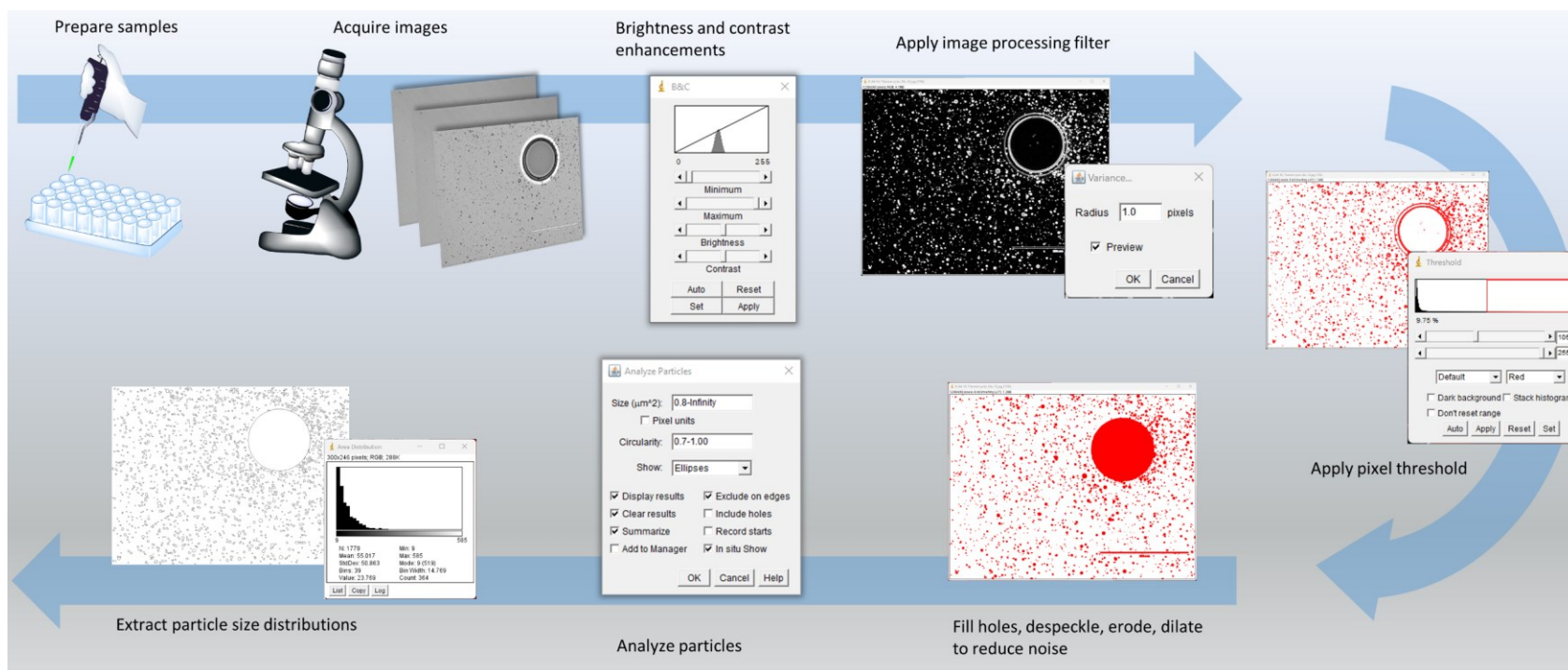


Figure 6.3. Core elements in the image acquisition and analysis sequence of perfluorocarbon nanoemulsions. Screenshots from ImageJ software.

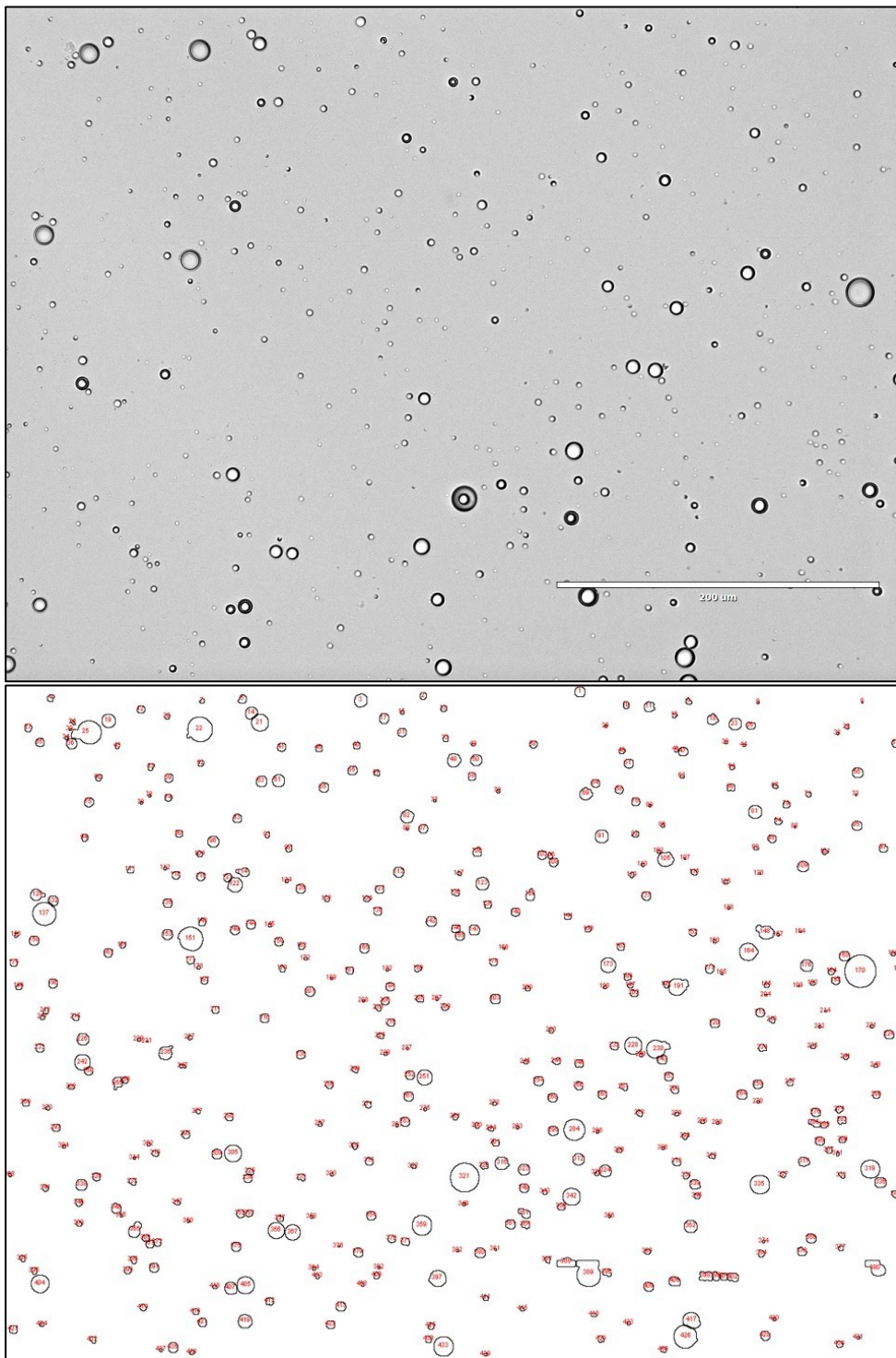


Figure 6.4. Example photograph of perfluorocarbon nanoemulsions and resulting binary processed image of outlined droplets. The scale bar is 200 μm .

Table 6.2. Descriptive statistics of nanoemulsion droplets imaged with the optical microscope.

Condition	Mean Circ	Std. Dev. Circ	Mean Feret	Std. Dev. Feret	Mean A	Std. Dev. A
day 15	0.963	0.049	5.27	2.70	21.05	28.81
Thermal cycle	0.955	0.058	4.58	2.01	13.57	14.60

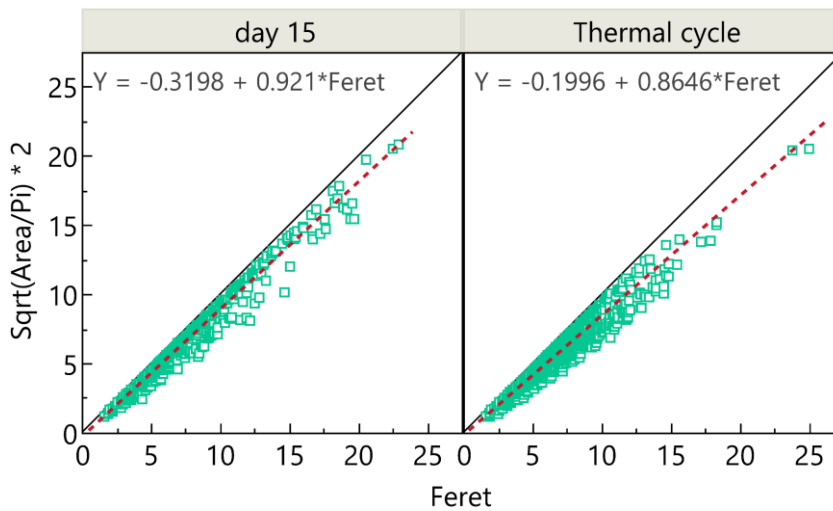


Figure 6.5. Scatterplot of $Feret$ and $2\left(\sqrt{\frac{A}{\pi}}\right)$ where $Feret$ and A are expressed in μm and μm^2 , respectively. Solid line is the line $y = x$ and dashed line is the linear regression line fit to the data.

To evaluate the quality of the image analysis algorithm, an image of a published sample scanning electron microscopy (SEM) photomicrograph of a glass particle size reference standard was utilized as a reference (312). The reported mean size of the standard was $12.8 \mu m$ with a standard deviation of 0.4 . The present analysis (Figure 6.6) found a mean size of $11.0 \mu m$ with a standard deviation of 4.2 . Visual analysis of the analyzed reference photomicrograph revealed that our analysis failed to recognize some of the smallest particles and failed to divide a small number of neighboring particles into

their constituent units, an operation known as watershedding. The authors analyzed more than 39,000 particles while our estimate was made after analyzing only 139 particles. Given this observation, there was a close agreement of the reported and measured means and the validity of the present reported method was confirmed.

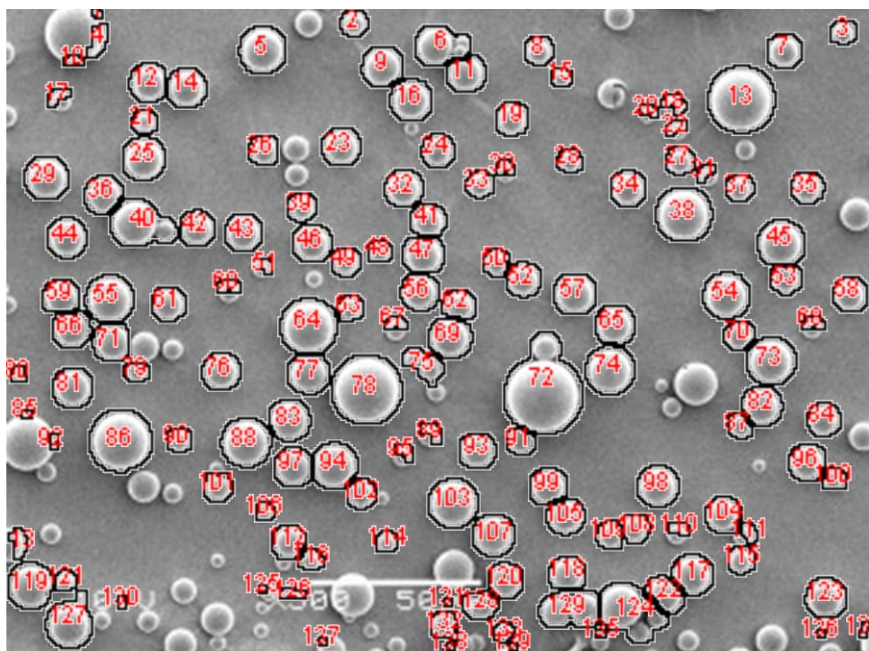


Figure 6.6. Image analysis applied to reference particles taken in scanning electron microscopy. Original image from “Theoretical calculation of uncertainty region based on the general size distribution in the preparation of standard reference particles for particle size measurement.” by Yoshida, H in *Advanced Powder Technology*, 23(2), 185-190. Copyright 2011 by The Society of Powder Technology Japan. Reused and adapted with permission.

To create droplet area distributions from the samples used in microscopy imaging, four images for each condition were analyzed. Altogether, there were 2,331 and 7,535 particles counted in the aggregated day 15 control and in the aggregated thermal cycling analysis, respectively. The fitted area density distribution showed the thermal cycling sample shift to smaller areas (Figure 6.7). This result was unexpected. However, because the optical images are showing only a fraction of the total droplet population, the

interpretation of area density distribution is taken carefully. Alternatively, Figure 6.8 shows frequency histograms of droplet area. This data is consistent with the area density distribution, where the mean of the distribution shifted to smaller areas. However, the frequency histogram highlights the total droplet number increase across the full range of areas after cycling. To account for the total number increase, it is likely that droplets which were initially undetected by optical microscopy increased to a detectable range of size after cycling.

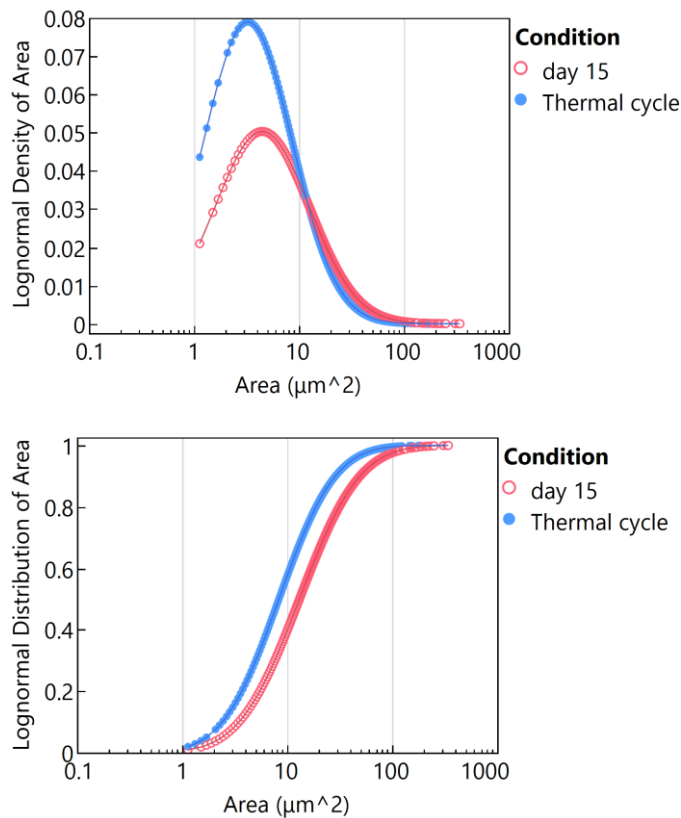


Figure 6.7. Lognormal density and cumulative distributions fit to particle area for comparison of perfluorocarbon nanoemulsion conditions.

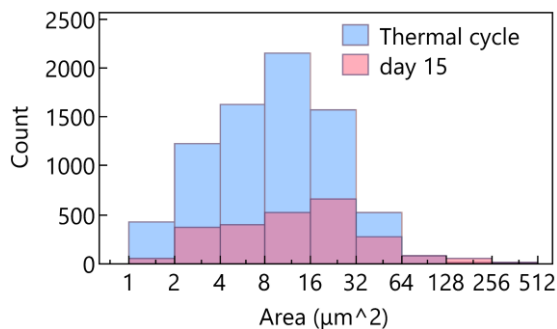


Figure 6.8. Frequency histograms of particle area for comparison of perfluorocarbon nanoemulsion conditions.

6.2.3. Image analysis automation

One primary limitation is the image acquisition and analysis can be very time-consuming tasks. For this reason, the image analysis method was automated. ImageJ provides several algorithms for automatic pixel thresholding. The thresholding algorithms are briefly described in Table 6.3. The algorithms were evaluated in two sequential steps using one selected NE image. The first step qualitatively examined all algorithms side by side in a photomicrograph montage where each image was the resulting thresholded image from one algorithm. Percentile, Triangle, and Yen algorithms were excluded right away when visually screening the montage of thresholded images obtained from the ‘try all’ option accessible in ImageJ’s menu options. The threshold limits selected with these algorithms failed to separate the background from the droplets and the associated images appeared over-exposed. The montage appears in Figure E.1.

Table 6.3. Automatic thresholding algorithms.

Algorithm	Description	Reference
Default	Variation of IsoData	(313)
Huang	Sets the threshold such that a fuzzy index describing the distance between the original and thresholded image is minimized	(314)
Huang2	Computationally more efficient version of Huang	(314)
Intermodes	In a bimodal pixel histogram, sets the threshold at the pixel brightness value which occurs halfway between the two peak maximums	(315)
IsoData	Iteratively divides the image into object and background, incrementing the threshold until the threshold $>$ composite average of object and background pixels	(313)
Li	Sets the threshold such that the cross entropy between the original and thresholded image is minimized	(316)
MaxEntropy	Defines two probability distributions (objects and background) which maximize the sum of entropy	(317)
Mean	Sets the threshold to the mean of all pixel values	(318)
MinError(I)	Similar to Otsu, but minimizes a different objective function	(319)
Minimum	In a bimodal pixel histogram, sets the threshold at the pixel brightness value which falls at the pixel count minimum	(315)

Algorithm	Description	Reference
Moments	Matches the first three moments of the thresholded image to those of the gray-level image	(320)
Otsu	Sets the threshold such that the intraclass variance of the thresholded object and background pixels is minimized	(321)
Percentile	Sets the threshold at a specified percentile of the pixel intensity distribution	(322)
RenyiEntropy	Defines two probability distributions (objects and background) which maximize the sum of Renyi entropy	(317)
Shanbhag	Sets the threshold such that the sum of the fuzzy entropies is minimized	(323)
Triangle	Sets the threshold such that the distance of a line drawn from the pixel brightness histogram to a line constructed from the histogram peak maximum and the highest pixel brightness value is maximized	(324)
Yen	Defines two probability distributions (objects and background) which maximize the sum of Yen's defined entropy	(325)

The second step of the evaluation applied the remaining algorithms one at a time to the same image and area distributions were created for each result. The Lognormal density functions were saved and subsequently compared to the Lognormal density function obtained in the manual thresholding. Examination of a scatterplot of the two Lognormal density functions ($y =$ automatic and $x =$ manual) made it possible to choose the automatic thresholding algorithm that closest matched the manual thresholding result. In this scatterplot, a perfect match would yield a best fit line with a slope of 1 and bias of 0 (*i.e.*, identity line). Figure 6.9 demonstrated these comparisons. Mean and MinError algorithms selected the same upper (255) and lower bounds (35) in thresholding. Therefore, the image analysis results should be identical for these two algorithms and the density function scatterplot should produce data superimposed on the identity line. This was confirmed in the scatterplot in Figure 6.9A. Therefore, the closer the limits selected in the auto thresholding method to the manual thresholding method, the better the result. Of the scatterplots which compared automatic to manual thresholding in Figure 6.9, five produced data closely aligned with the identity line. These algorithms correspond to Otsu, Moments, Isodata, Intermodes, and Default. Among these, the Moments algorithm had no discernible offset from the identity line (Figure 6.9G) and was chosen as the automatic thresholding algorithm.

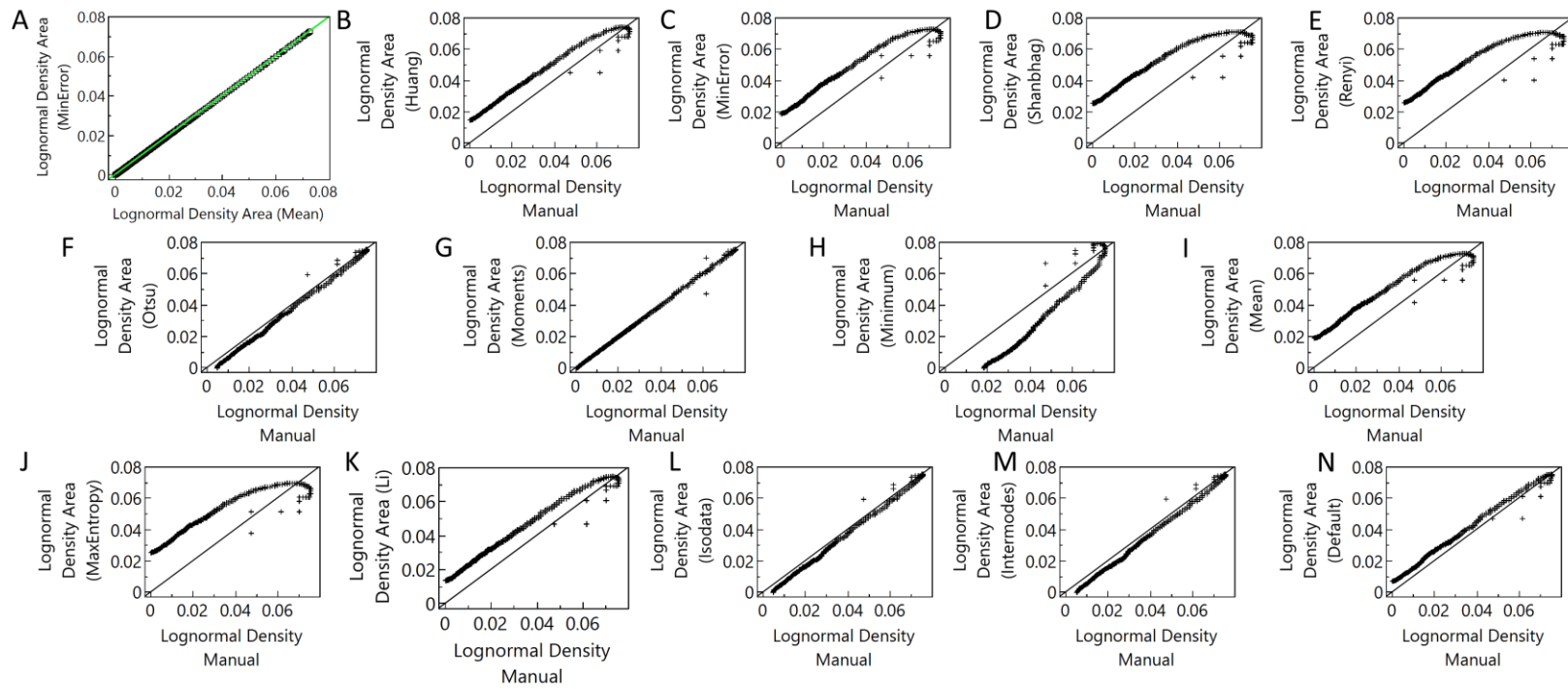


Figure 6.9. Comparisons between automatic thresholding algorithms and the manual threshold selection for sample photomicrograph of a perfluorocarbon nanoemulsion after thermal cycling. The solid line is the line $y = x$.

6.2.4. PFAT5 calculation

The microscopy image analysis is capable of providing rich data regarding the existence and number of droplets larger than 1 μm . A rough estimate of the PFAT5 from the image analysis can be attempted. The dimensions of one image were $556.5 \mu\text{m} \times 417.4 \mu\text{m}$, giving a total analyzed area of $9.3 \times 10^5 \mu\text{m}^2$ per sample (4 images). The area of one chamber slide well was $7 \times 10^8 \mu\text{m}^2$. The total volume of droplets $>5 \mu\text{m}$ counted in the sample was $260,853 \mu\text{m}^3$ ($n = 2,118$). Assuming a uniform distribution of particle number and volume across the well, the total volume of droplets in one well was $1.96 \times 10^8 \mu\text{m}^3$. Accounting for the sample dilution factor (80) and total sample volume (20 μL), the total volume of droplets with diameter $>5 \mu\text{m}$ was $1.97 \times 10^{13} \mu\text{m}^3$. For more precise calculations, one can assume the droplets visible on the photomicrographs are at rest on the well bottom, forming a hemisphere. The equivalent spherical dimensions can be obtained from equating the volume of hemisphere to the volume of a sphere and calculating the equivalent spherical radius: $V_h = V_s = \frac{2\pi}{3} r_h^3 = \frac{4\pi}{3} r_s^3$, where superscript h and s represent a hemisphere and sphere, respectively, and V and r represent the volume and radius of the object, respectively. The equivalent spherical radius is

$$r_s = \sqrt[3]{\frac{1}{2}} \times r_h \quad (6-2)$$

Calculations using the r_s gives $6.5 \times 10^{12} \mu\text{m}^3$ as the total volume of droplets with diameter $>5 \mu\text{m}$. Compared to the total volume of liquid in the NE internal phase, this estimated volume is in excess of the internal phase volume. This approximate calculation of volume fraction of droplets $>5 \mu\text{m}$ described above gives an unrealistic number. A key assumption that would need reexamination is the uniform number distribution across the well. In practice, this would require a perfectly leveled microscope sample surface. Slight slopes on the surface of the well could be

present due to the chamber slide manufacturing process or the placement of the microscope which would violate this assumption. Analysis of a higher number of images can help to increase the confidence of the sample distribution across the well. Examining more images will result in a higher area of analysis and a larger number of counted and analyzed particles. This latter point allows a higher confidence in fitting size distributions to the imaged population of particles. Further, this method can be applied to other imaging techniques in which cryogenic temperatures would prevent a uniform sample from drifting during data acquisition.

6.3. Discussion and conclusions

The present discussion offers a complementary method to DLS for characterizing the large droplet population of injectable NEs in addition to DLS. This method involves the use of digital image analysis to extract particle dimensions of particles $>1 \mu\text{m}$ in diameter. In general, this method is capable of distinguishing the foreground objects from the background in samples of PFC/HC/W NE droplets, counting them, and computing dimensions and shape descriptors of them. Here, the method was applied to light microscopy to evaluate the kinetic stability of NEs under temperature cycling stress. However, it could also be applied to electron microscopy which offers much higher resolution in capturing particle size information. Further, ImageJ's built-in thresholding algorithms facilitated the automation of the image analysis. The automation was optimized by comparing the automated size distributions to the manual size distributions, where the Moments algorithm performed almost identically to the manual thresholding. To assess the method against a sample of known dimensions, it was successfully applied to a photomicrograph of spherical glass reference particles taken with SEM. The reported mean diameter of the reference particles was similar to the mean diameter calculated with the present method, despite counting fewer than 200 particles. This suggests that the method is accurate. In

this reference photomicrograph, the method had few problems with watershedding and loss of information from failing to detect particles. The problems encountered with the reference image were possibly due to background light gradations which were more prominent in the SEM reference image than in images taken by our group with the optical microscope. A rough calculation of the PFAT5 from the analyzed optical images was then attempted. This calculation strongly overestimated the PFAT5, considering the calculated total volume of particles $> 5 \mu\text{m}$ was in excess of the total volume of the internal phase components. The inconsistent background lighting can complicate the thresholding operation. To improve this method, cryogenic sample preparation prevents droplet motion during image acquisition. Alternatively, using a viscous dispersion medium would reduce droplet motion. This would prevent the droplets from collecting in the sample well depressions and would make the uniform spatial distribution assumption more appropriate. In addition, analyzing a larger number of images and thus a larger number of particles would result in an increase in the statistical confidence of the particle size distribution. Without a doubt, the automation of the image analysis method will be instrumental in managing a larger number of image files and producing a more reliable method to characterize the oversized droplet population of NEs.

Chapter 7. Summary

IRI presents significant problems to graft survival in transplantation. Both solid organ and vascularized composite allograft survival would benefit from the existence of commercially available artificial oxygen carriers and a reactive oxygen species scavenger to alleviate hypoxia and reduce oxidative stress during preservation. PFC-NEs exemplify one such candidate oxygen carrier. Progress of PFC-NEs toward clinical approval has recently been stagnant, and we hypothesized that introducing a systematic approach to product development would yield stable and functional NEs to be used as artificial oxygen carriers. We employed Quality by Design, a systematic process development philosophy which has gradually gained traction in the pharmaceutical industry but has not appeared in the development of PFC oxygen carriers.

In the first specific aim, the focus was primarily on the application of a QbD methodology to the development of triphasic PFC-NEs as AOCs. Here, we intended on identifying the critical factors of the composition and processing method that governed oxygen release and colloidal stability with the overall objective of maximizing the oxygen delivery without compromising the colloidal stability. We noted that few reports existed regarding multivariate statistical modeling in the formulation of PFC/W NEs, which is one way to learn key information in pharmaceutical product development. In Chapter 2, our goal was to develop and validate a methodology to support the construction of such models that would help to formulate stable PFC-NEs. With a tool like this in our toolbox, we would be confident in applying QbD to PFC-NE development. A statistical design of experiments was employed to generate a small library of NE formulations representing a wide variety of formulation chemical space. The composition diversity included hydrocarbon phase (type and amount), PFC phase (type and amount), and presence or absence of a conjugated HC-PFC reagent. In this study we

established the general methodology of multivariate modeling of colloidal properties of both conventional biphasic (HC/W or PFC/W) NEs and complex triphasic (PFC/HC/W) NEs. A multiple linear regression model was constructed that described how the formulation impacted the droplet diameter. We also noted that the triphasic formulations were more stable than the biphasic PFC formulations.

With the methodology to create multivariate models of colloidal properties established, we formalized the QbD approach in Chapter 3. We created a preliminary quality target product profile for the generation-1 triphasic PFC-NE AOCs and defined the critical quality attributes. We used quality risk management to justify the screening experimental design that was carried out. The screening study facilitated how we studied the colloidal stability and the oxygen release of triphasic PFC-NEs. We constructed MLR models to describe these attributes and learned that the composition of the dispersed phase influenced both attributes. Comparison of the model coefficients divulged that while increasing the PFC amount contributed to better oxygen delivery, it also resulted in poorer colloidal stability. This same trend was suspected from interpretation of the data reported in the PFC-NE literature. The regression models were exploited to describe a formulation design space where both oxygen delivery and colloidal stability attributes could be managed.

We optimized the composition of the PFC-NE AOC, defined the optimized formulation ‘generation-2’ NEs, and assessed its cellular viability in murine macrophages. Then we utilized a fluorescent, oxygen-sensitive, surrogate intracellular marker (Hypoxia Green Reagent) to investigate the impact of the oxygen-loaded PFC-NE AOC in hypoxic macrophages. Flow cytometry confirmed that the O₂-PFC-NE was able to nearly return macrophages cultured at 1% O₂ back to normoxic O₂ levels during a 4-hr hypoxic treatment incubation.

The optimized formulation was utilized to validate the multivariate oxygen delivery model from Chapter 3. Because the validation statistics were unsatisfactory, we were prompted to reexamine and refine the model, which is described in Chapter 4. We found that a simple linear regression model, consisting of f_{PFC} as the independent variable, predicted the C_{max} of G2-NEs exceptionally better. This is encouraging, especially considering the composition diversity of the calibration and validation samples (*i.e.*, the G1- and G2-NEs).

Injectable NEs are a potential risk for embolism if not formulated and prepared properly. The existence of droplets larger than 5 μm can be trapped in the lungs. Therefore, characterization of the full range of droplet size distribution is of paramount importance. In our historical characterization of NE droplet size distribution and colloidal stability information, we have exclusively used dynamic light scattering. This is the standard method of characterizing nanoparticle size but has limitations on the reliability of particle size over 1 μm . Therefore, in Chapter 6 we introduced a complementary digital optical imaging and analysis method that can provide information on the oversized droplet size distribution. This method proved to be effective at segmenting the PFC-NE droplets (objects) from the background and computing object shape and size descriptors. The method was then automated, which will facilitate the application of this analysis to larger numbers of objects. This method could be applied to transmission electron microscopy images to achieve a complete analysis of the particle size distribution range.

Specific aim 1 formalized the QbD framework for PFC-NE AOCs. An element of the QbD is the quality target product profile (QTPP). The QTPP describes the intended critical quality attributes and sets acceptable limits on the CQAs. The QTPP encompasses the entire life cycle of the product and is used to measure and monitor the product quality. The defined QTPP

is shown in Table 7.1.

Table 7.1. Quality Target Product Profile (QTPP) for perfluorocarbon nanoemulsion artificial oxygen carriers.

Attribute	Target / specification	Rationale
Indications	Ischemic event and reperfusion injury	
Dosage form	PFC-in-HC-in-water nanoemulsion	Disperse PFC in water; encapsulate ROS scavenger
Route of administration	<i>Ex vivo</i> continuous infusion	<i>Ex vivo</i> machine perfusion product
Administration rate and duration	20 mL/hr for 24 hrs	Infusion rate dependent on tissue type
Packaging	Sterile bottle, protected from light	Light sensitive API
Droplet size (z-average)	100 ± 10 nm	Standard quality attribute; surface area available for release; cell uptake
Dispersity index (PDI)	< 0.2	Monomodal distributions more likely to be stable
Zeta potential (ZP)	-15 ± 10 mV	positive ZP interacts with cell membranes
Diameter stability	≤ 30% diameter change over 6 mo	small initial diameter change is normal
Size distribution stability	PDI ≤ 0.25 at 6 mo	small initial diameter change is normal
PFC encapsulation	100 ± 15%	influences API loading
ROS-scavenger encapsulation	100 ± 25%	API protects from oxidative damage
In vitro oxygen release rate	Oxygen $C_{max} \geq 2$ mg/L; $t_{Max} \leq 1$ min	Oxygen rate of extraction in MP
In vitro drug release	Sustained ≥ 72 hr release	Minimize dosing frequency
Cellular viability	100 ± 20% @ 40 µL/mL	Safety measure
Hypoxia green activity	returns fluorescence @ 1% pO ₂ to within 1.2 × basal levels	Oxygen delivery measure
NO activity	returns NO to within 1.2 × basal levels	ROS scavenger action

The specifications set here are more comprehensive and pragmatic than the CQA specifications set in Table 3.1, which was created at the time when QbD was initially implemented. It is natural for the QTPP to evolve as more product information is acquired. For example, one of the attributes measured to describe long-term stability of G1-NEs was the size and PDI change 30 d after preparation. Most of the G1-NEs were stable over this length of

storage and met the specifications (Table 3.3). However, the allowable z-average change and PDI at 6 months is 30% and 0.25, respectively as defined in Table 7.1. Both of these G1-NE attributes violated the specifications established by the QTPP considering the onset of phase separation by 3 months. Notably, G2-NEs displayed no signs of phase separation and satisfied the CQA specifications. Importantly, this stability enhancement of the optimized formulation coincided with the maintenance of satisfaction of the C_{\max} specification. In fact, C_{\max} was nearly 4 mg/L, which is a 2+-fold increase.

Oxidative stress is a result of the immune response during reperfusion that occurs regardless of how well the tissue is oxygenated during preservation. Therefore, the second aim focused on formulating and evaluating a model antioxidant-loaded version of the optimized PFC-NE AOC. We chose the small molecule, BCS Class II antioxidant RSV, which has shown potential in eliminating oxidative stress. Because of RSV's poor water solubility, its efficacy is limited as an aqueous solution. Fortunately, the triphasic NE offered the opportunity to load it into the oil phase of the AOC. In Chapter 5, we describe the loading, chemical stability, and *in vitro* release of RSV. We found that the oxygen on-loading process did not affect the stability of RSV regardless of the dosage form (aqueous solution or NE). However, the oil-encapsulated form demonstrated a marked increase in stability compared to the aqueous form in routine storage conditions. Further, we demonstrated a sustained *in vitro* RSV release over at least one wk in duration. Therefore, this could be a key advantage as preservation times in transplantation can be extended in duration. Finally, we investigated the RSV-loaded PFC-NE AOC in an *in vitro* oxidative stress model. Macrophages were stimulated with LPS to elicit a proinflammatory reaction, and the RSV-NE treatment eliminated the nitric oxide metabolite nitrite in a dose dependent manner and comparable in magnitude to the RSV aqueous solution.

The attributes for the safety and efficacy of the RSV-NE were also folded into the QTPP. Our RSV loading efficiency formed the basis of our defined drug encapsulation efficiency specification. Because of the interest in extending tissue preservation durations, we assigned the *in vitro* release to be sustained over three or more days to prevent a burst release from dominating the release profile. Finally, we set reasonable limits for cell viability and efficacy in a hypoxic cell model.

A commercially available pharmaceutical product is expected to undergo scale-up from laboratory to production plant quantities. In specific aim 3, the focus therefore turned to manufacturing the PFC-NE AOCs. In Chapter 4, we evaluated the scalability and reproducibility of the optimized PFC-NE AOC. We analyzed size distributions, fluorescence profiles, and PFC incorporation as metrics of comparison of 27 batches of optimized PFC-NE AOCs and formed comparisons across three different Microfluidizers. Inspection of size distributions revealed trends that were not easily explained by the known sources of variability during manufacturing. Consequently, we conducted principal components analysis to aid in deciphering trends. Although we did not advance past laboratory scale production manufacturing, we transferred the production process from 25 mL to 600 mL batch size on benchtop Microfluidizer processors. This batch size would be sufficient to support *in vivo* studies with large animal models. Further, we demonstrated that our process was amenable to corrective action. one PFC-NE AOC batch, which was by mistake underprocessed and failed to satisfy the droplet size attribute specifications, was salvaged and reprocessed after troubleshooting the processor. The droplet size attributes returned to within the specification limits.

Altogether, this work has established that QbD offers valuable methodologies in the development of PFC-NEs as oxygen carriers. Up until the present, PFC-based AOCs have not

been clinically successful in part because of inadequate stability. QbD was instrumental here in the accrument of the combination of: oxygen delivery proficiency, small molecule loading, and colloidal stability. In the future, this technology would benefit from studies in *ex vivo* transplantation models to fully evaluate the oxygen and RSV delivery proficiencies and to evaluate the impact on overall preserved tissue quality.

References

1. Herneisey M, Liu L, Lambert E, Schmitz N, Loftus S, Janjic JM. Development of Theranostic Perfluorocarbon Nanoemulsions as a Model Non-Opioid Pain Nanomedicine Using a Quality by Design (QbD) Approach. *AAPS PharmSciTech*. 2019;20(2):65.
2. Farris AL, Rindone AN, Grayson WL. Oxygen Delivering Biomaterials for Tissue Engineering. *J Mater Chem B*. 2016;4(20):3422-32.
3. GLOBAL OBSERVATORY ON DONATION AND TRANSPLANTATION [Web page]. 2022 [Available from: <http://www.transplant-observatory.org/contador1/>].
4. Israni AK, Zaun D, Gauntt K, Schaffhausen C, McKinney W, Snyder JJ. OPTN/SRTR 2020 Annual Data Report: DOD. *American Journal of Transplantation*. 2022;22(S2):519-52.
5. Aufhauser DD, Foley DP. Beyond Ice and the Cooler: Machine Perfusion Strategies in Liver Transplantation. *Clinics in Liver Disease*. 2021;25(1):179-94.
6. Jing L, Yao L, Zhao M, Peng LP, Liu M. Organ preservation: From the past to the future. *Acta Pharmacologica Sinica*. 2018;39(5):845-57.
7. de Rougemont O, Lehmann K, Clavien P-A. Preconditioning, organ preservation, and postconditioning to prevent ischemia-reperfusion injury to the liver. *Liver Transplantation*. 2009;15(10):1172-82.
8. Moers C, Pirenne J, Paul A, Ploeg RJ. Machine perfusion or cold storage in deceased-donor kidney transplantation. *New England Journal of Medicine*. 2012;366(8):770-1.
9. Shimizu F, Okamoto O, Katagiri K, Fujiwara S, Wei FC. Prolonged ischemia increases severity of rejection in skin flap allotransplantation in rats. *Microsurgery*. 2010;30(2):132-7.
10. Eltzschig HK, Eckle T. Ischemia and reperfusion--from mechanism to translation. *Nat Med*. 2011;17(11):1391-401.
11. Ogawa S, Gerlach H, Esposito C, Pasagian-Macaulay A, Brett J, Stern D. Hypoxia modulates the barrier and coagulant function of cultured bovine endothelium. Increased monolayer permeability and induction of procoagulant properties. *The Journal of Clinical Investigation*. 1990;85(4):1090-8.
12. Eltzschig HK, Carmeliet P. Hypoxia and Inflammation. *New England Journal of Medicine*. 2011;364(7):656-65.

13. Krüger B, Krick S, Dhillon N, Lerner SM, Ames S, Bromberg JS, et al. Donor Toll-like receptor 4 contributes to ischemia and reperfusion injury following human kidney transplantation. *Proceedings of the National Academy of Sciences*. 2009;106(9):3390-5.
14. Chouchani ET, Pell VR, Gaude E, Aksentijević D, Sundier SY, Robb EL, et al. Ischaemic accumulation of succinate controls reperfusion injury through mitochondrial ROS. *Nature*. 2014;515(7527):431-5.
15. Jorch SK, Kubes P. An emerging role for neutrophil extracellular traps in noninfectious disease. *Nature Medicine*. 2017;23(3):279-87.
16. Huang H, Tohme S, Al-Khafaji AB, Tai S, Loughran P, Chen L, et al. Damage-associated molecular pattern-activated neutrophil extracellular trap exacerbates sterile inflammatory liver injury. *Hepatology*. 2015;62(2):600-14.
17. Lowe KC. Perfluorochemicals in Vascular Medicine. *Vascular Medicine Review*. 1994;vmr-5(1):15-32.
18. Ahrens ET, Zhong J. In vivo MRI cell tracking using perfluorocarbon probes and fluorine-19 detection. *NMR Biomed*. 2013;26(7):860-71.
19. Chapelin F, Capitini CM, Ahrens ET. Fluorine-19 MRI for detection and quantification of immune cell therapy for cancer. *Journal for ImmunoTherapy of Cancer*. 2018;6(1):105.
20. Chen J, Pan H, Lanza GM, Wickline SA. Perfluorocarbon Nanoparticles for Physiological and Molecular Imaging and Therapy. *Advances in Chronic Kidney Disease*. 2013;20(6):466-78.
21. Chen Q, Yu J, Kim K. Review: optically-triggered phase-transition droplets for photoacoustic imaging. *Biomedical Engineering Letters*. 2018;8(2):223-9.
22. Jirak D, Galisova A, Kolouchova K, Babuka D, Hruby M. Fluorine polymer probes for magnetic resonance imaging: quo vadis? *Magnetic Resonance Materials in Physics, Biology and Medicine*. 2019;32(1):173-85.
23. Rapoport N. Drug-Loaded Perfluorocarbon Nanodroplets for Ultrasound-Mediated Drug Delivery. *Adv Exp Med Biol*. 2016;880:221-41.
24. Srivastava AK, Kadayakkara DK, Bar-Shir A, Gilad AA, McMahon MT, Bulte JWM. Advances in using MRI probes and sensors for in vivo cell tracking as applied to regenerative medicine. *Disease Models & Mechanisms*. 2015;8(4):323-36.

25. Yu YB. Fluorinated dendrimers as imaging agents for ¹⁹F MRI. *WIREs Nanomedicine and Nanobiotechnology*. 2013;5(6):646-61.
26. Riess JG. Understanding the fundamentals of perfluorocarbons and perfluorocarbon emulsions relevant to in vivo oxygen delivery. *Artif Cells Blood Substit Immobil Biotechnol*. 2005;33(1):47-63.
27. Riess JG. Fluorous Materials for Biomedical Uses. In: Gladysz JA, Curran DP, Horvath IT, editors. *Handbook of Fluorous Chemistry*2005.
28. Ruiz-Cabello J, Barnett BP, Bottomley PA, Bulte JWM. Fluorine (¹⁹F) MRS and MRI in biomedicine. *NMR Biomed*. 2011;24(2):114-29.
29. Menon DK. Fluorine-19 MRS: General Overview and Anaesthesia. *Encyclopedia of Magnetic Resonance*2007.
30. Phillips LC, Puett C, Sheeran PS, Wilson Miller G, Matsunaga TO, Dayton PA. Phase-shift perfluorocarbon agents enhance high intensity focused ultrasound thermal delivery with reduced near-field heating. *J Acoust Soc Am*. 2013;134(2):1473-82.
31. Rapoport N, Gao Z, Kennedy A. Multifunctional nanoparticles for combining ultrasonic tumor imaging and targeted chemotherapy. *J Natl Cancer Inst*. 2007;99(14):1095-106.
32. Cabrales P, Friedman JM. HBOC vasoactivity: interplay between nitric oxide scavenging and capacity to generate bioactive nitric oxide species. *Antioxid Redox Signal*. 2013;18(17):2284-97.
33. Smith CR, Travis Parsons J, Zhu J, Spiess BD. The effect of intravenous perfluorocarbon emulsions on whole-body oxygenation after severe decompression sickness. *Diving Hyperbaric Med*. 2012;42(1):10-7.
34. Spahn DR. Blood substitutes artificial oxygen carriers: perfluorocarbon emulsions. *Critical Care*. 1999;3(5):R93-R7.
35. Spiess BD. Perfluorocarbon emulsions: One approach to intravenous artificial respiratory gas transport. *International Anesthesiology Clinics*. 1995;33(1):103-13.
36. Torres LN, Spiess BD, Torres Filho IP. Effects of perfluorocarbon emulsions on microvascular blood flow and oxygen transport in a model of severe arterial gas embolism. *J Surg Res*. 2014;187(1):324-33.

37. Herneisey M, Williams J, Mirtic J, Liu L, Potdar S, Bagia C, et al. Development and characterization of resveratrol nanoemulsions carrying dual-imaging agents. *Ther Deliv.* 2016;7(12):795-808.
38. Janjic JM, Shao P, Zhang S, Yang X, Patel SK, Bai M. Perfluorocarbon nanoemulsions with fluorescent, colloidal and magnetic properties. *Biomaterials.* 2014;35(18):4958-68.
39. Keipert PE, Otto S, Flaim SF, Weers JG, Schutt EA, Pelura TJ, et al. Influence of perflubron emulsion particle size on blood half-life and febrile response in rats. *Artif Cells Blood Substit Immobil Biotechnol.* 1994;22(4):1169-74.
40. Anton N, Vandamme TF. Nano-emulsions and micro-emulsions: clarifications of the critical differences. *Pharm Res.* 2011;28(5):978-85.
41. Fang J, Nakamura H, Maeda H. The EPR effect: Unique features of tumor blood vessels for drug delivery, factors involved, and limitations and augmentation of the effect. *Advanced Drug Delivery Reviews.* 2011;63(3):136-51.
42. Jahromi AH, Wang C, Adams SR, Zhu W, Narsinh K, Xu H, et al. Fluorous-Soluble Metal Chelate for Sensitive Fluorine-19 Magnetic Resonance Imaging Nanoemulsion Probes. *ACS Nano.* 2019;13(1):143-51.
43. Patrick MJ, Janjic JM, Teng H, O'Hear MR, Brown CW, Stokum JA, et al. Intracellular pH measurements using perfluorocarbon nanoemulsions. *J Am Chem Soc.* 2013;135(49):18445-57.
44. Patel SK, Patrick MJ, Pollock JA, Janjic JM. Two-color fluorescent (near-infrared and visible) triphasic perfluorocarbon nanoemulsions. *Journal of Biomedical Optics.* 2013;18(10):101312.
45. Hitchens TK, Ye Q, Eytan DF, Janjic JM, Ahrens ET, Ho C. ¹⁹F MRI detection of acute allograft rejection with in vivo perfluorocarbon labeling of immune cells. *Magn Reson Med.* 2011;65(4):1144-53.
46. Srinivas M, Turner MS, Janjic JM, Morel PA, Laidlaw DH, Ahrens ET. In vivo cytometry of antigen-specific t cells using ¹⁹F MRI. *Magn Reson Med.* 2009;62(3):747-53.
47. Jacoby C, Temme S, Mayenfels F, Benoit N, Krafft MP, Schubert R, et al. Probing different perfluorocarbons for in vivo inflammation imaging by ¹⁹F MRI: image reconstruction, biological half-lives and sensitivity. *NMR Biomed.* 2014;27(3):261-71.

48. Janjic JM, Srinivas M, Kadayakkara DKK, Ahrens ET. Self-delivering Nanoemulsions for Dual Fluorine-19 MRI and Fluorescence Detection. *Journal of the American Chemical Society*. 2008;130(9):2832-41.
49. Srinivas M, Heerschap A, Ahrens ET, Figdor CG, de Vries IJ. (19)F MRI for quantitative in vivo cell tracking. *Trends Biotechnol*. 2010;28(7):363-70.
50. Srinivas M, Morel PA, Ernst LA, Laidlaw DH, Ahrens ET. Fluorine-19 MRI for visualization and quantification of cell migration in a diabetes model. *Magnetic Resonance in Medicine*. 2007;58(4):725-34.
51. Balducci A, Wen Y, Zhang Y, Helfer BM, Hitchens TK, Meng WS, et al. A novel probe for the non-invasive detection of tumor-associated inflammation. *Oncoimmunology*. 2013;2(2):e23034.
52. Patel SK, Beaino W, Anderson CJ, Janjic JM. Theranostic nanoemulsions for macrophage COX-2 inhibition in a murine inflammation model. *Clin Immunol*. 2015;160(1):59-70.
53. Stoll G, Basse-Lusebrink T, Weise G, Jakob P. Visualization of inflammation using (19)F-magnetic resonance imaging and perfluorocarbons. *Wiley Interdiscip Rev Nanomed Nanobiotechnol*. 2012;4(4):438-47.
54. Weise G, Basse-Luesebrink TC, Wessig C, Jakob PM, Stoll G. In vivo imaging of inflammation in the peripheral nervous system by 19F MRI. *Experimental Neurology*. 2011;229(2):494-501.
55. Balducci A, Helfer BM, Ahrens ET, O'Hanlon CF, 3rd, Wesa AK. Visualizing arthritic inflammation and therapeutic response by fluorine-19 magnetic resonance imaging (19F MRI). *J Inflamm (Lond)*. 2012;9(1):24.
56. Zhong J, Narsinh K, Morel PA, Xu H, Ahrens ET. In Vivo Quantification of Inflammation in Experimental Autoimmune Encephalomyelitis Rats Using Fluorine-19 Magnetic Resonance Imaging Reveals Immune Cell Recruitment outside the Nervous System. *PLoS One*. 2015;10(10):e0140238.
57. Richard J-P, Hussain U, Gross S, Taga A, Kouser M, Almad A, et al. Perfluorocarbon Labeling of Human Glial-Restricted Progenitors for 19F Magnetic Resonance Imaging. *Stem Cells Translational Medicine*. 2019;8(4):355-65.
58. Helfer BM, Balducci A, Sadeghi Z, O'hanlon C, Hijaz A, Flask CA, et al. 19F MRI Tracer Preserves in Vitro and in Vivo Properties of Hematopoietic Stem Cells. *Cell Transplantation*. 2013;22(1):87-97.

59. Ahrens ET, Helfer BM, O'Hanlon CF, Schirda C. Clinical cell therapy imaging using a perfluorocarbon tracer and fluorine-19 MRI. *Magn Reson Med.* 2014;72(6):1696-701.
60. Zhao D, Jiang L, P. Mason R. Measuring Changes in Tumor Oxygenation. *Methods in enzymology.* 386: Academic Press; 2004. p. 378-418.
61. Liu L, Bagia C, Janjic JM. The First Scale-Up Production of Theranostic Nanoemulsions. *Biores Open Access.* 2015;4(1):218-28.
62. Jamieson RW, Friend PJ. Organ reperfusion and preservation. *Front Biosci.* 2008;13:221-35.
63. Hameed AM, Hawthorne WJ, Pleass HC. Advances in organ preservation for transplantation. *ANZ J Surg.* 2016.
64. Kallenborn-Gerhardt W, Hohmann SW, Syhr KM, Schroder K, Sisignano M, Weigert A, et al. Nox2-dependent signaling between macrophages and sensory neurons contributes to neuropathic pain hypersensitivity. *Pain.* 2014;155(10):2161-70.
65. Zuidema MY, Zhang C. Ischemia/reperfusion injury: The role of immune cells. *World J Cardiol.* 2010;2(10):325-32.
66. Nishikawa H, Manek S, Barnett SS, Charlett A, Green CJ. Pathology of warm ischaemia and reperfusion injury in adipomusculocutaneous flaps. *Int J Exp Pathol.* 1993;74(1):35-44.
67. Bon D, Delpech PO, Chatauret N, Hauet T, Badet L, Barrou B. Does machine perfusion decrease ischemia reperfusion injury? *Progres en Urologie.* 2014;24(SUPPL.1):S44-S50.
68. Gorantla VS, Davis MR. Vascularized Composite Allograft Preservation: Ubi Sumus? *Transplantation.* 2017;101(3):469-70.
69. Tripathy S, Das S. Strategies for organ preservation: Current prospective and challenges. *Cell Biology International.* 2023;47(3):520-38.
70. Mulligan DC, Reddy KS, Moss Jr AA. New preservation solutions for use in liver transplantation. *Current Opinion in Organ Transplantation.* 2004;9(2):159-62.
71. Jahania MS, Sanchez JA, Narayan P, Lasley RD, Mentzer RM, Jr. Heart preservation for transplantation: principles and strategies. *The Annals of Thoracic Surgery.* 1999;68(5):1983-7.
72. Chen Y, Shi J, Xia TC, Xu R, He X, Xia Y. Preservation Solutions for Kidney Transplantation: History, Advances and Mechanisms. *Cell Transplantation.* 2019;28(12):1472-89.

73. Chen F, Nakamura T, Wada H. Development of New Organ Preservation Solutions in Kyoto University. *Yonsei Med J.* 2004;45(6):1107-14.
74. Omasa M, Hasegawa S, Bando T, Hanaoka N, Yoshimura T, Nakamura T, et al. Application of ET-Kyoto solution in clinical lung transplantation. *The Annals of Thoracic Surgery.* 2004;77(1):338-9.
75. Ostróзка-Cieslik A, Dolinska B, Ryszka F. Tips for optimizing organ preservation solutions. *Acta Biochimica Polonica.* 2018;65(1):9-15.
76. Fard A, Pearson R, Lathan R, Mark PB, Clancy MJ. Perfusate Composition and Duration of Ex-Vivo Normothermic Perfusion in Kidney Transplantation: A Systematic Review. *Transpl Int.* 2022;35:10236.
77. Aburawi MM, Fontan FM, Karimian N, Eymard C, Cronin S, Pendexter C, et al. Synthetic hemoglobin-based oxygen carriers are an acceptable alternative for packed red blood cells in normothermic kidney perfusion. *American Journal of Transplantation.* 2019;19(10):2814-24.
78. Ravikumar R, Jassem W, Mergental H, Heaton N, Mirza D, Perera MTPR, et al. Liver Transplantation After Ex Vivo Normothermic Machine Preservation: A Phase 1 (First-in-Man) Clinical Trial. *American Journal of Transplantation.* 2016;16(6):1779-87.
79. Husen P, Boffa C, Jochmans I, Krikke C, Davies L, Mazilescu L, et al. Oxygenated End-Hypothermic Machine Perfusion in Expanded Criteria Donor Kidney Transplant: A Randomized Clinical Trial. *JAMA Surgery.* 2021;156(6):517-25.
80. van Rijn R, Karimian N, Matton APM, Burlage LC, Westerkamp AC, van den Berg AP, et al. Dual hypothermic oxygenated machine perfusion in liver transplants donated after circulatory death. *British Journal of Surgery.* 2017;104(7):907-17.
81. Matton APM, Burlage LC, van Rijn R, de Vries Y, Karangwa SA, Nijsten MW, et al. Normothermic machine perfusion of donor livers without the need for human blood products. *Liver Transpl.* 2018;24(4):528-38.
82. Laing RW, Bhogal RH, Wallace L, Boteon Y, Neil DAH, Smith A, et al. The Use of an Acellular Oxygen Carrier in a Human Liver Model of Normothermic Machine Perfusion. *Transplantation.* 2017;101(11):2746-56.
83. Muir WW, Wellman ML. Hemoglobin solutions and tissue oxygenation. *J Vet Intern Med.* 2003;17(2):127-35.

84. Cabrales P, Intaglietta M. Blood substitutes: evolution from noncarrying to oxygen- and gas-carrying fluids. *ASAIO J.* 2013;59(4):337-54.
85. Lalla FR, Ning J, Chang TMS. Effects of Pyridoxalated Polyhemoglobin and Stroma-Free Hemoglobin on ADP-Induced Platelet Aggregation. *Biomaterials, Artificial Cells and Artificial Organs.* 1989;17(3):363-9.
86. Zhu H, Du Q, Chen C, Chang TMS. The Immunological Properties of Stroma-free Polyhemolysate Containing Catalase and Superoxide Dismutase Activities Prepared by Polymerized Bovine Stroma-free Hemolysate. *Artificial Cells, Blood Substitutes, and Biotechnology.* 2010;38(2):57-63.
87. Marcus AJ, Broekman MJ. Cell-Free Hemoglobin as an Oxygen Carrier Removes Nitric Oxide, Resulting in Defective Thromboregulation. *Circulation.* 1996;93(2):208-9.
88. Rafikova O, Sokolova E, Rafikov R, Nudler E. Control of plasma nitric oxide bioactivity by perfluorocarbons: physiological mechanisms and clinical implications. *Circulation.* 2004;110(23):3573-80.
89. Turick CE, Bulmer DK. Enhanced reduction of nitrous oxide by *Pseudomonas denitrificans* with perfluorocarbons. *Biotechnology Letters.* 1998;20(2):123-5.
90. Riess JG. Oxygen carriers ("blood substitutes")--raison d'etre, chemistry, and some physiology. *Chem Rev.* 2001;101(9):2797-920.
91. Clark LC, Jr., Gollan F. Survival of mammals breathing organic liquids equilibrated with oxygen at atmospheric pressure. *Science.* 1966;152(3730):1755-6.
92. Castro CI, Briceno JC. Perfluorocarbon-based oxygen carriers: review of products and trials. *Artif Organs.* 2010;34(8):622-34.
93. Vercellotti GM, Hammerschmidt DE, Craddock PR, Jacob HS. Activation of plasma complement by perfluorocarbon artificial blood: probable mechanism of adverse pulmonary reactions in treated patients and rationale for corticosteroids prophylaxis. *Blood.* 1982;59(6):1299-304.
94. Millard RW. Oxygen solubility, rheology and hemodynamics of perfluorocarbon emulsion blood substitutes. *Artif Cells Blood Substit Immobil Biotechnol.* 1994;22(2):235-44.
95. Kozhura VL, Basarab DA, Timkina MI, Golubev AM, Reshetnyak VI, Moroz VV. Reperfusion injury after critical intestinal ischemia and its correction with perfluorochemical emulsion "perftoran". *World J Gastroenterol.* 2005;11(45):7084-90.

96. Paxian M, Keller SA, Huynh TT, Clemens MG. Perflubron emulsion improves hepatic microvascular integrity and mitochondrial redox state after hemorrhagic shock. *Shock*. 2003;20(5):449-57.
97. Kuznetsova IN. Perfluorocarbon emulsions: stability in vitro and in vivo (a review). *Pharmaceutical Chemistry Journal*. 2003;37(8):415-20.
98. Flaim SF. Pharmacokinetics and side effects of perfluorocarbon-based blood substitutes. *Artif Cells Blood Substit Immobil Biotechnol*. 1994;22(4):1043-54.
99. Niiler E. Setbacks for blood substitute companies. *Nature Biotechnology*. 2002;20(10):962-3.
100. Cabrales P, Tsai AG, Intaglietta M. Perfluorocarbon in Microcirculation During Ischemia Reperfusion. *Journal of the American College of Surgeons*. 2007;204(2):225-35.
101. Cyna A, Yang Z-j, Price CD, Bosco G, Tucci M, El-Badri NS, et al. The Effect of Isovolemic Hemodilution with Oxycyte®, a Perfluorocarbon Emulsion, on Cerebral Blood Flow in Rats. *PLoS ONE*. 2008;3(4).
102. Zhou Z, Sun D, Levasseur JE, Merenda A, Hamm RJ, Zhu J, et al. Perfluorocarbon emulsions improve cognitive recovery after lateral fluid percussion brain injury in rats. *Neurosurgery*. 2008;63(4):799-806; discussion -7.
103. Haque A, Scultetus AH, Arnaud F, Dickson LJ, Chun S, McNamee G, et al. The Emulsified PFC Oxycyte((R)) Improved Oxygen Content and Lung Injury Score in a Swine Model of Oleic Acid Lung Injury (OALI). *Lung*. 2016;194(6):945-57.
104. Shi G, Coger RN. Use of perfluorocarbons to enhance the performance of perfused three-dimensional hepatic cultures. *Biotechnology Progress*. 2013;29(3):718-26.
105. Deuchar GA, Brennan D, Holmes WM, Shaw M, Macrae IM, Santosh C. Perfluorocarbon enhanced Glasgow Oxygen Level Dependent (GOLD) magnetic resonance metabolic imaging identifies the penumbra following acute ischemic stroke. *Theranostics*. 2018;8(6):1706-22.
106. Demchenko IT, Mahon RT, Allen BW, Piantadosi CA. Brain oxygenation and CNS oxygen toxicity after infusion of perfluorocarbon emulsion. *J Appl Physiol*. 2012;113(2):224-31.
107. Torres Filho IP, Pedro JRP, Narayanan SV, Nguyen NM, Roseff SD, Spiess BD. Perfluorocarbon emulsion improves oxygen transport of normal and sickle cell human blood in vitro. *J Biomed Mater Res Part A*. 2014;102(7):2105-15.

108. Helmi N, Andrew PW, Pandya HC. Perfluorocarbon emulsion therapy attenuates pneumococcal infection in sickle cell mice. *J Infect Dis.* 2015;211(10):1677-85.
109. Abutarboush R, Mullah SH, Saha BK, Haque A, Walker PB, Aligbe C, et al. Brain oxygenation with a non-vasoactive perfluorocarbon emulsion in a rat model of traumatic brain injury. *Microcirculation.* 2018;25(3).
110. Spiess BD, Zhu J, Pierce B, Weis R, Berger BE, Reses J, et al. Effects of perfluorocarbon infusion in an anesthetized swine decompression model. *J Surg Res.* 2009;153(1):83-94.
111. Gale SC, Gorman GD, Copeland JG, McDonagh PF. Perflubron Emulsion Prevents PMN Activation and Improves Myocardial Functional Recovery After Cold Ischemia and Reperfusion. *J Surg Res.* 2007;138(1):135-40.
112. Nolte D, Pickelmann S, Lang M, Keipert P, Messmer K. Compatibility of different colloid plasma expanders with perflubron emulsion: an intravital microscopic study in the hamster. *Anesthesiology.* 2000;93(5):1261-70.
113. Radisic M, Deen W, Langer R, Vunjak-Novakovic G. Mathematical model of oxygen distribution in engineered cardiac tissue with parallel channel array perfused with culture medium containing oxygen carriers. *Am J Physiol Heart Circ Physiol.* 2005;288(3):H1278-89.
114. Tan Q, El-Badry AM, Contaldo C, Steiner R, Hillinger S, Welte M, et al. The effect of perfluorocarbon-based artificial oxygen carriers on tissue-engineered trachea. *Tissue Eng Part A.* 2009;15(9):2471-80.
115. Noveck RJ, Shannon EJ, Leese PT, Shorr JS, Flaim KE, Keipert PE, et al. Randomized safety studies of intravenous perflubron emulsion. II. Effects on immune function in healthy volunteers. *Anesth Analg.* 2000;91(4):812-22.
116. Spahn DR, Waschke KF, Standl T, Motsch J, Van Huynegem L, Welte M, et al. Use of perflubron emulsion to decrease allogeneic blood transfusion in high-blood-loss non-cardiac surgery: results of a European phase 3 study. *Anesthesiology.* 2002;97(6):1338-49.
117. Zhuang J, Ying M, Spiekermann K, Holay M, Zhang Y, Chen F, et al. Biomimetic Nanoemulsions for Oxygen Delivery In Vivo. *Advanced Materials.* 2018;30(49):1804693.
118. Bialas C, Moser C, Sims CA. Artificial Oxygen Carriers and Red Blood Cell Substitutes: An Historic Overview and Recent Developments Toward Military and Clinical Relevance. *J Trauma Acute Care Surg.* 2019.
119. Wooster TJ, Golding M, Sanguansri P. Impact of Oil Type on Nanoemulsion Formation and Ostwald Ripening Stability. *Langmuir.* 2008;24(22):12758-65.

120. Tadros T, Izquierdo P, Esquena J, Solans C. Formation and stability of nano-emulsions. *Advances in Colloid and Interface Science*. 2004;108–109:303-18.
121. Davis SS, Round HP, Purewal TS. Ostwald ripening and the stability of emulsion systems: an explanation for the effect of an added third component. *Journal of Colloid and Interface Science*. 1981;80(2):508-11.
122. Ren H, Liu J, Li Y, Wang H, Ge S, Yuan A, et al. Oxygen self-enriched nanoparticles functionalized with erythrocyte membranes for long circulation and enhanced phototherapy. *Acta Biomater*. 2017;59:269-82.
123. Vorob'ev SI, Moiseenko OM, Belyaev BL, Srednyakov VA, Luzganov YV. Colloid-chemical and medico-biological characteristics of the perfluorocarbon Ftoemulsion III. *Pharmaceutical Chemistry Journal*. 2009;43(5):267.
124. Fraker CA, Mendez AJ, Inverardi L, Ricordi C, Stabler CL. Optimization of perfluoro nano-scale emulsions: The importance of particle size for enhanced oxygen transfer in biomedical applications. *Colloids and Surfaces B: Biointerfaces*. 2012;98:26-35.
125. Freire MG, Dias AMA, Coutinho JAP, Coelho MAZ, Marrucho IM. Enzymatic method for determining oxygen solubility in perfluorocarbon emulsions. *Fluid Phase Equilibria*. 2005;231(1):109-13.
126. Engelman RM, Rousou JH, Dobbs WA. Fluosol-DA: an artificial blood for total cardiopulmonary bypass. *Ann Thorac Surg*. 1981;32(6):528-35.
127. Yu P, Han X, Yin L, Hui K, Guo Y, Yuan A, et al. Artificial Red Blood Cells Constructed by Replacing Heme with Perfluorodecalin for Hypoxia-Induced Radioresistance. *ADVANCED THERAPEUTICS*. 2019;2(6):1900031.
128. Zhou Z, Zhang B, Wang H, Yuan A, Hu Y, Wu J, et al. Two-stage oxygen delivery for enhanced radiotherapy by perfluorocarbon nanoparticles. *Theranostics*. 2018;8(18):4898-911.
129. Benjamin S, Sheyn D, Ben-David S, Oh A, Kallai I, Li N, et al. Oxygenated environment enhances both stem cell survival and osteogenic differentiation. *Tissue Eng Part A*. 2013;19(5-6):748-58.
130. Goh F, Gross JD, Simpson NE, Sambanis A. Limited beneficial effects of perfluorocarbon emulsions on encapsulated cells in culture: experimental and modeling studies. *J Biotechnol*. 2010;150(2):232-9.

131. Ma T, Wang Y, Qi F, Zhu S, Huang L, Liu Z, et al. The effect of synthetic oxygen carrier-enriched fibrin hydrogel on Schwann cells under hypoxia condition in vitro. *Biomaterials*. 2013;34(38):10016-27.
132. Song X, Feng L, Liang C, Yang K, Liu Z. Ultrasound Triggered Tumor Oxygenation with Oxygen-Shuttle Nanoperfluorocarbon to Overcome Hypoxia-Associated Resistance in Cancer Therapies. *Nano Lett*. 2016.
133. Wang YG, Kim H, Mun S, Kim D, Choi Y. Indocyanine green-loaded perfluorocarbon nanoemulsions for bimodal (19)F-magnetic resonance/nearinfrared fluorescence imaging and subsequent phototherapy. *Quant Imaging Med Surg*. 2013;3(3):132-40.
134. Lorton O, Hyacinthe J-N, Desgranges S, Gui L, Klauser A, Celicanin Z, et al. Molecular oxygen loading in candidate theranostic droplets stabilized with biocompatible fluorinated surfactants: Particle size effect and application to in situ ¹⁹F MRI mapping of oxygen partial pressure. *Journal of Magnetic Resonance*. 2018;295:27-37.
135. Yao Y, Zhang M, Liu T, Zhou J, Gao Y, Wen Z, et al. Perfluorocarbon-Encapsulated PLGA-PEG Emulsions as Enhancement Agents for Highly Efficient Reoxygenation to Cell and Organism. *ACS Appl Mater Interfaces*. 2015;7(33):18369-78.
136. Janjic JM, Vasudeva K, Saleem M, Stevens A, Liu L, Patel S, et al. Low-dose NSAIDs reduce pain via macrophage targeted nanoemulsion delivery to neuroinflammation of the sciatic nerve in rat. *J Neuroimmunol*. 2018;318:72-9.
137. Patel SK, Williams J, Janjic JM. Cell Labeling for ¹⁹F MRI: New and Improved Approach to Perfluorocarbon Nanoemulsion Design. *Biosensors (Basel)*. 2013;3(3):341-59.
138. Lambert E, Janjic JM. Multiple linear regression applied to predicting droplet size of complex perfluorocarbon nanoemulsions for biomedical applications. *Pharm Dev Technol*. 2019;24(6):1-11.
139. Pharmaceutical Development Q8(R2): U.S. Food and Drug Administration; 2009 [Available from: Available from https://www.ich.org/fileadmin/Public_Web_Site/ICH_Products/Guidelines/Quality/Q8_R1/Step4/Q8_R2_Guideline.pdf.
140. Collins PC. Chemical engineering and the culmination of quality by design in pharmaceuticals. *AIChE Journal*. 2018;64(5):1502-10.
141. Johnson AS, Fisher RJ, Weir GC, Colton CK. Oxygen consumption and diffusion in assemblages of respiring spheres: Performance enhancement of a bioartificial pancreas. *Chemical Engineering Science*. 2009;64(22):4470-87.

142. Polizzotti BD, Thomson LM, O'Connell DW, McGowan FX, Kheir JN. Optimization and characterization of stable lipid-based, oxygen-filled microbubbles by mixture design. *J Biomed Mater Res B Appl Biomater*. 2014;102(6):1148-56.
143. Tripathi CB, Parashar P, Arya M, Singh M, Kanoujia J, Kaithwas G, et al. QbD-based development of α -linolenic acid potentiated nanoemulsion for targeted delivery of doxorubicin in DMBA-induced mammary gland carcinoma: in vitro and in vivo evaluation. *Drug Delivery and Translational Research*. 2018.
144. Nagi A, Iqbal B, Kumar S, Sharma S, Ali J, Baboota S. Quality by design based silymarin nanoemulsion for enhancement of oral bioavailability. *Journal of Drug Delivery Science and Technology*. 2017;40:35-44.
145. Đorđević SM, Cekić ND, Savić MM, Isailović TM, Randelović DV, Marković BD, et al. Parenteral nanoemulsions as promising carriers for brain delivery of risperidone: Design, characterization and in vivo pharmacokinetic evaluation. *International Journal of Pharmaceutics*. 2015;493(1–2):40-54.
146. Rahman Z, Xu X, Katragadda U, Krishnaiah YSR, Yu L, Khan MA. Quality by Design Approach for Understanding the Critical Quality Attributes of Cyclosporine Ophthalmic Emulsion. *Molecular Pharmaceutics*. 2014;11(3):787-99.
147. Herneisey M, Lambert E, Kachel A, Shychuck E, Drennen JK, 3rd, Janjic JM. Quality by Design Approach Using Multiple Linear and Logistic Regression Modeling Enables Microemulsion Scale Up. *Molecules*. 2019;24(11).
148. Critical Path Opportunities Initiated During 2006 2006 [Available from: Available from <http://wayback.archive-it.org/7993/20180125142843/https://www.fda.gov/ScienceResearch/SpecialTopics/CriticalPathInitiative/CriticalPathOpportunitiesReports/ucm077251.htm>].
149. Challenge and Opportunity on the Critical Path to New Medical Products: U.S. Food and Drug Administration; 2004 [Available from: Available from <http://wayback.archive-it.org/7993/20180125035500/https://www.fda.gov/downloads/ScienceResearch/SpecialTopics/CriticalPathInitiative/CriticalPathOpportunitiesReports/UCM113411.pdf>].
150. Kaur R, Garg T, Das Gupta U, Gupta P, Rath G, Goyal AK. Preparation and characterization of spray-dried inhalable powders containing nanoaggregates for pulmonary delivery of anti-tubercular drugs. *Artificial cells, nanomedicine, and biotechnology*. 2015:1-6.
151. Grapentin C, Barnert S, Schubert R. Monitoring the Stability of Perfluorocarbon Nanoemulsions by Cryo-TEM Image Analysis and Dynamic Light Scattering. *PLOS ONE*. 2015;10(6):e0130674.

152. Aqil M, Kamran M, Ahad A, Imam SS. Development of clove oil based nanoemulsion of olmesartan for transdermal delivery: Box–Behnken design optimization and pharmacokinetic evaluation. *Journal of Molecular Liquids*. 2016;214:238-48.
153. Pund S, Shete Y, Jagadale S. Multivariate analysis of physicochemical characteristics of lipid based nanoemulsifying cilostazol—Quality by design. *Colloids and Surfaces B: Biointerfaces*. 2014;115:29-36.
154. Amani A, York P, Chrystyn H, Clark BJ. Factors Affecting the Stability of Nanoemulsions—Use of Artificial Neural Networks. *Pharmaceutical Research*. 2009;27(1):37.
155. Wang W, Sedykh A, Sun H, Zhao L, Russo DP, Zhou H, et al. Predicting Nano–Bio Interactions by Integrating Nanoparticle Libraries and Quantitative Nanostructure Activity Relationship Modeling. *ACS Nano*. 2017;11(12):12641-9.
156. Epa VC, Burden FR, Tassa C, Weissleder R, Shaw S, Winkler DA. Modeling biological activities of nanoparticles. *Nano Lett*. 2012;12(11):5808-12.
157. Shaw SY, Westly EC, Pittet MJ, Subramanian A, Schreiber SL, Weissleder R. Perturbational profiling of nanomaterial biologic activity. *Proc Natl Acad Sci U S A*. 2008;105(21):7387-92.
158. McClements DJ. Nanoemulsions versus microemulsions: Terminology, differences, and similarities. *Soft Matter*. 2012;8(6):1719-29.
159. Shakeel F, Shafiq S, Haq N, Alanazi FK, Alsarra IA. Nanoemulsions as potential vehicles for transdermal and dermal delivery of hydrophobic compounds: an overview. *Expert Opin Drug Deliv*. 2012;9(8):953-74.
160. Kotta S, Khan AW, Pramod K, Ansari SH, Sharma RK, Ali J. Exploring oral nanoemulsions for bioavailability enhancement of poorly water-soluble drugs. *Expert Opin Drug Deliv*. 2012;9(5):585-98.
161. McClements DJ, Rao J. Food-grade nanoemulsions: formulation, fabrication, properties, performance, biological fate, and potential toxicity. *Critical reviews in food science and nutrition*. 2011;51(4):285-330.
162. Rajpoot P, Pathak K, Bali V. Therapeutic applications of nanoemulsion based drug delivery systems: a review of patents in last two decades. *Recent patents on drug delivery & formulation*. 2011;5(2):163-72.
163. Sarker DK. Engineering of nanoemulsions for drug delivery. *Curr Drug Deliv*. 2005;2(4):297-310.

164. Mitri K, Vauthier C, Huang N, Menas A, Ringard-Lefebvre C, Anselmi C, et al. Scale-up of nanoemulsion produced by emulsification and solvent diffusion. *J Pharm Sci*. 2012;101(11):4240-7.
165. Muller RH, Harden D, Keck CM. Development of industrially feasible concentrated 30% and 40% nanoemulsions for intravenous drug delivery. *Drug Dev Ind Pharm*. 2012;38(4):420-30.
166. Kim HW, Greenburg AG. Toward 21st century blood component replacement therapeutics: artificial oxygen carriers, platelet substitutes, recombinant clotting factors, and others. *Artif Cells Blood Substit Immobil Biotechnol*. 2006;34(6):537-50.
167. Kim HW, Greenburg AG. Artificial oxygen carriers as red blood cell substitutes: a selected review and current status. *Artif Organs*. 2004;28(9):813-28.
168. Lowe KC. Perfluorinated blood substitutes and artificial oxygen carriers. *Blood Reviews*. 1999;13(3):171-84.
169. Kadayakkara DK, Beatty PL, Turner MS, Janjic JM, Ahrens ET, Finn OJ. Inflammation driven by overexpression of the hypoglycosylated abnormal mucin 1 (MUC1) links inflammatory bowel disease and pancreatitis. *Pancreas*. 2010;39(4):510-5.
170. Boissenot T, Fattal E, Bordat A, Houvenagel S, Valette J, Chacun H, et al. Paclitaxel-loaded PEGylated nanocapsules of perfluorooctyl bromide as theranostic agents. *Eur J Pharm Biopharm*. 2016;108:136-44.
171. Rapoport N, Nam KH, Gupta R, Gao Z, Mohan P, Payne A, et al. Ultrasound-mediated tumor imaging and nanotherapy using drug loaded, block copolymer stabilized perfluorocarbon nanoemulsions. *J Control Release*. 2011;153(1):4-15.
172. Lanza GM, Winter PM, Caruthers SD, Hughes MS, Hu G, Schmieder AH, et al. Theragnostics for tumor and plaque angiogenesis with perfluorocarbon nanoemulsions. *Angiogenesis*. 2010;13(2):189-202.
173. Patel SK, Zhang Y, Pollock JA, Janjic JM. Cyclooxygenase-2 inhibiting perfluoropoly (ethylene glycol) ether theranostic nanoemulsions-in vitro study. *PLoS One*. 2013;8(2):e55802.
174. Dewitte H, Geers B, Liang S, Himmelreich U, Demeester J, De Smedt SC, et al. Design and evaluation of theranostic perfluorocarbon particles for simultaneous antigen-loading and ¹⁹F-MRI tracking of dendritic cells. *Journal of Controlled Release*. 2013;169(1):141-9.
175. Chen X. Introducing *Theranostics Journal* - From the Editor-in-Chief. *Theranostics*. 2011;1:1-2.

176. Winter PM, Schmieder AH, Caruthers SD, Keene JL, Zhang H, Wickline SA, et al. Minute dosages of alpha(nu)beta3-targeted fumagillin nanoparticles impair Vx-2 tumor angiogenesis and development in rabbits. *FASEB J.* 2008;22(8):2758-67.
177. Lanza GM, Yu X, Winter PM, Abendschein DR, Karukstis KK, Scott MJ, et al. Targeted antiproliferative drug delivery to vascular smooth muscle cells with a magnetic resonance imaging nanoparticle contrast agent: implications for rational therapy of restenosis. *Circulation.* 2002;106(22):2842-7.
178. Cyrus T, Zhang H, Allen JS, Williams TA, Hu G, Caruthers SD, et al. Intramural delivery of rapamycin with alpha(nu)beta3-targeted paramagnetic nanoparticles inhibits stenosis after balloon injury. *Arterioscler Thromb Vasc Biol.* 2008;28(5):820-6.
179. Patel SK, Janjic JM. Macrophage targeted theranostics as personalized nanomedicine strategies for inflammatory diseases. *Theranostics.* 2015;5(2):150-72.
180. Patel SK. Macrophage COX-2 as a target for imaging and therapy of inflammatory diseases using theranostic nanoemulsions [PhD]. ProQuest: Duquesne University; 2015.
181. Mountain GA, Jelier BJ, Bagia C, Friesen CM, Janjic JM. Design and formulation of nanoemulsions using 2-(poly(hexafluoropropylene oxide)) perfluoropropyl benzene in combination with linear perfluoro(polyethylene glycol dimethyl ether). *J Fluor Chem.* 2014;162:38-44.
182. O'Hanlon CE, Amede KG, O'Hear MR, Janjic JM. NIR-labeled perfluoropolyether nanoemulsions for drug delivery and imaging. *J Fluor Chem.* 2012;137:27-33.
183. Ikomi F, Hanna GK, Schmid-Schönbein GW. Size- and surface-dependent uptake of colloid particles into the lymphatic system. *Lymphology.* 1999;32(3):90-102.
184. Krafft MP, Riess JG. Highly fluorinated amphiphiles and colloidal systems, and their applications in the biomedical field. A contribution. *Biochimie.* 1998;80(5-6):489-514.
185. Onodera T, Kuriyama I, Andoh T, Ichikawa H, Sakamoto Y, Lee-Hiraiwa E, et al. Influence of particle size on the in vitro and in vivo anti-inflammatory and anti-allergic activities of a curcumin lipid nanoemulsion. *Int J Mol Med.* 2015;35(6):1720-8.
186. He C, Hu Y, Yin L, Tang C, Yin C. Effects of particle size and surface charge on cellular uptake and biodistribution of polymeric nanoparticles. *Biomaterials.* 2010;31(13):3657-66.
187. Tsuda Y, Yamanouchi K, Okamoto H, Yokoyama K, Heldebrant C. Intravascular behavior of a perfluorochemical emulsion. *J Pharmacobiodyn.* 1990;13(3):165-71.

188. Klang V, Valenta C. Lecithin-based nanoemulsions. *Journal of Drug Delivery Science and Technology*. 2011;21(1):55-76.
189. Freire MG, Dias AMA, Coelho MAZ, Coutinho JAP, Marrucho IM. Aging mechanisms of perfluorocarbon emulsions using image analysis. *Journal of Colloid and Interface Science*. 2005;286(1):224-32.
190. Hannah A, Luke G, Wilson K, Homan K, Emelianov S. Indocyanine Green-Loaded Photoacoustic Nanodroplets: Dual Contrast Nanoconstructs for Enhanced Photoacoustic and Ultrasound Imaging. *ACS Nano*. 2014;8(1):250-9.
191. Eriksson L, Johansson E, Wikström C. Mixture design - Design generation, PLS analysis, and model usage. *Chemometrics and Intelligent Laboratory Systems*. 1998;43(1-2):1-24.
192. Janjic JM, Ahrens ET. Fluorine-containing nanoemulsions for MRI cell tracking. *Wiley Interdiscip Rev Nanomed Nanobiotechnol*. 2009;1(5):492-501.
193. Krafft MP, Riess JG. Chemistry, physical chemistry, and uses of molecular fluorocarbon-hydrocarbon diblocks, triblocks, and related compounds--unique "apolar" components for self-assembled colloid and interface engineering. *Chem Rev*. 2009;109(5):1714-92.
194. Krafft MP, Riess JG. Selected physicochemical aspects of poly- and perfluoroalkylated substances relevant to performance, environment and sustainability-part one. *Chemosphere*. 2015;129:4-19.
195. Riess JG, Krafft MP. Fluorinated materials for in vivo oxygen transport (blood substitutes), diagnosis and drug delivery. *Biomaterials*. 1998;19(16):1529-39.
196. Riess JG. Fluorous micro- and nanophases with a biomedical perspective. *Tetrahedron*. 2002;58(20):4113-31.
197. Patel V, Agrawal Y. Nanosuspension: An approach to enhance solubility of drugs. *Journal of Advanced Pharmaceutical Technology & Research*. 2011;2(2):81-7.
198. Weers JG, Arlauskas RA, Tarara TE, Pelura TJ. Characterization of fluorocarbon-in-water emulsions with added triglyceride. *Langmuir*. 2004;20(18):7430-5.
199. Kaufman RJ, Richard TJ, inventors Emulsions of highly fluorinated organic compounds. US patent US5171755A. 1992.
200. Schweighardt FK, Kayhart CR, inventors Concentrated stable fluorochemical aqueous emulsions containing triglycerides U.S. patent US4895876A. 1990.

201. Snee RD, Hoerl RW, Bucci G. A statistical engineering strategy for mixture problems with process variables. *Quality Engineering*. 2016;28(3):263-79.
202. Ferenz KB, Steinbicker AU. Artificial oxygen carriers—past, present, and future—a review of the most innovative and clinically relevant concepts. *Journal of Pharmacology and Experimental Therapeutics*. 2019;369(2):300-10.
203. Lowe KC. Fluorinated blood substitutes and oxygen carriers. *Journal of Fluorine Chemistry*. 2001;109(1):59-65.
204. Chen JY, Scerbo M, Kramer G. A review of blood substitutes: examining the history, clinical trial results, and ethics of hemoglobin-based oxygen carriers. *Clinics (Sao Paulo)*. 2009;64(8):803-13.
205. Benitez Cardenas AS, Samuel PP, Olson JS. Current Challenges in the Development of Acellular Hemoglobin Oxygen Carriers by Protein Engineering. *Shock*. 2019;52(1S):28-40.
206. Lowe KC. Perfluorochemical respiratory gas carriers: benefits to cell culture systems. *Journal of Fluorine Chemistry*. 2002;118(1):19-26.
207. Ju LK, Lee JF, Armiger WB. Enhancing oxygen transfer in bioreactors by perfluorocarbon emulsions. *Biotechnology Progress*. 1991;7(4):323-9.
208. Elibol M, Mavituna F. Effect of perfluorodecalin as an oxygen carrier on actinorhodin production by *Streptomyces coelicolor* A3(2). *Appl Microbiol Biotechnol*. 1995;43(2):206-10.
209. McMillan JD, Wang DI. Enhanced oxygen transfer using oil-in-water dispersions. *Ann N Y Acad Sci*. 1987;506:569-82.
210. Davis SC, Cazzaniga AL, Ricotti C, Zalesky P, Hsu LC, Creech J, et al. Topical oxygen emulsion: a novel wound therapy. *Arch Dermatol*. 2007;143(10):1252-6.
211. Li J, Zhang Y-P, Zarei M, Zhu L, Sierra JO, Mertz PM, et al. A topical aqueous oxygen emulsion stimulates granulation tissue formation in a porcine second-degree burn wound. *Burns*. 2015;41(5):1049-57.
212. Bezinover D, Ramamoorthy S, Uemura T, Kadry Z, McQuillan PM, Mets B, et al. Use of a Third-Generation Perfluorocarbon for Preservation of Rat DCD Liver Grafts. *J Surg Res*. 2012;175(1):131-7.
213. Mohan C, Gennaro M, Marini C, Ascer E. Reduction of the extent of ischemic skeletal muscle necrosis by perfusion with oxygenated perfluorocarbon. *Am J Surg*. 1992;164(3):194-8.

214. Segel LD, Follette DM, Iguidbashian JP, Contino JP, Castellanos LM, Berkoff HA, et al. Posttransplantation function of hearts preserved with fluorochemical emulsion. *J Heart Lung Transplant*. 1994;13(4):669-80.
215. Mayer D, Ferenz KB. Perfluorocarbons for the treatment of decompression illness: how to bridge the gap between theory and practice. *European Journal of Applied Physiology*. 2019;119(11-12):2421-33.
216. Lambert E, Gorantla VS, Janjic JM. Pharmaceutical design and development of perfluorocarbon nanocolloids for oxygen delivery in regenerative medicine. *Nanomedicine (Lond)*. 2019;14(20):2697-712.
217. Cunha S, Costa CP, Moreira JN, Sousa Lobo JM, Silva AC. Using the quality by design (QbD) approach to optimize formulations of lipid nanoparticles and nanoemulsions: A review. *Nanomedicine: Nanotechnology, Biology, and Medicine*. 2020;28.
218. Grangeia HB, Silva C, Simões SP, Reis MS. Quality by design in pharmaceutical manufacturing: A systematic review of current status, challenges and future perspectives. *European Journal of Pharmaceutics and Biopharmaceutics*. 2020;147:19-37.
219. Singh B, Kapil R, Nandi M, Ahuja N. Developing oral drug delivery systems using formulation by design: vital precepts, retrospect and prospects. *Expert Opinion on Drug Delivery*. 2011;8(10):1341-60.
220. Patel S, Mehra A. Modeling of oxygen transport in blood-perfluorocarbon emulsion mixtures: Part I: oxygen uptake in tubular vessels. *ASAIO J*. 1998;44(3):144-56.
221. Patel S, Mehra A. Modeling of oxygen transport in blood-perfluorocarbon emulsion mixtures: Part II: tissue oxygenation. *ASAIO J*. 1998;44(3):157-65.
222. Hanna GK, Ojeda MC, Sklenar TA. Application of computer-based experimental design to optimization of processing conditions for perfluorocarbon emulsion. *Biomaterials, Artificial Cells, and Immobilization Biotechnology*. 1991;19(2):391.
223. Hu Y, Wang Y, Jiang J, Han B, Zhang S, Li K, et al. Preparation and characterization of novel perfluorooctyl bromide nanoparticle as ultrasound contrast agent via layer-by-layer self-assembly for folate-receptor-mediated tumor imaging. *BioMed Research International*. 2016;2016.
224. Riess JG, Postel M. Stability and stabilization of fluorocarbon emulsions destined for injection. *Biomaterials, Artificial Cells and Immobilization Biotechnology*. 1992;20(4 -- Feb):819-30.

225. Higuchi WI, Misra J. Physical degradation of emulsions via the molecular diffusion route and the possible prevention thereof. *J Pharm Sci.* 1962;51:459-66.
226. Bertilla SM, Thomas JL, Marie P, Krafft MP. Cosurfactant effect of a semifluorinated alkane at a fluorocarbon/water interface: impact on the stabilization of fluorocarbon-in-water emulsions. *Langmuir.* 2004;20(10):3920-4.
227. Zaggia A, Ameduri B. Recent advances on synthesis of potentially non-bioaccumulable fluorinated surfactants. *Current Opinion in Colloid & Interface Science.* 2012;17(4):188-95.
228. Janjic JM, Patel SK, Bagia C. Utilization of Near-Infrared Fluorescent Imaging for Pharmaceutically Relevant Applications. *Methods Mol Biol.* 2016;1444:97-108.
229. Nosal R, Schultz T. PQLI Definition of Criticality. *Journal of Pharmaceutical Innovation.* 2008;3(2):69-78.
230. Everitt BS. Criteria of Optimality. In: Everitt BS, editor. *Cambridge Dictionary of Statistics.* 2nd ed. ed. Cambridge, UK: Cambridge UP; 2002. p. 100.
231. Bharti SK, Roy R. Quantitative ¹H NMR spectroscopy. *TrAC Trends in Analytical Chemistry.* 2012;35:5-26.
232. Maillard E, Juszczak MT, Langlois A, Kleiss C, Sencier MC, Bietiger W, et al. Perfluorocarbon Emulsions Prevent Hypoxia of Pancreatic β -Cells. *Cell Transplantation.* 2012;21(4):657-69.
233. Taylor P. Ostwald ripening in emulsions: estimation of solution thermodynamics of the disperse phase. *Adv Colloid Interface Sci.* 2003;106:261-85.
234. Jiao J, Burgess DJ. Ostwald ripening of water-in-hydrocarbon emulsions. *Journal of Colloid and Interface Science.* 2003;264(2):509-16.
235. Kabalnov AS, Shchukin ED. Ostwald ripening theory: applications to fluorocarbon emulsion stability. *Advances in Colloid and Interface Science.* 1992;38(Supplement C):69-97.
236. Goke K, Roese E, Bunjes H. Heat Treatment of Poloxamer-Stabilized Triglyceride Nanodispersions: Effects and Underlying Mechanism. *Mol Pharm.* 2018;15(8):3111-20.
237. Stewart ZA. UW solution: Still the "gold standard" for liver transplantation. *American Journal of Transplantation.* 2015;15(2):295-6.

238. Chang Y, McLandsborough L, McClements DJ. Physical properties and antimicrobial efficacy of thyme oil nanoemulsions: influence of ripening inhibitors. *J Agric Food Chem*. 2012;60(48):12056-63.
239. Lowe KC. Engineering blood: synthetic substitutes from fluorinated compounds. *Tissue Eng*. 2003;9(3):389-99.
240. Kok MB, de Vries A, Abdurrachim D, Prompers JJ, Gröll H, Nicolay K, et al. Quantitative ¹H MRI, ¹⁹F MRI, and ¹⁹F MRS of cell-internalized perfluorocarbon paramagnetic nanoparticles. *Contrast Media & Molecular Imaging*. 2011;6(1):19-27.
241. Zhang F, Zhuang J, Esteban Fernández de Ávila B, Tang S, Zhang Q, Fang RH, et al. A Nanomotor-Based Active Delivery System for Intracellular Oxygen Transport. *ACS Nano*. 2019;13(10):11996-2005.
242. Anton N, Benoit J-P, Saulnier P. Design and production of nanoparticles formulated from nano-emulsion templates—A review. *Journal of Controlled Release*. 2008;128(3):185-99.
243. Ahrens ET, Flores R, Xu H, Morel PA. In vivo imaging platform for tracking immunotherapeutic cells. *Nat Biotechnol*. 2005;23(8):983-7.
244. Vasiukhina A, Eshraghi J, Ahmadzadegan A, Goergen CJ, Vlachos PP, Solorio L. Stable thermally-modulated nanodroplet ultrasound contrast agents. *Nanomaterials*. 2021;11(9).
245. Huang Y, Vezeridis AM, Wang J, Wang Z, Thompson M, Mattrey RF, et al. Polymer-Stabilized Perfluorobutane Nanodroplets for Ultrasound Imaging Agents. *J Am Chem Soc*. 2017;139(1):15-8.
246. Solans C, Solé I. Nano-emulsions: Formation by low-energy methods. *Current Opinion in Colloid & Interface Science*. 2012;17(5):246-54.
247. Seekkuarachchi IN, Tanaka K, Kumazawa H. Formation and characterization of submicrometer oil-in-water (O/W) emulsions, using high-energy emulsification. *Ind Eng Chem Res*. 2006;45(1):372-90.
248. Pinnamaneni S, Das NG, Das SK. Comparison of oil-in-water emulsions manufactured by microfluidization and homogenization. *Pharmazie*. 2003;58(8):554-8.
249. Lee L, Norton IT. Comparing droplet breakup for a high-pressure valve homogeniser and a Microfluidizer for the potential production of food-grade nanoemulsions. *Journal of Food Engineering*. 2013;114(2):158-63.

250. Alliod O, Almouazen E, Nemer G, Fessi H, Charcosset C. Comparison of Three Processes for Parenteral Nanoemulsion Production: Ultrasounds, Microfluidizer, and Premix Membrane Emulsification. *Journal of Pharmaceutical Sciences*. 2019;108(8):2708-17.
251. Schultz S, Wagner G, Urban K, Ulrich J. High-Pressure Homogenization as a Process for Emulsion Formation. *Chemical Engineering & Technology*. 2004;27(4):361-8.
252. Olson DW, White CH, Richter RL. Effect of pressure and fat content on particle sizes in microfluidized milk. *Journal of Dairy Science*. 2004;87(10):3217-23.
253. Ozturk OK, Turasan H. Applications of microfluidization in emulsion-based systems, nanoparticle formation, and beverages. *Trends in Food Science & Technology*. 2021;116:609-25.
254. Mahdi Jafari S, He Y, Bhandari B. Nano-Emulsion Production by Sonication and Microfluidization—A Comparison. *International Journal of Food Properties*. 2006;9(3):475-85.
255. TORNBERG E. FUNCTIONAL CHARACTERISTICS OF PROTEIN STABILIZED EMULSIONS: EMULSIFYING BEHAVIOR OF PROTEINS IN A SONIFIER. *Journal of Food Science*. 1980;45(6):1662-8.
256. Zahel T, Hauer S, Mueller EM, Murphy P, Abad S, Vasilieva E, et al. Integrated Process Modeling—A Process Validation Life Cycle Companion. *Bioengineering*. 2017;4(4):86.
257. Food and Drug Administration Center for Drugs Evaluation Research. *Guidance for Industry on Process Validation: General Principles and Practices*. FDA; 2011.
258. Garrelts JC. Fluosol: An Oxygen-Delivery Fluid for use in Percutaneous Transluminal Coronary Angioplasty. *DICP*. 1990;24(11):1105-12.
259. Weers JG, Liu J, Fields T, Resch P, Cavin J, Arlauskas RA. Room temperature stable perfluorocarbon emulsions with acceptable half-lives in the reticuloendothelial system. *Artificial Cells, Blood Substitutes, and Biotechnology*. 1994;22(4):1175-82.
260. Lambert E, Janjic JM. Quality by design approach identifies critical parameters driving oxygen delivery performance in vitro for perfluorocarbon based artificial oxygen carriers. *Scientific Reports*. 2021;11(1):5569.
261. Rajalahti T, Kvalheim OM. Multivariate data analysis in pharmaceuticals: A tutorial review. *International Journal of Pharmaceutics*. 2011;417(1–2):280-90.
262. Boonkhao B, Li RF, Wang XZ, Tweedie RJ, Primrose K. Making use of process tomography data for multivariate statistical process control. *AIChE Journal*. 2011;57(9):2360-8.

263. de Oliveira Honse S, Kashefi K, Charin RM, Tavares FW, Pinto JC, Nele M. Emulsion phase inversion of model and crude oil systems detected by near-infrared spectroscopy and principal component analysis. *Colloids and Surfaces A: Physicochemical and Engineering Aspects*. 2018;538:565-73.
264. Wold S, Esbensen K, Geladi P. Principal component analysis. *Chemometrics and Intelligent Laboratory Systems*. 1987;2(1):37-52.
265. Ward JH. Hierarchical Grouping to Optimize an Objective Function. *Journal of the American Statistical Association*. 1963;58(301):236-44.
266. Griffin WC. Classification of Surface-Active Agents by "HLB". *Journal of the Society of Cosmetic Chemists*. 1949;1(5):311-26.
267. Rao MRP, Aghav S, Sukre G, Kumar M. Determination of Required HLB of Capryol 90. *Journal of Dispersion Science and Technology*. 2014;35(2):161-7.
268. Lee YH, Kuo PW, Chen CJ, Sue CJ, Hsu YF, Pan MC. Indocyanine green-camptothecin co-loaded perfluorocarbon double-layer nanocomposite: A versatile nanotheranostics for photochemotherapy and FDOT diagnosis of breast cancer. *Pharmaceutics*. 2021;13(9).
269. Lee E-H, Kim J-K, Lim J-S, Lim S-J. Enhancement of indocyanine green stability and cellular uptake by incorporating cationic lipid into indocyanine green-loaded nanoemulsions. *Colloids and Surfaces B: Biointerfaces*. 2015;136:305-13.
270. Costabile F, Birmili W, Klose S, Tuch T, Wehner B, Wiedensohler A, et al. Spatio-temporal variability and principal components of the particle number size distribution in an urban atmosphere. *Atmos Chem Phys*. 2009;9(9):3163-95.
271. Guenette E, Barrett A, Kraus D, Brody R, Harding L, Magee G. Understanding the effect of lactose particle size on the properties of DPI formulations using experimental design. *International Journal of Pharmaceutics*. 2009;380(1):80-8.
272. Jafari SM, He Y, Bhandari B. Production of sub-micron emulsions by ultrasound and microfluidization techniques. *Journal of Food Engineering*. 2007;82(4):478-88.
273. Tang SY, Shridharan P, Sivakumar M. Impact of process parameters in the generation of novel aspirin nanoemulsions – Comparative studies between ultrasound cavitation and microfluidizer. *Ultrasonics Sonochemistry*. 2013;20(1):485-97.
274. Schlegel A, Dutkowski P. Role of hypothermic machine perfusion in liver transplantation. *Transplant International*. 2015;28(6):677-89.

275. Dupré-Crochet S, Erard M, Nüße O. ROS production in phagocytes: why, when, and where? *Journal of Leukocyte Biology*. 2013;94(4):657-70.
276. Van Erp AC, Hoeksma D, Rebolledo RA, Ottens PJ, Jochmans I, Monbaliu D, et al. The crosstalk between ROS and autophagy in the field of transplantation medicine. *Oxid Med Cell Longevity*. 2017:7120962/1-13.
277. Beckman JS, Beckman TW, Chen J, Marshall PA, Freeman BA. Apparent hydroxyl radical production by peroxynitrite: implications for endothelial injury from nitric oxide and superoxide. *Proc Natl Acad Sci U S A*. 1990;87(4):1620-4.
278. Radi R. Oxygen radicals, nitric oxide, and peroxynitrite: Redox pathways in molecular medicine. *Proc Natl Acad Sci U S A*. 2018;115(23):5839-48.
279. Radi R, Beckman JS, Bush KM, Freeman BA. Peroxynitrite-induced membrane lipid peroxidation: the cytotoxic potential of superoxide and nitric oxide. *Arch Biochem Biophys*. 1991;288(2):481-7.
280. Guo R, Su Y, Liu B, Li S, Zhou S, Xu Y. Resveratrol suppresses oxidised low-density lipoprotein-induced macrophage apoptosis through inhibition of intracellular reactive oxygen species generation, lox-1, and the p38 MAPK pathway. *Cellular Physiology and Biochemistry*. 2014;34(2):603-16.
281. Leonard SS, Xia C, Jiang BH, Stinefelt B, Klandorf H, Harris GK, et al. Resveratrol scavenges reactive oxygen species and effects radical-induced cellular responses. *Biochemical and Biophysical Research Communications*. 2003;309(4):1017-26.
282. Zhou X, Chen M, Zeng X, Yang J, Deng H, Yi L, et al. Resveratrol regulates mitochondrial reactive oxygen species homeostasis through Sirt3 signaling pathway in human vascular endothelial cells. *Cell Death and Disease*. 2014;5(12).
283. Song J, Huang Y, Zheng W, Yan J, Cheng M, Zhao R, et al. Resveratrol reduces intracellular reactive oxygen species levels by inducing autophagy through the AMPK-mTOR pathway. *Frontiers of Medicine*. 2018;12(6):697-706.
284. Cheng PW, Lee HC, Lu PJ, Chen HH, Lai CC, Sun GC, et al. Resveratrol Inhibition of Rac1-Derived Reactive Oxygen Species by AMPK Decreases Blood Pressure in a Fructose-Induced Rat Model of Hypertension. *Scientific Reports*. 2016;6.
285. Gao D, Zhang X, Jiang X, Peng Y, Huang W, Cheng G, et al. Resveratrol reduces the elevated level of MMP-9 induced by cerebral ischemia-reperfusion in mice. *Life Sciences*. 2006;78(22):2564-70.

286. Chang C, Zhao Y, Song G, She K. Resveratrol protects hippocampal neurons against cerebral ischemia-reperfusion injury via modulating JAK/ERK/STAT signaling pathway in rats. *Journal of Neuroimmunology*. 2018;315:9-14.
287. Herneisey M, Salcedo PF, Domenech T, Bagia C, George SS, Tunney R, et al. Design of Thermoresponsive Polyamine Cross-Linked Perfluoropolyether Hydrogels for Imaging and Delivery Applications. *ACS Med Chem Lett*. 2020;11(10):2032-40.
288. Angelova PR, Abramov AY. Functional role of mitochondrial reactive oxygen species in physiology. *Free Radical Biology and Medicine*. 2016;100:81-5.
289. Chen R, Lai UH, Zhu L, Singh A, Ahmed M, Forsyth NR. Reactive Oxygen Species Formation in the Brain at Different Oxygen Levels: The Role of Hypoxia Inducible Factors. *Frontiers in Cell and Developmental Biology*. 2018;6.
290. Ganta S, Talekar M, Singh A, Coleman TP, Amiji MM. Nanoemulsions in Translational Research—Opportunities and Challenges in Targeted Cancer Therapy. *AAPS PharmSciTech*. 2014;15(3):694-708.
291. Zupančič Š, Lavrič Z, Kristl J. Stability and solubility of trans-resveratrol are strongly influenced by pH and temperature. *European Journal of Pharmaceutics and Biopharmaceutics*. 2015;93:196-204.
292. Silva RCD, Teixeira JA, Nunes WDG, Zangaro GAC, Pivatto M, Caires FJ, et al. Resveratrol: A thermoanalytical study. *Food Chem*. 2017;237:561-5.
293. López-Nicolás JM, García-Carmona F. Aggregation State and pKa Values of (E)-Resveratrol As Determined by Fluorescence Spectroscopy and UV–Visible Absorption. *Journal of Agricultural and Food Chemistry*. 2008;56(17):7600-5.
294. Waterhouse AL, Laurie VF. Oxidation of Wine Phenolics: A Critical Evaluation and Hypotheses. *American Journal of Enology and Viticulture*. 2006;57(3):306-13.
295. Jiang L. An Investigation on Nonenzymatic Autoxidation of Phenolic Compounds in Natural Waters [Masters Thesis]: Western Michigan University; 1996.
296. Singleton VL. Oxygen with Phenols and Related Reactions in Musts, Wines, and Model Systems: Observations and Practical Implications. *American Journal of Enology and Viticulture*. 1987;38(1):69-77.
297. Tulyathan V. OXIDATION OF PHENOLICS COMMON TO FOODS AND WINES (GALLIC ACID) [Ph.D. thesis]. California, United States: University of California, Davis; 1984.


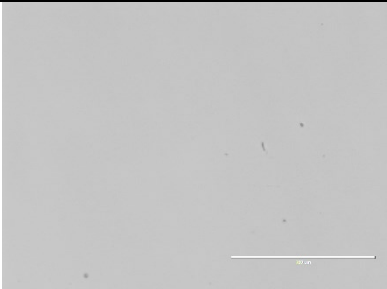
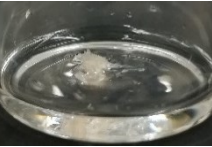

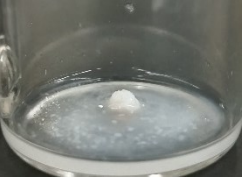
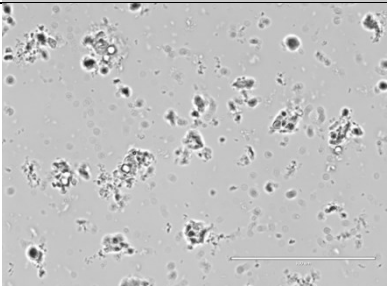
298. Cilliers JJJ, Singleton VL. Characterization of the products of nonenzymic autoxidative phenolic reactions in a caffeic acid model system. *Journal of Agricultural and Food Chemistry*. 1991;39(7):1298-303.
299. Formento JL, Berra E, Ferrua B, Magné N, Simos G, Brahimi-Horn C, et al. Enzyme-linked immunosorbent assay for pharmacological studies targeting hypoxia-inducible factor 1 α . *Clinical and Diagnostic Laboratory Immunology*. 2005;12(5):660-4.
300. Arteel GE, Briviba K, Sies H. Protection against peroxynitrite. *FEBS Letters*. 1999;445(2):226-30.
301. Yu S, Go G-w, Kim W. Medium Chain Triglyceride (MCT) Oil Affects the Immunophenotype via Reprogramming of Mitochondrial Respiration in Murine Macrophages. *Foods*. 2019;8(11):553.
302. Deng L, Vrieling F, Stienstra R, Hooiveld GJ, Feitsma AL, Kersten S. Macrophages take up VLDL-sized emulsion particles through caveolae-mediated endocytosis and excrete part of the internalized triglycerides as fatty acids. *PLOS Biology*. 2022;20(8):e3001516.
303. Galkin A, Higgs A, Moncada S. Nitric oxide and hypoxia. *Essays Biochem*. 2007;43:29-42.
304. Benita S, Levy MY. Submicron Emulsions as Colloidal Drug Carriers for Intravenous Administration: Comprehensive Physicochemical Characterization. *Journal of Pharmaceutical Sciences*. 1993;82(11):1069-79.
305. van Westen T, Groot RD. Effect of Temperature Cycling on Ostwald Ripening. *Crystal Growth & Design*. 2018;18(9):4952-62.
306. Bera B, Khazal R, Schroën K. Coalescence dynamics in oil-in-water emulsions at elevated temperatures. *Scientific Reports*. 2021;11(1):10990.
307. Driscoll DF. Lipid Injectable Emulsions: Pharmacopeial and Safety Issues. *Pharmaceutical Research*. 2006;23(9):1959-69.
308. Klang MG. PFAT5 and the Evolution of Lipid Admixture Stability. *Journal of Parenteral and Enteral Nutrition*. 2015;39(1S):67S-71S.
309. United States Pharmacopeia. (729) GLOBULE SIZE DISTRIBUTION IN LIPID INJECTABLE EMULSIONS. Rockville, MD. 2023.
310. Xu R. Light scattering: A review of particle characterization applications. *Particuology*. 2015;18:11-21.

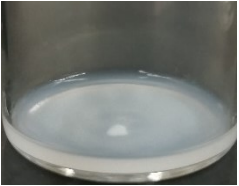
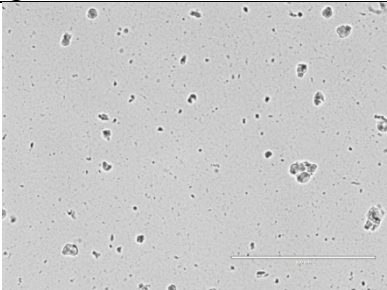

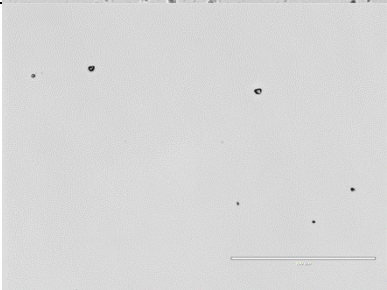

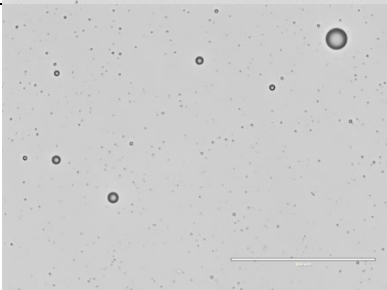
311. Wang Z, He C, Gong X, Wang J, Ngai T. Measuring the Surface–Surface Interactions Induced by Serum Proteins in a Physiological Environment. *Langmuir*. 2016;32(46):12129-36.
312. Yoshida H, Yamamoto T, Fukui K, Masuda H. Theoretical calculation of uncertainty region based on the general size distribution in the preparation of standard reference particles for particle size measurement. *Advanced Powder Technology*. 2012;23(2):185-90.
313. Ridler TW, Calvard S. Picture Thresholding Using an Iterative Selection Method. *IEEE Transactions on Systems, Man & Cybernetics*. 1978;8(8):630-2.
314. Huang LK, Wang MJJ. Image thresholding by minimizing the measures of fuzziness. *Pattern Recognition*. 1995;28(1):41-.
315. Prewitt JMS, Mendelsohn ML. THE ANALYSIS OF CELL IMAGES*. *Annals of the New York Academy of Sciences*. 1966;128(3):1035-53.
316. Li CH, Tam PKS. An iterative algorithm for minimum cross entropy thresholding. *Pattern Recognition Letters*. 1998;19(8):771-6.
317. Kapur JN, Sahoo PK, Wong AKC. A new method for gray-level picture thresholding using the entropy of the histogram. *Computer Vision, Graphics and Image Processing*. 1985;29(3):273-85.
318. Glasbey CA. An Analysis of Histogram-Based Thresholding Algorithms. *CVGIP: Graphical Models and Image Processing*. 1993;55(6):532-7.
319. Kittler J, Illingworth J. Minimum error thresholding. *Pattern Recognition*. 1986;19(1):41-7.
320. Tsai WH. Moment-Preserving Thresholding: A New Approach. *Computer Vision, Graphics, and Image Processing* 1985;29(3):377.
321. Otsu N. A Threshold Selection Method from Gray-Level Histograms. *IEEE Transactions on Systems, Man & Cybernetics*. 1979;9(1):62-6.
322. Doyle W. Operations Useful for Similarity-Invariant Pattern Recognition. *Journal of the ACM*. 1962;9(2):259-67.
323. Shanbhag AG. Utilization of Information Measure as a Means of Image Thresholding. *CVGIP: Graphical Models and Image Processing*. 1994;56(5):414-9.
324. Zack GW, Rogers WE, Latt SA. Automatic measurement of sister chromatid exchange frequency. *Journal of Histochemistry and Cytochemistry*. 1977;25(7):741-53.

325. Yen J-C, Chang F-J, Chang S. A new criterion for automatic multilevel thresholding. IEEE Transactions on Image Processing. 1995;4(3):370.

Appendix A. Chapter 2 Supplemental Data

Table A.1. PFPE-tyramide solubility results by visual analysis. Scale bar reads 100 μm . Transcutol was selected as the carrier for PFPE-tyramide on the basis of appearance of each sample to the naked eye and appearance under 40x magnification.

Excipient	No magnification	40x magnification	Comment
Miglyol 812			Large solid chunk visible at 1x; clear; very small amount visible under 40x; very low solubility
Olive oil			Large solid chunk visible at 1x; clear; small amount visible under 40x; low solubility
PFPE-oxide			Moderate solid chunk visible at 1x; translucent; considerable amount visible under 40x; low solubility

Excipient	No magnification	40x magnification	Comment
PCE			Small solid chunk visible at 1x; opaque; considerable amount visible under 40x; low solubility
CrEL			Large solid chunk visible at 1x; clear; small amount visible under 40x; low solubility
Transcutol			No solid chunk visible at 1x; clear to translucent; moderate amount visible under 40x; good solubility. Evidence of self-assembly

Inclusion of process variables among mixture variables in multiple linear regression analysis introduces certain limitations in which a process main effect cannot be analyzed in the presence of mixture main effects; therefore a preliminary analysis of the data was conducted on: 1) the main effect of PFPE-tyramide in simple linear regression and 2) the PFPE-tyramide interactions in the presence of mixture main effects and interaction effects.

Table A.1 and Table A.2 show that none of the PFPE-tyramide regression coefficients are statistically significant in these analyses, so they were omitted from the subsequent regression analysis.

Table A.2. Regression coefficients for PFPE-tyramide in simple linear regression.

Term	Estimate	Std Error	<i>t</i> Ratio	<i>p</i> -value
Intercept	144.17	2.94	49.12	<.0001
T	1.58	5.08	0.31	0.759

Table A.3. Regression coefficients for special cubic model.

Term	Estimate	Std Error	<i>t</i> Ratio	<i>p</i> -value
Intercept	126.17	4.66	27.09	<.0001
A	6.42	6.04	1.06	0.3233
B	29.95	6.04	4.96	0.0016
C	21.49	6.04	3.56	0.0093
D	49.05	6.04	8.11	<.0001
AC	-41.43	14.03	-2.95	0.0214
AD	-72.13	14.03	-5.14	0.0013
AT	4.04	5.40	0.75	0.4782
BC	-19.42	14.03	-1.38	0.2089
BD	-69.88	14.03	-4.98	0.0016
BT	-1.25	5.40	-0.23	0.8234
CT	12.55	5.40	2.33	0.053
DT	3.61	5.40	0.67	0.5253
ACT	26.32	34.93	0.75	0.4757
ADT	-51.68	34.93	-1.48	0.1826
BCT	26.50	34.93	0.76	0.4729
BDT	41.72	34.93	1.19	0.2713

Note: the NE naming convention in this section (Appendix A) is based off indexing used in Chapter 2. Z-average droplet size and zeta potential for all NEs were examined periodically using dynamic light scattering. Multiple representations of the measurements are included to demonstrate long-term stability in Figure A.1, Figure A.2, Figure A.3, Figure A.8, Figure A.5, Figure A.6, and Figure A.7.

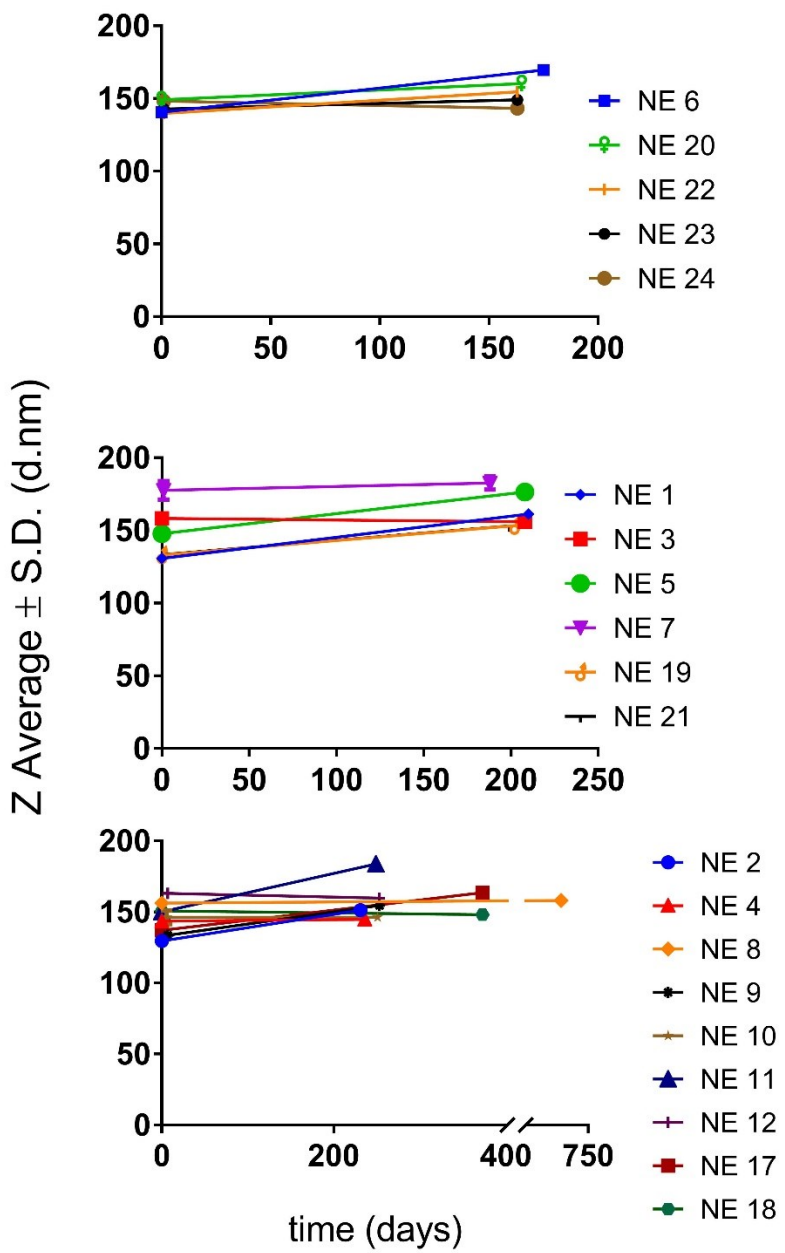


Figure A.1. Nanoemulsions were stored at 4 °C and monitored for change in size over time to demonstrate shelf-life. Lines are put in place only to aid the reader.

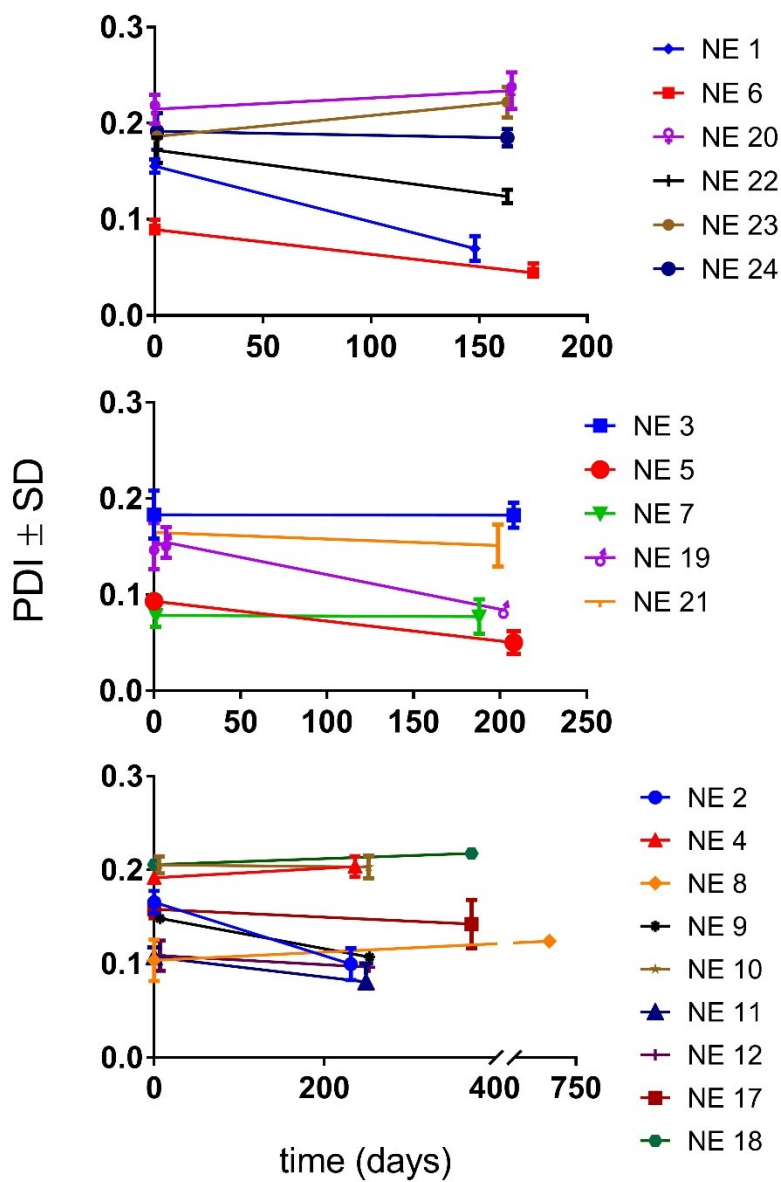


Figure A.2. Nanoemulsions were stored at 4 °C and monitored for change in PDI over time to demonstrate shelf-life. Lines are put in place only to aid the reader.

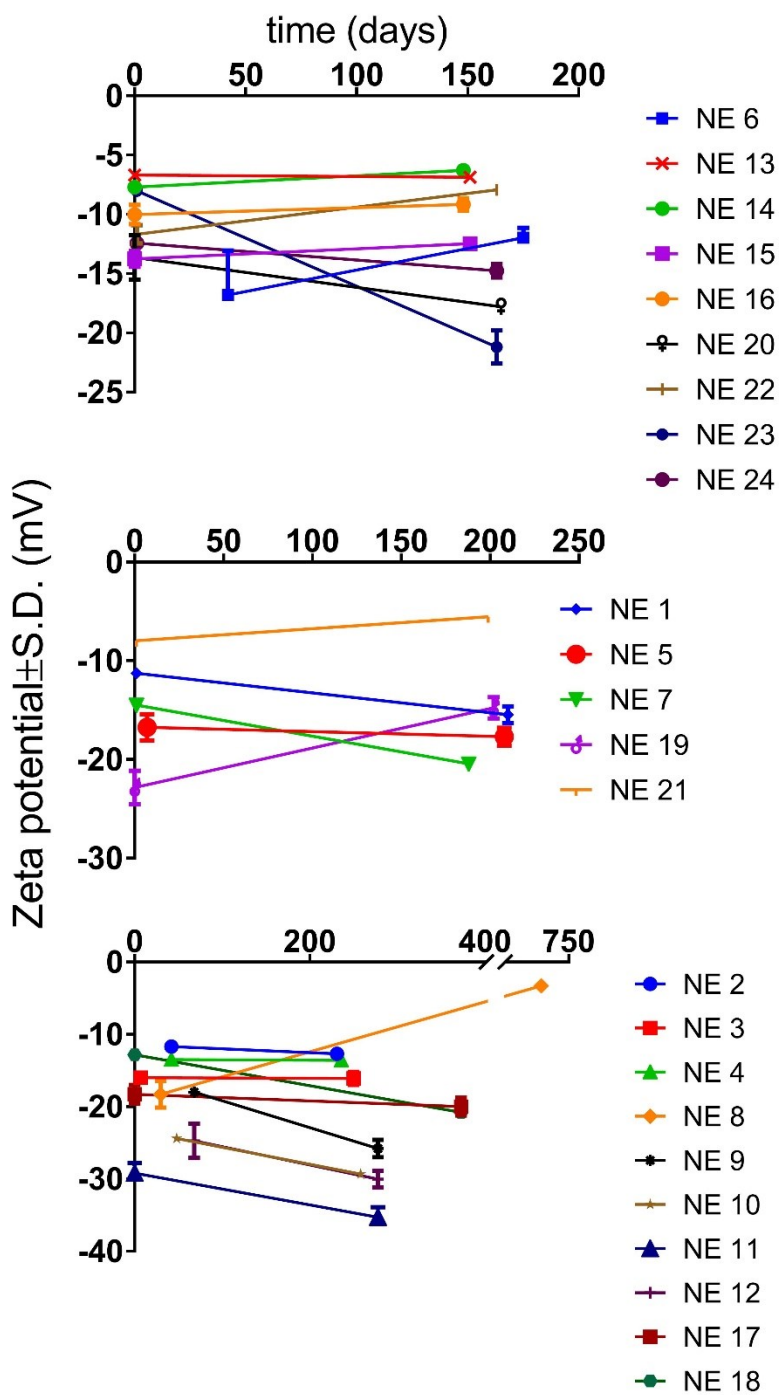


Figure A.3. Nanoemulsions were stored at 4 °C and monitored for change in zeta potential over time to demonstrate shelf-life. Lines are put in place only to aid the reader.

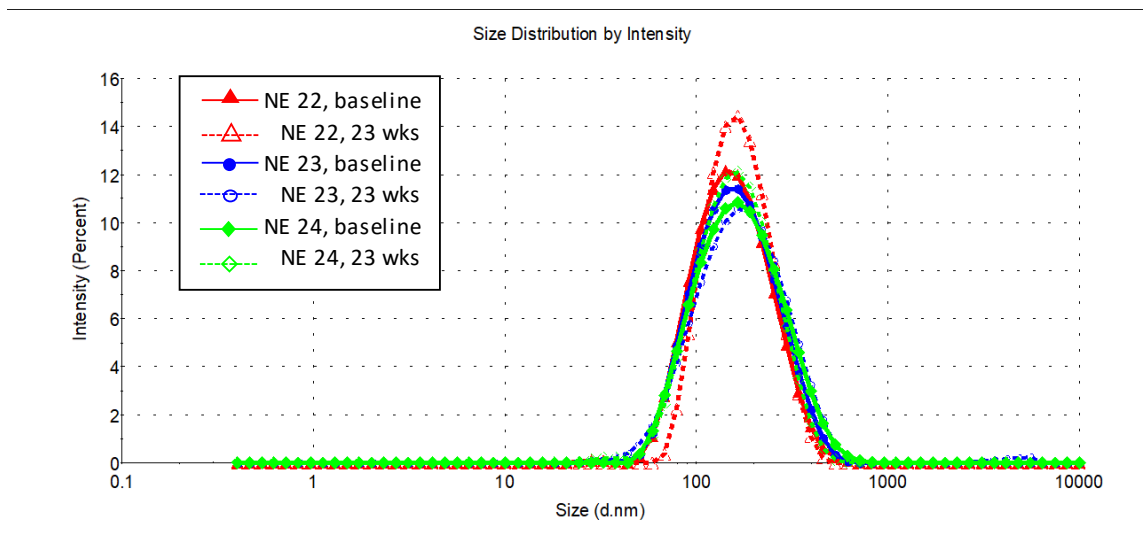


Figure A.4. Size distribution overlays for selected nanoemulsions. Solid lines represent measurements made within the first wk of production. Dashed lines represent measurements made at a later follow up time (23 wk post-production).

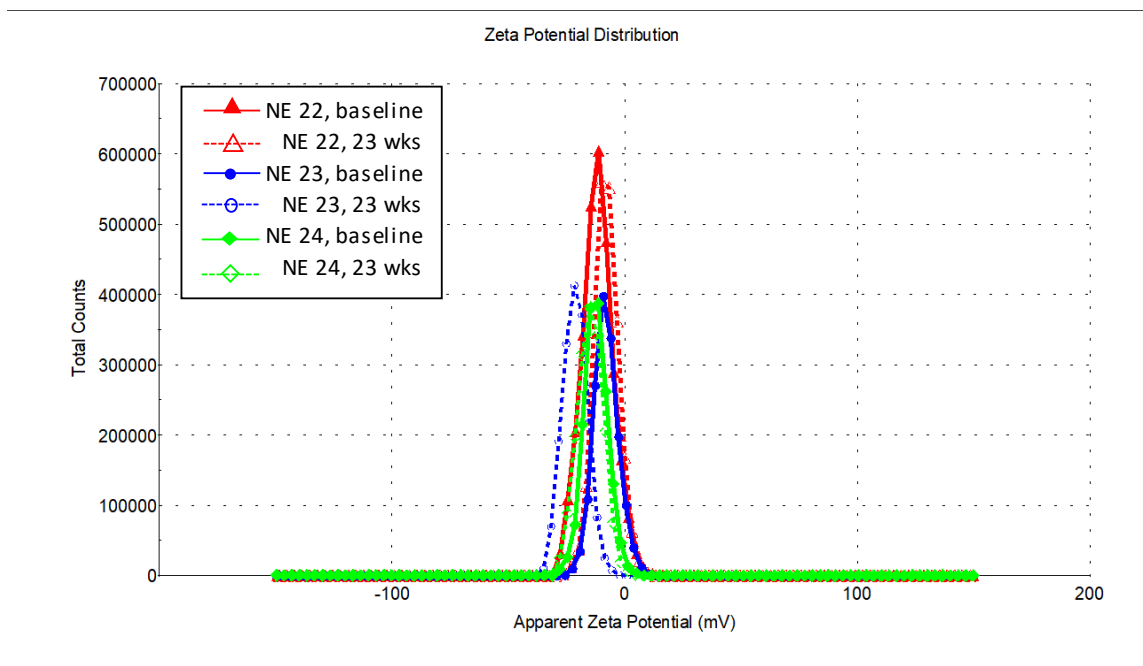


Figure A.5. Zeta potential distribution overlays for selected nanoemulsions. Solid lines represent measurements made within the first wk of production. Dashed lines represent measurements made at a later follow up time (23 wk post-production).

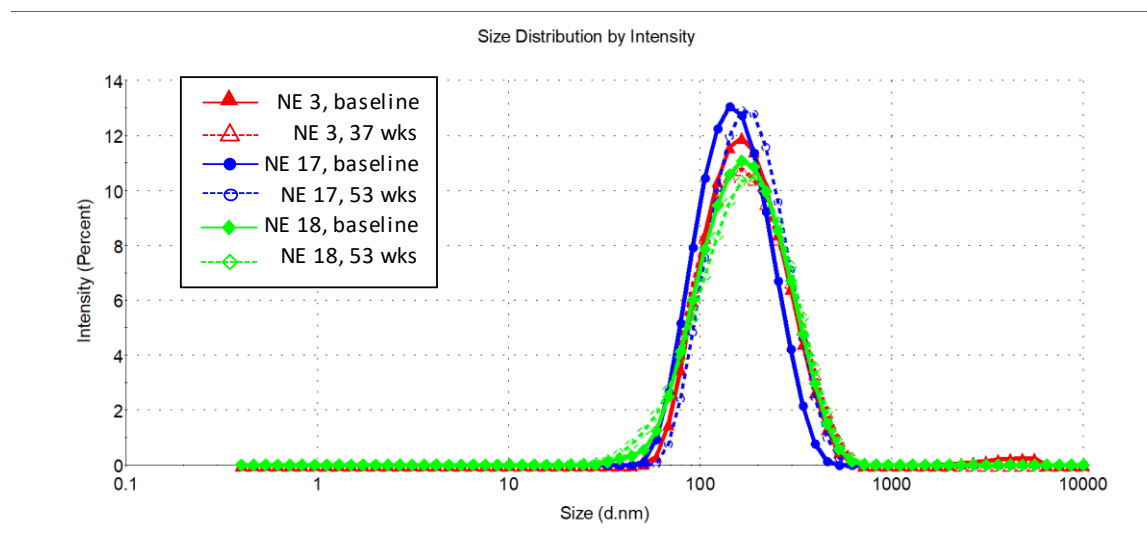


Figure A.6. Size distribution overlays for selected nanoemulsions. Solid lines represent measurements made within the first wk of production. Dashed lines represent measurements made at a later follow up time (37, 53, and 53 wk post-production for NEs 3, 17, and 18, respectively).

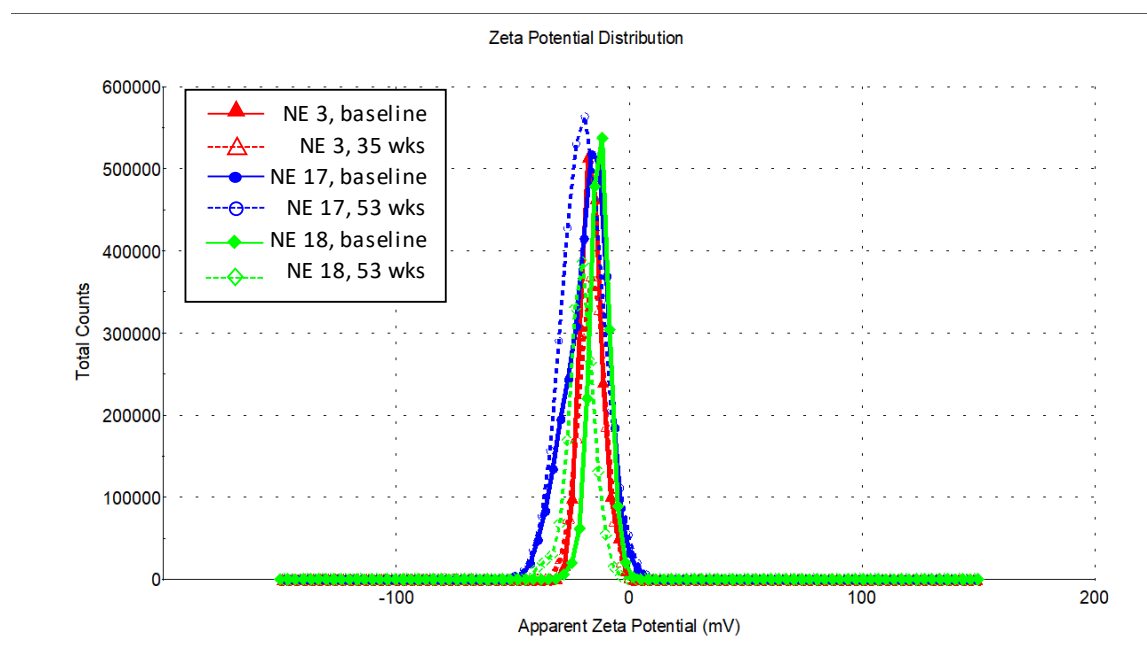


Figure A.7. Zeta potential distribution overlays for selected nanoemulsions. Solid lines represent measurements made within the first wk of production. Dashed lines represent measurements made at a later follow up time (37, 53, and 53 wk post-production for NEs 3, 17, and 18, respectively).

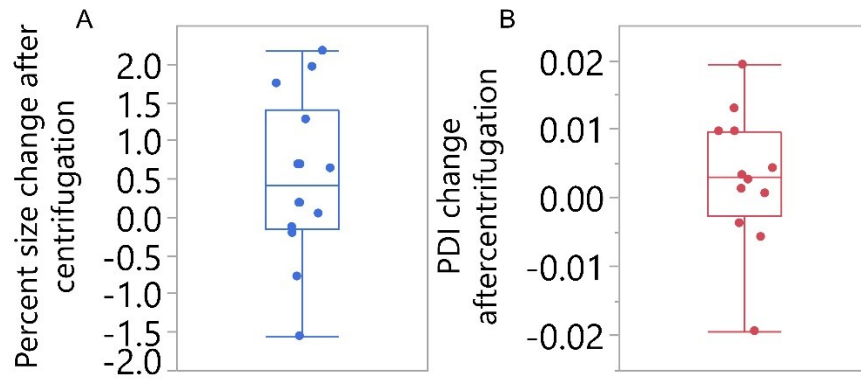


Figure A.8. Centrifugation conditions elicited very small responses for all two-phase nanoemulsions and consequently the test was abandoned for remainder of emulsions.

Appendix B. Chapter 3 Supplemental Data

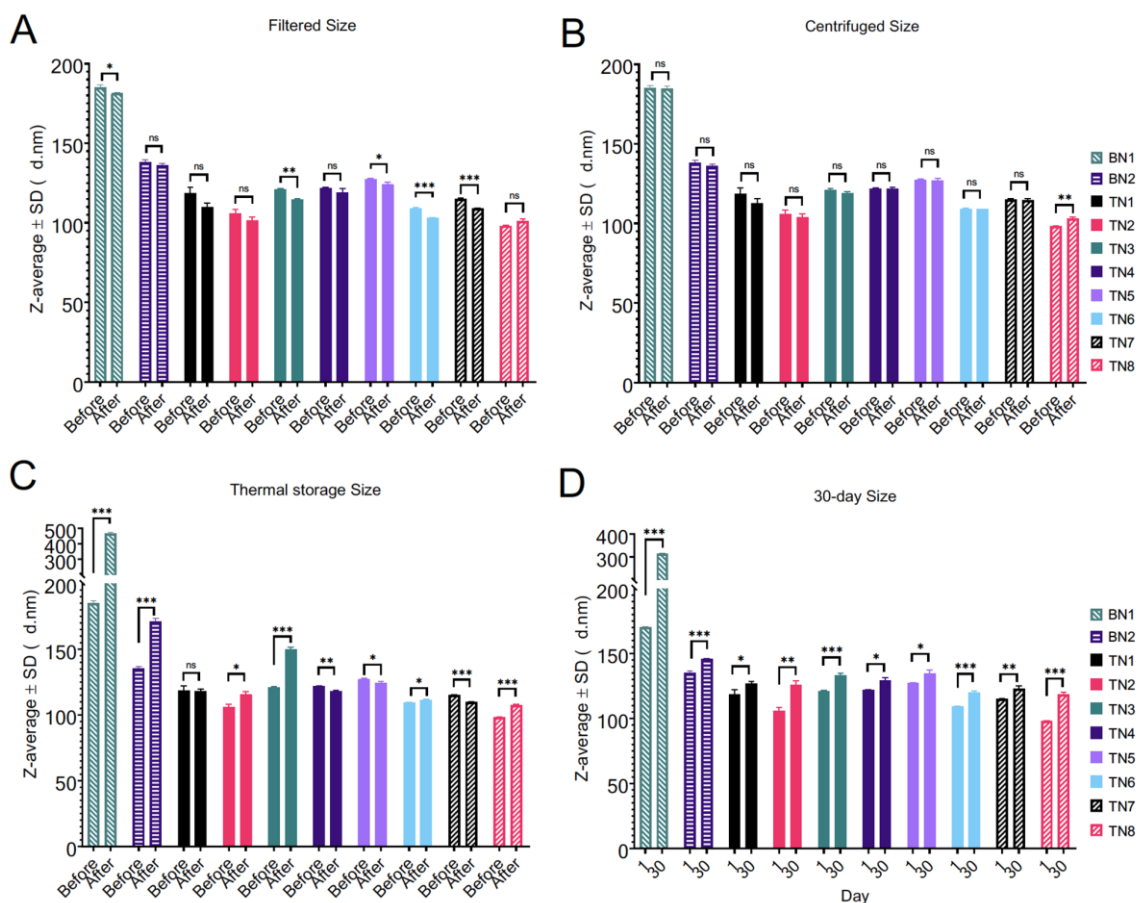


Figure B.1. Z-average diameter evaluation of biphasic and triphasic nanoemulsions (BN and TN, respectively). (A) Stability to filtration through 0.22 μm syringe filter was good in all samples. (B) Stability in centrifugation conditions ($218\times g$ for 5 min) was good in all samples. (C) Storage in 50°C for 2 wk resulted in destabilization of biphasic emulsions. (D) 30-day storage at 4°C shows a 30-day z-average measurement compared to a 1-day-old measurement for comparison. 4°C storage resulted in destabilization of PFOB biphasic formulation only (BN1). All measurements are mean \pm standard deviation from 3 measurements. ns, *, **, *** indicate not significant, $p>0.05$, $p<0.05$, $p<0.01$, and $p<0.001$, respectively.

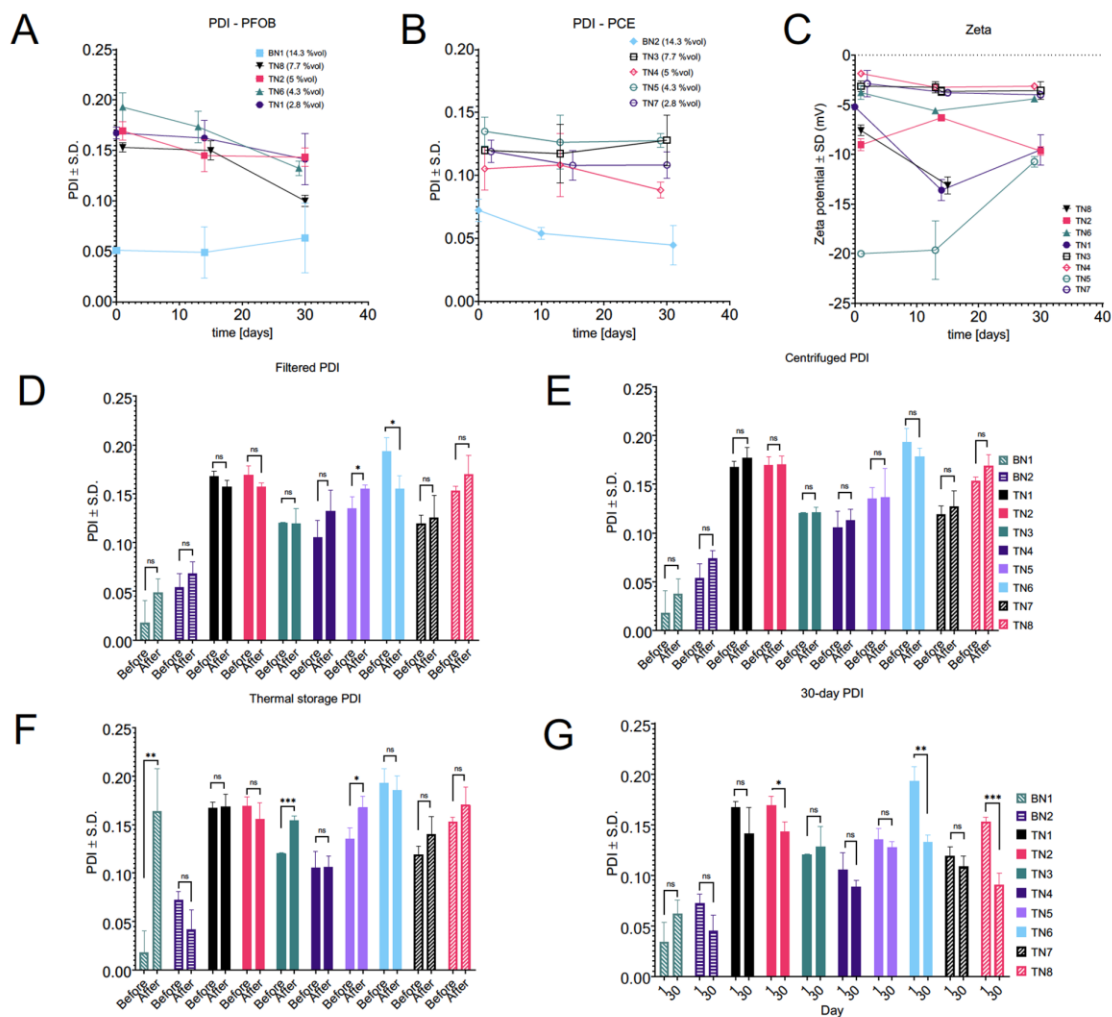


Figure B.2. Size distribution (PDI) and zeta potential evaluation of biphasic and triphasic nanoemulsions (BN and TN, respectively). (A, B) Nanoemulsion PDI was followed for 30 d to evaluate stability in refrigerated storage conditions (4 °C). (C) Nanoemulsion zeta potential was followed for 30 d to evaluate stability in refrigerated storage conditions (4 °C). No evidence of destabilization occurs from observing PDI and zeta potential. (D) Stability to filtration through 0.22 μm syringe filter was good in all samples. (E) Stability in centrifugation conditions (218 \times g for 5 min) was good in all samples. (F) Storage in 50 °C for 2 wk resulted in destabilization of biphasic PFOB emulsion. (G) 30-day storage at 4 °C shows a 30-day z-average measurement compared to a 1-day-old measurement for comparison. 30-day storage at 4 °C was acceptable in all emulsions. All measurements are mean \pm standard deviation from 3 measurements. ns, *, **, *** indicate not significant, $p > 0.05$, $p < 0.05$, $p < 0.01$, and $p < 0.001$, respectively. %vol concentration numbers indicate the concentration of perfluorocarbon.

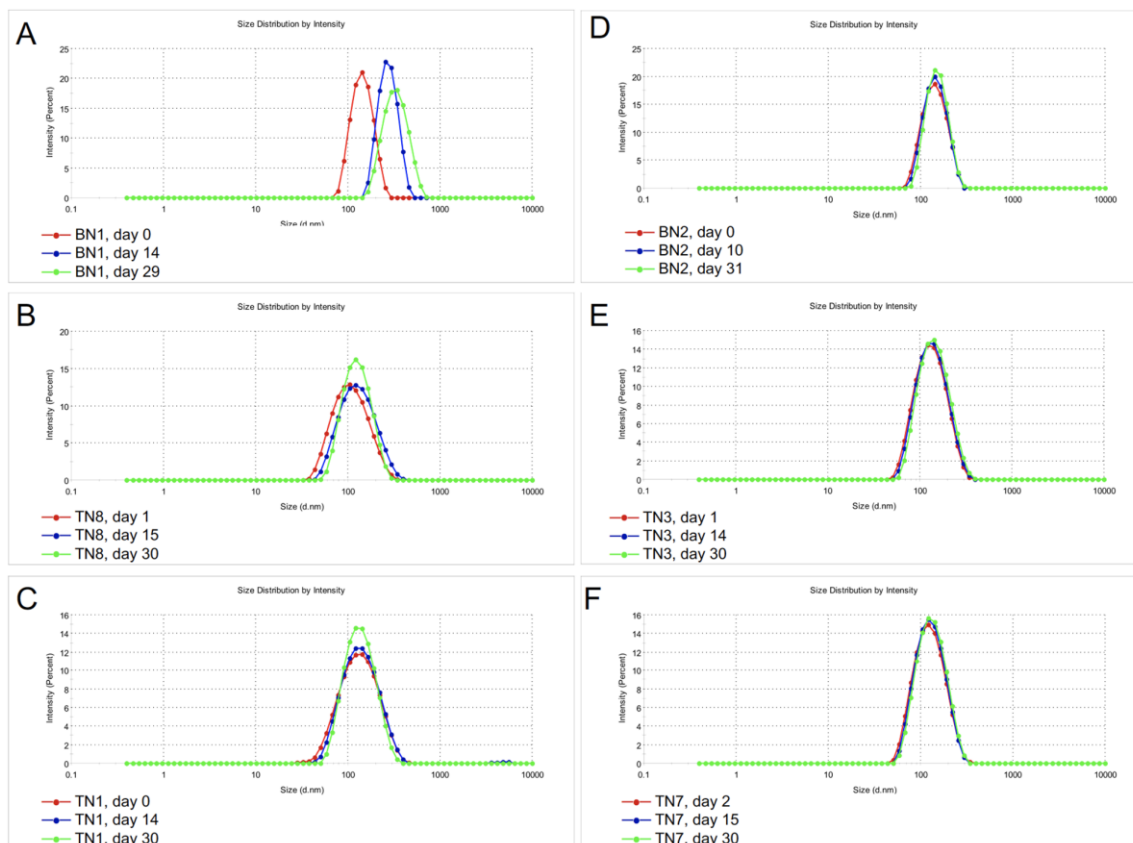


Figure B.3. Size distribution overlays of representative perfluorocarbon nanoemulsions (PFC-NEs). Each panel overlays one representative NE at 3 different ages, up to 31 d after production, as indicated in the figure legends. Selected PFC-NEs are biphasic perfluorooctyl bromide (PFOB) and perfluoro-15-crown-5-ether (PCE) NEs, and triphasic NEs comprised of highest and lowest PFC concentration. PFOB NEs appear in A, B, and C, while PCE NEs appear in D, E, and F. These comparisons show that the size distribution of BN1 shifts to higher sizes rapidly, while BN2 and TNs approximately maintain constant distribution. BN, biphasic nanoemulsion; TN, triphasic nanoemulsion.

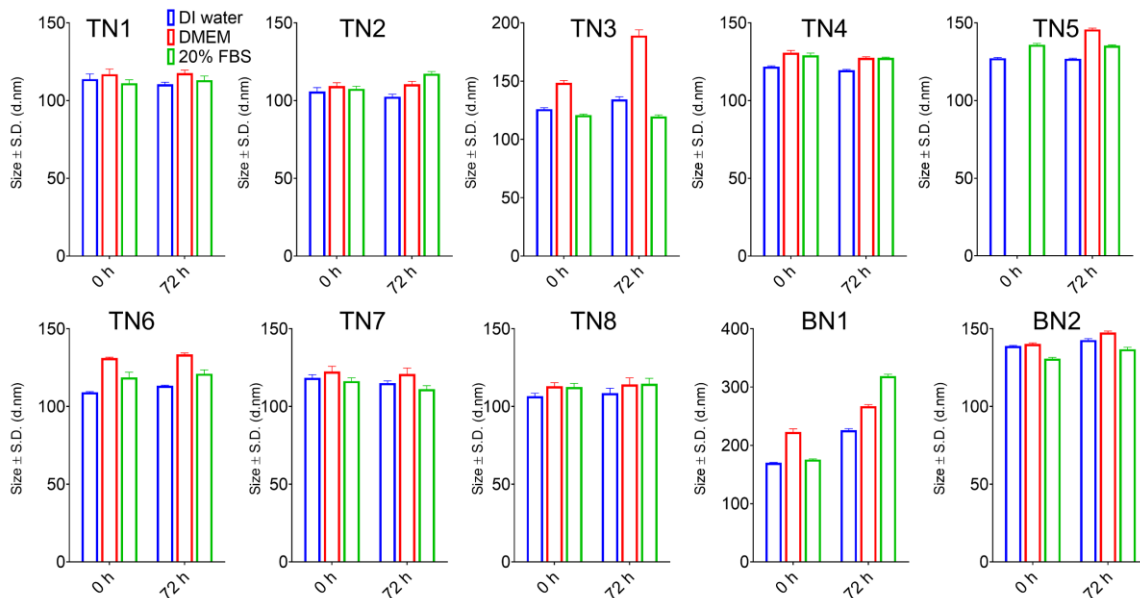


Figure B.4. Graphs of z-average size in response to serum stability test. Samples were incubated for 72 hr in biological media at 37 °C and size was recorded before and after. All measurements are mean \pm standard deviation from 3 measurements. TN, triphasic nanoemulsion; BN, biphasic nanoemulsion; DI, deionized; DMEM, Dulbecco's Modified Eagle's Medium; FBS, fetal bovine serum.

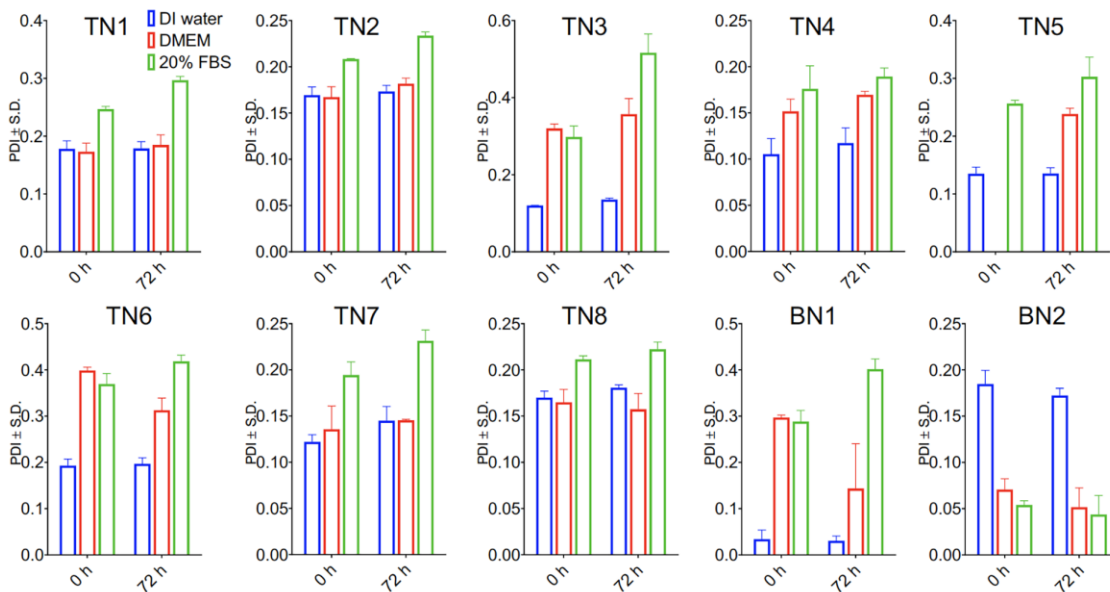


Figure B.5. Graphs of polydispersity index (PDI) in response to serum stability test. Samples were incubated for 72 hr in biological media at 37 °C and PDI was recorded before and after. All measurements are mean \pm standard deviation from 3 measurements. DI, deionized; DMEM, Dulbecco's Modified Eagle's Medium; FBS, fetal bovine serum.

Table B.1. Multiple linear regression (MLR) was used to fit models to two attributes (responses): oxygen release C_{\max} and thermal stability % size change. These two responses make up the backbone of a successful artificial oxygen carrier. Goodness of fit statistics for reduced models is demonstrated by R^2 , root mean square error (RMSE), and leave-one-out cross validation (LOOCV) RMSE.

	C_{\max}	Thermal stability Δ diameter
Mean of Response	1.462 (mg/L)	4.25 (%)
Number of samples	8	8
R^2	0.9950	0.9708
Adjusted R^2	0.9883	0.9489
Root Mean Square Error	0.027 (mg/L)	2.179 (%)
LOOCV RMSE	0.065 (mg/L)	2.777 (%)

Table B.2. Analysis of variance (ANOVA) for reduced MLR models. ANOVA compares the variance explained by the model and the variance unaccounted for (error) and based off this calculates the F ratio. From the F ratio at the specified degrees of freedom (DF), a p-value (Prob > F) is calculated for each model. Significance was taken at $p < 0.05$.

Source	C_{\max} (mg/L)					Thermal stability Δ size (%)				
	DF	Sum of Squares	Mean Square	F Ratio	Prob > F	DF	Sum of Squares	Mean Square	F Ratio	Prob > F
Model	4	0.433659	0.108415	148.7484	0.0009	3	631.405	210.468	44.321	0.0016
Error	3	0.002187	0.000729			4	18.995	4.749		
Corrected Total	7	0.435846				7	650.400			

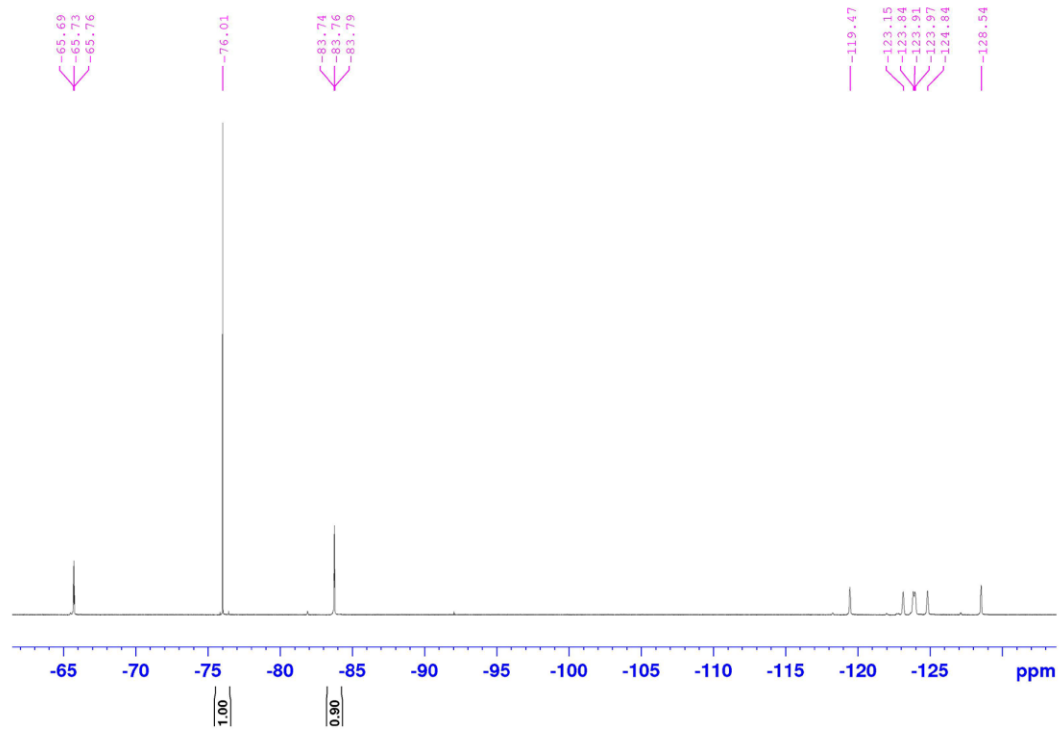


Figure B.6. ^{19}F NMR spectra of TN1. Reference compound trifluoroacetic acid displays chemical shift at -76 ppm.

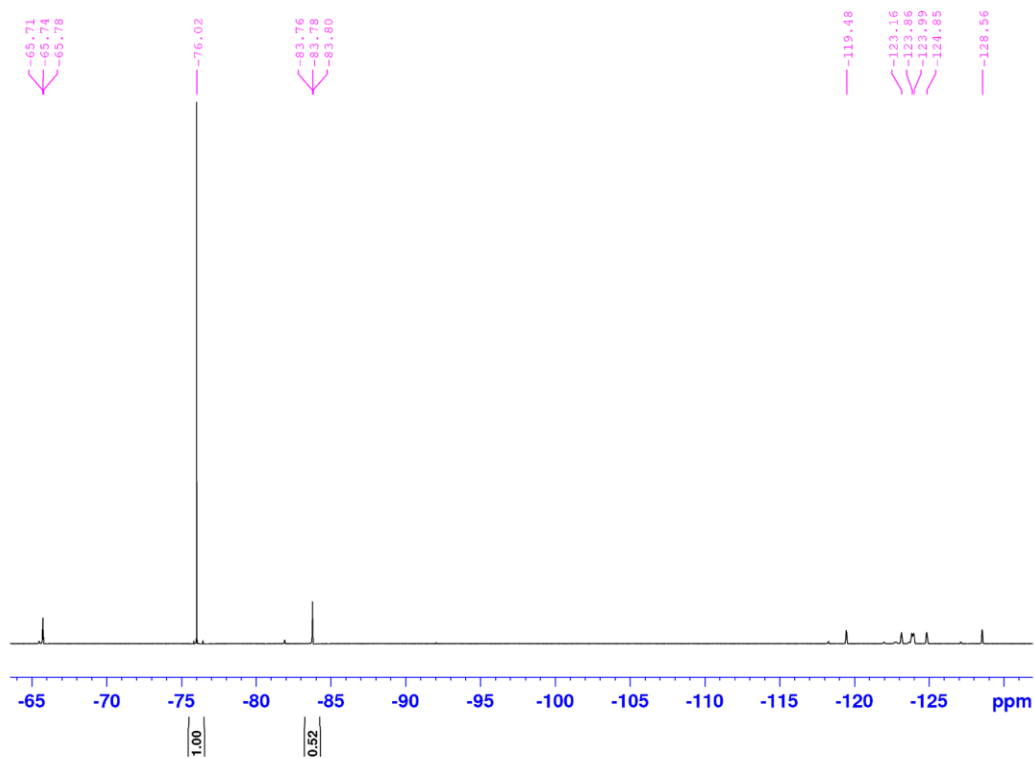


Figure B.7. ^{19}F NMR spectra of TN2. Reference compound trifluoroacetic acid displays chemical shift at -76 ppm.

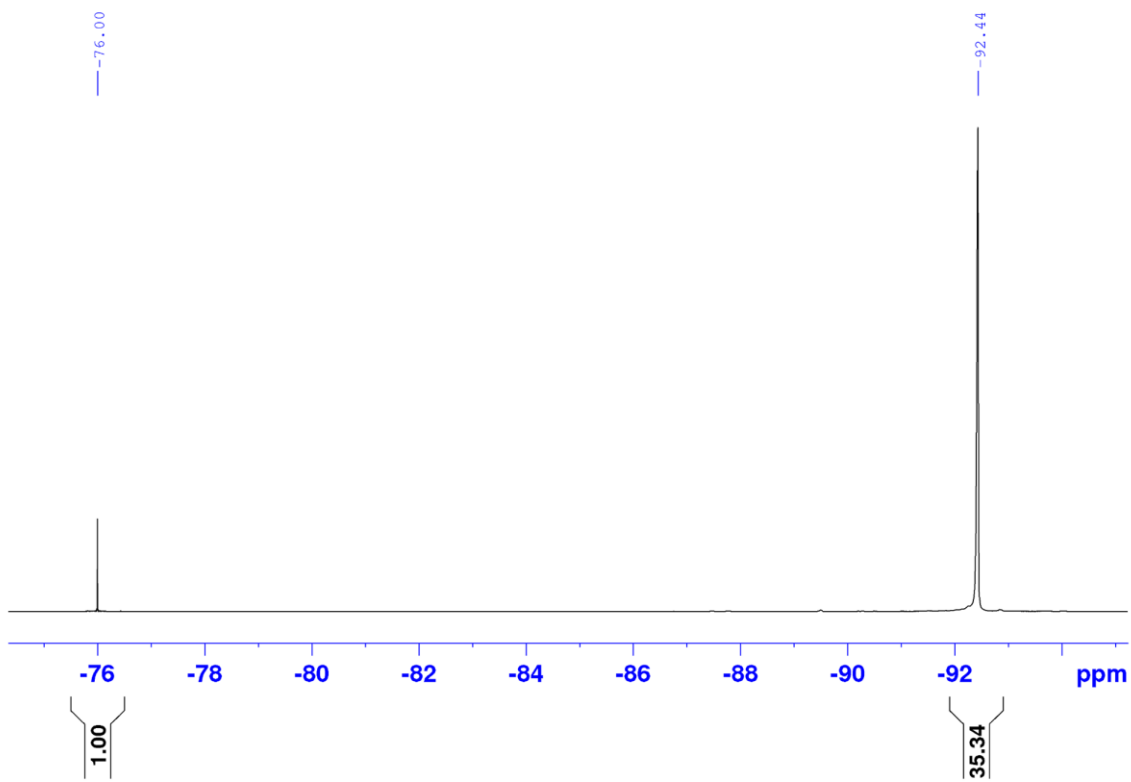


Figure B.8. ^{19}F NMR spectra of TN3. Reference compound trifluoroacetic acid displays chemical shift at -76 ppm.

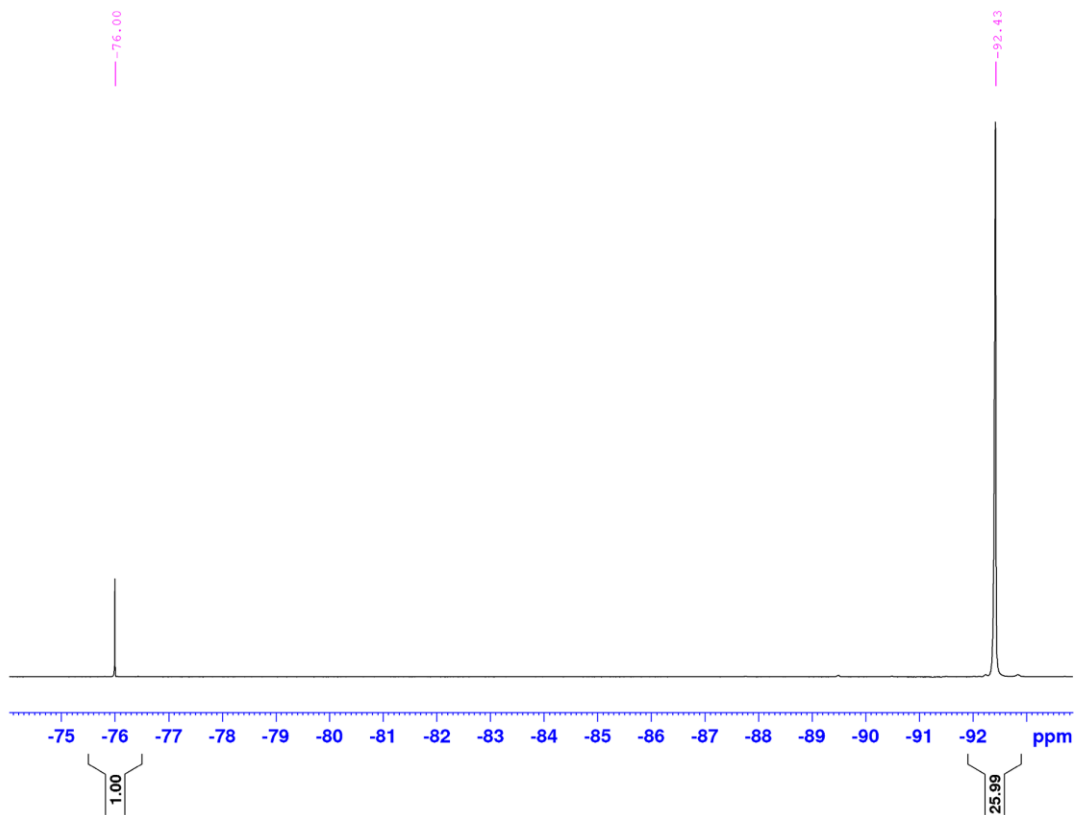


Figure B.9. ^{19}F NMR spectra of TN4. Reference compound trifluoroacetic acid displays chemical shift at -76 ppm.

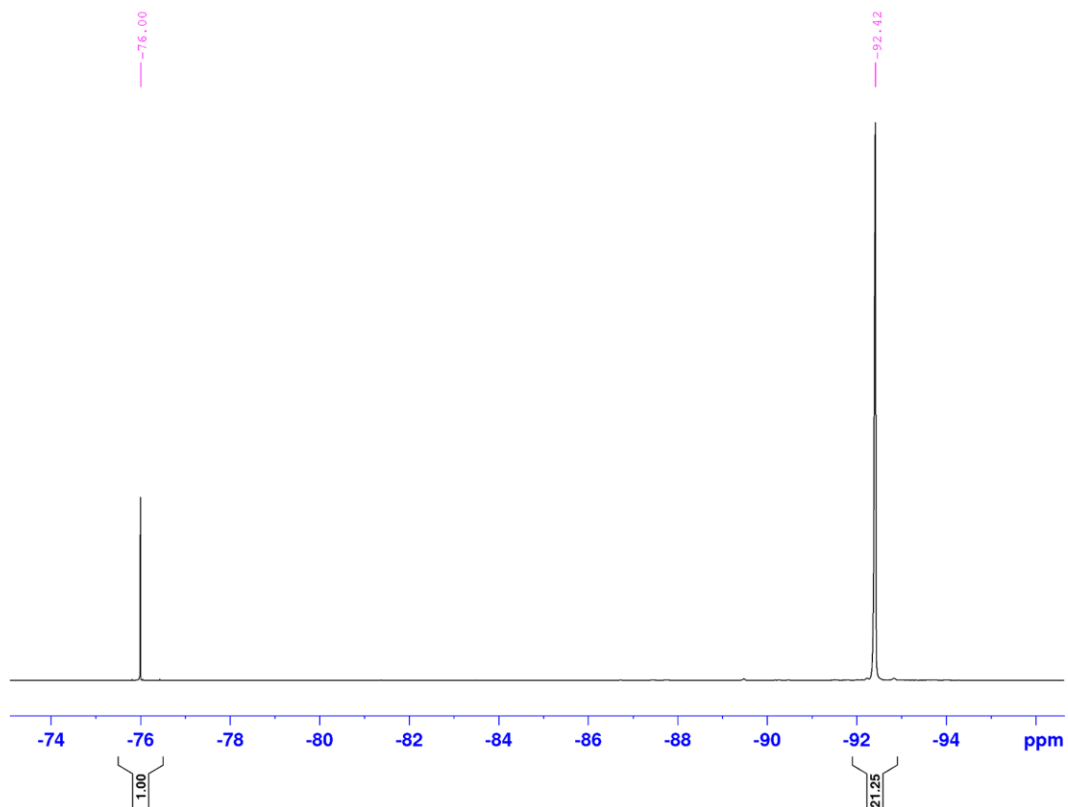


Figure B.10. ^{19}F NMR spectra of TN5. Reference compound trifluoroacetic acid displays chemical shift at -76 ppm.

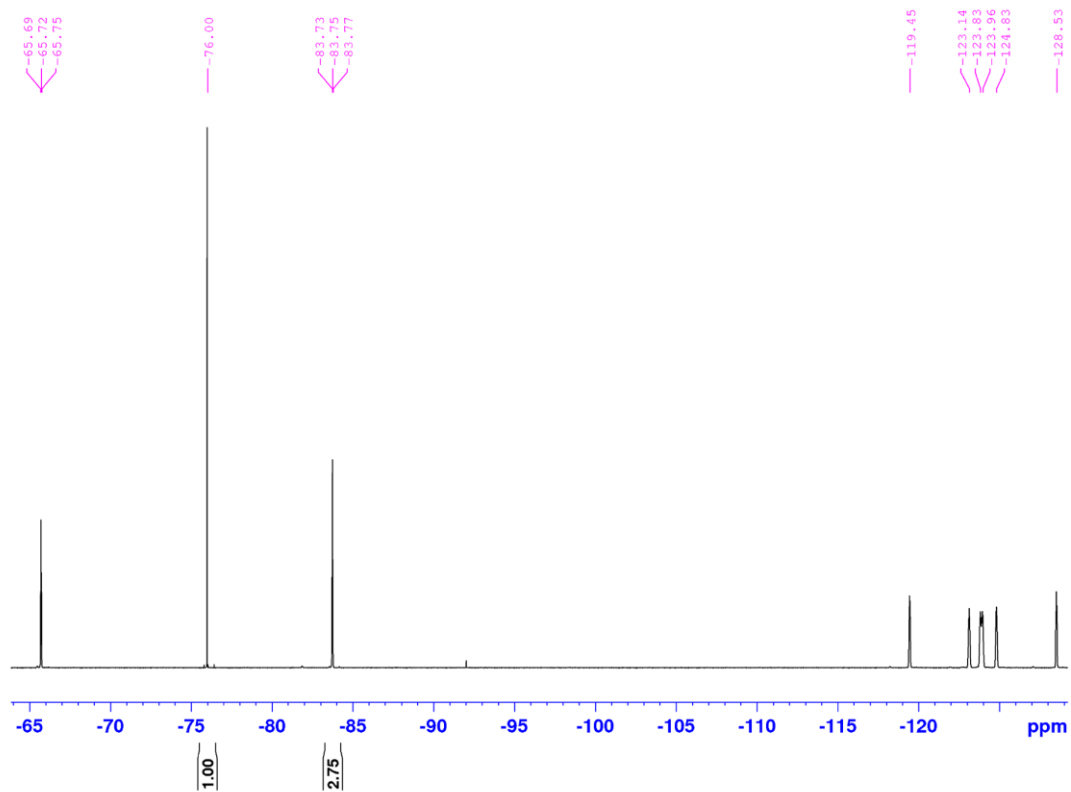


Figure B.11. ^{19}F NMR spectra of TN6. Reference compound trifluoroacetic acid displays chemical shift at -76 ppm.

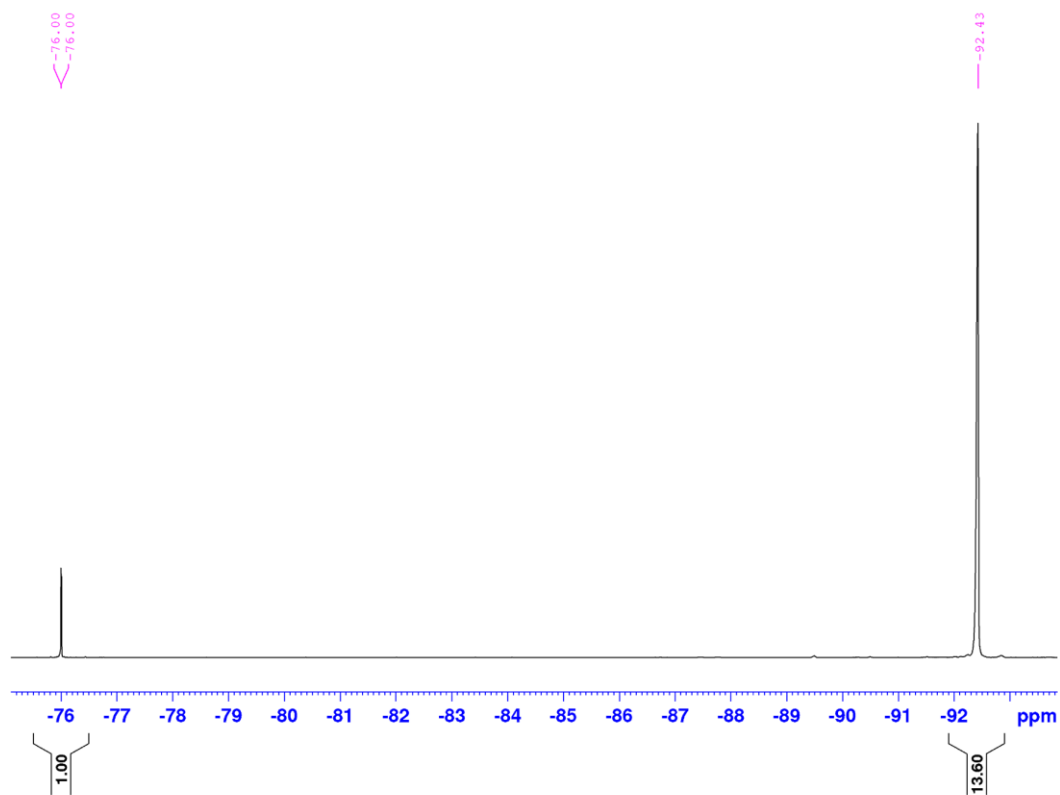


Figure B.12. ^{19}F NMR spectra of TN7. Reference compound trifluoroacetic acid displays chemical shift at -76 ppm.

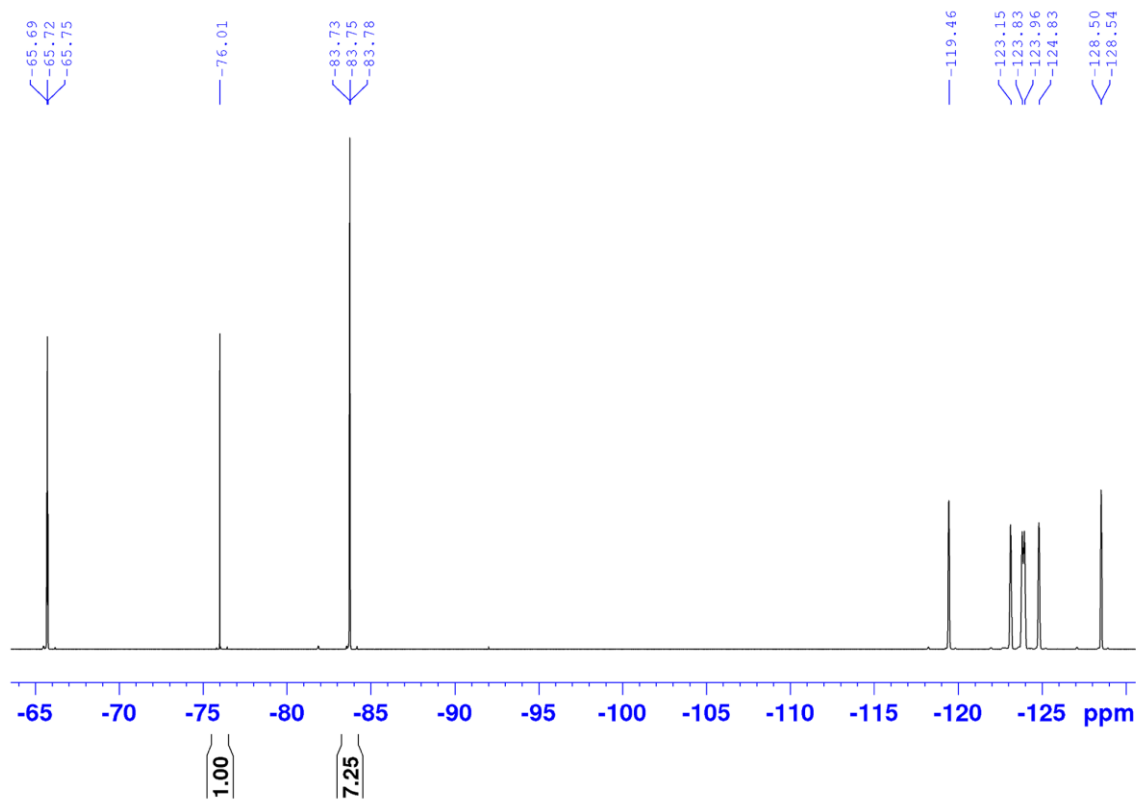


Figure B.13. ^{19}F NMR spectra of TN8. Reference compound trifluoroacetic acid displays chemical shift at -76 ppm.

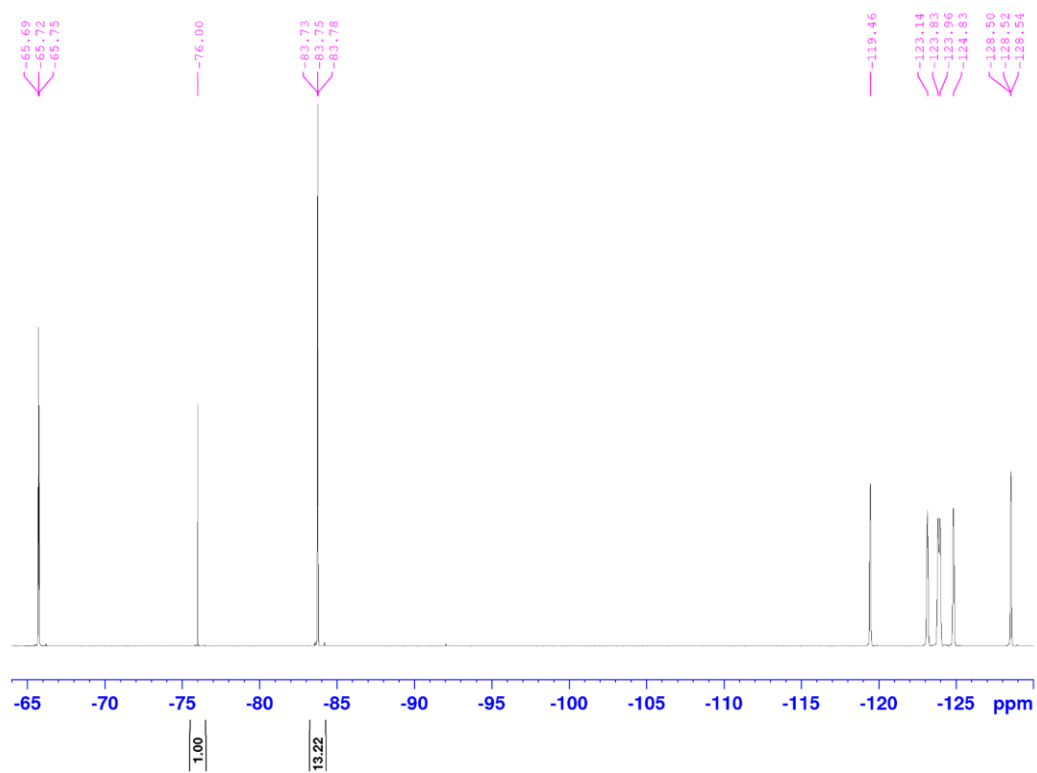


Figure B.14. ^{19}F NMR spectra of BN1. Reference compound trifluoroacetic acid displays chemical shift at -76 ppm.

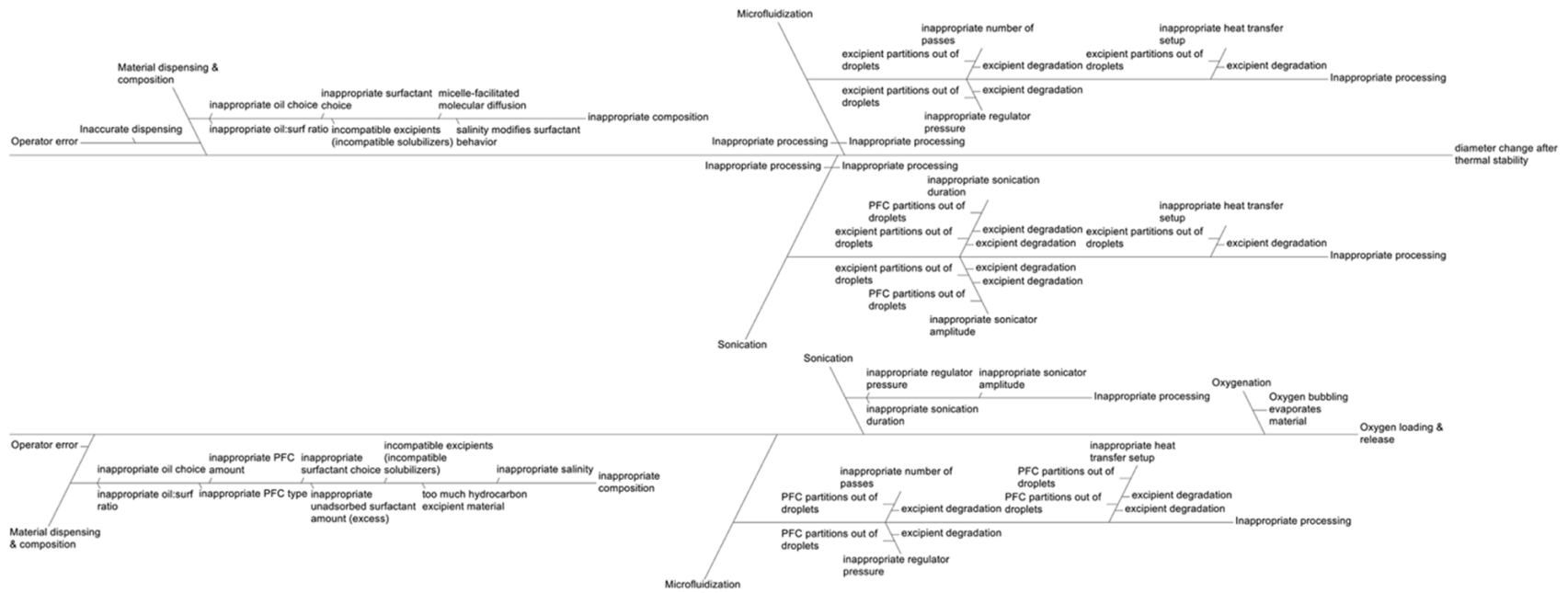


Figure B.15. Cause and effect diagrams for oxygen loading & release and size change after thermal stability. All branches of the diagram represent sources of variability of the quality attribute in question.

Appendix C. Chapter 4 Supplemental Data

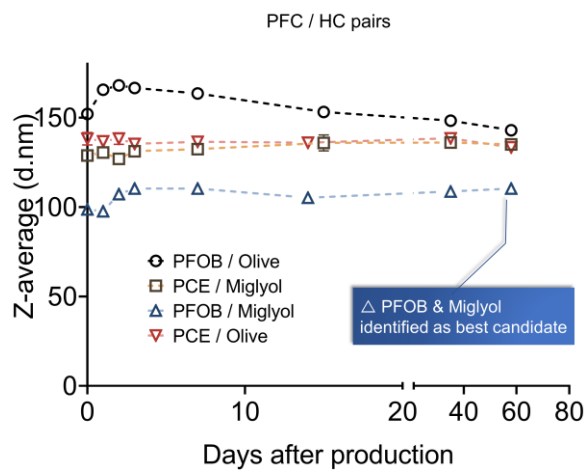


Figure C.1. Nanoemulsion sizes of four different perfluorocarbon (30 wt%) & hydrocarbon (6 wt%) pairs. Selection of the optimal pair was made based off the minimization of z-average.

Table C.1. General compositions of generation 1 and 2 nanoemulsions. G2-NE1 (bottom row) was used to validate the C_{\max} model developed in Chapter 3. PFC, perfluorocarbon; PCE, perfluoro-15-crown-5-ether; PFOB, perfluorooctyl bromide; IP, internal phase; HC, hydrocarbon; CP, continuous phase; MLR, multiple linear regression

Index	Screening Design Factors ^{††}						$f_{\text{PFC}}^{\dagger\dagger}$	$C_{\max} / \log f_{\text{PFC}}$ (mg/L)
	PFC type	IP fraction*	HC:PFC ratio*	Transcutol fraction*	CP	Number of passes*		
G1-NE1	PCE	0.080	1.857	0.30	Saline	6	0.028	-0.814
G1-NE2	PFOB	0.080	1.857	0.30	H ₂ O	4	0.028	-0.748
G1-NE3	PCE	0.080	0.857	0.05	H ₂ O	4	0.043	-0.966
G1-NE4	PFOB	0.080	0.857	0.05	Saline	4	0.043	-0.956
G1-NE5	PCE	0.143	1.857	0.05	Saline	4	0.050	-1.123
G1-NE6	PFOB	0.143	1.857	0.30	H ₂ O	4	0.050	-1.188
G1-NE7	PCE	0.143	0.857	0.30	Saline	4	0.077	-1.672
G1-NE8	PFOB	0.143	0.857	0.05	H ₂ O	6	0.077	-1.591
G2-NE01	PFOB	0.220	0.407	0.00	PBS	5	0.156	-4.634

^{††} * Indicates parameter in the earlier established, reduced MLR model for C_{\max} fit to G1-NEs (refer to Chapter 3)

^{††} PFC fraction is calculated by $f_{\text{PFC}} = \frac{\text{IP fraction}}{1 + \text{HC:PFC}}$

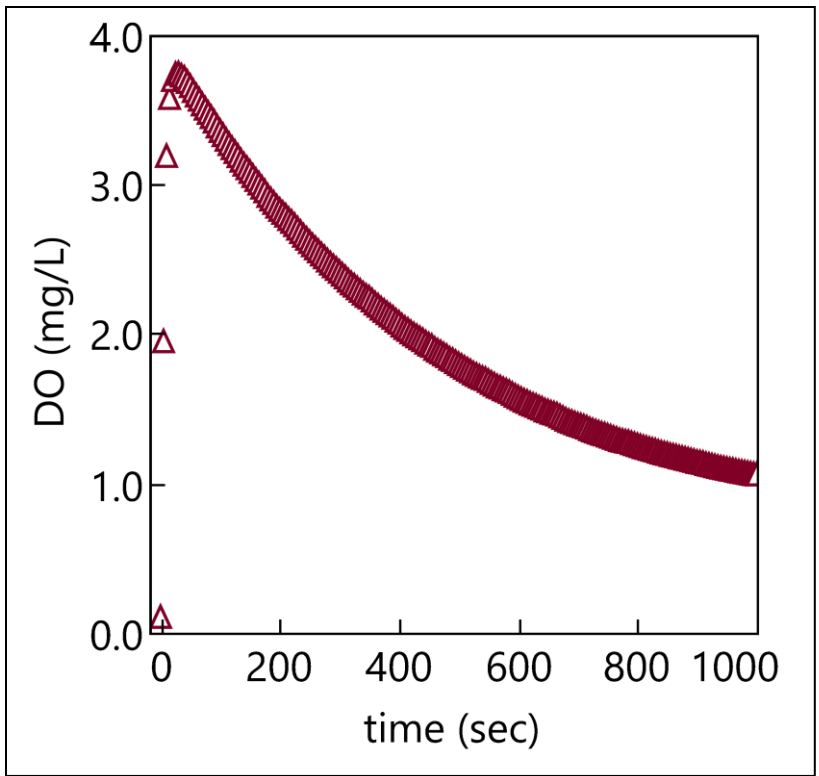


Figure C.2. *In vitro* oxygen release profile of a representative G2-NE, NE01.

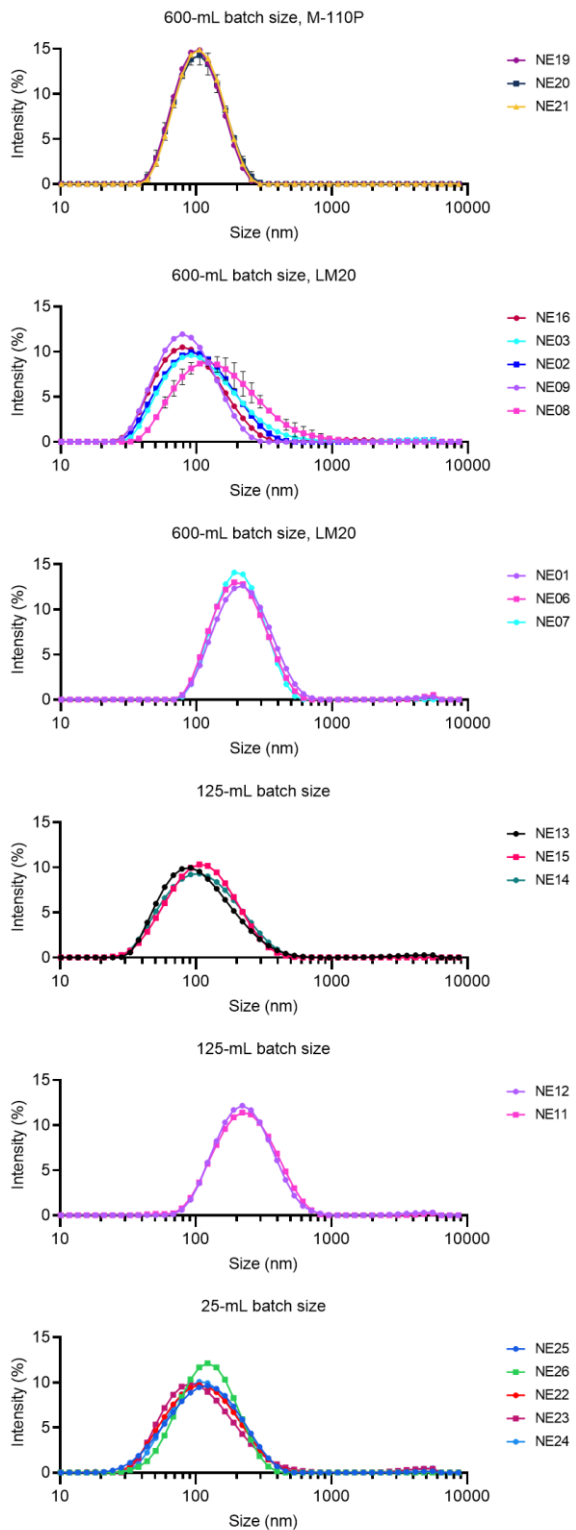


Figure C.3. Size distribution comparisons at each batch size demonstrate the process reproducibility within batch size and processor.

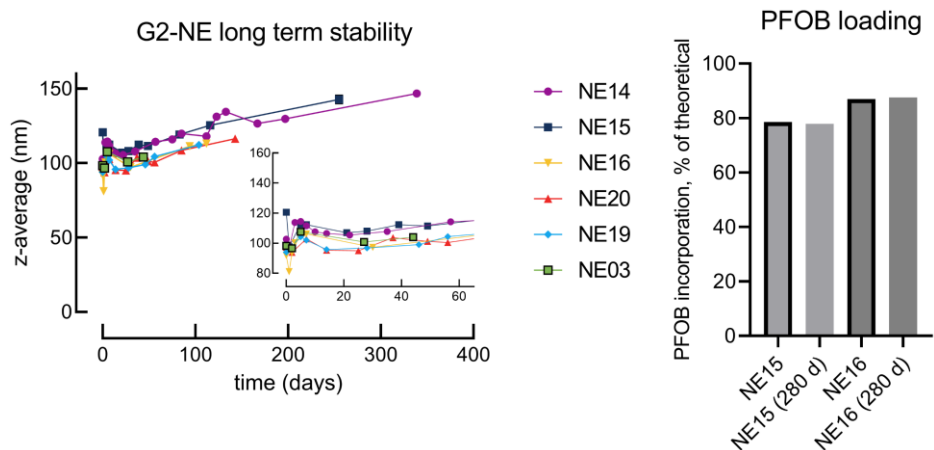


Figure C.4. Long term colloidal stability of G2-NEs. Left panel shows the z-average for selected batches. The inset shows the same data rescaled to show only the first 60 d in greater detail. Right panel shows 280-day ^{19}F qNMR follow ups for two representative G2-NEs.

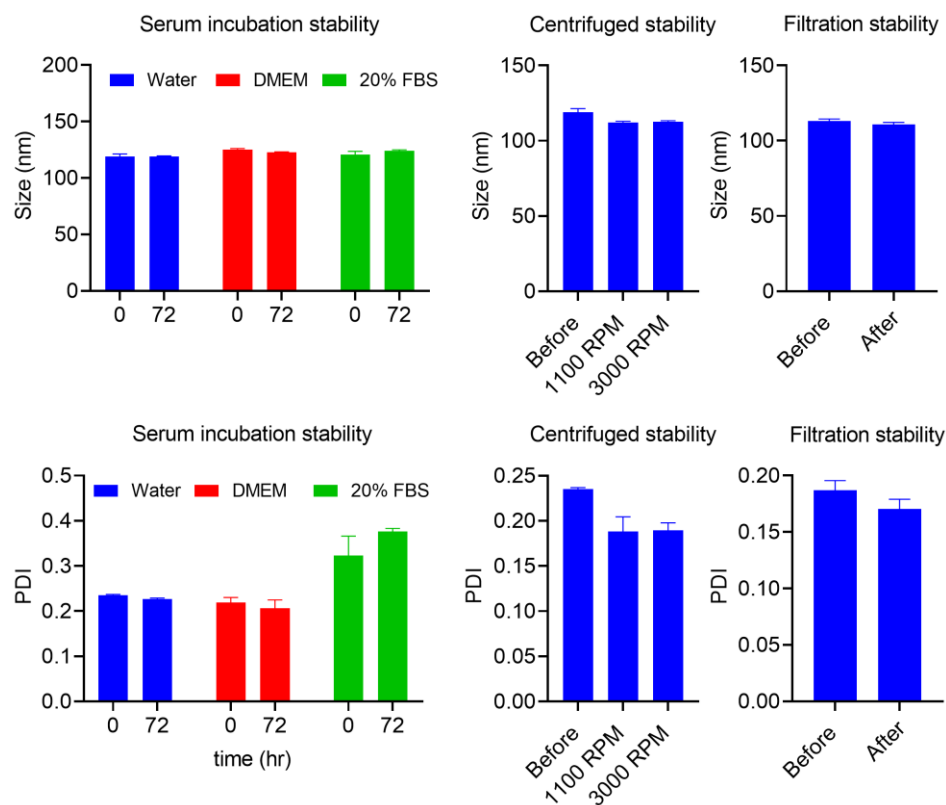


Figure C.5. Stress stability of G2-NE16 as a representative sample. From left to right: serum incubation stability, centrifuged stability, and filtration stability. From top to bottom: z-average size and PDI. DMEM, Dulbecco's Modified Eagles Medium; FBS, fetal bovine serum.

Table C.2. Eigenvalues and variance explained from the first 10 principal components from PCA on all data.

PC Number	Eigenvalue	Percent	Cum. Percent
1	171.6527	77.201	77.201
2	32.633	14.677	91.878
3	11.1549	5.017	96.894
4	4.3847	1.972	98.867
5	1.0945	0.492	99.359
6	0.5627	0.253	99.612
7	0.4259	0.192	99.803
8	0.163	0.073	99.877
9	0.1106	0.05	99.926
10	0.0696	0.031	99.958

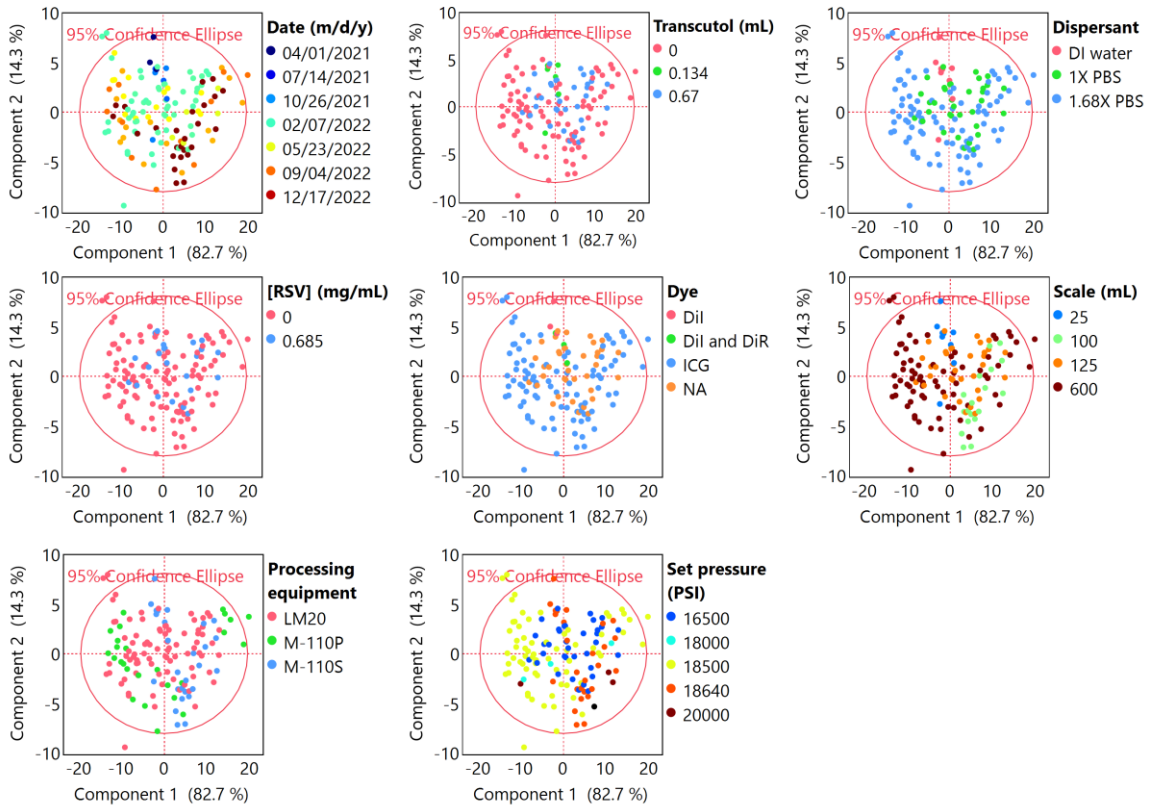


Figure C.6. Examination of factor variance in PCA scores space from Cluster 1 defined in the text.

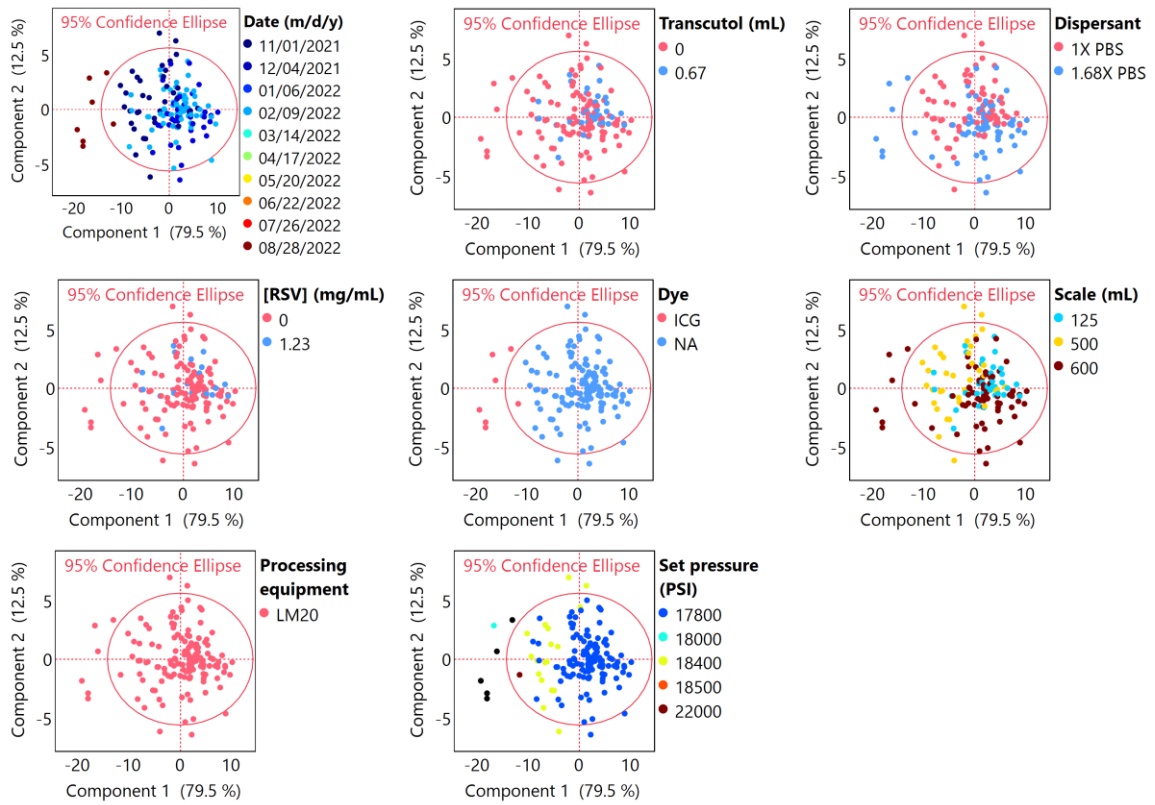


Figure C.7. Examination of factor variance in PCA scores space from Cluster 2 defined in the text.

Appendix D. Chapter 5 Supplemental Data

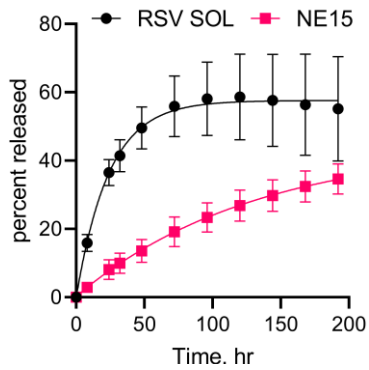


Figure D.1. Resveratrol *in vitro* drug release data without accounting for drug degradation.

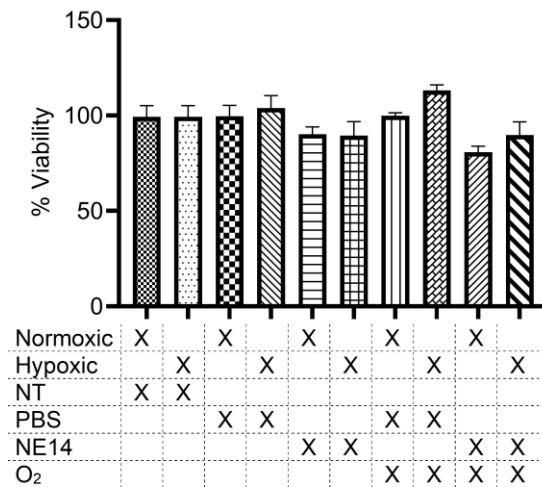


Figure D.2. Cell viability of macrophage hypoxia conditions measured by Cell Titer Glo. pO_2 in the hypoxic environment was 1%. pO_2 in the normoxic environment ranged from 18-20%. Treatment concentration was constant at 40 $\mu\text{L}/\text{mL}$. O_2 indicates the treatment was equilibrated with O_2 for 10 min prior to treating the cells. NT, no treatment; PBS, phosphate buffered saline.

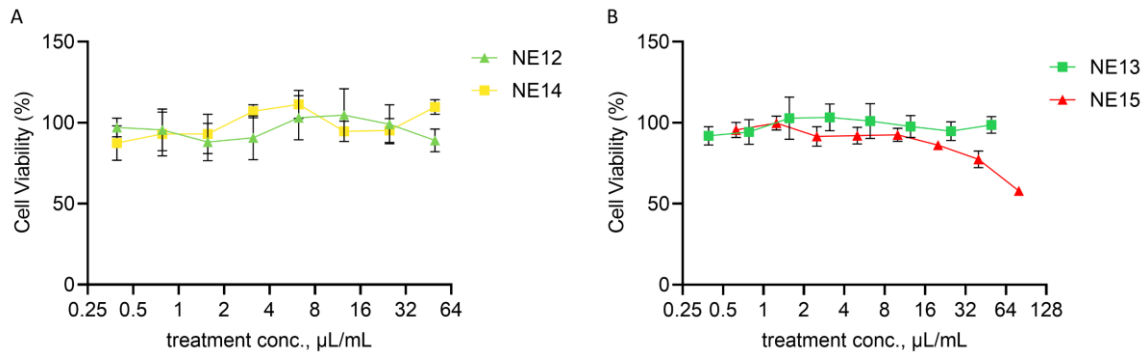


Figure D.3. Cell viability of representative G2-NEs measured by Cell Titer Glo. (A) Resveratrol-free formulations, and (B) resveratrol-loaded formulations.

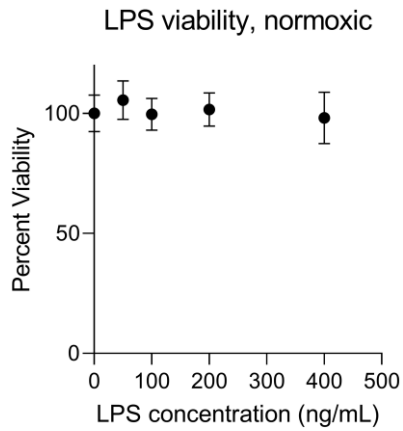


Figure D.4. Cell viability of lipopolysaccharide (LPS) conditions used in the nitrite/nitrate assay measured by Cell Titer Glo.

Appendix E. Chapter 6 Supplemental Data

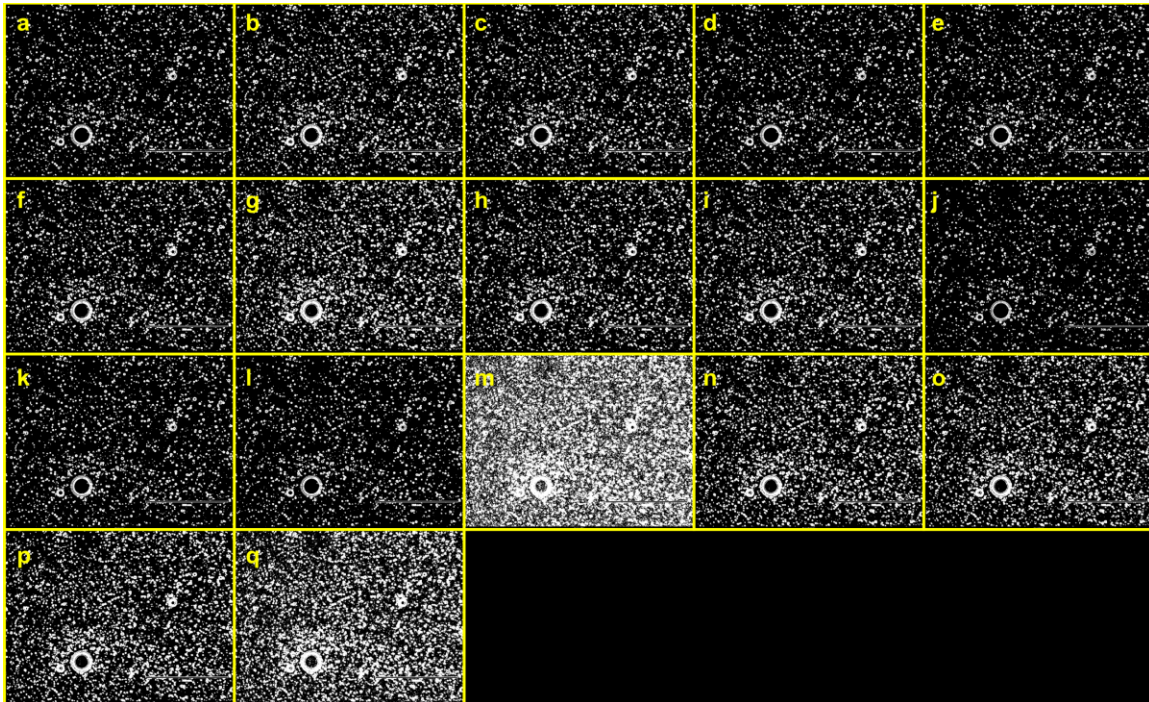


Figure E.1. Automatic thresholding algorithm montage resulting from imageJ's 'try all' menu option. Algorithms in alphabetical order of panel labels (a-q): Default, Huang, Huang2, Intermodes, Isodata, Li, MaxEntropy, Mean, MinError(I), Minimum, Moments, Otsu, Percentile, RenyiEntropy, Shanbhag, Triangle, Yen.